REPORT

OF

HYDROGRAPHIC RESEARCHES

No. 15, March, 1980

駿河トラフ（舟状海盆）のマルチチャンネル反射法音波探査

桜井　操*・茂木昭夫*

MULTICHANNEL SEISMIC REFLECTION PROFILING IN THE SURUGA TROUGH

Misao Sakurai and Akio Mogi

Received 1979 September 10

Abstract

During January 1978, the Hydrographic Department, Maritime Safety Agency acquired approximately 94km of digitally recorded 48 channel seismic reflection data using high-pressure, large volume air guns on the R/V Takuyo-maru (Japan Petroleum Exploration Co.) on three track lines in the Suruga Trough off Sizuoka Prefecture, Japan (Figure 1, 2, 3 and Table 1).

Three multichannel seismic reflection profiles, which reveal a structure of the upper crust having a depth of 11–14km, were processed from the data using the common depth point technique with 24 folds

The authors found strata and faults from interpretation of the profiles (Figure 4), and also drew P wave velocity structure derived from velocity analysis using the common depth point technique (Table 2 and Figure 5).

Especially, the authors considered fault zone along the Suruga Trough as follows:

1) The fault zone located along the west side of the Trough axis is vertical or slanted apparently westward.

* 測量課　Surveying Division

2) The fault zone is possibly a reverse fault, because the Senoumi North Bank and South Bank in the western part of the fault zone are tilted blocks tilting to the west with the fault zone as a fault scarp, and strata of the eastern part of the fault zone show homocline-like structure slanting toward the Trough.

3) The strike of the fault zone shows a largely north-south trend.

4) The fault zone was formed after sedimentation of the B layer corresponding to the middle to late Tertiary (Table 3), and the tectonic movement which produced fault zone has continued until the recent period.

1. まえがき

1978年1月海上保安庁水路部は，駿河トラフの地殻深部構造を明らかにするため，3本の横断測線について総測線長94kmにわたるマルチチャンネル反射法音波探査を実施した（Figure 1).

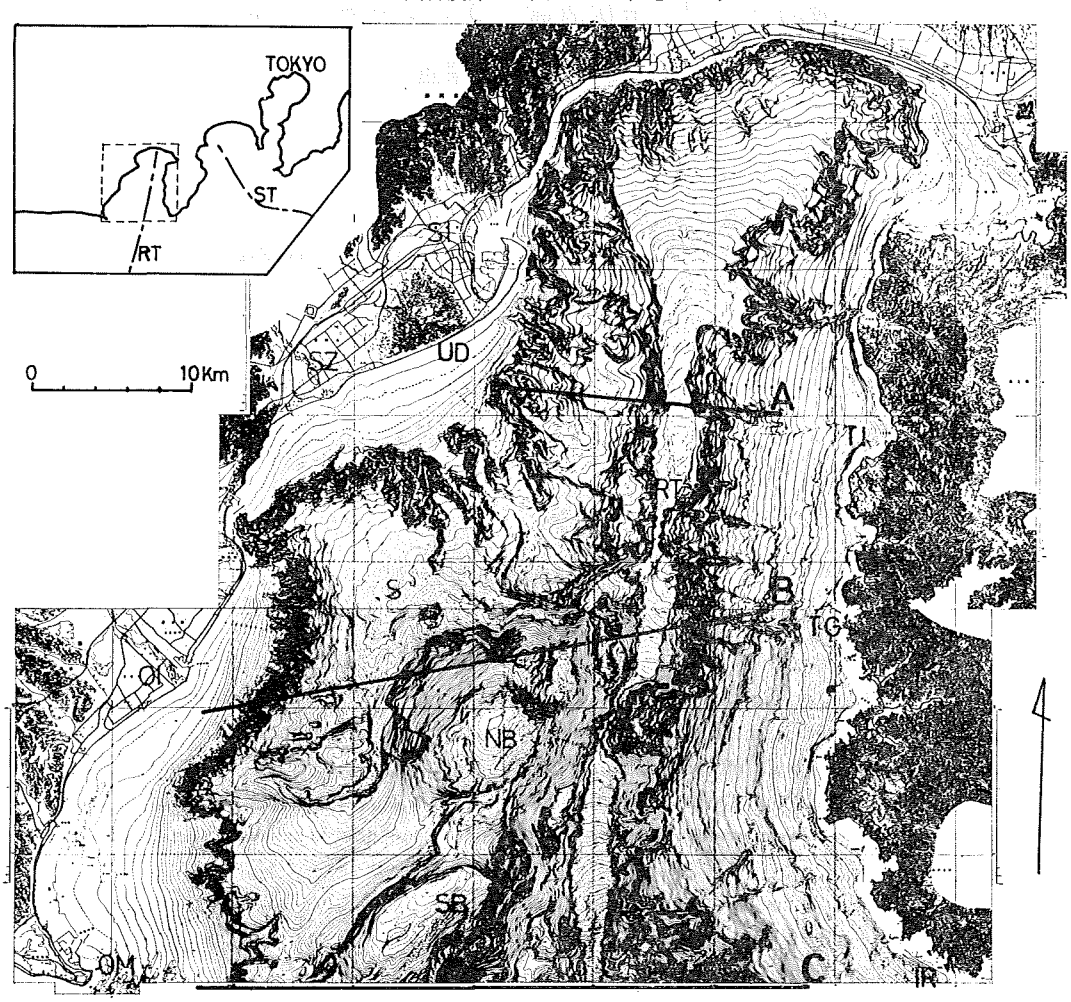

Figure 1 Location map of multichannel seismic reflection profiles of the Suruga Trough A・B・C: track lines, NB: Senoumi North Bank, SB: Senoumi South Bank, RT: Suruga Trough, ST: Sagami Trough, S: Senoumi Basin, UD: Udo Hill, SI: Simizu, SZ: Sizuoka, OI: Oigawa, OM: Omaezaki, TI: Toi, TG: Tago, IR: Irozaki, Bathymetry is from M. S. A. (1978, 1979).

駿河トラフは，南海トラフ東端から北上して駿河湾に入り込んでいる比較的せまい舟状海盆である．最近，このトラフに東海地震の発生が懸念されるに至り，東海地域について，地震予知や防災を目的とする地学的な基礎的研究が，関係省庁，研究機関などによって組織的に進められている．マルチチャンネル反射法音波探査もその一環として実施された．音波探査による駿河湾の海底地質構造調査は，これまで奈須ら（1968）を初めとする多くの調査研究が行われてきたが，明らかにされた構造は海底下約1km未満の浅部にとどまっており，マルチチャンネル反射法音波探査による深部構造の調査が期待されていた．

反射法音波探査は，1950年代末に Lamont-Doherty Geological Institute によって開発された技術であるが，1960年代になってエアガン(air gun)，マルチチャンネルハイドロフォンやコンピュータ技術を用いたマルチチャンネル反射法音波探査装置が開発され，深部構造の調査が可能になった．マルチチャンネル反射法音波探査は，調査船から等間隔に配置したハイドロフォン(群)の列―マルチチャンネル　ストリーマーケーブル（multichannel streamer cable）―を曳航しながら一定距離ごとに可聴周波数の音波を発射し，各発射点において，すべてのチャンネルの入力をデジタル化して磁気テープに集録し，共通反射点（common depth point (CDP)）トレースの編集，ＣＤＰ重合，マイグレーション(wave equation migration)などのデジタルコンピュータ処理によって，海底下深部の音波探査プロファイルを取得する技術である（Figure 2）〔竹内・石井（1968），井川・斉藤（1973），Dobrin（1976）〕．

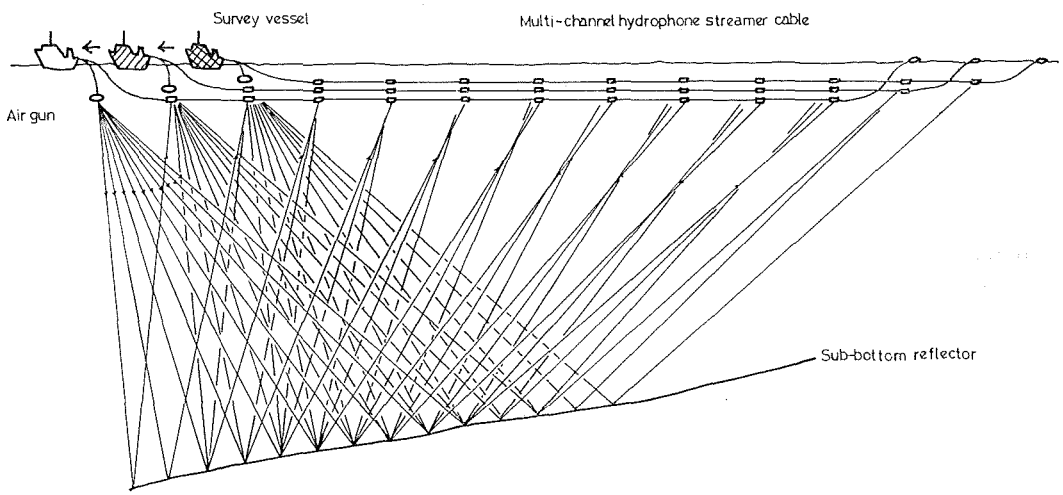

Figure 2　Multichannel seismic reflection profiling
In this survey, air guns were fired once every 50m, and seismic data at 25m intervals along a track line were digitally recorded through 48 channel streamer cable every firing. Finally, 24 seismic data were stacked each common depth point.

今回のマルチチャンネル反射法音波探査の結果，静岡―土肥間18km，大井川―田子間37km，御前埼―石廊埼間39kmの各測線について，それぞれ海面下11～14kmに達する音波探査プロファイルを得た．この報告では，取得した音波探査プロファイルに基づく駿河トラフの深部構造，及びＣＤＰ重合過程で得られた層内速度による構造について記載し，断層について概括な考察を加えた．以下調査方法，海底地形および表層地質の概要，深部構造，層内速度分布からみた成層構造について述べる．

2. 調査方法

調査作業は，水路部から受注した石油資源開発株式会社が実施したものである．調査船は拓洋丸（340トン）で，48チャンネル—全長2,750mのストリーマーケーブルと，エアガン18箇，総吐出容量15.7ℓを両舷に分けて曳航した．深度はストリーマーケーブル15m，エアガン10mである．エアガンは航走距離50mごと（船速5ノットのとき約20秒ごと）に，吐出圧力140kg/cm²で同時に発音した．ストリーマーケーブルのハイドロフォン(群)の間隔も50mである．音波探査データは，Texas Instruments の DFS Ⅳ デジタル探鉱機に集録し，最も船尾に近いハイドロフォン入力はアナログ記録し，モニターした．データ集録時間長は海底下8秒，サンプル間隔は4ミリ秒である．

調査測線は，「1978年伊豆大島近海地震」の発生や天候不良などのため，2ないし3部分測線に分割して行った（Table 1）．Figure 3 に10点ごとの発音点の位置を示す．調査測線の計画にあたっては，駿河トラフ軸の構

Table 1 Track line and shot point number

track line	shot point number	date of survey
A—1	240— 1	Jan. 14 1978
A—2	367—211	〃 15
B—1	1—270	〃 15
B—2	300— 1	〃 15
B—3	600—271	〃 18
C—1	1—480	〃 18
C—2	330— 1	〃 19

造のほか，糸魚川—静岡線の南側延長にあたるトラフ西側海域の構造にも留意した。位置の決定には Decca Hi-Fix を用いた．

音波探査データは，ＣＤＰ重合による通常処理を行った．共通反射点間隔25m，重合数24である．速度解析は測線上3kmごとに定速度走査法によって実施した．通常処理後，トラフの特徴的な構造を示す石花海（せのうみ）、北堆から駿河トラフ軸までの区間（測線B—2，発音点番号1—201）10km分についてマイグレーション処理をして顕著な反射点によって生ずる散乱波パターンを消去した．

3. 海底地形・表層地質構造の概要

マルチチャンネル反射法音波探査と前後して，駿河湾の詳細な1/5万海底地形図・同地質構造図が作成された（海上保安庁水路部，1978：同 1979）．この図に基づいて，あらかじめ測線沿いの海底地形，表層地質構造の概要について述べる（Figure 1）．

測線Aは，駿河湾北部の有度丘陵沖合の水深360m付近から，伊豆半島の土肥沖，水深約550mまでのほぼ東西方向の区間である．有度丘陵側の2/3区間の海底地形は，大陸棚外縁付近から大陸斜面を南東に下刻する海底谷群と，水深820m付近に広がる小平坦面によって特徴づけられ，水深約1,530mでトラフ底に達している．トラフ底は，北から南に向かって緩やかに傾斜する幅約1.6kmの比較的平坦な所である．伊豆側の1/3区間は，大陸斜面下部に発達するガリー（gully）状の海底谷にほぼ並走する．構造について見ると，有度丘陵側の大陸斜面は北西—南東方向の断層群，伊豆側は北北東—南南西方向の推定を含む断層群によって切られている．

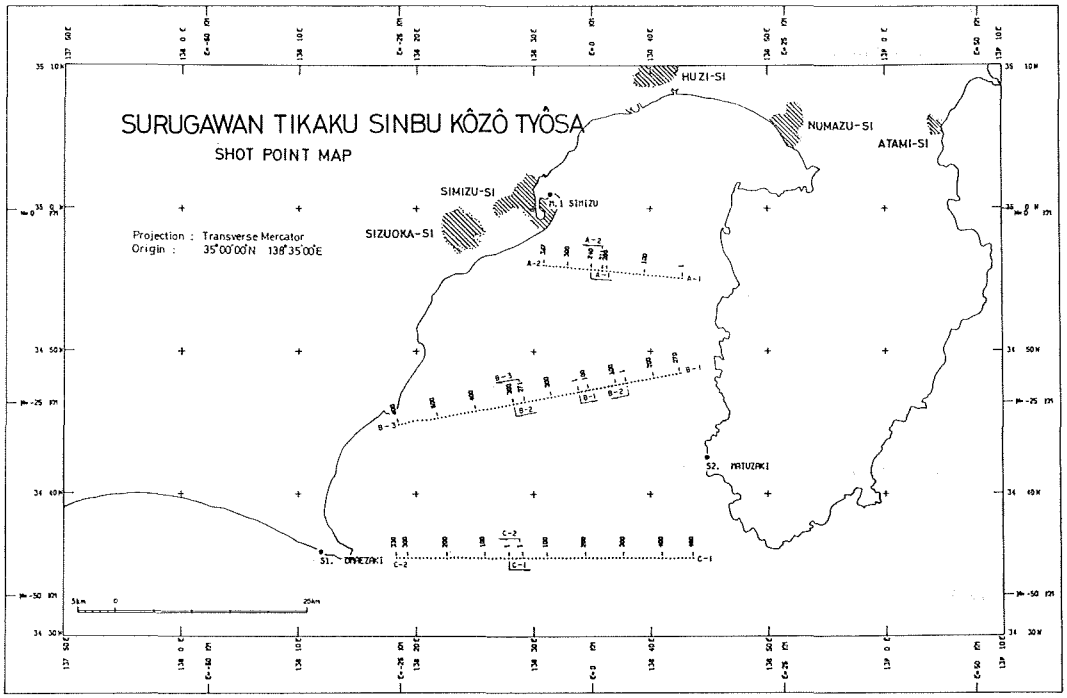

Figure 3 Shot point map

測線Bは，駿河湾中部の大井川河口沖，水深約20mの地点から東北東に延び，石花海北堆（以下，北堆）の北側を通って伊豆半島中部の田子沖，水深約 330m に達する．大井川河口沖の大陸棚外縁から，北堆の北西麓にかけては石花海海盆にあたり，北堆西麓の海底地すべり跡と見られる地形の下流域を形成している．別の海底地すべりが見られる北堆の北斜面からトラフ底までは，比較的急斜面となり，途中には鞍部に隔てられた海丘（以下海丘）がある．トラフ底は水深 1,680～1,690m，幅約1.5km のほぼ平坦な面を形成している．伊豆側の区間は大陸斜面の下部にあたり，ガリー状の海底谷と交差している．地質構造については，石花海海盆及び北堆北東方の斜面や海丘付近には南北方向の断層が推定されており，石花海海盆の大井川側の斜面では，海岸線にほぼ平行な北東—南西方向性の断層に変わっている．また伊豆側は西北西—東南東，北東—南西及び北—南方向性の断層が測線付近の大陸斜面に見られる．

測線Cは，駿河湾湾口の御前埼東方，水深約 50mの地点から東方に延び，石廊埼の西方，水深約 440mに達する．御前埼沖からトラフ底までの海底地形は，大陸棚，同大陸棚と石花海南堆（以下，南堆）との間の鞍部，南堆南縁の傾斜が比較的緩やかな海域，南堆の南東側斜面からトラフ底までの比較的急斜面の海域によって構成されている．トラフ底は水深約2,460m，北から南に向かって緩やかに傾斜する平坦面を示し，幅約0.8kmと狭くなっている．伊豆側の区間は，大陸斜面の延びの方向が伊豆半島南西側で北西—南東を示す海域であり，海底谷が複雑な海底地形を形成している。表層の地質構造は，大陸棚—南堆間の鞍部に北東—南西方向性の断層が解釈されている．

4. 深部構造

音波探査プロファイルから解釈できた深部構造を，音響的層相などに基づく層区分，成層構造，断層に分けて

述べる．音波探査プロファイルとその解釈を Figure 4 に示す．

（1） 音響的層相などに基づく層区分

層の境界は一般に不明瞭であるが，堆積環境の変化を示す非整合面や音響的層相，散乱波によって生ずる記録パターンの分布，後述する層内速度分布から見た成層構造などに基づいて，上位からA，B，C，の3層に分けて見ることができる．

最上位のA層は，成層が比較的明瞭でかつ連続性の良いのが特徴である．特に，清水沖の水深約820mの平坦部や北堆の北側斜面などでは著しい．A層の最大層厚は約0.5秒（音波の往復に要する時間）である．

B層は，成層がA層に比べて不連続かつ不明瞭となり，層の追跡が難しくなる．清水沖の820m平坦部や北堆の北西側斜面部では，A層がB層に対してアバット（abut）している．B層の層厚は3～5秒である．

C層は，散乱波による強い反射面が優勢となる層である．3～3.3km/sec付近の速度構造（後述）が辛うじてその境界の存在を支持している．

（2） 成層構造

層面のSN比が一般に悪く，同一層準の面を追跡することは非常に難しい．断片的な強い反射面を追跡しながら測線ごとの成層構造を記載する．

〔**測線A**〕 上位層の大半を占めるB層は，静岡及び伊豆半島の両側から駿河トラフの南北方向の軸（以下トラフ軸）に向かって緩やかに傾き下がっている．静岡側の大陸棚外縁付近，清水沖の820m平坦部付近，トラフ軸付近は，層の追跡が特に難しくなっており，層が大きく変位変形している可能性がある．静岡及び伊豆半島側の大陸斜面には浸食によって形成された起伏が認められる．また，清水沖の820m平坦部及びトラフ軸には，厚さ0.2～0.4秒のA層が堆積し，比較的平坦な海底を形成している．海面下約5秒以深は，C層とした強い散乱波によるパターンが卓越してくる所である．

〔**測線B**〕 この測線の特徴的な構造は，石花海海盆がAB両層の下方撓曲（down warping）の軸部にあたっていること，石花海海盆の北堆側斜面には同海盆に向かって厚くなる成層の明瞭なAB両層が見られ，A層は前述のようにB層に対してアバットしていること，そしてこのA層（あるいはB層も）は，同海盆の反対側の静岡側斜面を構成している比較的透明な層と同時異相関係にあること，石花海海盆と北堆付近の海底は（南堆付近も同様であるが）下方あるいは側方浸食を受けていること，北堆の東側斜面にあたる同堆とトラフ軸の間の地域は海丘など大きな起伏を伴う急斜面を示し，B層の露頭が確認あるいは推定できること，伊豆半島側のA及びB層は北堆東側斜面基部のトラフ軸に向かって緩やかに傾いていること，トラフ底はA層に埋積されて平坦化していること，石花海海盆の西部や北堆付近の海面下3～5秒に著しい散乱波パターンが見られ，北堆付近では海底地形と調和して高まっているように見えることなどである．

〔**測線C**〕 南堆付近のB及びC層は見かけ上西方に傾斜しているが，石花海海盆の南縁にあたる御前埼沖の大陸棚と南堆間の鞍部付近においては，これらの層の追跡は困難となっている．また南堆の東縁からトラフ軸にかけてのB層は，トラフ軸に向かって緩やかに傾斜している可能性が高いが明瞭ではない．伊豆半島側のB層は，見かけ上西に向かって緩やかに傾斜するか，またはほぼ水平に近い成層を示す．C層とした散乱波の卓越する層は，断層によって数キロメートル単位の地塊に分かれる（後述）．各地塊の層面はトラフ軸をはさんでそれぞれ南堆側では見かけ上西方に，伊豆半島側では東方に緩やかに傾斜しているのが見られ，上位のB層との間は非整合関係を示す．

Figure 4 Multichannel seismic reflection profiles and its interpretations.
(a) : Line-A section (compiled).

thin rigid line (horizontal) : main reflector
thick rigid line (vertical) : fault
Depth shows in two way travel time, seconds.
Vertical exaggeration is 2 to 1.2.

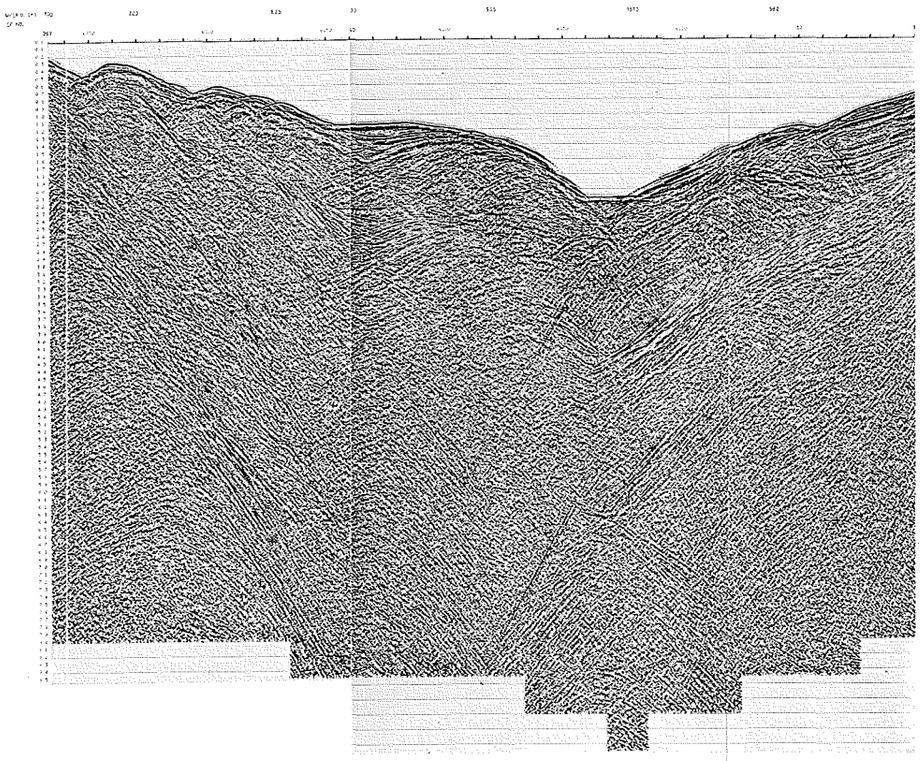

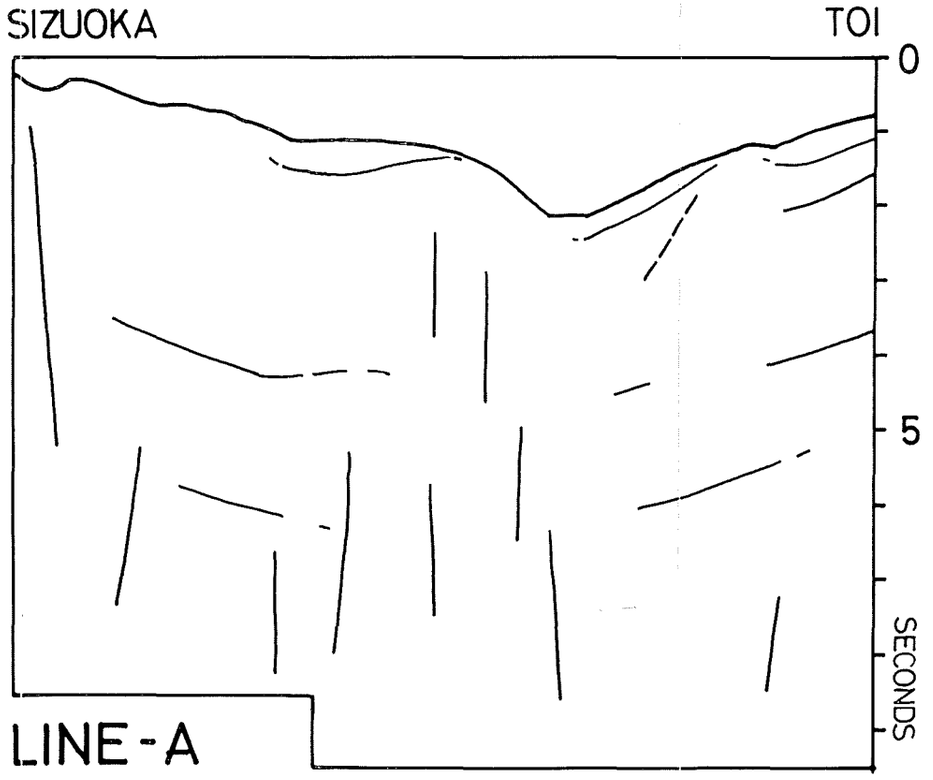

Figure 4–(b)

Line-B section (compiled).

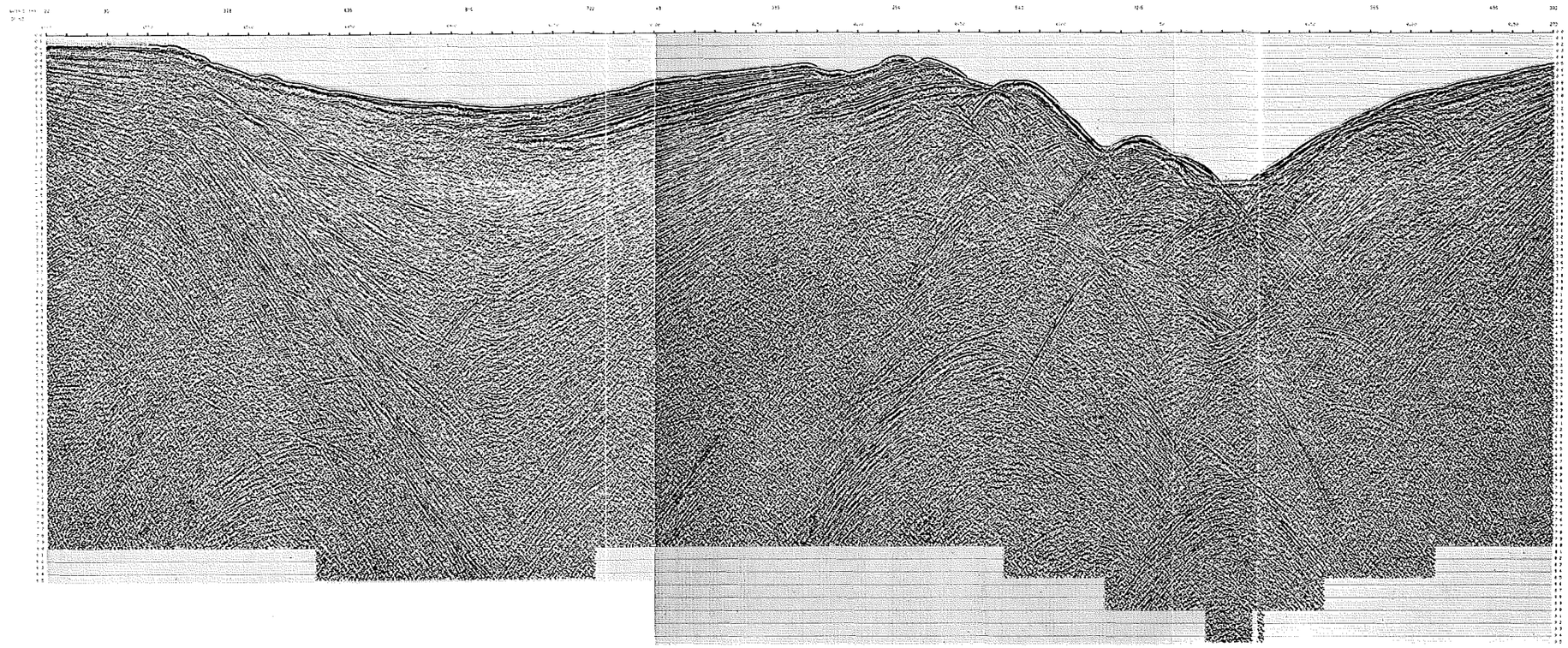

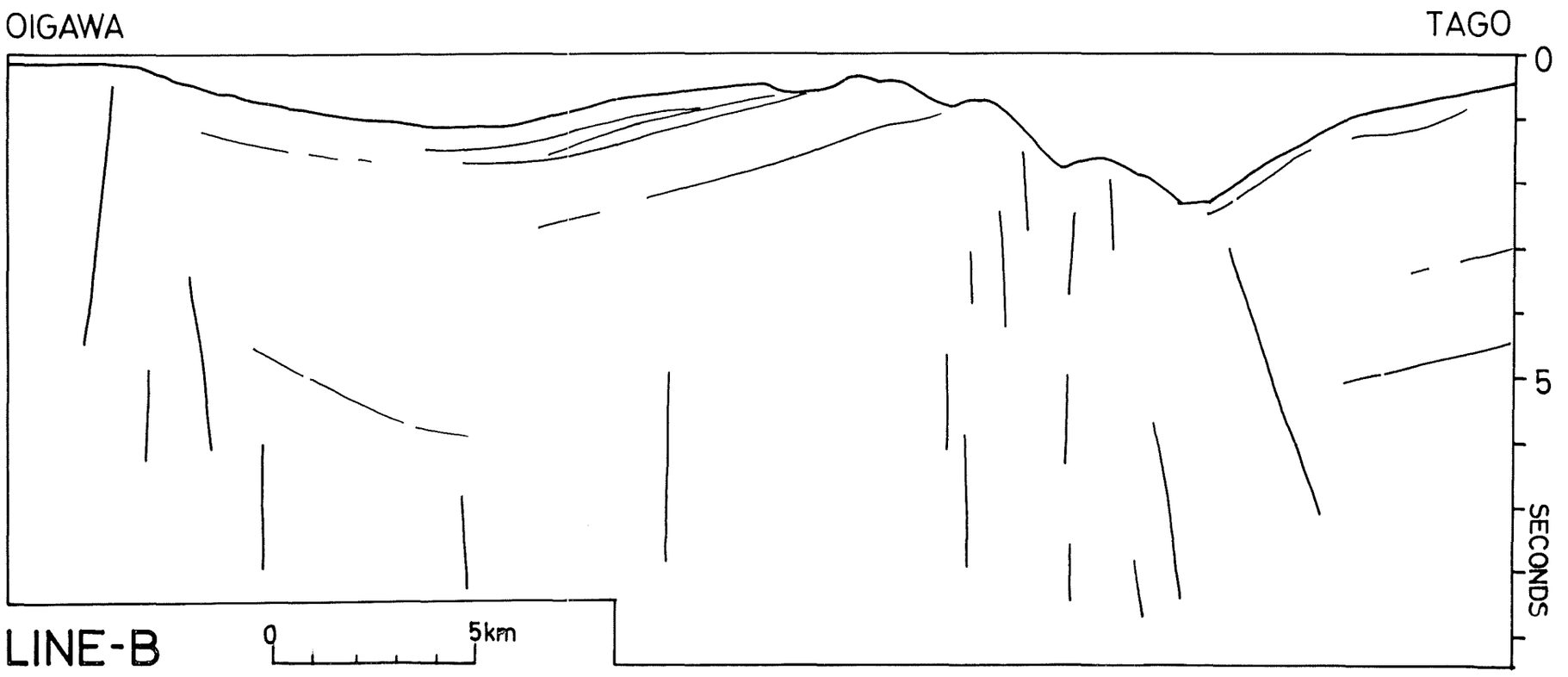

Figure 4-(c)

Line-C section (compiled).

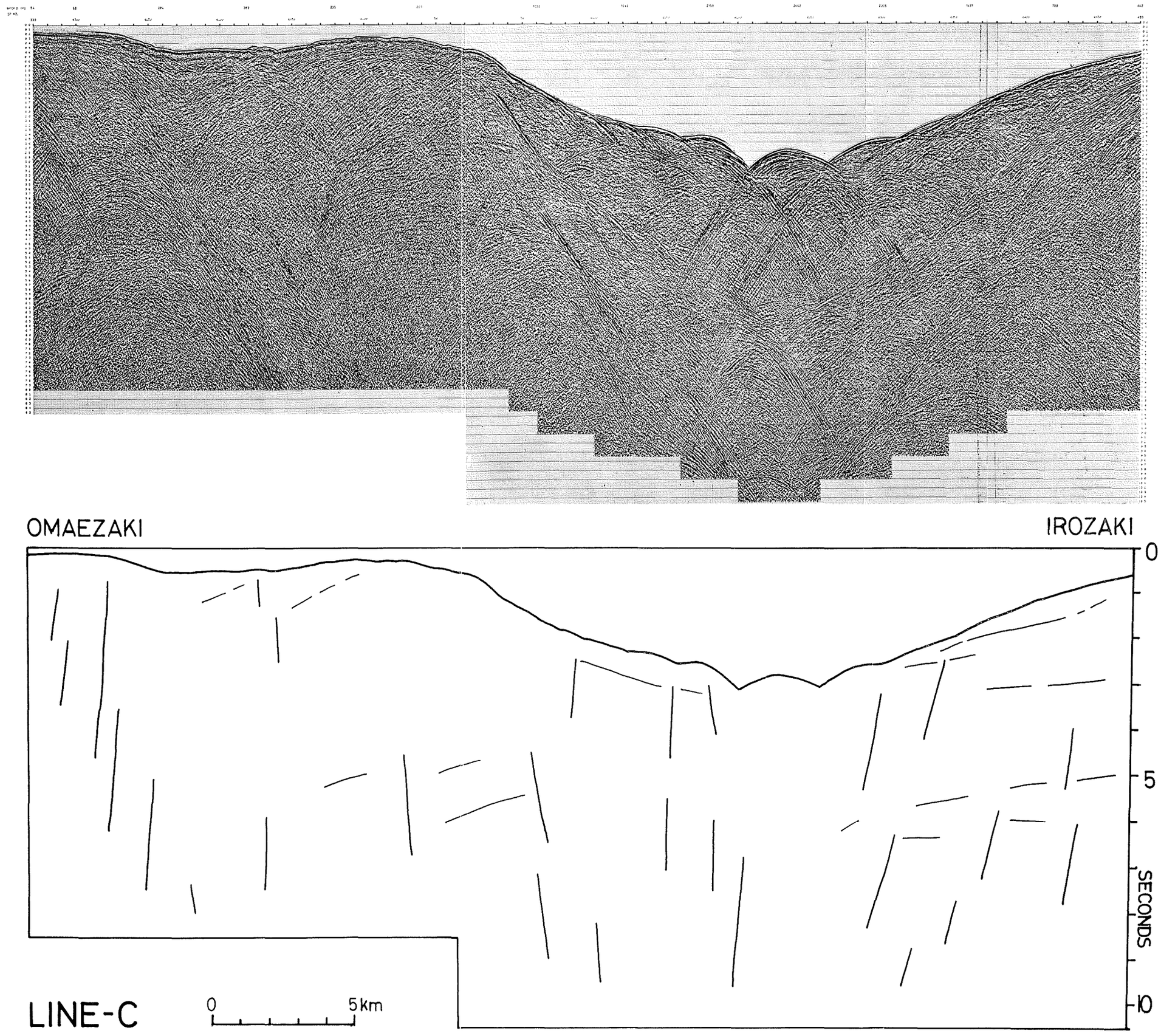

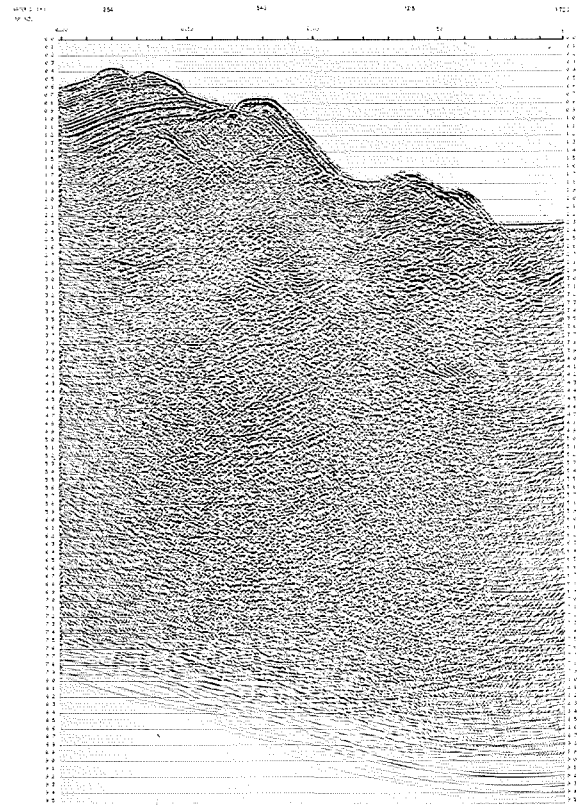

Figure 4-(d) Migration section (a part of B-2).

(3) 断 層

ほとんどの断層は，断層面に沿って生ずると考えられている散乱波パターンの連続性に基づいて解釈した (Dobrin 1976, Fitch 1976).

i まず地域的には断層は，トラフ軸付近と静岡—御前埼側の大陸棚外縁付近の2箇所に集中が見られ，それぞれの状況は次のとおりである.

（トラフ軸付近の断層群） 測線A及びBの断層群は，ともにトラフ軸西側の大陸斜面下部や北堆東縁の急斜面に分布しており，清水沖の820m平坦面の外縁付近や北堆—海丘間には，深さ7～8秒に達するほぼ垂直に近い断層群があって，互いに重なるようにして深部に延びている．これらの断層群は，それぞれ見かけ上西方に傾く断層帯を構成している可能性がある．一方，北堆東方のトラフ軸には，見かけ上東方に傾斜する断層面がある.

測線C上の断層は，トラフ軸付近の南堆寄りを境にして，南堆側は見かけ上東方に傾斜する断層面を，伊豆半島側は西方に傾斜する断層面を見せている．これらの断層は，トラフ軸の南堆寄りに，ほぼ垂直方向ないし南堆側に傾斜する大きい断層帯を構成している可能性がある．また伊豆半島側にも，見かけ上西方に傾斜するやや低角度の大断層帯が解釈出来る.

（静岡—御前埼側大陸棚外縁付近の断層群） 測線A・B・Cの大陸棚外縁付近にあたる有度丘陵沖，大井川河口沖，御前埼沖には連続して追跡できる深さ3～5秒の断層があり，ほぼ垂直ないし見かけ上西方に傾斜する顕著な大断層帯を構成している．このうち，御前埼沖の断層は他に比べてせまい間隔で重なり合っている．このほかの断層として御前埼—南堆間の鞍部，すなわち石花海海盆の南北軸延長上に，見かけ上東方に傾斜する断層がある.

ii 次に断層の分布深度については，大きくA・B層，及びC層以下を切る断層に分けて見ることができる．A・B層を切る断層は，トラフ軸，静岡—御前埼側大陸棚外縁付近などに集中して分布する．これに対して，下位のC層を切る断層は上位層に比べて多数認められるが，集中度がやや低くほぼ全域にわたっていると見られ，C層を地塊化している可能性がある.

5. 層内速度分布から見た成層構造

地殻構造を調査するために，屈折波によって地震波速度を観測し成層構造を調べることが行われる．音波探査データのCDP重合処理のために行った速度解析結果 (Table 2) を用い，速度分布から見た成層構造を調べた．解析された層内速度の精度は定量的に吟味していないが，解析資料の条件，特に層面の明確さに左右されるといわれている．調査範囲内の層内速度は1.5～4 km/sec 内にあり，等速度線は考察上の都合を考慮し，2.0，2.4，3.0，3.3 km/sec を選択し，図上で内挿，描画した (Figure 5)．その結果次のような事柄が明らかになった.

Table 2 Results of velocity analysis

ID : identification number　　CDP : CDP number

SPN : shot point number　　TIME : depth in two way travel time in second

VRMS : root mean square velocity　　VINT : interval velocity

LINE A-1

ID 1 CDP 48 SPN 1			
TIME SEC	VRMS M/SEC	VINT M/SEC	DEPTH M
0.720	1500	1500	540
0.900	1540	1691	692
1.280	1680	1972	1067
1.520	1860	2619	1381
1.860	2020	2618	1826
3.420	2350	2691	3925
4.200	2500	3072	5124
4.870	2600	3155	6181
5.650	2700	3256	7450
8.000	3100	3897	12029

ID 2 CDP 168 SPN 61			
TIME SEC	VRMS M/SEC	VINT M/SEC	DEPTH M
1.210	1500	1500	907
1.310	1510	1626	989
1.380	1560	2304	1069
1.520	1620	2123	1218
1.850	1660	1833	1520
2.580	1900	2403	2398
3.680	2250	2910	3998
5.150	2520	3094	6273
8.500	3100	3824	12677

ID 3 CDP 288 SPN 121			
TIME SEC	VRMS M/SEC	VINT M/SEC	DEPTH M
2.080	1500	1500	1560
2.250	1520	1746	1708
2.600	1680	2473	2141
3.290	1860	2421	2976
5.080	2300	2942	5609
7.380	2650	3294	9397
9.500	3000	3985	13622

ID 4 CDP 408 SPN 181			
TIME SEC	VRMS M/SEC	VINT M/SEC	DEPTH M
1.280	1500	1500	960
1.660	1580	1824	1307
2.000	1640	1906	1631
2.320	1820	2684	2060
2.820	1980	2596	2709
3.420	2100	2591	3486
4.490	2300	2847	5009
5.890	2580	3322	7335
8.500	3000	3780	12268

LINE A-2

ID 1 CDP 48 SPN 211			
TIME SEC	VRMS M/SEC	VINT M/SEC	DEPTH M
1.110	1500	1500	832
1.220	1520	1709	926
1.360	1560	1873	1058
1.620	1660	2107	1331
1.840	1820	2723	1631
2.260	2100	3036	2269
3.300	2400	2948	3802
8.500	3000	3325	12447

ID 2 CDP 168 SPN 271			
TIME SEC	VRMS M/SEC	VINT M/SEC	DEPTH M
0.810	1500	1500	607
0.900	1520	1689	684
0.960	1560	2069	746
1.120	1620	1941	901
1.380	1700	2009	1162
1.920	2020	2669	1883
2.520	2200	2696	2692
5.050	2600	2945	6417
8.000	3050	3695	11867

ID 3 CDP 288 SPN 331			
TIME SEC	VRMS M/SEC	VINT M/SEC	DEPTH M
0.320	1500	1500	240
0.550	1640	1817	449
0.880	1780	1992	778
1.530	1980	2222	1500
3.200	2400	2729	3778
4.560	2600	3019	5831
6.520	2720	2981	8752
8.000	3020	4087	11777

LINE B-1

ID 1 CDP 48 SPN 1			
TIME SEC	VRMS M/SEC	VINT M/SEC	DEPTH M
0.730	1500	1500	547
0.960	1540	1661	738
1.170	1680	2210	970
1.390	1780	2238	1217
2.510	2250	2723	2741
4.670	2700	3143	6136
8.500	3200	3720	13259

ID 2 CDP 168 SPN 61			
TIME SEC	VRMS M/SEC	VINT M/SEC	DEPTH M
1.620	1500	1500	1215
2.120	1720	2292	1788
2.450	1900	2792	2249
3.200	2150	2816	3305
4.030	2300	2804	4468
6.690	2700	3212	8741
9.000	3040	3859	13198

ID 3 CDP 288 SPN 121			
TIME SEC	VRMS M/SEC	VINT M/SEC	DEPTH M
2.280	1500	1500	1710
2.620	1600	2154	2076
2.860	1740	2852	2418
3.100	1860	2934	2770
3.760	2020	2645	3643
4.780	2180	2689	5015
7.180	2550	3160	8807
9.500	2900	3783	13196

ID 4 CDP 408 SPN 181			
TIME SEC	VRMS M/SEC	VINT M/SEC	DEPTH M
1.200	1500	1500	900
1.350	1540	1829	1037
1.830	1680	2022	1523
2.140	1860	2687	1939
2.760	2100	2773	2729
3.750	2250	2623	4097
6.460	2700	3221	8461
8.500	3060	3991	12532

ID 5 CDP 528 SPN 241			
TIME SEC	VRMS M/SEC	VINT M/SEC	DEPTH M
0.660	1500	1500	495
0.840	1540	1678	646
1.120	1660	1977	923
1.480	1820	2246	1327
1.910	1980	2452	1854
2.800	2200	2610	3016
3.900	2400	2846	4581
8.000	3100	3643	12050

LINE B-2

ID 1
CDP 48
SPN 1

TIME SEC	VRMS M/SEC	VINT M/SEC	DEPTH M
2.170	1500	1500	1627
2.280	1540	2184	1748
2.380	1620	2896	1892
2.800	1860	2862	2494
3.020	1940	2763	2797
4.160	2200	2778	4367
5.540	2450	3078	6506
9.000	3000	3715	12933

ID 2
CDP 168
SPN 61

TIME SEC	VRMS M/SEC	VINT M/SEC	DEPTH M
1.590	1500	1500	1192
1.970	1560	1789	1532
2.210	1640	2189	1795
2.850	1820	2337	2543
3.480	1940	2409	3302
4.320	2100	2662	4420
4.970	2260	3122	5435
6.730	2600	3380	8409
9.000	3000	3955	12898

ID 3
CDP 288
SPN 121

TIME SEC	VRMS M/SEC	VINT M/SEC	DEPTH M
0.730	1500	1500	547
1.020	1540	1636	785
1.180	1620	2058	949
1.480	1780	2304	1295
2.780	2250	2687	3041
4.850	2650	3107	6257
8.500	3200	3810	13210

ID 4
CDP 408
SPN 181

TIME SEC	VRMS M/SEC	VINT M/SEC	DEPTH M
0.350	1500	1500	262
0.600	1560	1640	468
0.980	1680	1854	820
1.980	1940	2165	1902
2.320	2060	2653	2353
3.200	2300	2837	3601
4.580	2500	2911	5610
6.170	2800	3524	8412
8.000	3100	3947	12023

ID 5
CDP 528
SPN 241

TIME SEC	VRMS M/SEC	VINT M/SEC	DEPTH M
0.510	1500	1500	382
0.700	1540	1643	539
0.900	1620	1873	726
1.340	1860	2273	1226
2.190	2150	2541	2306
3.000	2300	2664	3385
4.210	2450	2787	5071
5.620	2650	3173	7308
6.420	2800	3686	8782
8.000	3100	4099	12020

LINE B-3

ID 1
CDP 48
SPN 271

TIME SEC	VRMS M/SEC	VINT M/SEC	DEPTH M
0.610	1500	1500	457
0.780	1540	1676	600
0.900	1640	2181	731
1.380	1900	2310	1285
1.600	2100	3071	1623
2.720	2400	2773	3176
4.400	2650	3011	5705
8.000	3200	3765	12481

ID 2
CDP 168
SPN 331

TIME SEC	VRMS M/SEC	VINT M/SEC	DEPTH M
0.950	1500	1500	712
1.200	1580	1853	944
1.430	1780	2584	1241
1.910	2100	2848	1925
2.540	2300	2821	2813
3.650	2500	2906	4426
4.590	2650	3166	5914
6.330	2900	3474	8237
8.500	3150	3786	13045

ID 3
CDP 288
SPN 391

TIME SEC	VRMS M/SEC	VINT M/SEC	DEPTH M
1.100	1500	1500	825
1.380	1560	1776	1074
1.560	1700	2528	1301
1.970	1980	2800	1875
2.640	2200	2747	2795
3.140	2450	3484	3666
4.120	2650	3208	5238
5.830	2900	3428	8169
8.500	3300	4038	13560

ID 4
CDP 408
SPN 451

TIME SEC	VRMS M/SEC	VINT M/SEC	DEPTH M
0.870	1500	1500	652
1.040	1540	1730	800
1.450	1600	1743	1157
2.170	1940	2487	2052
3.270	2350	2999	3702
4.570	2600	3142	5744
6.210	2900	3607	8701
8.500	3250	4050	13338

ID 5
CDP 528
SPN 511

TIME SEC	VRMS M/SEC	VINT M/SEC	DEPTH M
0.470	1500	1500	352
0.630	1520	1577	479
0.960	1600	1743	766
1.410	1820	2218	1265
1.830	1980	2442	1778
2.630	2250	2770	2886
4.320	2550	2957	5385
5.790	2800	3431	7906
8.000	3200	4065	12399

ID 6
CDP 648
SPN 571

TIME SEC	VRMS M/SEC	VINT M/SEC	DEPTH M
0.160	1500	1500	120
0.280	1540	1592	216
0.690	1660	1737	572
1.080	1860	2169	995
1.680	2020	2280	1679
2.500	2250	2660	2769
3.860	2500	2904	4744
4.810	2650	3188	6258
8.000	3160	3802	12322

LINE C-1

ID 1 CDP 48 SPN 1

TIME SEC	VRMS M/SEC	VINT M/SEC	DEPTH M
0.460	1500	1500	345
0.800	1560	1638	623
0.930	1620	1949	750
1.180	1780	2279	1035
1.940	2100	2517	1992
3.660	2550	2977	4552
8.000	3200	3659	12493

ID 2 CDP 168 SPN 61

TIME SEC	VRMS M/SEC	VINT M/SEC	DEPTH M
1.410	1500	1500	1057
1.680	1600	2044	1333
1.890	1700	2352	1580
2.100	1860	2930	1888
2.900	2250	3045	3106
3.800	2450	3005	4458
5.600	2700	3164	7305
9.000	3200	3886	13911

ID 3 CDP 288 SPN 121

TIME SEC	VRMS M/SEC	VINT M/SEC	DEPTH M
2.160	1500	1500	1620
2.360	1560	2102	1830
2.890	1820	2688	2542
3.420	2060	3053	3352
4.580	2300	3094	5030
6.890	2600	3110	8623
9.500	2980	3805	13588

ID 4 CDP 408 SPN 181

TIME SEC	VRMS M/SEC	VINT M/SEC	DEPTH M
2.460	1500	1500	1845
2.740	1540	1855	2105
3.030	1640	2386	2451
3.410	1820	2877	2997
5.120	2200	2808	5398
10.00	2900	3486	13905

ID 5 CDP 528 SPN 241

TIME SEC	VRMS M/SEC	VINT M/SEC	DEPTH M
2.760	1500	1500	2070
3.190	1520	1643	2423
3.370	1600	2643	2661
3.610	1660	2346	2942
4.180	1820	2615	3688
5.130	2060	2888	5060
6.000	2200	2891	6317
10.50	2800	3441	14059

ID 6 CDP 648 SPN 301

TIME SEC	VRMS M/SEC	VINT M/SEC	DEPTH M
2.480	1500	1500	1860
2.600	1520	1886	1973
2.790	1600	2444	2205
3.410	1900	2887	3100
3.740	1980	2670	3541
4.010	2060	2953	3940
5.800	2500	3276	6873
10.00	3100	3775	14801

ID 7 CDP 768 SPN 361

TIME SEC	VRMS M/SEC	VINT M/SEC	DEPTH M
1.840	1500	1500	1380
2.180	1620	2157	1747
2.440	1780	2780	2108
2.990	2020	2851	2892
3.560	2200	2971	3739
4.710	2400	2934	5426
9.000	3200	3893	13777

ID 8 CDP 888 SPN 421

TIME SEC	VRMS M/SEC	VINT M/SEC	DEPTH M
1.060	1500	1500	795
1.210	1540	1797	930
1.640	1740	2208	1404
1.820	1820	2430	1623
2.350	1980	2451	2273
4.330	2450	2911	5155
5.770	2650	3176	7442
8.500	3050	3758	12571

LINE C-2

ID 1 CDP 48 SPN 1

TIME SEC	VRMS M/SEC	VINT M/SEC	DEPTH M
0.920	1500	1500	690
1.060	1520	1645	805
1.420	1600	1815	1132
1.680	1700	2166	1414
1.950	1820	2437	1743
2.630	2200	3037	2775
3.280	2450	3272	3830
4.500	2700	3279	5839
6.490	3000	3587	9408
8.000	3250	4157	12546

ID 2 CDP 168 SPN 61

TIME SEC	VRMS M/SEC	VINT M/SEC	DEPTH M
0.300	1500	1500	225
0.520	1540	1593	400
0.650	1620	1907	524
1.340	1860	2061	1235
2.200	2150	2537	2326
3.780	2400	2710	4467
5.000	2600	3140	6382
5.900	2750	3467	7942
8.000	3100	3920	12058

ID 3 CDP 288 SPN 121

TIME SEC	VRMS M/SEC	VINT M/SEC	DEPTH M
0.300	1500	1500	225
0.460	1520	1557	350
0.810	1680	1870	677
1.180	1860	2203	1084
2.130	2150	2493	2254
3.440	2450	2872	4135
5.020	2700	3177	6645
8.000	3200	3900	12456

ID 4 CDP 408 SPN 181

TIME SEC	VRMS M/SEC	VINT M/SEC	DEPTH M
0.500	1500	1500	375
0.860	1600	1729	686
1.330	1820	2165	1195
2.330	2150	2523	2457
3.540	2400	2820	4162
8.000	3150	3637	12273

ID 5 CDP 528 SPN 241

TIME SEC	VRMS M/SEC	VINT M/SEC	DEPTH M
0.480	1500	1500	360
0.760	1580	1708	599
1.210	1860	2255	1107
1.870	2200	2715	2003
2.980	2500	2937	3633
4.240	2700	3122	5600
8.000	3180	3646	12459

ID 6 CDP 648 SPN 301

TIME SEC	VRMS M/SEC	VINT M/SEC	DEPTH M
0.150	1500	1500	112
0.310	1520	1539	236
0.480	1620	1788	388
0.990	1860	2061	913
2.440	2200	2405	2656
4.710	2650	3061	6130
6.350	2900	3521	9017
8.000	3160	4006	12322

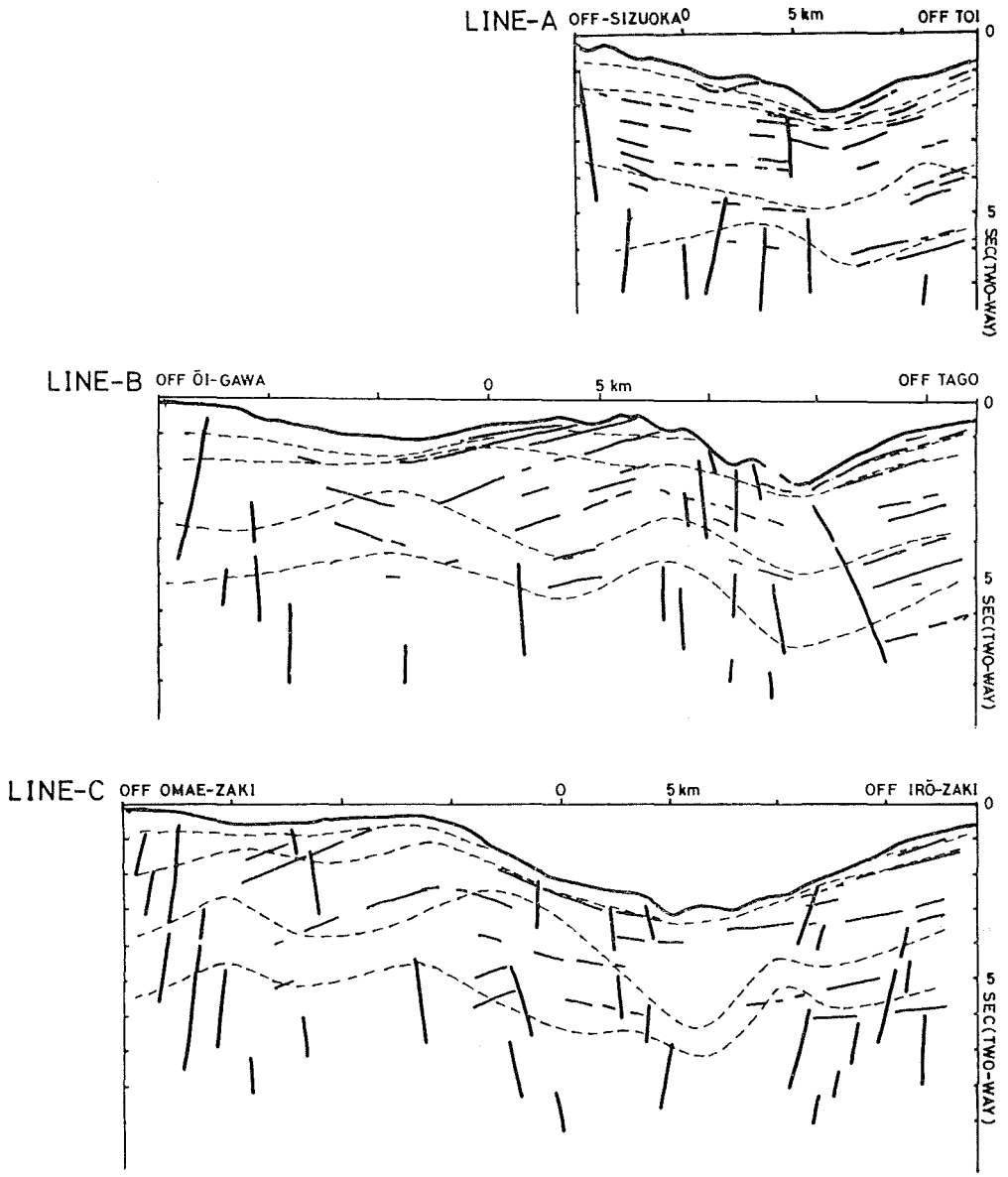

Figure 5 Derived P wave velocity structure of the Suruga Trough.
Dashed lines show iso-velocity of each 2.0, 2.4, 3.0, 3.3 km/sec in descended order, derived from multichannel seismic reflection data themselves, by velocity analysis.

（1） 2.0km/sec の面は海底下約0.6秒までの範囲内にあり，2.0km/sec より遅い層の厚さは，東西方向では大陸棚に厚く大陸斜面で薄い傾向を示し，南北方向では北部に厚く南部に薄くなる傾向が見られる．北・南両堆の東側斜面では区分されていない．

（2） 2.0～2.4km/sec 層は，最大層厚が2.0km/sec 以下の層とほぼ同じ約0.7秒であるが，北部に厚く南部に薄くなる傾向は2.0km/sec 以下の層ほど明瞭ではない．

（3） 3.0及び3.3km/sec の等速度面は，ほぼ整合したうねりを見せる．この上部層にあたる2.4～3.0km/sec 層は，このうねりをあたかも埋積して平坦化するように覆っている．

（4） うねりの背斜部は，石花海海盆の南北軸上や北・南両堆の東縁に見られ，トラフ軸は向斜軸にあたっている．

（5） 相模湾における地震速度と地質との対応（早川・飯塚，1972）を準用すると，2.0km/sec 以下：第四系，2.4～3.0km/sec：第三系，3.3km/sec 以上：第三系（湯ケ島層群火山岩層）とすることができる（Table 3）．

Table 3 P wave velocity structure correlation

velocity-geology-thickness correlation in Sagami Bay (Hayakawa・Iizuka, 1972)				velocity-thickness in Suruga Trough	
layer	P wave velocity (km/sec)	geology	thickness (km)	derived P wave velocity (km/sec)	thickness (km)
1	1.5 ～2.0	Quaternary	0～0.3	1.5～2.0	0 ～0.7
2	2.45～3.0	Tertiary (Sirahama fms.)	4～6	2.4～3.0	0.8～3.9
3	3.3 ～4.15	Tertiary (Yugasima group volcanic)	3.5	3.3～	

（6） 音響的層相などに基づいて区分した層の成層構造とは必ずしも一致しない．おおよそ2.0km/sec 以下の層はA層，2.0～3.0km/sec 層がB層，3.0km/sec 層以上がC層として見ることができる．

6. 考 察

トラフ軸の静岡側に沿って，断層面が垂直かやや伊豆半島側に傾斜する断層群があり，大きな断層帯を構成していることが明らかになった．大きな断層帯の断層面が海底面と交わると考えられる位置は，3本の測線ともトラフ軸の西側1～6km内にあり，測線B・Cでは2つ以上の断層面によって構成されている可能性がある（Figure 5）．

大構造としての大きな断層帯の走向は，石花海北・南両堆の地形的な長軸方向などに見られる北東―南西方向性の断層，あるいはこれとほぼ直交する北西―南東方向性の断層に規制されているものの，トラフの大地形や北・南両堆の列方向などの方向性から見て，トラフ軸にほぼ平行な南北方向をとるものと考えられる．周辺海域に見られる天竜海底谷，石花海海盆などの構造谷あるいは沈降性の海盆の長軸方向は，この考えを支持しているように見える．また大きな断層帯を構成する断層面の傾斜は，測線A・B及び測線Cの南堆東縁の基部では垂直もしくは見かけ上西方向と考えられる．しかし，測線Cのトラフ軸西縁の断層面は垂直または見かけ上東方向と見られ，トラフ軸から伊豆半島南端の石廊埼にかけて見られる断層帯の傾斜方向は西方向をとる．

トラフ軸沿いの大きな断層帯は，全体として逆断層を構成している可能性が大きい．石花海海盆の北堆側斜面を構成しているAB両層間のアバット関係，石花海海盆の海底地すべりを示唆する海底地形や構造，北・南両堆トラフ軸側の急斜面のB層の露頭などから推論される，北・南両堆のトラフ軸側急斜面を前面とし，石花海海盆側緩斜面を背面とする隆起上昇を伴う傾動地塊の運動，これに対する伊豆半島側層面の沈降を示唆する，トラフ

軸に向かう比較的単調な同斜状構造，そしてこの両者間に存在する垂直ないし西に傾斜する大断層面がその根拠となろう．この考えは820m平坦部の基盤として小規模の傾動地塊の存在を積極的に推定させる．なお，大きな断層帯の横ずれ成分については明らかでない．

大きな断層帯の形成時期はB層堆積（第三紀後期）以後であり，その運動は現世にまで及んでいると考えられる．その根拠は次のとおりである．C層は堆積後多くの断層によって切られて地塊化し，B層堆積後ひき続いて石花海北・南堆などの傾動を含んで駿河トラフ，石花海海盆が形成された可能性が高いこと，石花海海盆のA層（第四紀）はその軸部に厚く，かつ同時異相を示し運動の継続を示唆していることなどが挙げられる．

石花海海盆の西縁にあたる，静岡—御前埼側大陸棚外縁付近の著しい断層群の走向や連続性については不明確である．しかし，大陸棚外縁がその走向や連続性を示唆している可能性がある．

この報告は調査結果の記載と，これに基づく概観的な考察にとどまった．当海域の構造を一層明らかにするためには，遠州灘・伊豆小笠原海嶺北部の海底地形，地質，沿岸陸域の地質などより広域的な総合が必要である．特に駿河トラフと天竜川，天竜海底谷にはさまれた静岡県の陸域と同南方海域の構造を明らかにすることは，駿河トラフ沿いの構造運動の解明上重要な課題であると考える．

この調査は，昭和52年度特別研究促進調整費による「東海地域の地震予知に関する総合研究」の一環である，駿河湾の地殻深部構造の研究として実施した．この研究はさらに2分され，海上保安庁水路部が反射法による観測の研究を，地質調査所が反射法による観測データ解析の研究を担当した．

この研究を実施するにあたり，計画の段階から終始御協力を頂いた地質調査所の中条純輔・宮崎光旗両氏，マルチチャンネル反射法音波探査について御指導頂いた石油開発技術センターの石和田靖章氏，音波探査プロファイルの解釈について助言を頂いた石油資源開発株式会社の青木豊氏，作業の実施にあたった石油資源開発株式会社，海上保安庁の関係各位，これらの方々の御好意と並々ならぬ御尽力に対し厚く御礼申し上げたい．

引 用 文 献

Dobrin, M.B., 1976: Introduction to Geophysical Prospecting 3rd ed. McGraw-Hill, New York.

Fitch, A.A., 1976: Seismic Reflection Interpretation, Geoexploration Monographs Series 1, No. 8, GEBRÜDERBORNTRAEGER.

早川正巳・飯塚　進　1972：伊豆半島周辺の地球物理学的研究　伊豆半島，東海大学出版会　pp. 217—243.

井川　猛・斉藤正徳　1973：海上地震探鉱におけるデータ処理，海洋科学，8.

海上保安庁水路部　1978：沿岸の海の基本図，駿河湾北部　6362^{5}，6362^{5-8}.

海上保安庁水路部　1979：駿河湾南部海底地形図，同地質構造図，第47回地震予知連絡会配布資料.

奈須紀幸・土　隆一・本座栄一　1968：駿河湾西域の海底地質構造，日本地質学会第75年秋季学術大会総合討論会資料フオツサマグナ，pp. 191—195.

竹内　均・石井吉徳　1968：反射法とディジタル・データ処理，物理探鉱，21.

REPORT OF HYDROGRAPHIC RESEARCHES No. 15, March, 1980

電子計算機を利用したシングルチャンネル音波探査データの信号強調技術

岡田　貢*・打田明雄*

A SIGNAL ENHANCEMENT TECHNIQUE FOR SINGLE CHANNEL SEISMIC REFLECTION DATA

Mitsugu Okada* and Akio Uchida*

Received 1979 September 10

Abstract

Single channel seismic reflection profilings have been one of the most popular methods in hydrographic surveys and other geophysical investigations around Japan for the last 20 years. In the shallowwater environment, such as continental shelves and continental margins, large-amplitude multiple reflections obscure smaller-amplitude primary reflections, which prevent investigaters from detecting both finescale and more important geological structures in that area.

To detect more detailed geological information, a digital data processing method using the Wiener shaping filter and conventional stacking was developed to remove noises and multiple reflections from the original data. This method was applied to the digital single channel seismic data obtained at sea near Tokyo Bay, and results of the processing are given in the form of subbottom profiles drawn with an automatic plotter and compared with original analogue record seismograms. We can conclude that this method will be of much help in extraction of geological/geophysical information from single channel seismic data.

1. まえがき

海底下の地層を探査するには，音波を用い，海底面及び海底下の各地層表面で反射されて返ってくる反射波を調査船上で受信し記録する方式がある．しかしその記録には，直接反射されてくる有意な信号の他に，海底と水面間及び各地層間を何度か往復した後に受信される多重反射信号が含まれている．この多重反射信号は，記録上，地層に似たしま模様（疑似地層）として現れ，正常な地層断面と重複して記録を複雑化するため，地層解析のうえで大きな障害となっている．

そこで，この有害な信号を除去するための電子計算機によるディジタル処理と，グラフィックCOM(Computer Output on Microfilm) による結果の図化を試みたので，その原理と処理の概要について報告する．

* 測量課　Surveying Division

Figure 1 は多重反射の模式図であり，Figure 2 は典型的な多重反射信号のある地層断面記録の一例である．また Figure 3 の写真は，従来のアナログ記録と並行して，この処理のためにディジタル記録を作成したディジタル収録器である．この収録器は，長さ 730メートル のオープンリール方式磁気テープを使用し，9トラックで 1600ＢＰＩの記録密度を有する磁気録音部，162 db のダイナミックレンジを有するバイナリゲインアンプ，記憶制御部及び時刻表示部等により構成されている．本器は収録機能のほかに磁気テープ再生機能も有し，D/A 変換した信号を音波探査用アナログ記録器に導くことにより地層断面図を描かせることができる．

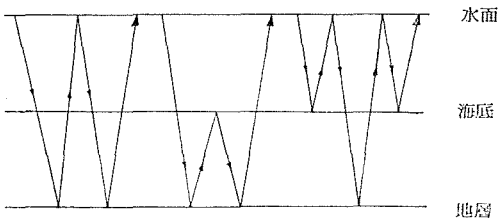

Figure 1 Sound paths of multiple seismic reflections.

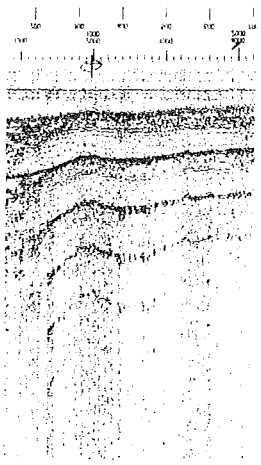

Figure 2 Seismic data showing typical multiple reflections.

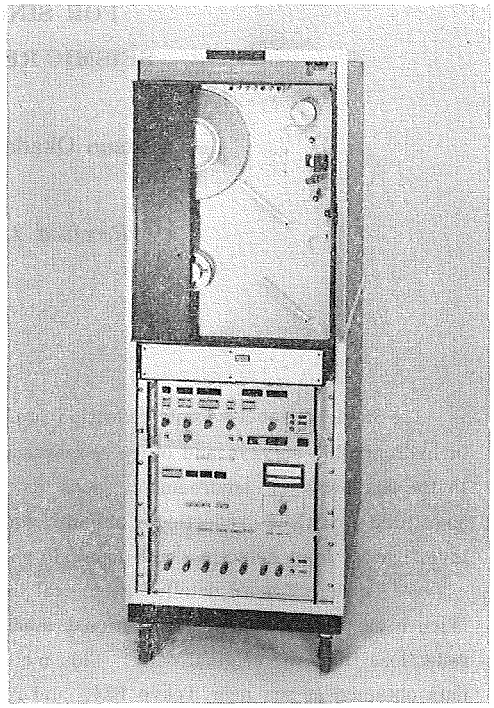

Figure 3 Digital seismic recording system.

2. 多重反射信号除去の原理

多重反射信号除去のプログラムは，Wiener shaping filter を使用し，Figure 4 に示すように多重反射信号除去処理を行うことにより，不要信号を除くものである．その原理は次のとおりである（芦田および鳥羽 1978）．

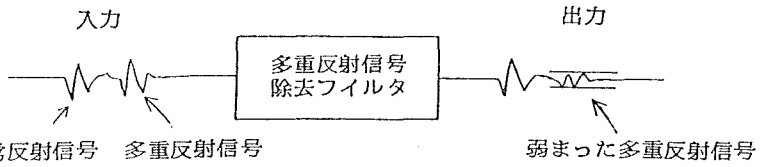

Figure 4 Illustration of function of the filter for multiple reflections.

いま，次のように各変数を定義する．

入力波形の時系列　　b_t　$(t=0,\ 1,\ 2,\cdots\cdots n)$

所望出力波形の時系列　　d_t　$(t=0,\ 1,\ 2,\cdots\cdots n)$

フィルタの時系列　　f_t　$(t=0,\ 1,\ 2,\cdots\cdots n)$

実際の出力波形の時系列　　y_t　$(t=0,\ 1,\ 2,\cdots\cdots n)$

ここで，本来，出力として欲しい d_t と実際の出力 y_t とについて

$$E=(d_0-y_0)^2+(d_1-y_1)^2+\cdots\cdots+(d_n-y_n)^2$$
$$=\sum_{t=0}^{n}(d_t-y_t)^2$$

のような自乗平均誤差のエネルギー E を考える．Wiener shaping filter とは，この E を最小にするという条件で f_t を求める方法である．

いま入力波形の時系列 b_t についてウインドウ幅を m 個として出力波形の時系列 y_t を求めると，

$$y_t=\sum_{s=0}^{m}(f_s\cdot b_{t-s})$$

したがって

$$E=\sum_{t=0}^{n}(d_t-\sum_{s=0}^{m}f_s\cdot b_{t-s})^2$$

となる．誤差のエネルギーは，$\partial E/\partial f_t=0$ の時，最小となるから

$$\frac{\partial E}{\partial f_t}=\sum_{t=0}^{n}2\,(d_t-\sum_{s=0}^{m}f_s\cdot b_{t-s})\ (-b_{t-i})=0$$

すなわち，

$$-\sum_{s=0}^{n}d_t\cdot b_{t-i}+\sum_{t=0}^{n}(\sum_{s=0}^{m}f_s\cdot b_{t-s})\ b_{t-i}=0$$

あるいは，

$$\sum_{s=0}^{m}f_s\cdot\sum_{t=0}^{n}b_{t-s}\cdot b_{t-i}=\sum_{t=0}^{n}d_t\cdot b_{t-i}\qquad(1)$$

となる．

ここで，

$$\phi_{i-s}=\sum_{t=0}^{n}b_{t-s}\cdot b_{t-i}\qquad(2)$$

$$\varphi_i=\sum_{t=0}^{n}d_t\cdot b_{t-i}\qquad(3)$$

とおく．(2)式は入力波形の自己相関関数であり，(3)式は入力波形と所望出力波形との相互相関関数である．(2)，(3)式で(1)式を書き換えると，

$$\sum_{s=0}^{m}f_s\cdot\phi_{i-s}=\varphi_i\qquad(i=0,\ 1,\ 2,\cdots\cdots m)\qquad(4)$$

となり，行列式を用いて書くと次のようになる．

$$\begin{pmatrix}\phi_0 & \phi_1 & \phi_2 & \cdots\cdots & \phi_m\\ \phi_1 & \phi_0 & \phi_1 & \cdots\cdots & \phi_{m-1}\\ \phi_2 & \phi_1 & \phi_0 & \cdots\cdots & \phi_{m-2}\\ \vdots & \vdots & \vdots & & \vdots\\ \phi_m & \phi_{m-1} & \phi_{m-2} & \cdots\cdots & \phi_0\end{pmatrix}\begin{pmatrix}f_0\\ f_1\\ f_2\\ \vdots\\ f_m\end{pmatrix}=\begin{pmatrix}\varphi_0\\ \varphi_1\\ \varphi_2\\ \vdots\\ \varphi_m\end{pmatrix}\qquad(5)$$

(5)式を解くことによりオペレータとも呼ばれるフィルタ（f_t）を求めることができる．このフィルタにより入力信号（音波探査データ）を処理（Convolution）すると，所望の出力波形との誤差が最小となるような出力を求めることができる．Figure 5 は以上の信号処理過程を示している．

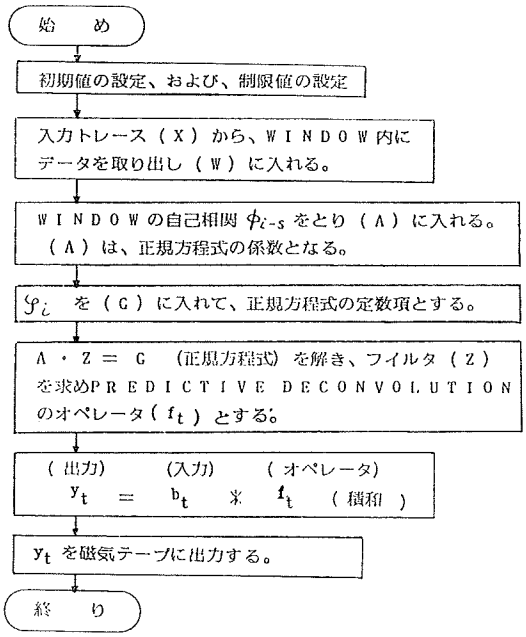

Figure 5 Block diagram of the signal processing.

処理結果を地層断面図として表現する際，ここではXYプロッタに替えて，グラフィックCOMを採用した．グラフィックCOMは，磁気テープから入力されたデータを，分解能の極めて高いブラウン管上に図形として再現し，これを35mmマイクロフィルム上に撮影するという機能を持ち，XYプロッタに比べ作図速度が100～200倍という利点がある．グラフィックCOMによる図化表示法には，Figure 6 に示すような5種類があるが，Figure 12 に示す例は，地層の連続性を最も効果的に表す〔面積表示—2〕によって描いたものである．

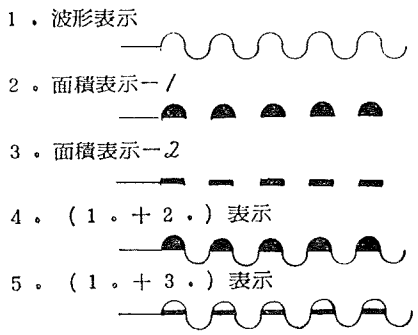

Figure 6 Five types of COM display patterns used for seismic traces.

3. 電子計算機を用いた地層断面図

解析処理には，昭和53年3月8日 測量船「明洋」（450総トン）に積載したディジタル収録器により収録した東京湾口における音波探査データを用いた．Figure 7 は収録時の航跡図で，4桁の数字はその地点におけるエアガンの発音番号を示す．使用したエアガンの吐出容量は0.6ℓである．

収録された受信信号強度の周波数スペクトルは，Figure 8 に示すとおりであり，10Hz付近に卓越周波

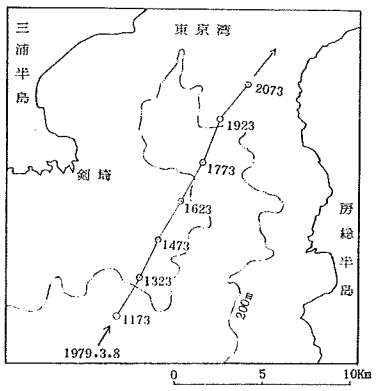

Figure 7 Track chart of seismic data acquisition.

数が見られる．Figure 9 はこれを1トレース分の時間経過における振幅の分布として表現した図で，10 Hz すなわち 0.1 秒周期の明瞭な波が読みとられる．このエアガンを製作したボルト社の資料では，0.6 ℓ のエアガンの最低発音周波数は 21 Hz であるから，記録されている 10Hz の波は有意な反射信号ではないといえる．

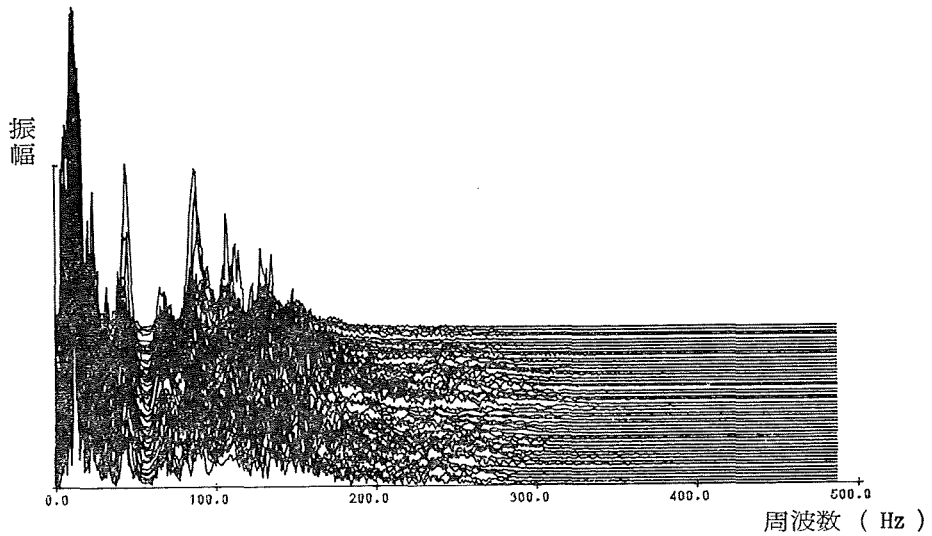

Figure 8 Amplitude spectrum of seismic signals.

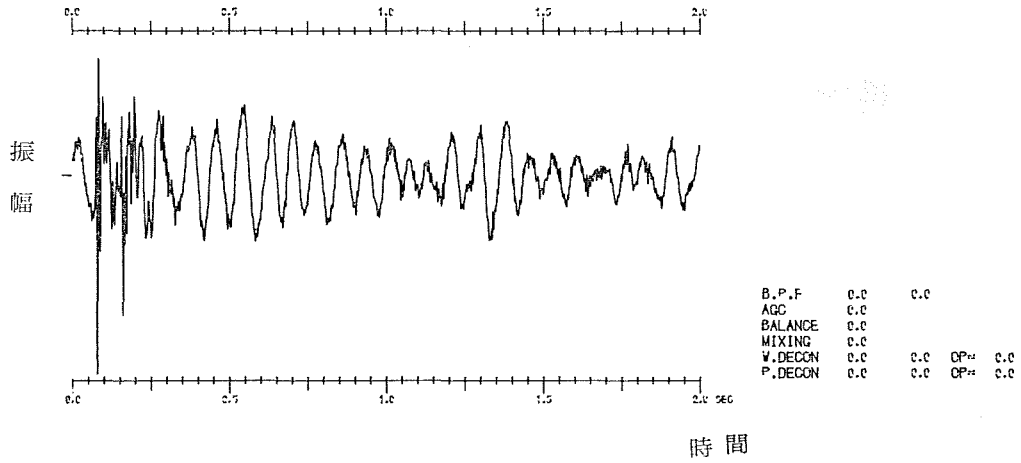

Figure 9 An example of wave form of received seismic signal.

Figure 10 は音波探査データの処理過程全体を示したフローチャートである．図に示すように主目的である多重反射信号除去に先立って，コード変換・信号周波数分析等の前処理を行っており，上に述べた10Hzの波などもこの段階で取り除かれる． Figure 11 は信号周波数分析の処理効果の一例で，Figure 9 と同様の表現方法で描いたものである．この例は，バンドパスフィルタを50～300Hz に設定して処理したもので，10Hz の大きな波が除去されたことを示している．Figure 10 の処理過程において設定したその他の定数は，周期信号振幅制御＝3周期，周期信号重合＝3周期，多重反射信号除去のオペレータのウィンドウ幅＝250である．

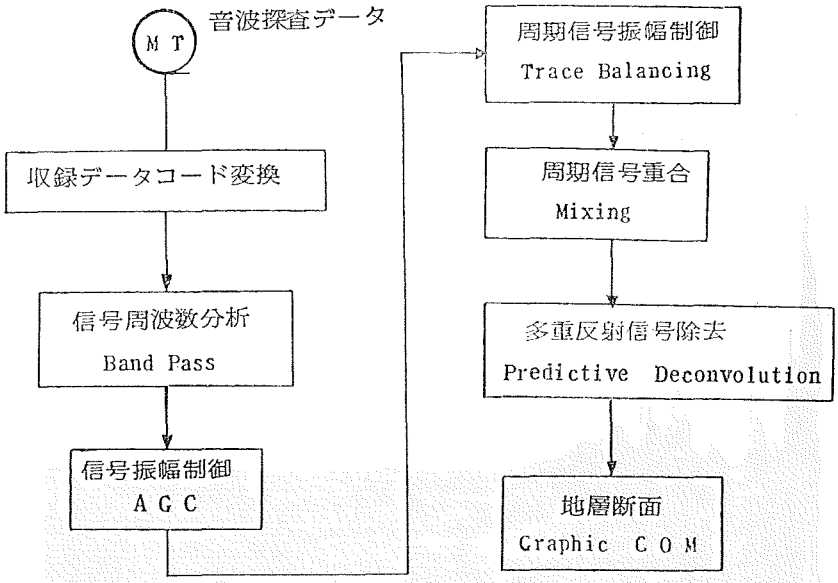

Figure 10 Flow chart illustrating whole digital seismic data processing.

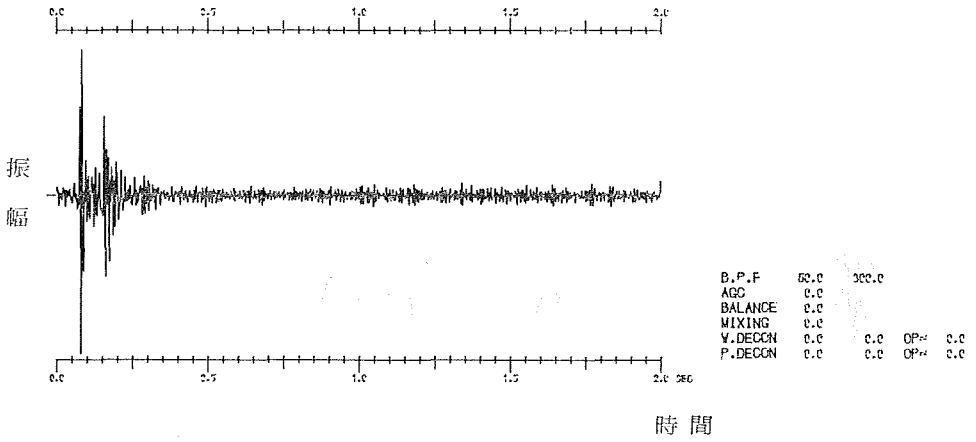

Figure 11 Seismic signals shown in Figure 9 after application of digital band-pass filter.

Figure 12 はこれらの処理を経て得られた地層断面の一例である．また，Figure 13 は，比較のために同一の場所で同時に収録した従来方式のアナログ記録である．両図とも，横軸は発音番号，縦軸は反射信号を受信するまでの時間（単位：秒）である．二つの図は縦横の比が同一ではないので，比較のために Figure 14 を掲げた．実線は，Figure 13 のアナログ記録では不明瞭だったものが，処理後の Figure 12 では鮮明に表されている線であり，破線は，アナログ記録では多重反射で数本のしまに現れていたものが，処理によって除かれるか弱められるかした部分である．

Figure 15 (a), (b) も，多重反射信号除去の処理前と処理後の地層断面図の一例である．同図 (a) では発音番号1600～1650，ほぼ 0.2 秒の付近に並行する数本の線が見られる．これは，水面と海底間を往復した音波による海底の疑似記録であるが，同図 (b) ではこれが非常に弱められていることが読みとれる．

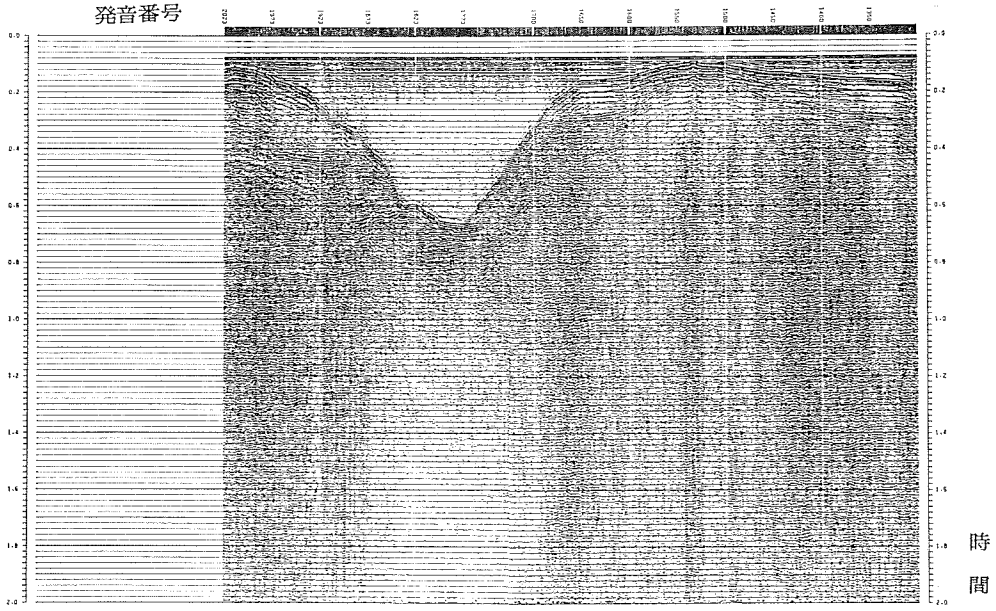

Figure 12 An example of processed subbottom profile.

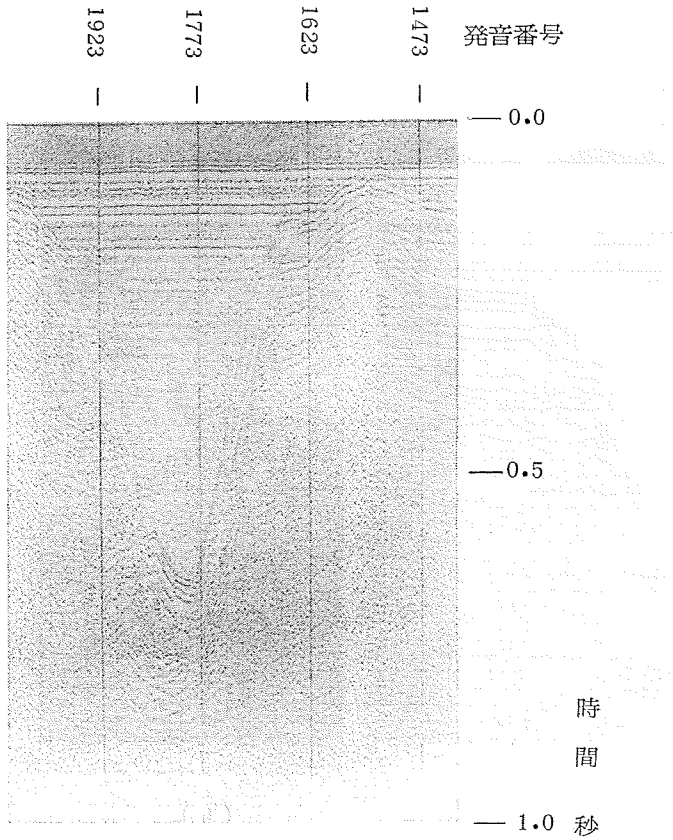

Figure 13 Original subbottom profile obtained by analogue recorder onboard the survey vessel.

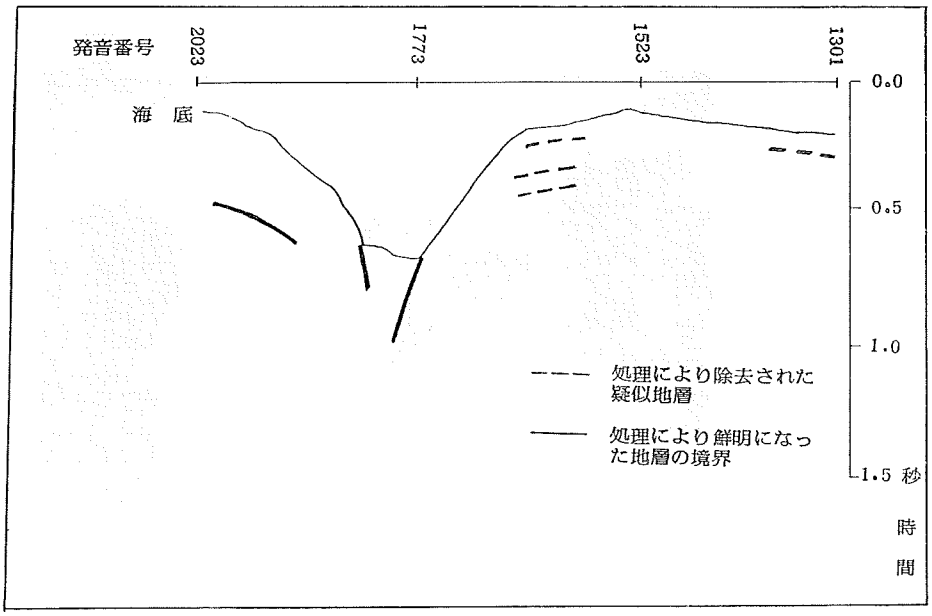

Figure 14 Section showing removed (dotted line) and enhanced (solid line) profiles.

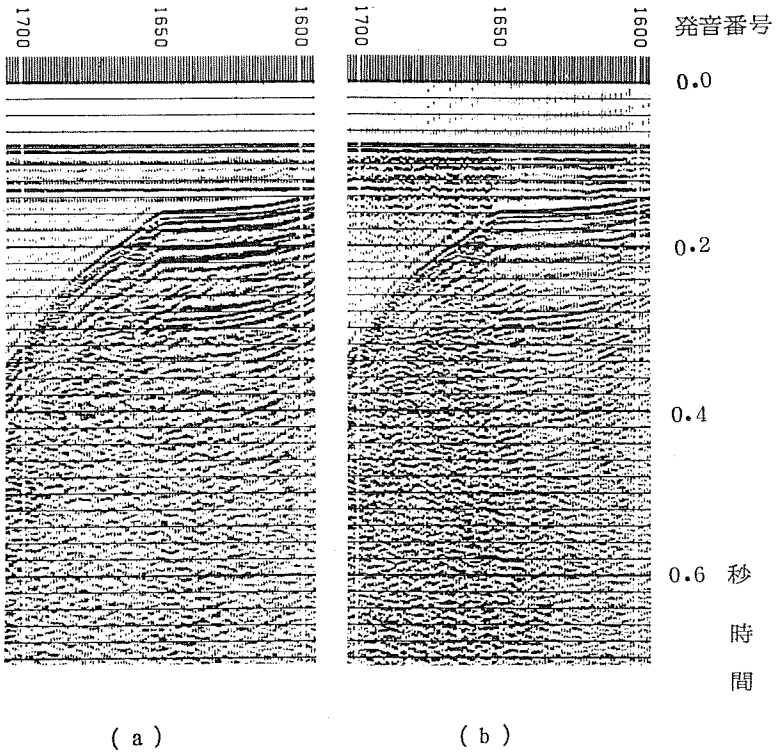

Figure 15 Two trace gathers showing the effect of removing multiple reflections.
(a) Before processing. (b) After processed.

Figure 16 は，Figure 12 から濃淡のしま模様や地層の流れを考慮して地層解析を行った結果である．従来方式のアナログ記録からでは，このような解析を行うのは非常に困難と思われる．

以上をまとめると，

（1） 電子計算機によって処理した地層断面図では海底の多重反射記録が弱められるので，疑似地層の中に埋もれていた実際の地層が鮮明となり，判別が容易になった．

（2） ＸＹプロッタを使用して行った地層断面の図化の場合に比較して，グラフィックＣＯＭによる図化速度は２桁も速く，かつ，フィルムに撮影されるので利用のうえで便利である．

の２点が処理の効果として挙げられる．

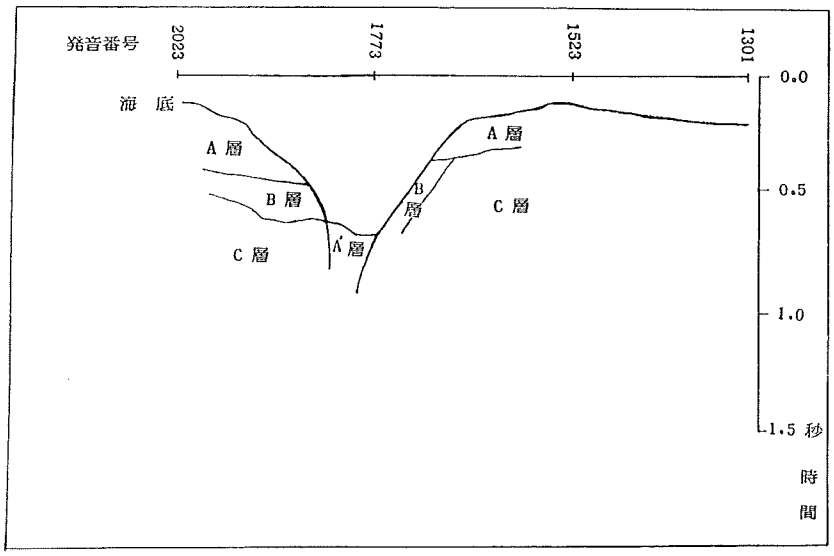

Figure 16 Structural configurations shown in Figure 12 after interpretation.

4. あとがき

電子計算機による探査データの処理は前述のような利点がある反面，ぼう大なデータを扱うために，電子計算機による処理時間が実収録時間の数百倍もかかる現状では，従来方式である船上収録の音波探査アナログ記録により地層解析を行い，疑似地層等で判読の困難な部分について本方式による処理を行うことになるが，将来は，船上にミニコンピュータを導入し，音波探査信号の受信中にオンラインで一部を処理して磁気テープに収録する方法，及びオフラインではミニコンピュータを含めた複数のコンピュータにより，並列的にデータを処理する方法等を採用して処理時間を短縮し，本方式の実用化を推進したい．

最後に，本研究に対して音波探査データの収録を実施していただいた測量船「明洋」及び測量課清水敬治氏，橋本鉄男氏に厚く御礼申し上げる．

参 考 文 献

芦田 譲，鳥明武文 (1978)：ウェブレット処理における基本波形の抽出とその応用，物理探鉱，31, No. 2, pp. 8—22

Lawrence C. Wood, Sven Treitel (1975) : Seismic Signal Processing, Proceeding of The IEEE, Vol. 63, No. 4, pp. 659—660

REPORT OF HYDROGRAPHIC RESEARCHES No. 15, March, 1980

西南日本周辺海域の地磁気異常

大島章一*・登崎隆志*・小野寺健英*

GEOMAGNETIC ANOMALIES AT SEA AROUND SOUTH-WEST JAPAN

Shoichi Oshima, Takashi Tozaki and Ken-ei Onodera

Received 1979 September 10

Abstract

Magnetic total intensity data collected around South-West Japan obtained through "The Basic Map of the Sea" project of the Japanese Hydrographic Department are compiled. Results were compared with the topographic and geological features of the sea floor and adjacent land area.

The smooth magnetic pattern with two weak magnetic positive zones along the deep sea terrace and the outer edge of the continental slope are characteristic between Nankai Trough and South-Western Japan. The Eastern China Sea and the Japan Sea area around S-W Japan show complicated magnetic patterns accompanied by NE-SW or NNE-SSW trending islet-seamount chains or uplifted zones of the basement rocks. The geological structure on land of Kyusyu and these magnetic features of the Eastern China Sea suggest that the opening or spreading of the marginal sea resulted from the intrusion of andesitic and other igneous rocks along fault zones caused by crustal movements of the trench.

key words: Solid earth geomagnetism, Island arc.

1. 序　論

水路部の大陸棚の海の基本図測量では，大陸棚と大陸斜面の地磁気全磁力，地形，地質構造及び重力の調査を系統的に実施しており，日本周辺全域の測量をほぼ終了している．成果は縮尺20万分の１の地磁気全磁力図，海底地形図，海底地質構造図及び重力異常図として順次刊行されている．この事業は，日本周辺海域で統一された方法により，広大な海域で密な測線沿いに実施された最初のものであり，画期的なものといえる．一方地球科学的観点からは，日本及び周辺海域の各種の調査成果，例えば地磁気の他に地形，重力，地殻熱流量，地震，地質，地殻変動などの成果をそれぞれ一定の規格でまとめて比較検討することが，日本及び周辺海域の地殻構造及びその動的状態を把握するためにきわめて重要である．地形については海上保安庁水路部及び国土地理院が各種の地図を刊行しており，すでにその概要は把握できる．重力異常分布については Tomoda (1973), Segawa and Tomoda (1976) 等により詳しくまとめられている．その他の種類のものについては，地磁気異常分布を含めていずれも本質的に地

* 測量課　Surveying Division

殻表層に起因する情報であるため複雑な分布が予測され，詳細にわたるまとめはなされていない．したがって日本周辺の大陸棚の海の基本図測量の成果をまとめることは極めて意義が深く，北海道及び東北地方周辺海域の磁気異常については既に報告（大島他・1975）したが，それらの一環としての西南日本周辺海域の地磁気異常分布についてまとめた結果を報告する．なお，ここでは南西諸島周辺の海域として，九州から種子島・屋久島を経て中之島周辺までの地域を取扱ったが，それ以南の海域については次の機会にゆずることとした．また，この報告で取扱う海域の東の境界は，日本海側では鳥取の東約 40km の東経134度40分付近，太平洋側では静岡県掛川沖の東経138度付近であり，調査海域の沖合への張り出しは距岸約 200km 程度である．

通産省工業技術院地質調査所は，地下資源開発を目的とする空中磁気探査を実施しており，その成果は調査海域ごとの空中磁気図のほか，地質調査所研究報告（1978, 1979）に報告されている．その調査は浅海域から海岸付近の陸上を含み，測線間隔は 2～3 km で，航空機に積載したプロトン磁力計により測定されたものである．その成果のうち，福井―隠岐，東海―紀伊沖，串本―延岡，宮崎沖，天草等の海域の成果を参考にした．

WAGEMAN et al.（1970）によると，九州西方の東シナ海では地磁気の局所的な異常が多数見出され，特に東海大陸棚の縁辺域にあたる台湾宍道褶曲帯に沿って音響学的不透明層が分布し，地磁気の正の異常帯を伴っている．この正異常帯の基盤岩は第三紀の堆積岩や酸性貫入岩で日本付近では露頭しているが，その南の海域ではより新しい地層に埋もれているとされている．その他にも東シナ海から南西諸島周辺にかけて，南西諸島にほぼ平行な北東―南西あるいは北北東―南南西の方向を示す多数の地磁気縞状異常が描かれており，測線間隔が数十から百キロメートルときわめて広いので詳細ではないが，一応この付近の地磁気異常分布の特性を表していると考えられる．

日本海の地磁気異常分布はIsezaki (1973)によってまとめられ，不明瞭ながらほぼ北東―南西の方向性を示し，日本海の拡大を示すものと考えられているが，測線間隔の広い調査に基づく結果であるため，特に今回の調査結果との整合性は検討しなかった．

四国海盆については，小林（1974）をはじめ多くの研究があり，地形的には九州パラオ海嶺や紀南海山列の示すほぼ南北の方向性が地磁気異常分布にもみられ，海底の拡大成長が四国海盆の成因であるとされている．一方南海トラフから陸測については，前述の地質調査所の成果以外には，地磁気分布に関する資料で参考とすべきものは見当たらなかった．

本論は，西南日本周辺の大陸棚及び大陸斜面の地磁気異常分布について，地磁気分布の特徴によっていくつかの区域に分け，それぞれについて地質構造の調査結果等を比較検討し，地殻表層部の構成について考察したものである．しかし陸域の地磁気異常分布に関する詳しい情報がほとんど得られなかったこともあって，西日本全域の地殻のダイナミクスについて論じるまでには至らなかった．

2. 測　量

本論に関する海域の調査は，水路部の測量船「昭洋」及び「明洋」により昭和44年から51年にかけて実施されたものである．測線の間隔は約 3.7km で，測位はロランA，ロランC，ＮＮＳＳ及び陸岸が見える範囲では六分儀による陸上物標の測角による三点両角法等の併用によるものである．海岸付近の測位誤差は最大約200m以内，沖合いで条件の悪い海域でも最大約 1.8km 以内で，平均的にはその数分の１程度と推定される．特に九州周辺については，デッカを使用したため沿岸部及び沖合い共に最大誤差は 300m 程度以内で，さらに海岸付近での陸上物標による測位により，デッカの電波伝ぱん経路の影響の補正値を求めて修正したので，測位誤差は図上では無視して良い程度と考えられる．

地磁気全磁力はプロトン磁力計により測定した．同時に音響測深機による地形調査，エアガンによる地質構造の調査，ＴＳＳＧ型重力計による重力の測定を行った．測線の方向は，調査海域ごとに地形や地質構造の方向性に直交する向きにしたため，日本海と四国海盆では南北に近い方向であり，東シナ海では東西に近い方向である．

3. 地磁気異常の算出と解析

地磁気の測量結果は，地球外部に起因する磁場の時間的変化（日変化，磁気嵐等）を含んでいる．日本では，Figure 1 に示す10か所で地磁気全磁力の連続観測が実施されており，測量区域ごとに最も近い観測点のデータを用い時間的変化の補正を行った．

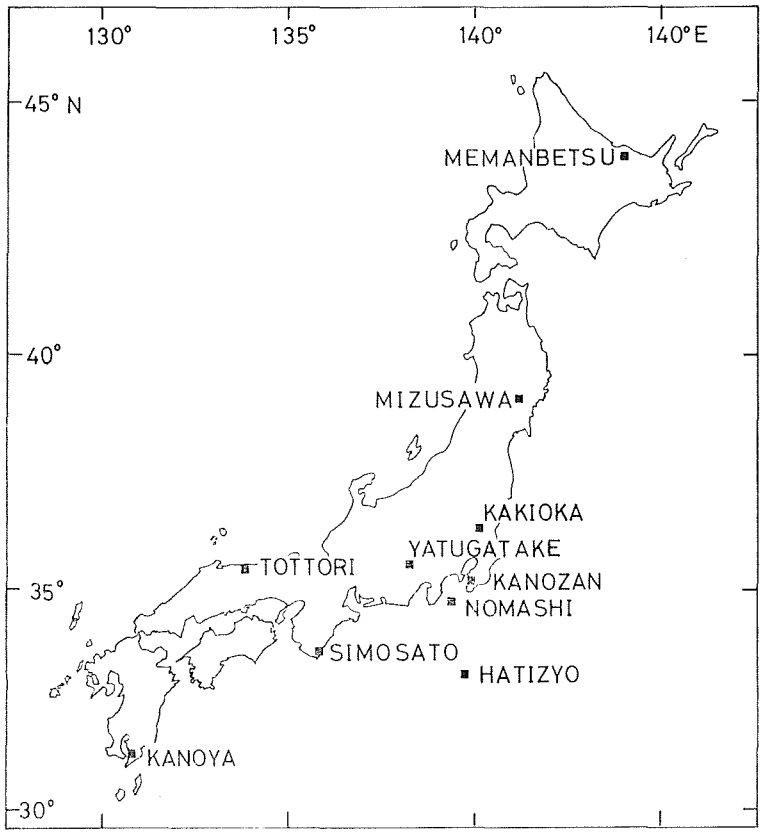

Figure 1 Geomagnetic stations used for the estimation of secular change of total intensity at sea around Japan since 1965.

地磁気異常算出の基準値は IGRF 1965.0 を用いたが，その経年変化は実際に日本で観測されたデータに全く合わないため，日本の観測所データを用いて次式により算出した．

$$\Delta F = F - (\mathrm{IGRF} + \mathrm{SECULAR}) \qquad (1)$$

ここで F は測量で得た全磁力値，IGRF は IGRF モデル1965.0年の値，SECULAR は次に述べる方法で決めた1965年以来の経年変化量，ΔF は求める地磁気全磁力異常である．

日本では，近年地震予知の目的で地磁気全磁力の連続観測点がいくつか設けられ，従来の観測所とあわせて合計10か所で全磁力観測が実施されているが，最近の地磁気全磁力経年変化は単純ではなく，1965年以来の１個の

観測点の変化を時間の関数として表わすには，変曲点の数から考えて4次以上の高次の式で表現しなければならない．そこである地点の経年変化量を時間の4次式で表現し，各観測点の年平均値を用いて最小自乗法によりその係数の値を決定した．すなわちある地点の観測値について次のように表現できる．

$$\mathrm{SECULAR}=A_1t+A_2t^2+A_3t^3+A_4t^4 \qquad (2)$$

ただし t は年単位で　　t＝測定時期−1965.0

さらに A_1〜A_4 はそれぞれ測定点の緯度 φ，経度 λ に関する3次式で近似できると考える．

$$A_i=a_{i0}+a_{i1}\varphi+a_{i2}\lambda+a_{i3}\varphi^2+a_{i4}\varphi\lambda+a_{i5}\lambda^2+a_{i6}\varphi^3+a_{i7}\varphi^2\lambda+a_{i8}\varphi\lambda^2+a_{i9}\lambda^3 \qquad (3)$$

ただし，φ 及び λ の値は測定点の北緯−34度，東経−136度を分単位であらわした数とする．これら a_{ij} (i=1〜4, J=0〜9) を求めた結果を Table 1 に示す．ただし，φ 及び λ で展開する時点で観測点数と未知数が同じとなり一意的に値が決まってしまうが，ここでは地球物理的意味よりも便宜上経年変化量を近似できれば良く，陸域付近の海上に関してはさほど問題はないであろう．結果を Figure 2 に，計算値と観測値の差を Table 2 に示す．この式により，日本及びその周辺の任意地点における1965年以降最近までの経緯度変化量を算出できる．なお，観測データのない期間については，水路部観測報告等の経年変化で推定値を求めて補間した．

Table 1 Coefficient values a_{ij} for equation 3

i \ j	0	1	2	3	4	5	6	7	8	9
1	−2.9109 ×10^{+1}	−3.9036 ×10^{-2}	2.0239 ×10^{-1}	5.1796 ×10^{-4}	−1.5340 ×10^{-3}	6.3386 ×10^{-4}	−1.8951 ×10^{-6}	5.1748 ×10^{-7}	7.3053 ×10^{-6}	−5.8753 ×10^{-6}
2	1.5833 ×10^{-1}	1.9022 ×10^{-3}	−4.3868 ×10^{-2}	−7.7773 ×10^{-5}	3.1104 ×10^{-4}	−1.3794 ×10^{-4}	3.9700 ×10^{-7}	−1.8774 ×10^{-7}	−1.5113 ×10^{-6}	1.2973 ×10^{-6}
3	1.6785 ×10^{-1}	9.2280 ×10^{-4}	3.1579 ×10^{-3}	3.9036 ×10^{-7}	−1.9720 ×10^{-5}	1.0403 ×10^{-5}	−2.9392 ×10^{-8}	3.6519 ×10^{-8}	8.5309 ×10^{-8}	−9.4351 ×10^{-3}
4	−4.6962 ×10^{-3}	−5.9788 ×10^{-5}	−7.9740 ×10^{-5}	1.8123 ×10^{-7}	3.9037 ×10^{-7}	−2.7714 ×10^{-7}	7.3192 ×10^{-10}	−1.6736 ×10^{-9}	−1.3188 ×10^{-9}	2.3853 ×10^{-9}

Table 2 Difference between observed and calculated geomagnetic total intensity secular change since 1965 at each magnetic stations (observed-calculated). Estimated values are given in parentheses.

STATION \ YEAR	1965	1966	1967	1968	1969	1970	1971	1972	1973	1974	1975	1976	1977	1978
MEMAMBETU	0.1	1.4	−2.6	−0.5	1.3	−0.4	1.5	2.4	−2.0	−2.8	−0.8	1.4	2.8	−1.8
MIZUSAWA	(1.3)	(−1.7)	(−1.4)	(0.9)	(1.4)	−0.6	1.8	−0.1	−0.9	−2.6	0.2	1.1	2.0	−1.4
KAKIOKA	0.9	−0.2	−1.9	−1.0	2.0	0.0	3.1	−0.3	−1.5	−3.3	−0.4	1.9	2.6	−2.0
KANOZAN	0.9	0.1	−2.8	−0.4	2.0	0.2	2.6	0.5	−1.2	−4.6	−0.2	2.3	3.0	−2.2
NOMASI	(0.8)	(−1.3)	(−1.0)	1.5	1.4	−0.8	−1.5	0.6	1.0	−0.6	−0.9	0.6	0.7	−0.4
HATIZYO	(0.0)	(−0.3)	(0.4)	(0.8)	−0.5	−3.3	2.4	3.0	−1.0	−2.9	−0.8	3.3	−1.3	—
YATUGATAKE	(0.6)	(−0.9)	(−0.6)	(0.8)	(1.2)	(−2.1)	(0.6)	1.6	0.5	−2.6	−0.3	0.4	1.9	−1.0
SIMOSATO	0.1	1.8	−3.1	−3.2	5.9	−0.4	1.4	−0.9	−2.9	−1.6	2.6	1.7	−1.4	—
TOTTORI	(0.6)	(−1.0)	(−0.3)	(1.0)	0.3	−0.6	0.2	−0.2	0.5	−1.1	−0.1	1.3	−0.6	—
KANOYA	1.1	−0.3	−2.5	−1.5	3.2	0.5	2.3	0.1	−1.2	−4.5	−0.3	2.3	3.4	−2.4

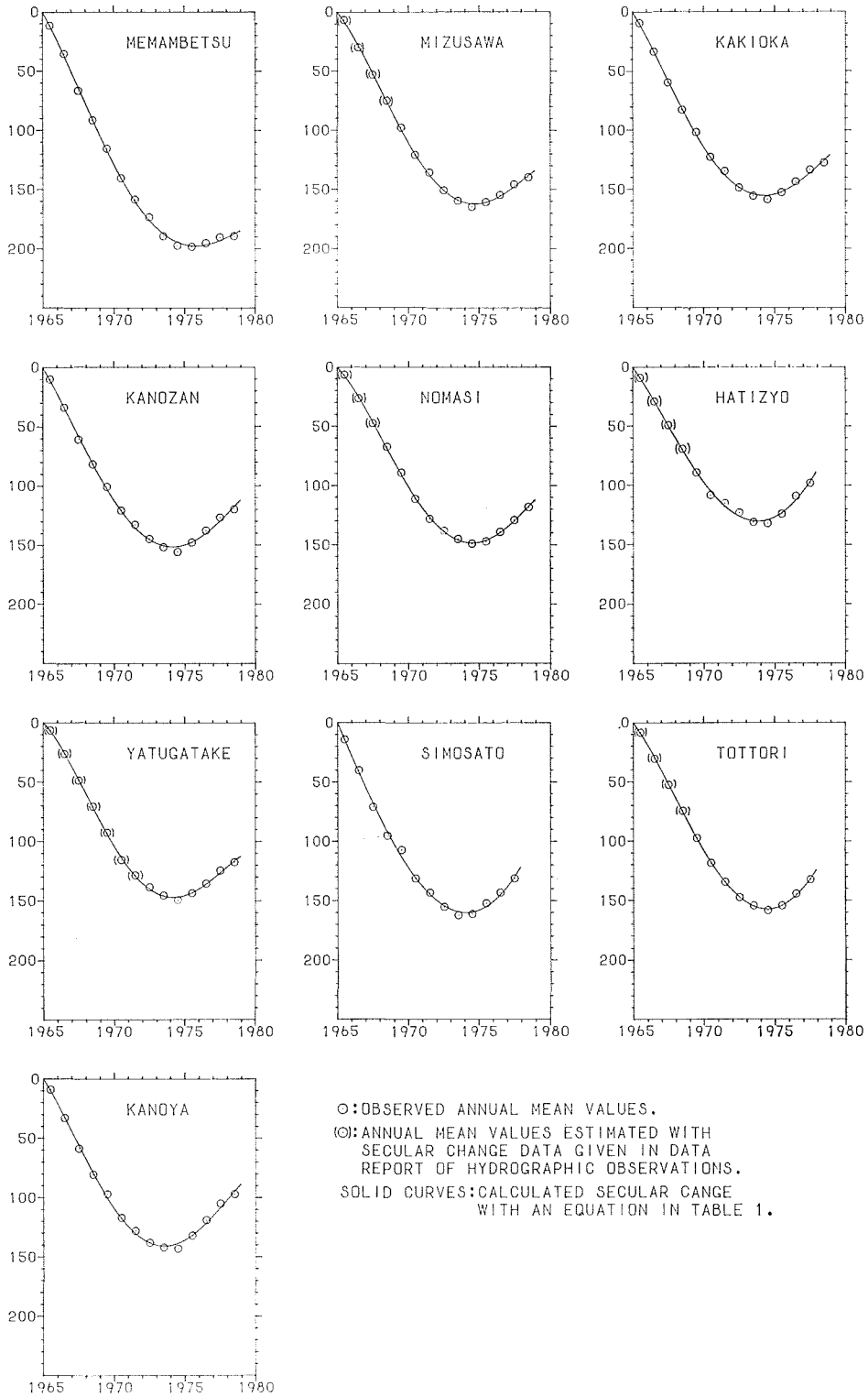

Figure 2 Observed and calculated annual mean values for each geomagnetic stations.

測量成果は全磁力分布に関する測量原図である．そのままでは計算機入力とはならないので，原図からディジタイザーにより磁気テープデータファイルを作成した．その際の読取り誤差は縮尺20万分1の原図上で0.5ミリ以内であり問題にならない．次に電子計算機により(1)式の計算を各測点について行い，求めた地磁気異常の数値を図化機で図上に記入した．地磁気異常の等値線はフリーハンドで描いた．(1)式の計算は，IGRF もSECULAR も共にかなり項数が多く繁雑であるが，用いた計算機（日本電機ＡＣＯＳ―６）が比較的高速で，5000点程度のデータの計算処理と図化機（オフライン）用の地磁気異常分布図データテープの作成に要する時間は数分以内であり，特に計算時間軽減の工夫は必要でなかった．

磁気異常の数値解析の方法は，得られた地磁気異常分布図，予見される帯磁物体の構造とその磁化の方向などに応じて最適の方法を選ぶ必要がある．本論の調査海域のうち，東海，四国沖のいわゆる四万十層群の海域では，大陸斜面沿いの堆積物の厚い深海平坦面に弱い正の異常帯がみられ，これについては既に地質調査所（1978）に解析結果が示されている．山陰沖と九州西方海域では，地磁気異常分布は極めて複雑であり，個々の異常について詳細な解析を行う事は有利でない．特に九州西方の東シナ海では厚い第３紀堆積層の下に強磁性の貫入岩が多数分布しているとみられ，この場合は貫入岩の表面の深度が問題である．

このような場合に最も簡単な方法は，HENDERSON and ZEITZ (1948) の方法であり，以下にその方法の概略を述べる．

まず，貫入岩は鉛直柱状モデルで近似できるとし，上面の深さにくらべ，底面は計算上その影響を無視できる程度に深いと仮定する．これが正の帯磁である場合，地磁気異常分布図上では通常強い正の異常と，その北寄りに弱い負の異常が現れる．正異常のピークを示す地点を原点とし，負異常の中心方向へ y 軸をとる．y 軸から反時計方向に90° の方向を x 軸，原点から下方へ z 軸をとる．x 軸から周囲磁場の磁北へ時計まわりに測った角度を β，周囲磁場の伏角を I とする．原点から y 軸の正の方向沿いに，正の異常値が原点の値の半分になるところまでの距離（仮に半値幅と呼ぶ）を E とし，原点から柱状モデル上面までの深さを D とすると

$$D=f(\beta, I)\cdot E \qquad (4)$$

という関係が成り立ち，HENDERSON and ZEITZ (1948) には β 及び I の値に対する $f(\beta, I)$ の値がグラフで示されている．β=90 度前後，つまり帯磁の方向が現在の磁場とほぼ同じ方向の場合，調査海域の伏角が40度から50度であるので，$f(\beta, I)$ の値は1.6から1.7程度である．したがって，貫入岩体の表面深度は，正の帯磁のものについてはきわめて容易に推定することができ，半値幅の1.6倍程度と考えてよい．鉛直板状モデルについても同様の手法により深さを推定することができる．その場合は x 軸を帯状地磁気異常の中心軸方向とし，y 軸はそれに直交する北寄りの方向にとり，(4)式と同様に深さ D は半値幅 E から

$$D=f'(\beta, I)\cdot E \qquad (5)$$

として求めることができ，$f'(\beta, I)$ の値がグラフに示されている．例として I=45度，β=90度の場合は，$f'(\beta, I)$=1.34 となり，磁性体の表面は半値幅のほぼ1.3倍と推定できる．なお，帯磁物質の磁化の伏角のちがいは，深さの推定値にほとんど影響しない．

4. 地磁気異常分布の特徴

地磁気異常分布を50ガンマごとの等値線で示した結果を Figure 3～Figure 8 に示す．これら全体をまとめて200ガンマごとの等値線で示した結果を Figure 9 に示す．

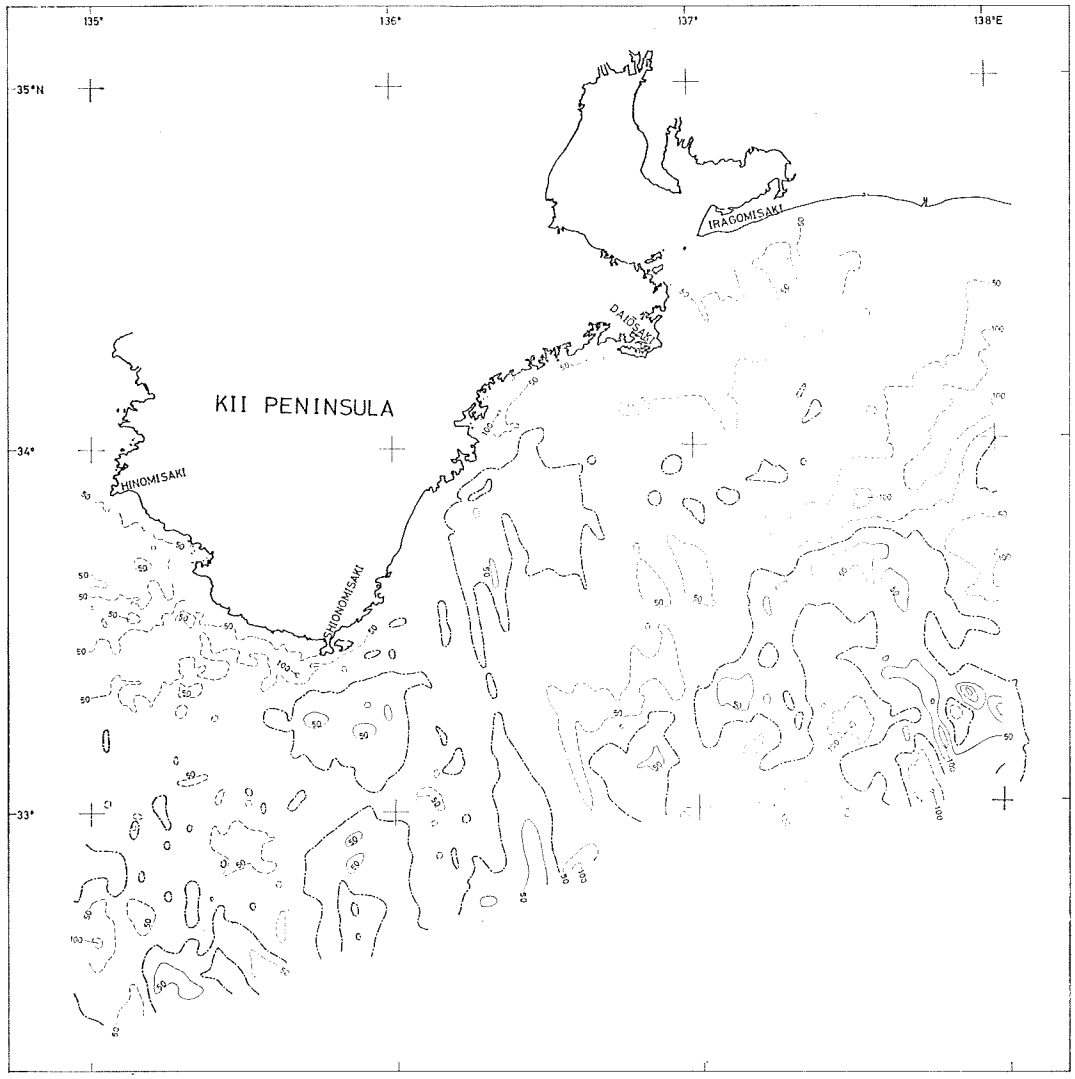

Figure 3 Geomagnetic total intensity anomalies. Contour interval is 50 nT. Solid lines are positive and dotted lines are negative values.

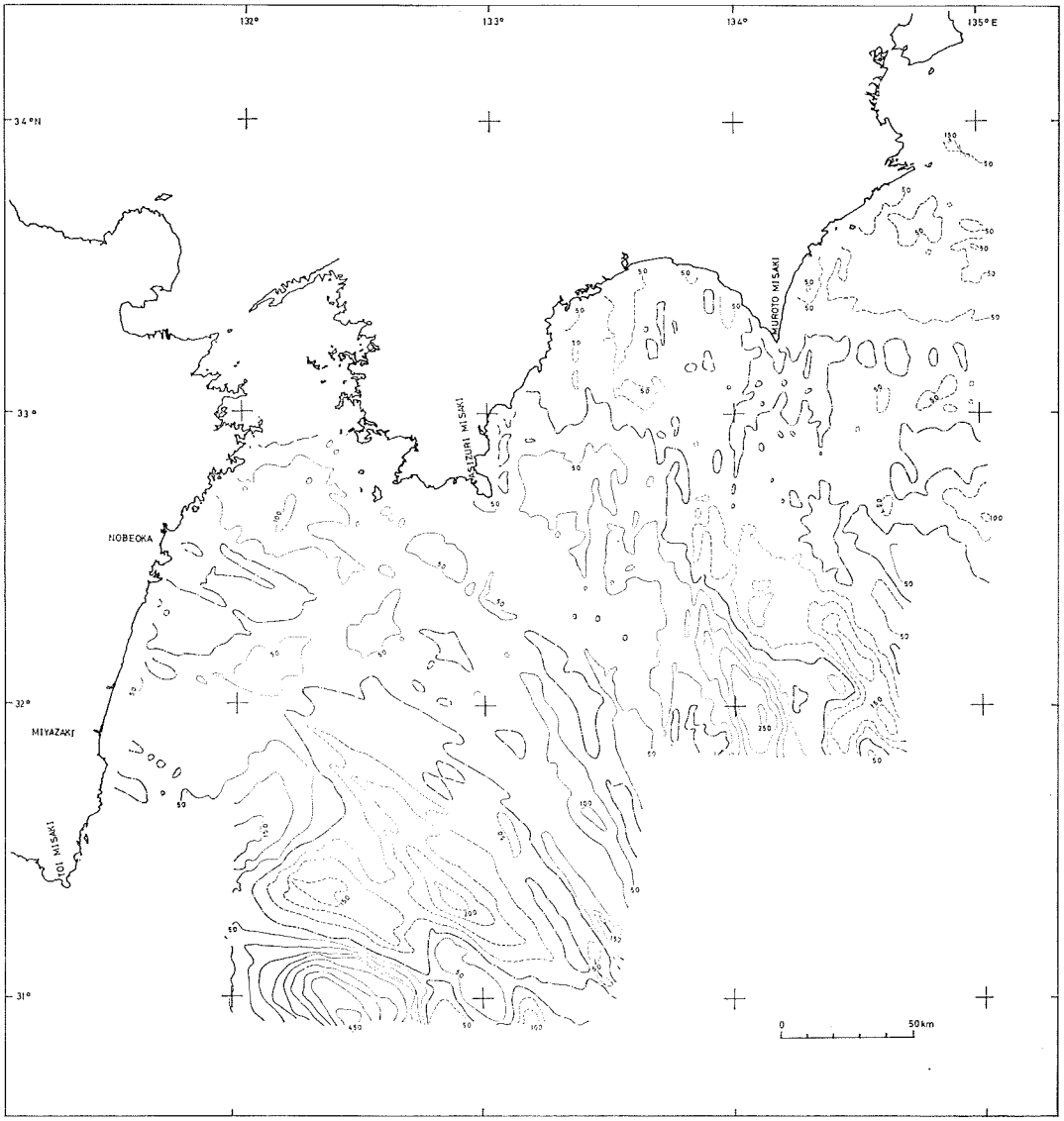

Figure 4 Geomagnetic total intensity anomalies. Contour interval is 50 nT. Solid lines are positive and dotted lines are negative values.

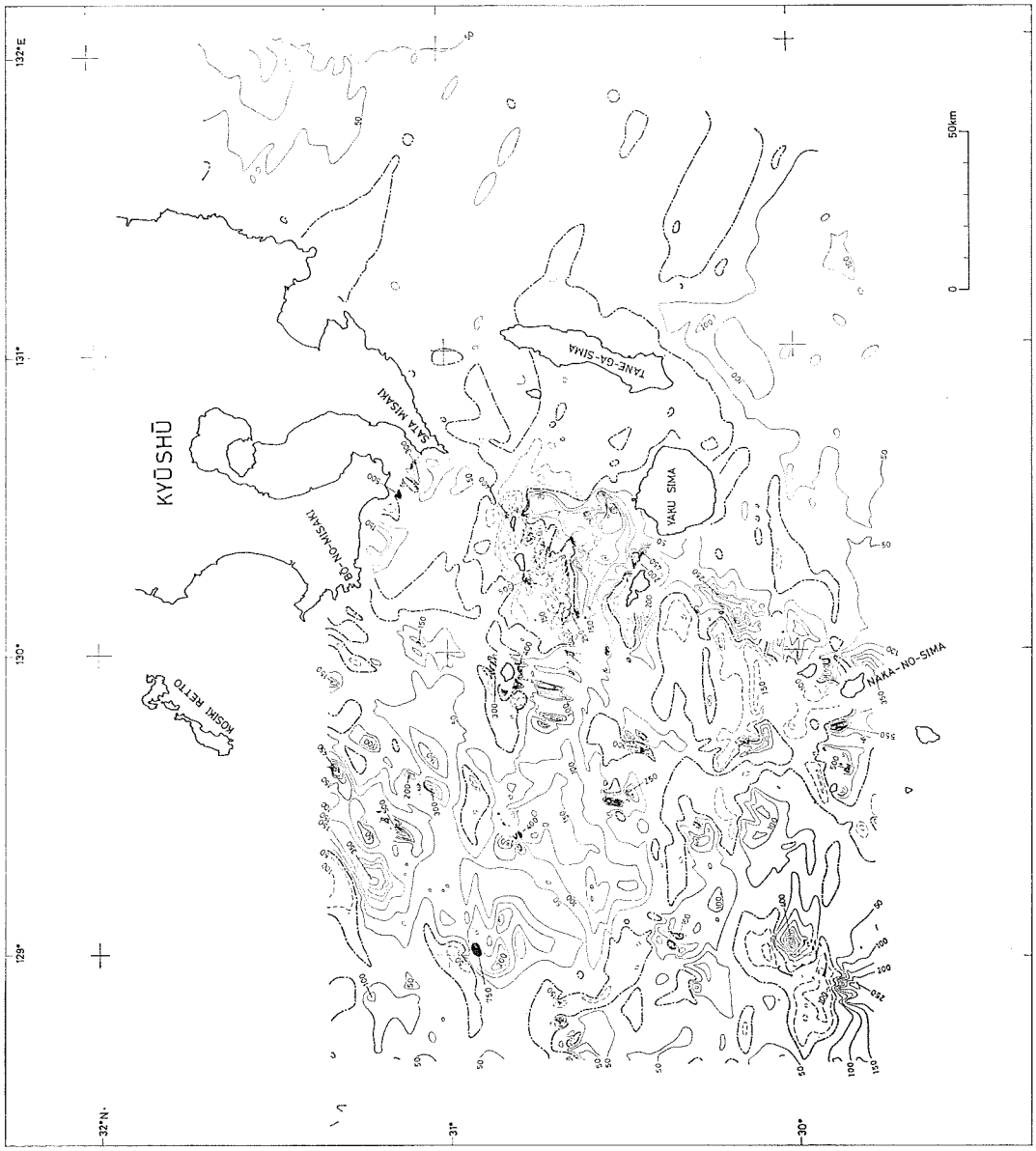

Figure 5 Geomagnetic total intensity anomalies. Contour interval is 50 nT. Solid lines are positive and dotted lines are negative values.

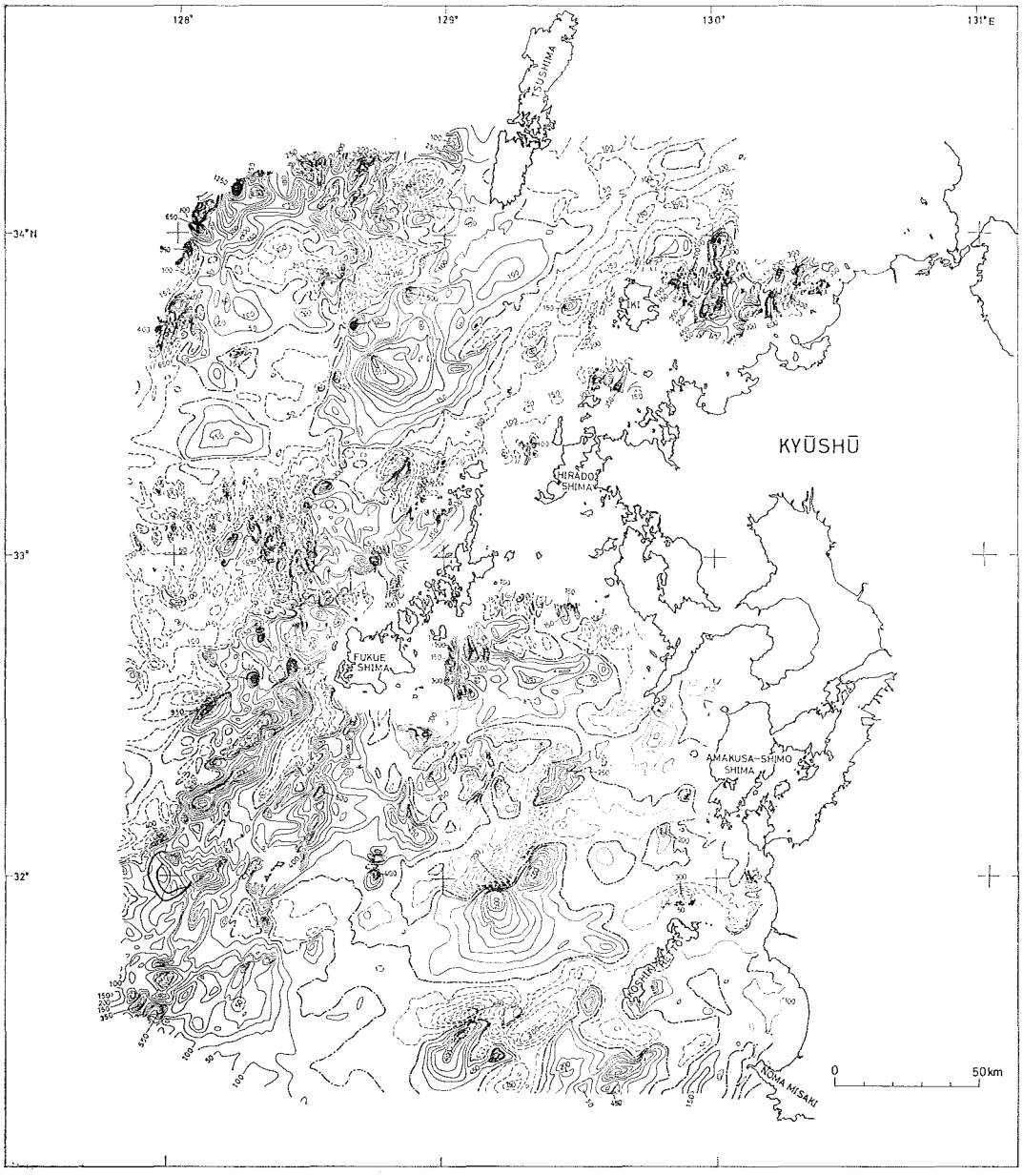

Figure 6 Geomagnetic total intensity anomalies. Contour interval is 50 nT. Solid lines are positive and dotted lines are negative values.

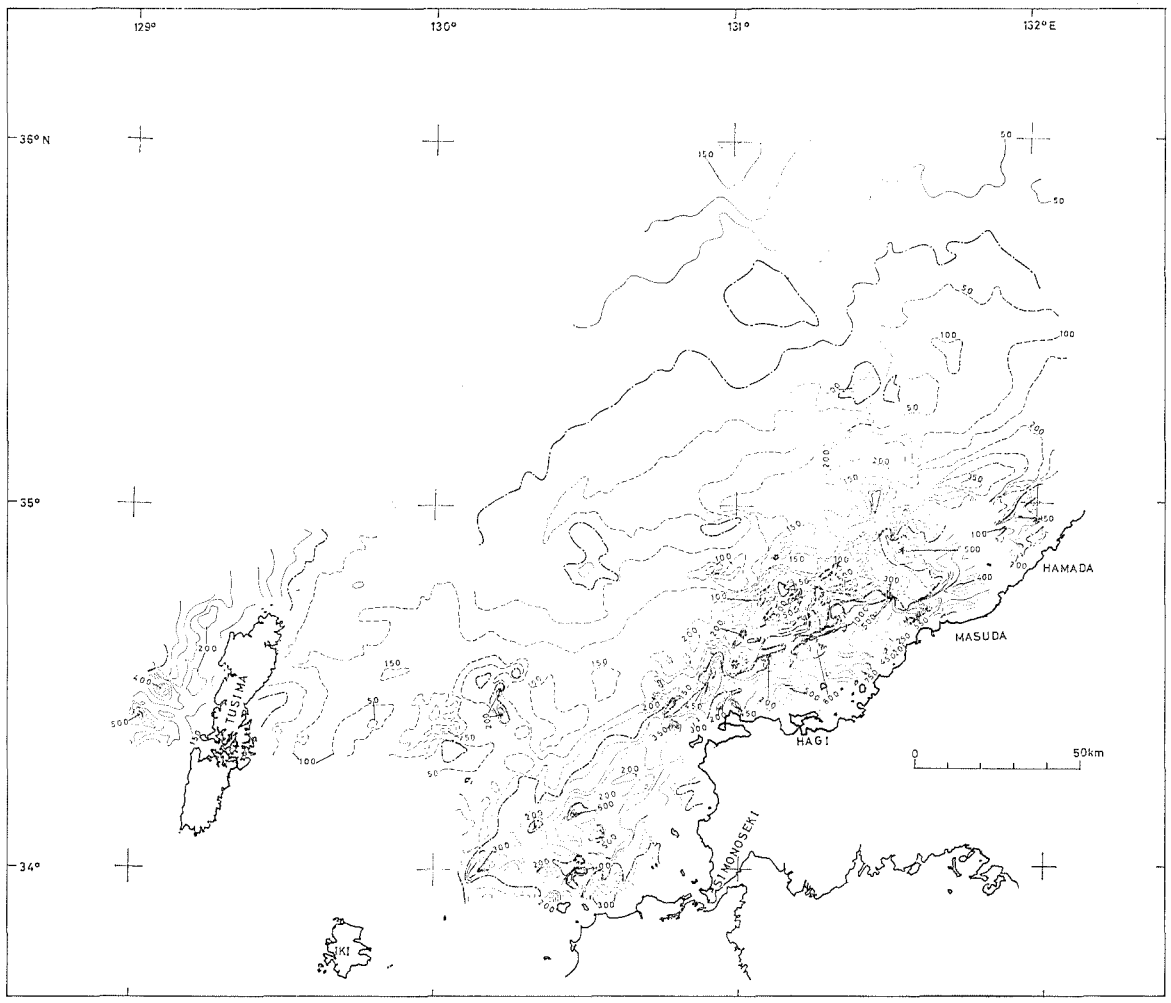

Figure 7 Geomagnetic total intensity anomalies. Contour interval is 50 nT. Solid lines are positive and dotted lines are negative values.

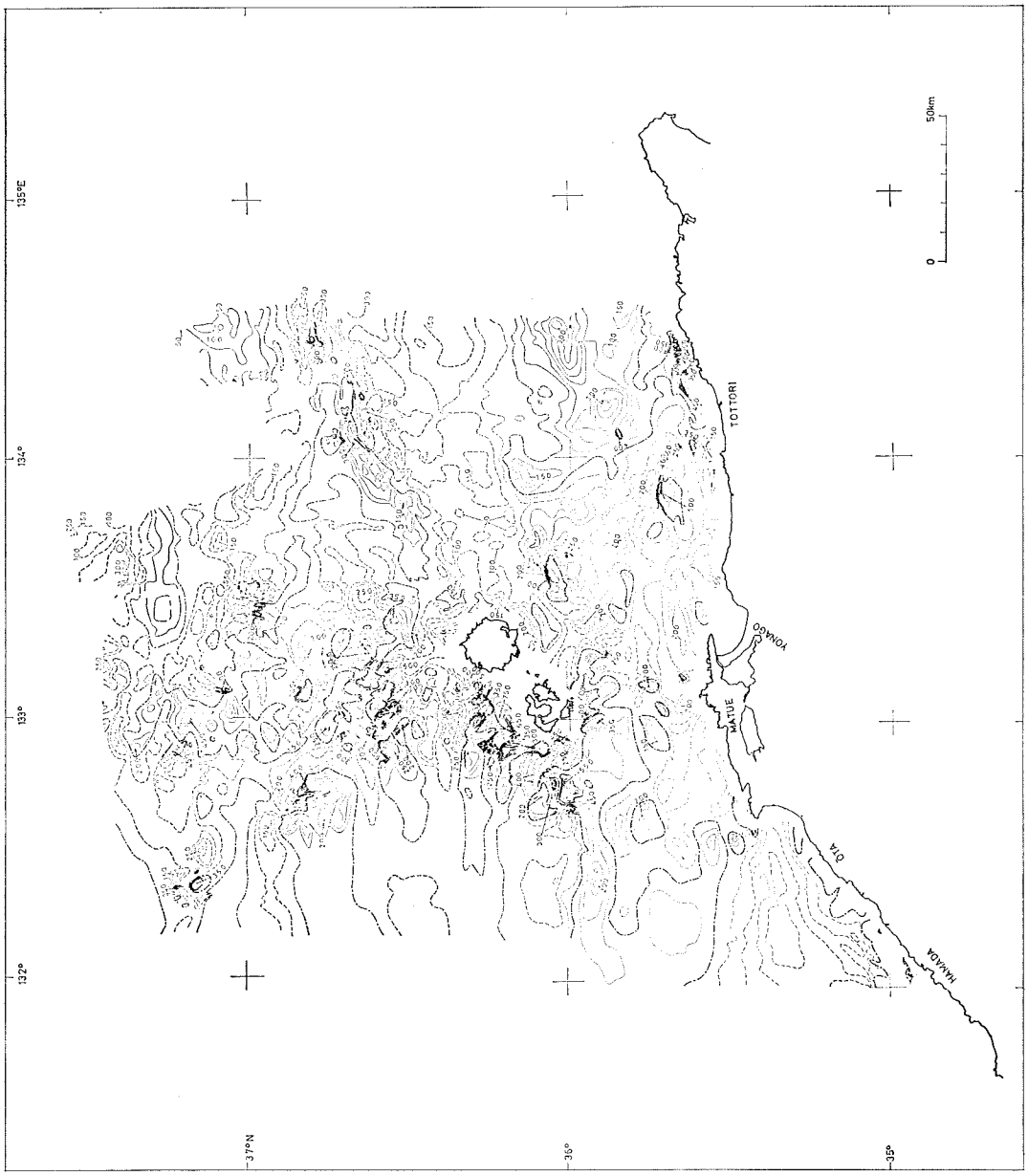

Figure 8 Geomagnetic total intensity anomalies. Contour interval is 50 nT. Solid lines are positive and dotted lines are negative values.

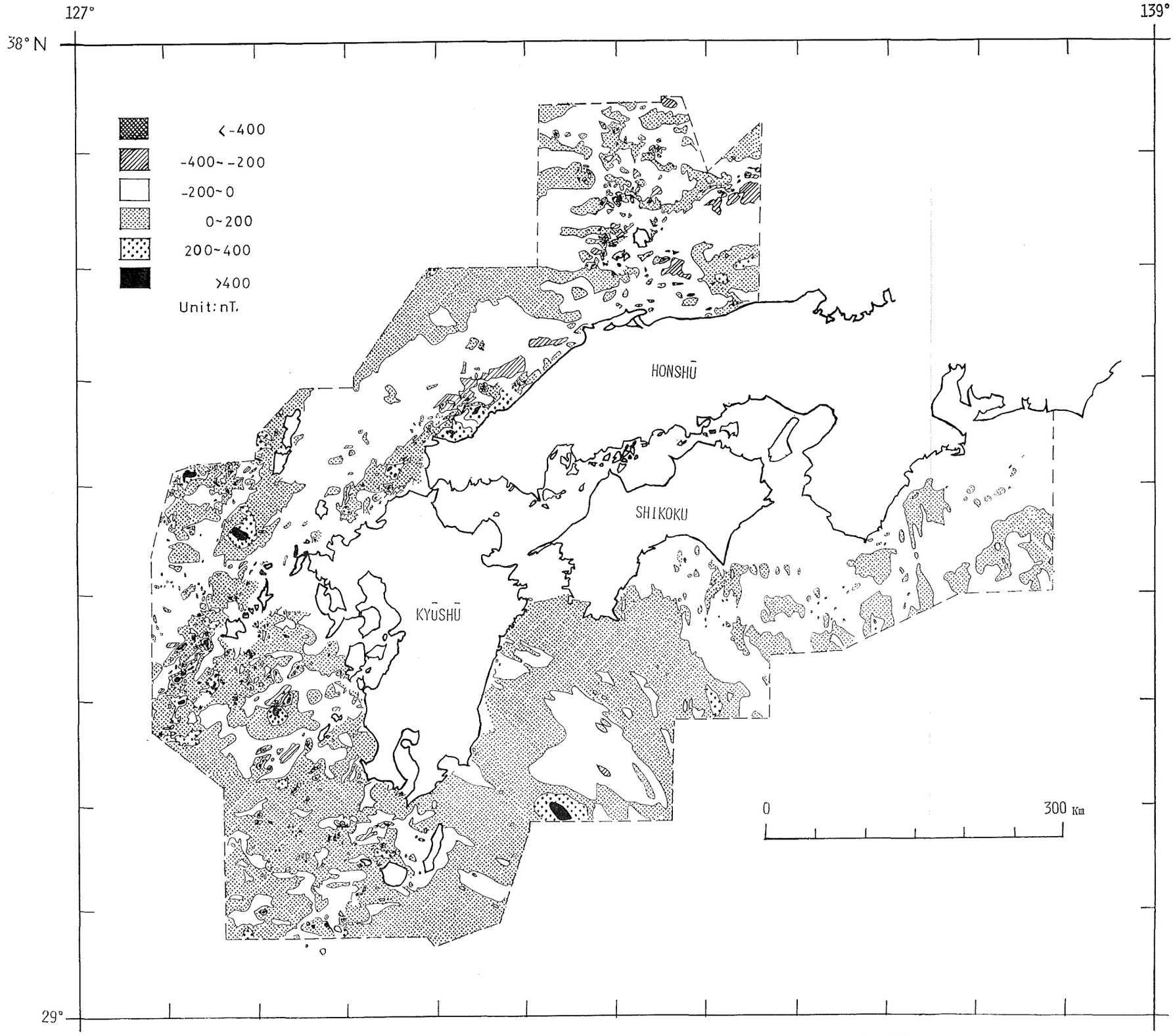

Figure 9 Geomagnetic total intensity anomaly patterns around South-West Japan. Contour interval is 200 nT.

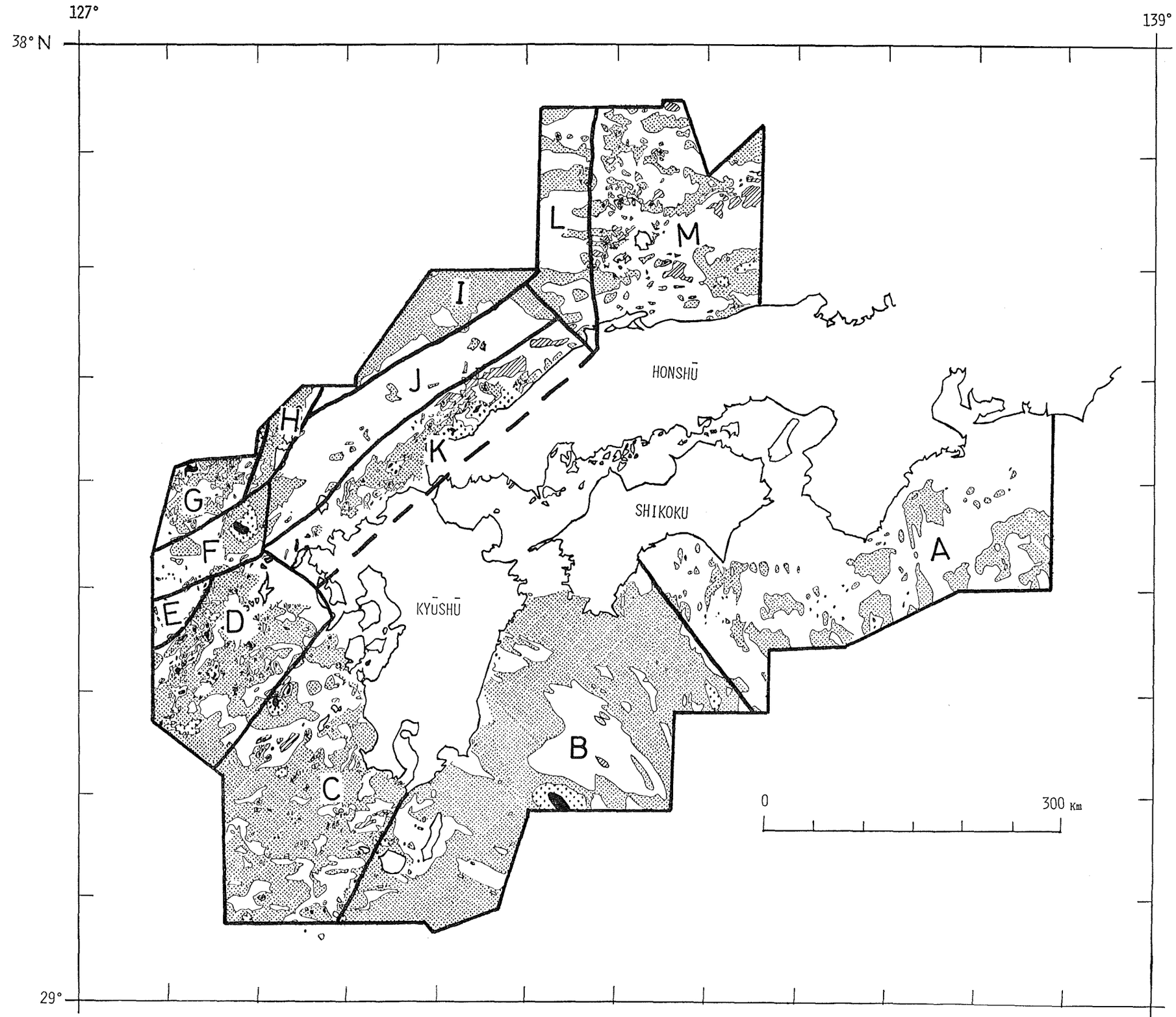

Figure 10 Location and symbols of areas divided according to the magnetic characteristics.

まず調査海域全体については，正の異常域が卓越して異常値算出に用いた標準磁場が不適当であるような印象を与える．特に九州周辺での正の異常域の卓越が顕著である．しかし，日本及び距岸約1,000km以内の海域に関する航空磁気測量の成果図（海上保安庁・1978）でも，この地域の地磁気全磁力の正の異常域の卓越を示している．特に山陰地方とその沿岸部から五島列島や九州北部，九州西岸沖の東シナ海にかけて，広大な正異常帯となっており，これに対して東海地方から四国，九州南部のいわゆる中央構造線沿いの陸上やその延長では負の異常が卓越し，その負の帯状分布域の南を並走する東海沖から九州東方に至る一帯では，弱い正の異常帯となっているように見える．この成果は高度4,500mでの航空磁気測量の結果であるので，地域的な異常分布の特徴を表していると考えてよく，この海域の今回の調査結果で正異常が卓越していることは，地学的に意味のあることであって，標準磁場が不適当なためではない．特に山陰から九州西方に至る正の異常帯は，付近の陸上に安山岩，玄武岩等の磁性岩体が広く分布していることから，沿岸海域に塩基性火成岩が多量に分布していると考えられ，さらに位置的には地質学分野で台湾—宍道褶曲帯と呼ぶものに重なっている．このことは前述の WAGEMAN et al. (1970) の結果と一致する．

次に，地磁気異常分布の特徴によって調査海域を Figure 10 のように区分し，それぞれの海域について地磁気異常の詳細と関連のある地形及び地質構造について述べる．

（1） A区域（東海，紀伊，四国東部沖）

海底地形は，海岸から南海トラフにかけて南海トラフとほぼ平行なならびで，大陸棚，大陸棚斜面，深海平坦面，堆および海丘列，起伏の多い大陸斜面，南海トラフの順に配列している．東海沖から紀伊沖にかけては，駿河湾口の石花海から御前埼堆を通り，南西に延びる海丘列は，熊野舟状海盆の厚い堆積物をせき止める外縁隆起帯となっている．音波探査の結果（永野他・1977）によると，熊野舟状海盆中心部は中新世末から洪積世中期の地層の向斜部となっている．しかし志摩半島の南では熊野舟状海盆の中心軸に沿って音響基盤の高まりがある．

地磁気異常分布は，まず潮岬より東の海域から見ていくと，顕著な異常はない．わずかに紀伊半島南東岸から御前埼東方にかけて熊野舟状海盆を通る正の異常帯が見られ，その振幅は付近の海域からたかだか50ガンマである．この異常帯は50ガンマごとの等値線では明瞭ではないが，原因となる磁性体の深さは海面下約10km程度と考えられる．地質調査所の研究報告（1978）によれば，この磁性岩体は深さ9～10km，帯磁率3～4×10^{-4}emu/ccで，第三紀花崗岩類および斑れい岩と考えられている．それらの沖合いに大陸斜面に沿って見られる正の異常帯は，音波探査による音響基盤の高まりの分布に一致する傾向を示すが，磁性岩体の深さは9km程度であり，表層付近の地形や音響基盤の高まりは，この地磁気異常の原因ではないと考えられる．

潮岬より東の海域でも地形，地磁気共に前記海域の特徴がそのまま続いており，土佐碆海丘群，安芸海丘群，須崎海丘群等の内側に土紀舟状海盆や土佐海段等の深海平坦面がよく発達している．大陸斜面では南海トラフの軸と平行して細長いトラフ状とリッジ状の地形が2～3列見られる．熊野舟状海盆沿いの地磁気正異常帯は，潮岬付近から西へ延びて室戸岬付近を通り足摺岬付近に至っているようである．大陸斜面沿いの正異常帯は，室戸岬南々東沖まで延びているが，それより西では南北に細長く，振幅も200ガンマ以上に及ぶ異なった特徴を示すものとなっている．

以上に見るように，A区域はいわゆる四万十層群の厚い堆積層に起因すると思われる平坦な地磁気分布と，深海平坦面及び大陸斜面の下の海面下10km前後の深さに，トラフに平行な弱い磁化（花崗岩程度）を示す磁性岩体が並走していることが特徴である．

（2） B区域（高知沖，日向灘，種子島東方）

地形的には南海トラフ，九州パラオ海嶺，琉球海溝の会合する海域で，足摺岬沖まではそれ以東の海域の特徴をそのまま西に延長した様子を示し，足摺岬沖から南西へは等深線を乱しながら徐々に琉球弧に沿った南北の方向性を示すようになる．音波探査の結果ではその境界はさらに明瞭で，断層，摺曲軸，基盤の高まり等の方向が足摺岬沖を境に東では東北東～西南西であり，西側では北向きである．豊後水道沖には，熊野舟状海盆，土紀舟状海盆，土佐海段等と同列の深海平坦面である日向海段が位置し，厚い堆積物をためている．

種子島東方では地形，地質構造共に琉球海溝に沿うほぼ南北に近い方向性を示し，種子島，屋久島等の地形の高まりから東へ大陸棚，大陸棚斜面，大陸斜面が並走している．大陸斜面には，ところどころに小規模な深海平坦面に似た地形が見られる．日向灘から種子島東方にかけての大陸棚の音波探査結果では，音響基盤の小規模で南北に長いリッジ及びトラフに似た起伏が多数分布しているのが特徴的である．このように地形，地質構造ともに足摺岬南方から日向灘にかけては，南海トラフに平行な西南日本弧の特徴と，琉球海溝に伴う琉球弧の特徴を示している．重力のフリーエア異常（海上保安庁海図第6354G，6355G）は日向灘から種子島東方の大陸棚沿いに－100～－140ミリガルの負の異常帯を形成しており，地殻深部では琉球弧の地殻運動が日向灘まで続いている事を明瞭に示している．しかし地質学的には中生代及び古第三紀の四万十層群が琉球弧に沿って南へ延長していると考えられており，足摺岬，大隅半島，屋久島ではそれを貫いている中新世の花崗岩類が露頭している．これら花崗岩類は前記A区域では堆積物に埋められているが，この海域ではより新しい琉球弧の活動に伴って隆起と浸食を受けて露頭したとも考えられる．

地磁気異常は足摺岬から南々東に引いた線付近を境にして，その西側は若干正の卓越する異常帯となると共に，九州パラオ海嶺の北への延長の大陸棚付近に＋450ガンマの正の異常，その北に振幅200ガンマの広い負異常域が広がっている．前者は九州パラオ海嶺の北端部で，原因の岩体はかなり深いと考えられる．後者についてはその原因は不明である．これらの異常域から南は，磁気的にきわめて平坦な海域であり，種子島はわずかであるが負異常域となっている．佐多岬から屋久島西岸へ延長する直線から西側は，急に地磁気異常の複雑な地域となっており，その境界はきわめて明瞭である．

（3） C区域（長崎沖から吐噶喇群島）

長崎半島から長崎海脚（鯵曽根，ヒラジ曽根，沖ヒラジ曽根）へと南西に延びる地形の高まりがこの海域の北の境界で，その南の男女群島と甑島列島の中間には，沖縄舟状海盆北部の海盆底が広がり，水深は700～800mである（永野地，1976）．その南は700～900mの比較的平坦な海盆底に島，堆，海丘が散在するが，その並びは北東—南西から北々東—南々西の方向性を示すように見える．例えば天草諸島—甑島列島，宇治群島—草垣島—盲曽根，坊ノ岬—黒島—東新曽根，西新曽根及び東新曽根—蟇曽根，佐多岬—竹島及び硫黄島—口永良部島—口之島—中之島などである．音波探査結果による基盤隆起や断層，摺曲の方向もこの向きのものが圧倒的に多い．陸上地質は九州中部を臼杵八代構造線が北東—南西に横切り，その南に秩父帯及び四万十帯が並走していると考えられている．しかし九州南西部では第三紀，第四紀の安山岩，玄武岩が広く分布していて四万十帯の北東—南西の方向性を覆い，不明瞭にしている．地磁気異常と直接関連すると思われる火成岩は，長崎半島付近の第三紀，第四紀安山岩及び玄武岩，天草諸島や宇治群島，草垣島，黒島の第三紀安山岩及び吐噶喇群島沿いの第三紀第四紀安山岩である．

地磁気異常はそれらの地形の高まりに伴うか，または地形では不明であるが音波探査で基盤の隆起がみられる位置に伴って分布する．長崎海脚の南西延長上の海盆底にある500ガンマの異常，甑島列島西方の400ガンマの異常の原因岩体の深さは海面下2km程度である．また前述の北東—南西から北々東—南々西向きの島や堆の

列の中間にも，地形や音波探査では不明な磁性岩体の凸部を示す異常がいくつか認められ，それらの深さは3～5㎞程度である．地磁気異常分布から，これらの堆や基盤凸部は，同じ基盤の高まりや島の列に属する陸上に分布する第三紀安山岩と考えられるが，吐噶喇群島だけは第四紀の安山岩がこれに重なって，現在の火山フロントを形成している．また火山フロントの東縁は，地磁気異常分布図上で明瞭な一線として認められる．四国から九州中央部に延びた四万十帯の東北東一西南西の方向性が九州西部においてより新しい安山岩類に覆われているが，その延長である当区域において島及び堆列の北東一南西の方向性として再び現れ，地磁気異常図にその傾向が表現されている．また音波探査結果の基盤の断層の方向もこの区域では北東一南西方向である（桜井，永野・1976）．

（4） D区域（五島列島及び男女群島付近）

中国地方の日本海沿岸から九州北部の延長線上にあたり，いわゆる台湾宍道褶曲帯（WAGEMAN et al.・1970）と呼ぶ基盤の隆起地帯である．地形は平戸島から五島列島，男女群島とその付近の堆などの方向性の他に，これと直交する方向の卓越する五島海底谷群の開口部及びその南の平坦面（福江海盆）が顕著である．五島列島付近の地殻ブロックは中新世中期まで沈降し，その後上昇に転じ陸化したと考えられており（桂，永野・1976），陸上には新第三紀の五島火山岩類（安山岩，玢岩，流紋岩）及び第四紀玄武岩がみられる．男女群島陸上の地質は第三紀塩基性岩類である．

地磁気異常分布は，この区域全体に五島列島及び男女群島と同じ方向性を強く示す．それらはリッジ状の基盤の隆起を示すもので，頂部の深さは海面下約2～4㎞で，地磁気異常の振幅から正に帯磁した安山岩等の塩基性岩と考えられ，福江島から南西へ延びる一帯及び同島から南々西へ延び，男女群島に至る一帯，男女群島の西20㎞から南々西への一帯が顕著である．

五島列島から長崎半島沖の間の海域は，北部が大陸棚，南部は500m以浅の平坦な海盆で，大陸棚外縁には音響基盤の露頭が見られる．地磁気異常分布は複雑で，五島列島付近ではほとんど海底付近，五島列島と長崎海脚中間では海面下1～4㎞程度の深さに正帯磁の塩基性火成岩の上面があり，複雑な起伏をしているものと推定される．

（5） E区域（福江島北西）

地形的には水深120～200mと浅く，五島海底谷群の開口部が集合する地域である．また東海大陸棚東縁の一部ともなっており，区域東縁は五島構造線（桂，永野・1976）である．

きわめて複雑な地磁気異常の等値線が特徴的で，負の異常が卓越し，振幅は100ないし450ガンマで，原因岩体の頂部は海面下1～数キロメートル程度できわめて浅いと推定される．これらは逆帯磁の貫入岩群によるものと思われる．それらの地質年代については不明である．

（6） F区域（対馬と五島列島の中間海域）

前記E区域の北，中五島海底谷群，東五島海底谷群の谷頭部で，水深は100～120mであり，地形及び音波探査の結果では対馬構造線と五島構造線の接続部付近をこの区域東縁と考える．

地磁気異常分布図では，周囲の海域に比べ等値線の屈曲がゆるやかで，明瞭に区別できる．区域全体の分布方向はほぼ東西で，地磁気異常の振幅は150～550ガンマ，原因岩体頂部の深さは5㎞前後，帯磁は正帯磁である．振幅から原因岩体を推定すると，区域東部では酸性岩，西部では塩基性岩が妥当であろう．この一帯は，東西方向に広がる基盤の沈降帯と考えられ，その上に厚い堆積層をのせているものである．

（7） G区域（対馬下島西方）

水深90～120mの平坦な海底で，大陸棚東縁であり，区域西縁は対馬構造線に一致する．地磁気異常分布は

複雑で，正負の異常が一面に分布し，振幅は200～1,250ガンマと大きい．原因岩体の深さは1～5km程度，帯磁は正で，これらの事から安山岩，玄武岩の貫入岩体が多数分布していると考えられる．

（8） H区域（対馬）

対馬ブロックそのもので，いわゆる対州層群が厚く(1,000mに達するといわれる)その下部は不明であるが，これを新第三紀後期の石英斑岩，花崗岩が貫いている．これらは磁性が弱く，付近海底にほとんど地磁気異常を伴っていない．

（9） I区域（対馬北東の大陸斜面）

水深130～1,500mで区域南部から北方へ，大陸棚外縁，縁辺台地，大陸斜面が東北東—西南西向きに並んでいる．音波探査結果によると，縁辺台地付近では基盤が対馬海盆の方向へ傾いている．地磁気異常は0～+150ガンマで，等値線はほぼ地形と同じ向きできわめて平坦である．したがって磁気的基盤は深いか，あるいは磁性の強い岩石を欠いているかである．

（10） J区域（対馬東北東海域）

地形は，水深120m程度の大陸棚外縁の平坦面で長門沖には岸線に直角に北へのびる高まりがあり，平坦面を東西に二分している。この区域は基盤の向斜部で堆積盆地となっている（登崎他・1978）．

地磁気異常は西半部の平坦面で0～−200ガンマと負で，かなり平坦である．対馬と長門の中間に位置する小規模な堆に伴って+200ガンマ程度が見られ，これによりこの区域が東西に二分されるが，その東の海域はさらに磁気的に平坦となる．これら弱い負の異常は，その南の大陸棚一帯に分布する磁性岩体が，全体として正に帯磁しているため，それらに伴う北側の負異常で，この海域海底は，磁気基盤は深いか欠除しているかである．

（11） K区域（九州北部および山口県，島根県北部沿岸）

海底地形は北へ傾く大陸棚海域で，海岸付近の陸上には白亜紀火山岩類，併入岩類，三群変成岩類，第三紀グリンタフ，さらにそれらを貫く第四紀火山岩類がパッチ状に入り乱れて分布し，第三紀末期以降の火成岩等がそれらを覆っていないため，各時代の火成，変成活動の産物を地表にとどめている．これらのうち，地磁気異常に特に関連の強いものは，浜田付近の中新世安山岩，玄武岩類，益田から萩，長門，豊浦付近の白亜紀安山岩，鮮新世及び更新世のアルカリ玄武岩類，見島付近の古第三紀安山岩玄武岩類，新第三紀末期アルカリ玄武岩，北九州福岡，唐津周辺の白亜紀前期の安山岩類を含む凝灰岩，これら海岸付近の島にみられる新第三紀末期のアルカリ玄武岩などであり，さらにこの区域沿岸に広く分布している花崗岩類も若干の関連を有するものと見られる．地磁気異常はこの区域全般に複雑な等値線で示されており，正の異常が卓越し，海底ないしうすい堆積層の下に，これら付近陸上にみられている岩石が広がっているのであろう．特に見島周辺や福岡沖海域の広い大陸棚では1,000ガンマ以上に達する強い異常がみられ，付近陸上では玄武岩の分布は小規模であるが海底にはかなり広く分布しているのであろう．

なお，この区域は前記D区域の北西延長上で，巨視的には基盤の隆起地帯であり，いわゆる台湾宍道褶曲帯の北西端をなすものである．

（12） L区域（日御碕北方の大陸斜面）

隠岐海脚西部の大陸斜面で，区域南部には大陸棚部を含む．音響基盤は深く不明である（南部を除く）．

地磁気異常は平坦で，等値線は東西向きであり，0ないし−50ガンマである．区域北部には，隠岐海脚北端部が西に張り出しているための小規模な基盤隆起を示す異常が見られる．区域中央部は磁気的にも基盤は深く，等値線からは深さ10km以上と推定される．

(13) M区域（鳥取沖）

隠岐海脚と隠岐堆が地形上の特徴を形作り，鳥取—松江沿いの大陸棚と共にそれら浅所には複雑な地磁気異常が伴っている．これら異常の原因となる火成岩は，前記K区域と同種のもの及び三瓶山や大山付近の第四紀カルクアルカリ安山岩などと考えられる．

地磁気異常分布では，前記K区域の北西延長としての異常帯は特に認められない．分布図から異常帯を区分するならば，隠岐海脚に伴う南北の異常帯，これに斜交する隠岐諸島及び隠岐堆沿いのもの及び隠岐諸島から鳥取付近に至る異常帯の三地帯である．いずれも音響基盤の隆起部に強い地磁気異常が伴っており，地磁気異常の等値線からも基盤は浅いと推定される．隠岐堆沿いのものは，K区域と同方向を示すが互いに雁行しており，台湾宍道褶曲帯との関連は不明である．

5. 考　察

調査海域全般に，地磁気異常図で見る限りすべての海域に北東—南西あるいは東北東—西南西の方向性がみられる．また，弧状構造との関連という観点からみると，南海トラフ，琉球海溝沿いの磁気的平坦海域及びトラフ沿いの花崗岩類の帯状配列を示すらしい2条の弱い正異常帯とその内側の陸，さらにその内側の複雑な地磁気異常で特徴づけられる縁辺海という順序で，海溝から縁辺海までの平行な帯状分布を示している．これらは縁辺海の生成に関して手がかりを与えるものと思われる．

例えば，九州南西の東シナ海沿岸部について見ると，音響基盤の断層が南西向きであり，島及び堆列がこれと同方向を示し，現在の火山フロントの内側にそれらが並走している．陸上地質は四国，中国から九州地方にかけて，三群，三波川，四万十層群等が帯状に並んでいるが，九州ではその配列が乱れ，北薩では地質学的に四万十層群等が南寄りの方向へ屈曲している（木崎・1979）といわれている．これらから，島弧内側では，島弧に平行な断層群が生じ，それらに沿って安山岩等の火成岩の貫入が起こり，縁辺海海底が拡大したと考えることができる．その場合には大洋中央海嶺のような整然とした地質年代の配列ではなく，ほぼ相前後した時期の火成岩活動帯状配列が順に並ぶこととなり，やや不規則で不明瞭な縞状異常がみられる事となる．そのような特徴は日本海，東シナ海，四国海盆で広く分布している．また九州西方の島及び堆列等の地形の高まりの地質年代が，おおむね北から南へ新しくなっていることとも整合する．北薩の屈曲は，そうした琉球弧縁辺海としての東シナ海の拡大によって起こったもので，北端部を九州北部の地塊に制止されたような運動が起こったためと考えられる．その結果，島や堆などの配列の方向が，五島付近では東北東—西南西であるが，南へ下がるにつれて徐々に反時計まわりに方向を変え，土噶喇群島ではほぼ南北に近い向きを示し，全体としてあたかも鳥取県の大山付近を扇のかなめとするような地形の配列を示すものと思われる．

また，種子島，屋久島の花崗岩や四万十層群と平行な深海平坦面に沿う海底下深部にあると推定される花崗岩の関係やそれらの成因なども，この海域の今後の研究課題として重要である．

6. おわりに

本論は水路部の大陸棚の海の基本図の測量成果によるものであり，調査に従事した測量船「昭洋」及び「明洋」の船長ほか乗組員の方々及びデータ処理を担当した，水路部　近藤忠，進林一彦，植田義夫，大森哲雄，塚本徹，穀田昇一，淵上勝義の各氏に厚くお礼申し上げる．

参 考 文 献

Henderson, R.G. and I. Zietz 1948 : Analysis of total magnetic intensity anomalies produced by point and line sources, *Geophysics*, **13**, 428—436.

Isezaki, N. 1973 : Geomagnetic anomalies and tectonics around the Japanese Islands, *Oceanograph. Magazine*, **24**, No. 2, 107—158.

海上保安庁 1978：水路部観測報告全国磁気測量編別冊（G．D．P．観測）

桂 忠彦，永野真男 1976：九州北西方の海底地形と地質構造運動，海洋学会誌，**32**，139—150.

木崎甲子郎 1979：九州西縁構造帯とその意義，地球科学，**33**，No. 3，144—151.

小林和男 1974：四国海盆の拡大と日本列島，海洋科学，**58**，27—34.

永野真男，桜井操，桂忠彦，中村啓美，北原祥二，小野寺健英 1976：九州西岸沖の海底地質，水路部研究報告，**11**，1—38.

永野真男，安城龍彦，登崎隆志 1977：遠州灘の海底地質，水路部研究報告，**12**，1—33.

大島章一，近藤忠，塚本徹，小野寺健英 1975：北海道及び東北地方周辺海域の地磁気異常，水路部研究報告，**10**，39—44.

桜井 操，永野真男 1976：九州西方の海底地形地質構造，地学雑誌，**85**，No. 6，19—31.

Segawa, J. and Y. Tomoda 1976 : Gravity measurements near Japan and study of the upper mantle beneath the oceanic trench-marginal Sea transition zones, *Geophysical Monograph*, **19**, 35—54.

地質調査所：百万分の一地質図，3.

地質調査所 1978：空中磁気探査に関する研究報告（その1），62—71.

地質調査所 1979：空中磁気探査に関する研究報告（その2），93—95.

登崎隆志，加藤茂，北原祥二 1978：山陰沖の海底地質，水路部研究報告，**13**，1—36,

Tomoda, Y. 1973, Maps of free air and Bouguer gravity anomalies in and around Japan, Univ. Tokyo Press.

Wageman, J. M., Thomas W. C. Hilde, and K.O. Emery 1970 ; structucral framework of East China Sea, Am. Assoc. Petro. Geol. Bull., **54**, 1611—1643.

REPORT OF HYDROGRAPHIC RESEARCHES No. 15, March, 1980

IMPROVED TIDAL CHARTS FOR THE WESTERN PART OF THE NORTH PACIFIC OCEAN

Hideo Nishida*

Received 1979 September 10

Abstract

The co-tidal charts of M_2 and K_1, and the co-range charts of $2(M_2+S_2)$ and $2(K_1+O_1)$ for the western part of the North Pacific Ocean drawn by Ogura (1933) have been re-examined and revised on the basis of new tidal data. The co-tidal charts of S_2 and O_1, and ratio charts of S_2/M_2 and O_1/K_1, have also been prepared. The co-tidal charts of M_2 and S_2 indicate a very weak counterclockwise rotation in the Philippine Sea. The comparison between M_2 and S_2, and between K_1 and O_1 show that they generally have the same features in phase and amplitude. But, a peculiar bending of the S_2 nodal line, which is not found in the M_2 tide, are seen in the Caroline Islands.

1. Introduction

Several authors have drawn tidal charts based on harmonic constants in the western part of the Pacific Ocean (Harris, 1904; Sterneck 1920, 1921; Ogura, 1933a; Dietrich 1944). Harris drew the co-tidal chart of the semi-diurnal tide (M_2) for the world. Sterneck drew the co-tidal chart of the diurnal tide (K_1) as well as the semi-diurnal tide (M_2). But the number of the data stations which were used by these authors is not sufficient to show detailed features in this portion of the Pacific Ocean. Dietrich drew the co-tidal charts of four major components (M_2, S_2, K_1, O_1) for the world, and also showed the amplitude along the coasts. His charts, based on 1665 tidal stations in the world, are considered to be the most reliable. But his work is confined to the open ocean and the conditions in the marginal seas are not shown in his charts.

The most comprehensive work on the tides in the western part of the North Pacific Ocean is Ogura's (1933) work. He compiled his earlier works (Ogura 1923a, 1923b, 1926, 1932) in his paper. He collected data from over 600 tidal stations in this area and drew the co-tidal charts of M_2 and K_1, and also the co-range charts of $2(M_2+S_2)$ and $2(K_1+O_1)$. The principal features in the western part of the North Pacific Ocean and the marginal seas (Okhotsk Sea, Japan Sea, Eastern China Sea, Yellow Sea, Bo Hai, Liaodong Wan and South China Sea) are described in his paper.

Four major tidal components which have relatively large amplitude were chosen. They are M_2, S_2, K_1, and O_1. Eight charts were prepared. Four of them are the co-tidal charts of each component. Two of them are the co-range charts of the semi-diurnal and diurnal spring tides, that is $2(M_2+S_2)$ and $2(K_1+O_1)$. The other two are the amplitude

* Oceanographic Division

ratio charts of S_2/M_2 and O_1/K_1.

Ogura's charts were used as basis for the co-tidal charts of M_2 and K_1, and also for the co-range charts of $2(M_2+S_2)$ and $2(K_1+O_1)$. His charts were examined based upon new tidal data, and in some portions of these charts modification of contors were made. The co-tidal charts of S_2 and O_1, and the ratio charts of S_2/M_2 and O_1/K_1 were newly drawn by the author.

In this paper, some characteristics obtained from the detailed examination of the Ogura's charts and from the charts drawn by the author are described.

The original purpose of this work was to estimate tidal constants for each one-degree square in the western part of the North Pacific Ocean from 0° to 55° N and from 115° to 160° E. Those tidal constants were read from the prepared charts and were intended for use in the processing of satellite altimetry data from the offshore regions. A table of the tidal constants can be obtained from the Oceanographic Division, Hydrographic Department.

2. Data and results

Tidal data are mainly from Ogura's collection (Ogura 1933a). These data cover Japanese islands, the coast of the Okhotsk Sea, the Tyosen Peninsula, the coast of China and the scattered islands in the western part of the North Pacific Ocean. In these areas no new tidal data important to tidal charts can be added to his collection. But along the coast of New Guinea, his collection is insufficient. Many tidal data have become available since then. In these regions, the IHB bulletin was referred for new tidal data.

The tidal data at Okino-Torisima (20° 25'N, 136° 03'E) obtained by the Central Meteorological Observatory (Kitagawa, 1943) and recently analyzed by the Hydrographic Department for harmonic constants, have also become available. The specifications of these data are shown in the table 1.

Table 1 Harmonic constants at Okino-Torisima

	H(cm)	κ(deg)	g(deg)		H(cm)	κ(deg)	g(deg)
K_1	15.9	209.7	209.0	N_2	8.3	195.7	179.6
O_1	12.2	185.7	175.1	L_2	1.9	77.2	70.9
P_1	5.3	209.7	208.2	ν_2	1.6	195.7	180.2
Q_1	3.2	168.6	153.1	μ_2	1.7	199.9	179.5
M_2	41.5	203.7	192.4	M_4	0.9	359.1	336.6
S_2	18.1	227.8	225.7	MS_4	1.0	3.1	349.7
K_2	4.9	227.8	226.4				

Figure 1 shows the geographical names referred to in this report.

Figure 2 and Figure 4 are the co-tidal charts of M_2 and K_1. The northern halves are almost the same as Ogura's charts. In the southern halves, small modifications were made to Ogura's charts. In some portions of these charts, the contors of 0.5 hour were added for convienience of estimation.

Figure 3 and Figure 5 are the co-tidal charts of S_2 and O_1 which were prepared by the author. Contors are drawn at every 1 hour, and in some places 0.5 hour contors are drawn.

The hours in all co-tidal charts are referred to 135° E.

Figure 6 and Figure 7 are the amplitude ratio charts. Contors are drawn at every 0.1 with additional 0.05 line.

The charts of the spring range of the semi-diurnal and diurnal tides, $2(M_2+S_2)$ and $2(K_1+O_1)$, are not shown in this paper, because they are essentially the same as Ogura's charts.

The amplitude of each tidal component, calculated from the range of spring tide and the ratio, are shown in Figures 8 to 11.

3. The co-tidal charts of four major tidal components

(1) M_2 tide

The number of tidal stations along the western coast of Kamchatka Peninsula is still small and we have no islands which can be used as tidal stations in the open ocean east of Japan. Therefore, the co-tidal lines in the eastern Okhotsk Sea and in the eastern sea of Japan are uncertain. In other areas, we have a good amount of tidal data along the coasts and at scattered islands, so co-tidal lines were drawn with higher confidence.

There appear eight amphidromic points in the marginal seas. Two of them, in the Bo Hai and the Liaodong Wan were confirmed by Ogura (1934, 1936), base on the offshore tidal observations which show very small amplitudes. The other amphidromic points th-ough they very probably exist near the points shown on the charts, have not been confi-rmed by a direct observation.

There is an area along 148°E which has very crowded contors in the southeastern part of this chart. This is a nodal line, which was first pointed out by Ogura (1933a) and later confirmed by Dietrich (1944). The additional data on the north coast of New Guinea and in the Admiralty Islands, taken from the IHB bulletin, show that the M_2 tide wave progresses from east to west. This supports the existence of the nodal line.

In the large area between the Philippine and Mariana Islands, the tidal hour is almost the same, taking the value of 6.5 to 7.0. But closer examination shows that the tidal hour in the western Caroline Islands is 30 minutes later than along the Pacific coast of the Philippines. This fact, along with the fact that the close contors in the nodal line spread as it goes northward, seems to show that there is a weak counterclockwise rotation of the M_2 tide wave.

(2) S_2 tide

The obtained co-tidal chart is similar to the M_2 tide chart. It has the same characteristics with respect to amphidromy and node.

In marginal seas, the pattern is almost the same as M_2's. The difference in phase (S_2-M_2) is about one hour in almost every marginal sea. But it takes a little higher value in the Okhotsk Sea, that is, 1.5 hours along the Kuril'skie Islands and 2 hours in the east of Sakhalin.

The greatest difference between the M_2 and S_2 phase diagrams is shown on the nodal line between Japan and New Guinea. To the north of 15°N, the nodal line of S_2 exhibits the same pattern and position as M_2. But it bends westward between 15°N and 8°N, and south of 8°N, the nodal line of S_2 is located about 200 miles west of the M_2 nodal line. The

difference between the above-mentioned two nodal lines in the Caroline Islands was pointed out by Ogura (1933a).

Similar to the M_2 phase, the S_2 phase in the western Caroline Islands is 30 minutes later than along the Pacific coast of the Philippines. But this is not represented on the chart because of the irreguralities of data.

(3) K_1 tide

The discussions concerning the density of data stations and uncertainty of co-tidal lines on the M_2 tide also are able to apply to the K_1 tide.

As for the area in the South China Sea a small correction was made to Ogura's chart.

(4) O_1 tide

The co-tidal chart of O_1 resembles the K_1 chart. The differences in phase (O_1-K_1) in most locations are about 2 hours, and these values in the open ocean in the western North Pacific are one hour.

4. The ratio charts of S_2/M_2 and O_1/K_1

(1) S_2/M_2

In the greater part of the marginal seas, the ratio between the amplitudes of S_2 and M_2, S_2/M_2, takes the value of 0.3 to 0.45. However there are several localities where it takes a higher value. These localities are the southeastern part of the Okhotsk Sea (including the Sōya Strait), which has the value of 0.45 to 0.6, the Tusima Strait, which has the value of 0.45 to 0.5 and the Celebes Sea, which has the value of 0.6 to 0.7.

On the eastern coast of Sakhalin, we can find the area where the ratio takes a very small value (0.1). This area is very near to the amphidromic points of both M_2 and S_2. This amphidromy may be the cause of this extreme small values.

At the location of about 8°N, 148°E, a very high value (over 6.0) is found, and at 200 miles west of this location, we find a very low value (below 0.2). These two extremes are due to the difference in the positions of the M_2 and S_2 nodal lines.

(2) O_1/K_1

The ratio between the amplitudes of O_1 and K_1, O_1/K_1, takes a relatively high value of about 1.0 in the area from the southwestern Okhotsk Sea to the Japan Sea. It is between 0.7 and 1.0 in the Eastern China Sea and the Yellow Sea. In the South China Sea, it is slightly higher, being about 0.9. In the major part of the Philippine Sea between the Philippine and Mariana Islands, the ratio is under 0.6. But we have very few data in this region, so this conclusion should be reexamined in the future.

5. The amplitude charts of four major tidal components

(1) M_2 tide

From the Kuril'skie Islands to New Guinea, a relatively low amplitude belt runs in a north-south direction. The southern part of this belt, where the amplitude is less than 10cm, coincides with the nodal line. This low amplitude belt stretches as far north as the Kurile Islands and continues to the low amplitude area of the southwestern Okhotsk Sea. When entering the Japan Sea, the amplitude decreases, reaching less than 10 cm.

In the western part of this nodal line, the amplitude increases as we proceed westward. Meanwhile, in the South China Sea, it is considerably smaller (less than 20 cm).

(2) S_2 tide

In general, the amplitude of the S_2 tide has a similar pattern to the amplitude of the M_2 tide. The low amplitude belt along the nodal line is deflected from a north-south direction corresponding to the bending of the S_2 nodal line itself.

(3) K_1 tide

We find a tendency for the amplitude to increase as we proceed from east to west. An area of relatively small amplitude stretches to the west as far as the Celebes Sea along 5°N. The amplitude of K_1 in the Japan Sea is as small as the M_2 tide, but, in the South China Sea it is large, contrary to the M_2 tide.

(4) O_1 tide

The amplitude of the O_1 tide has features similar to the K_1 tide. But, in the open sea where the amplitudes are small, high confidence should not be put on this chart.

acknowledgement;

Thanks are due to Mr. T. Itoh, Oceanographic Division, Hydrogr. Dept., who has helped to generate the magnetic tape and to draw the figures.

References

Defant, A. 1961: *Physical Oceanography*, vol 2, Macmillan Co., New York, 364—452, 475—496.

Dietrich, G. 1944: Die Schwingungssysteme der halb-und eintagigen tiden in der ozeanen, *Veroff. Inst. Meeresk., Univ. Berlin*, **41**, 1—68.

Harris, R.A. 1904: *Manual of Tides*, Part IV, U.S. Coast and Geodetic Surv. Rep., Wash., 313—400.

Intern. Hydrogr. Bureau: List of Harmonic Constants, Spe. Pub. No. 26.

Kitagawa, M. 1943: *Secret Meteorological Report*, vol 1, No. 4, the Central Meteorological Observatory (in Japanese).

Ogura, S. 1923: Preliminary note on the tides in the western part of the North Pacific Ocean, *Proc. Second Pan-Pacific Sci. Congress*, Sydney, 697—701.

Ogura, S. 1923b: The tides in the Okhotsk Sea, *Miscell. Rep. Hydrogr.*, **10**, 71—88 (in Japanese).

Ogura, S. 1926: On the tides in the seas of Eastern Asia, *Proc. Third Pan-Pacific Sci. Congress*, Tokyo, 167—181.

Ogura, S. 1932: On the tides in the Liantung Gulf, *Hydrogr. Bulletin*, **11**, 269—277 (in Japanese).

Ogura, S. 1933a: The tides in the Seas adjacent to Japan, *Bulletin fo Hydrogr. Dept.*, **7**, 1—189.

Ogura, S. 1933b: On the tidal currents and tides in the northern part of the Hwang Hai, *Hydrogr. Bull.*, **12**, 47—61, 89—98, 137—149 (in Japanese).

Ogura, S. 1934: Further notes on the tides and tidal currents in the Liantung Gulf, *Hydrogr. Bull.*, **13**, 91—98, 133—144, 179—187 (in Japanese).

Ogura, S. 1936: On the tides and tidal currents in Powk Hai, *Hydrogr. Bull.*, **15**, 147—158, 181—194 (in Japanese).

Sterneck, R. v. 1920, 1921: Die gezeiten der oxeane, *Zitz. Ber. Akad. Wiss. Wien*, **129**, 131—150, **130**, 363—371, cited by Dietrich, G. in Veroff. Inst. Meeresk., Univ. Berlin, 1944, 41, 363—371.

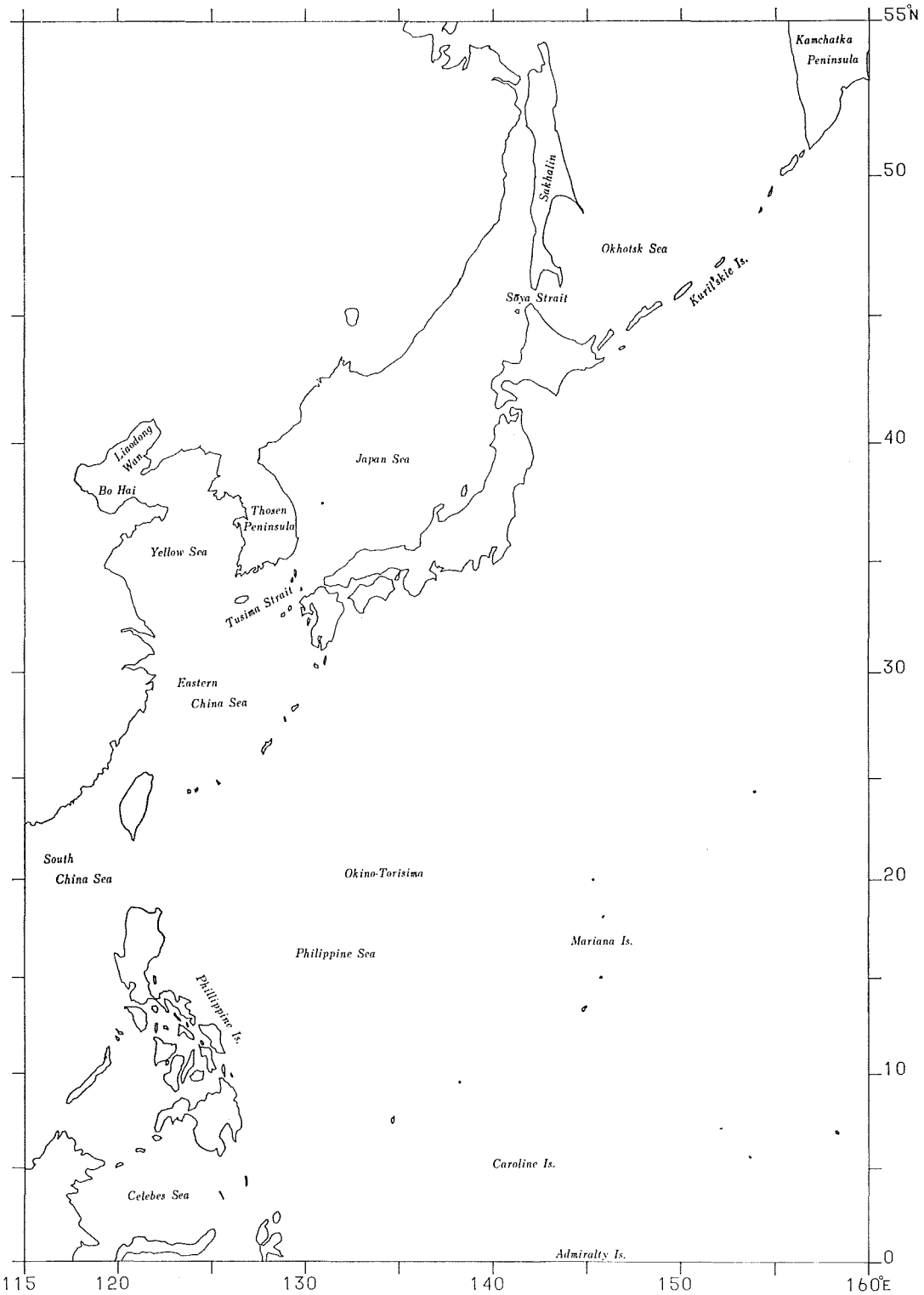

Figure 1 Chart showing geographical names.

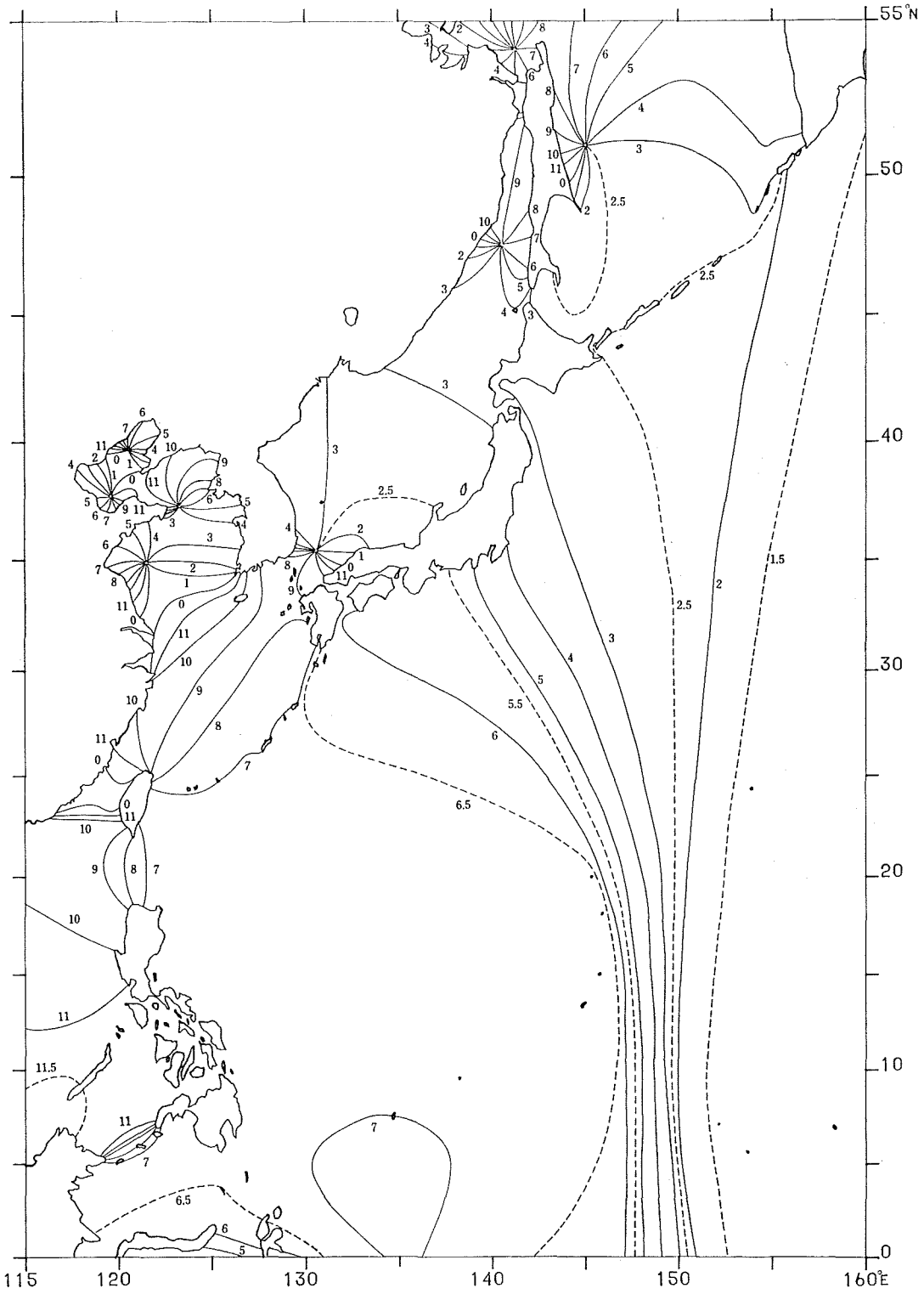

Figure 2 The co-tidal chart of M_2 referred to 135°E (unit ; component hours).

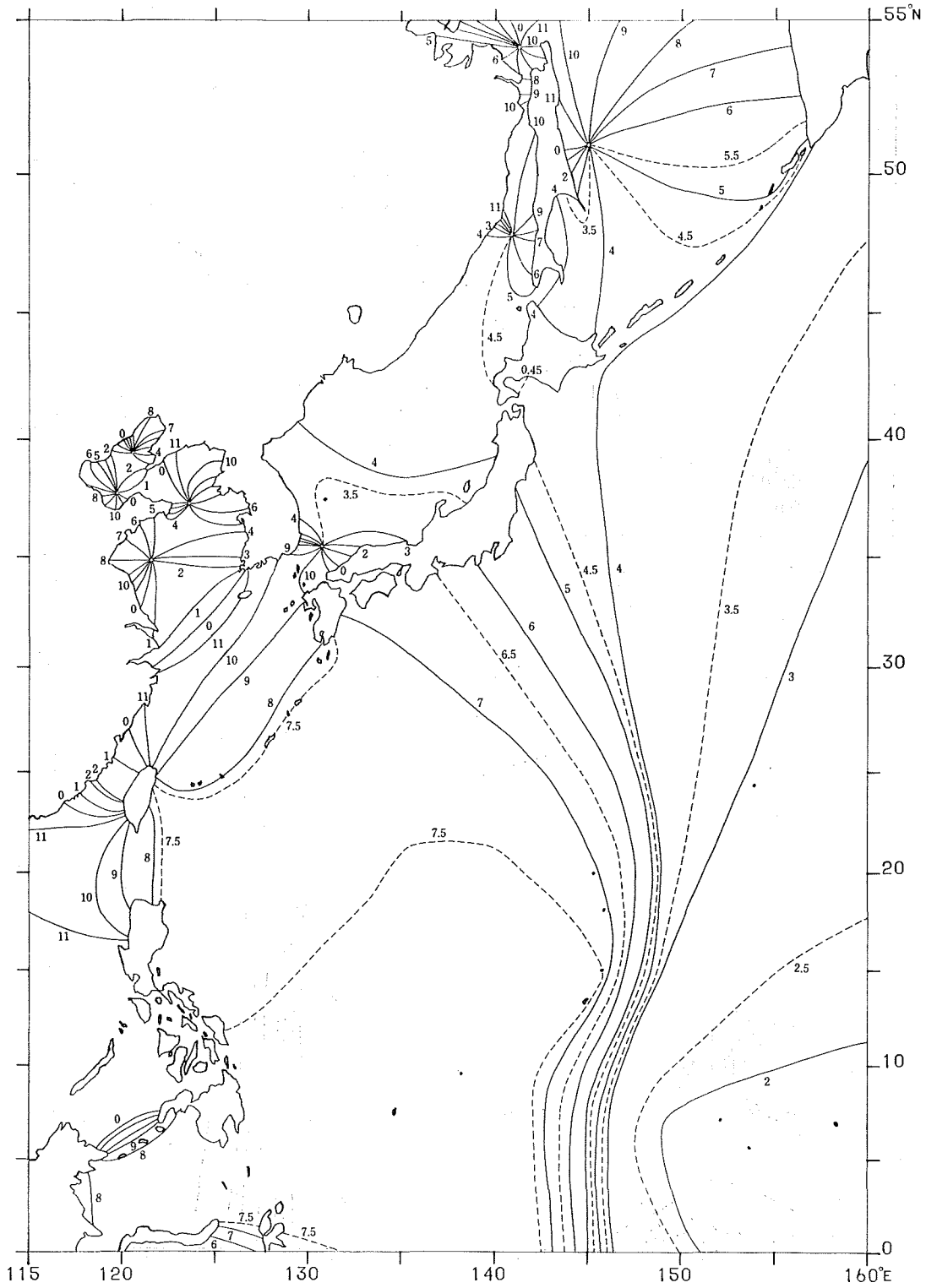

Figure 3 The co-tidal chart of S_2 referred to 135°E (unit ; component hours).

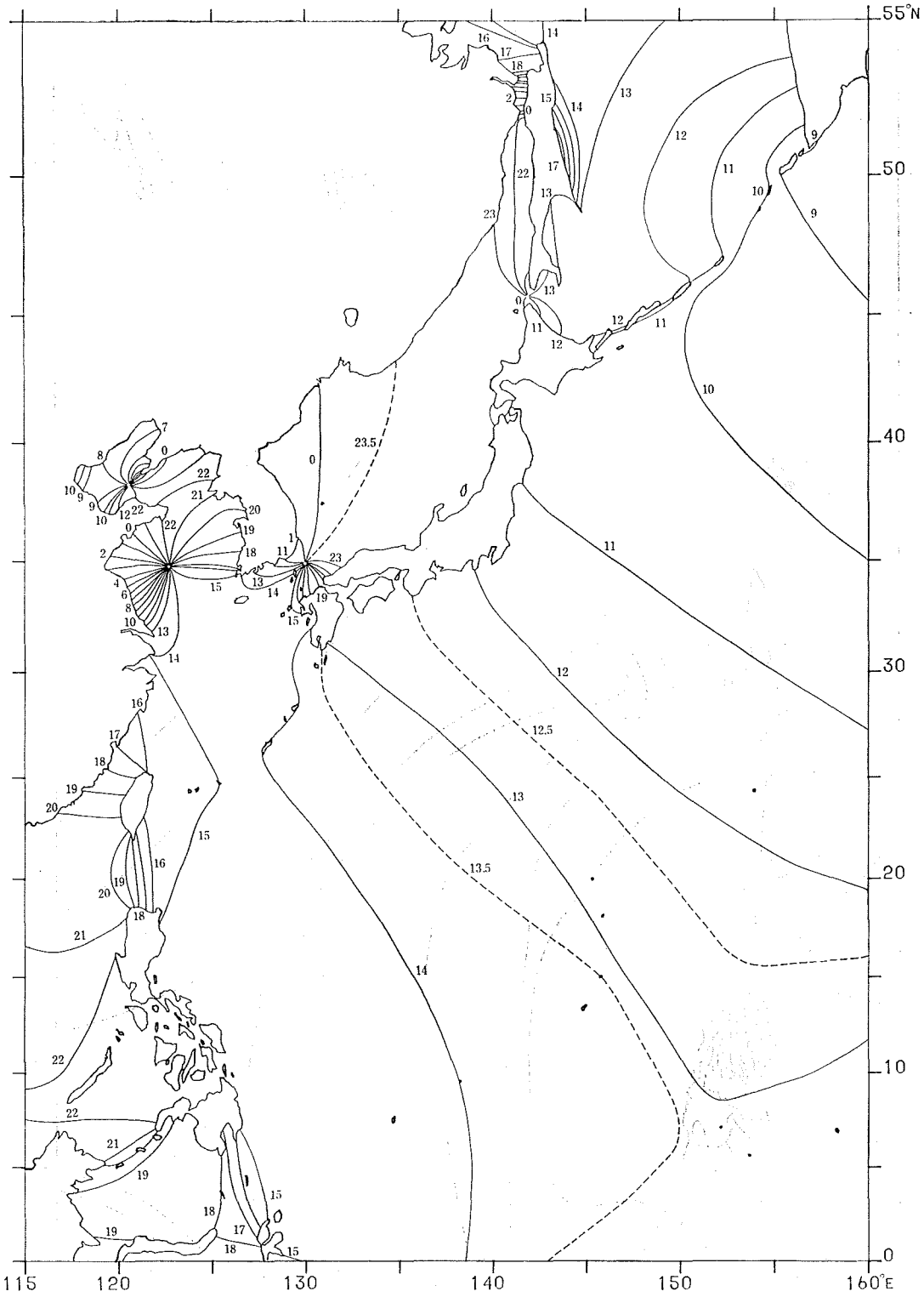

Figure 4 The co-tidal chart of K_1 referred to 135°E (unit ; component hours).

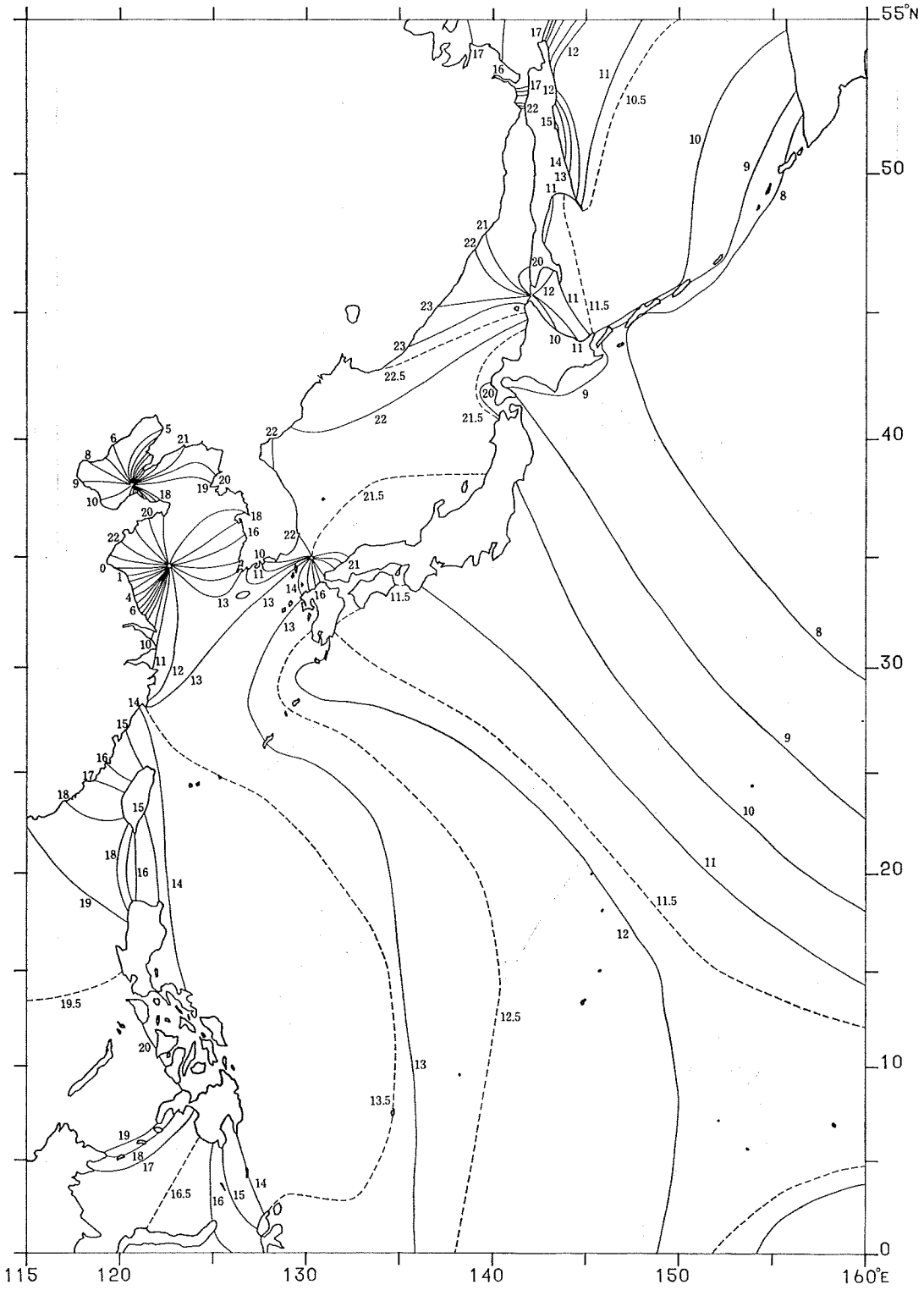

Figure 5 The co-tidal chart of O_1 referred to 135°E (unit ; component hours).

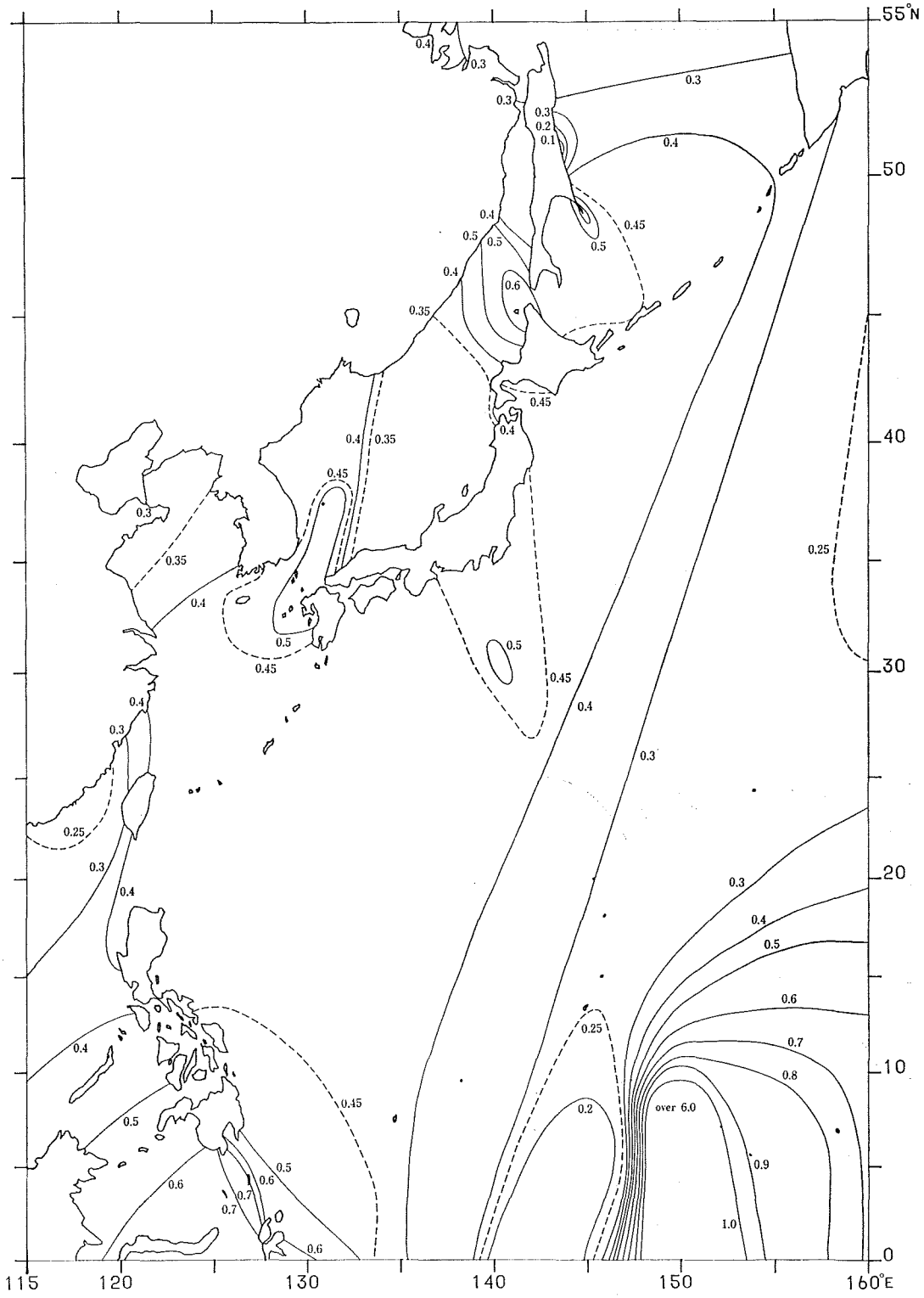

Figure 6 The ratio chart of S_2/M_2.

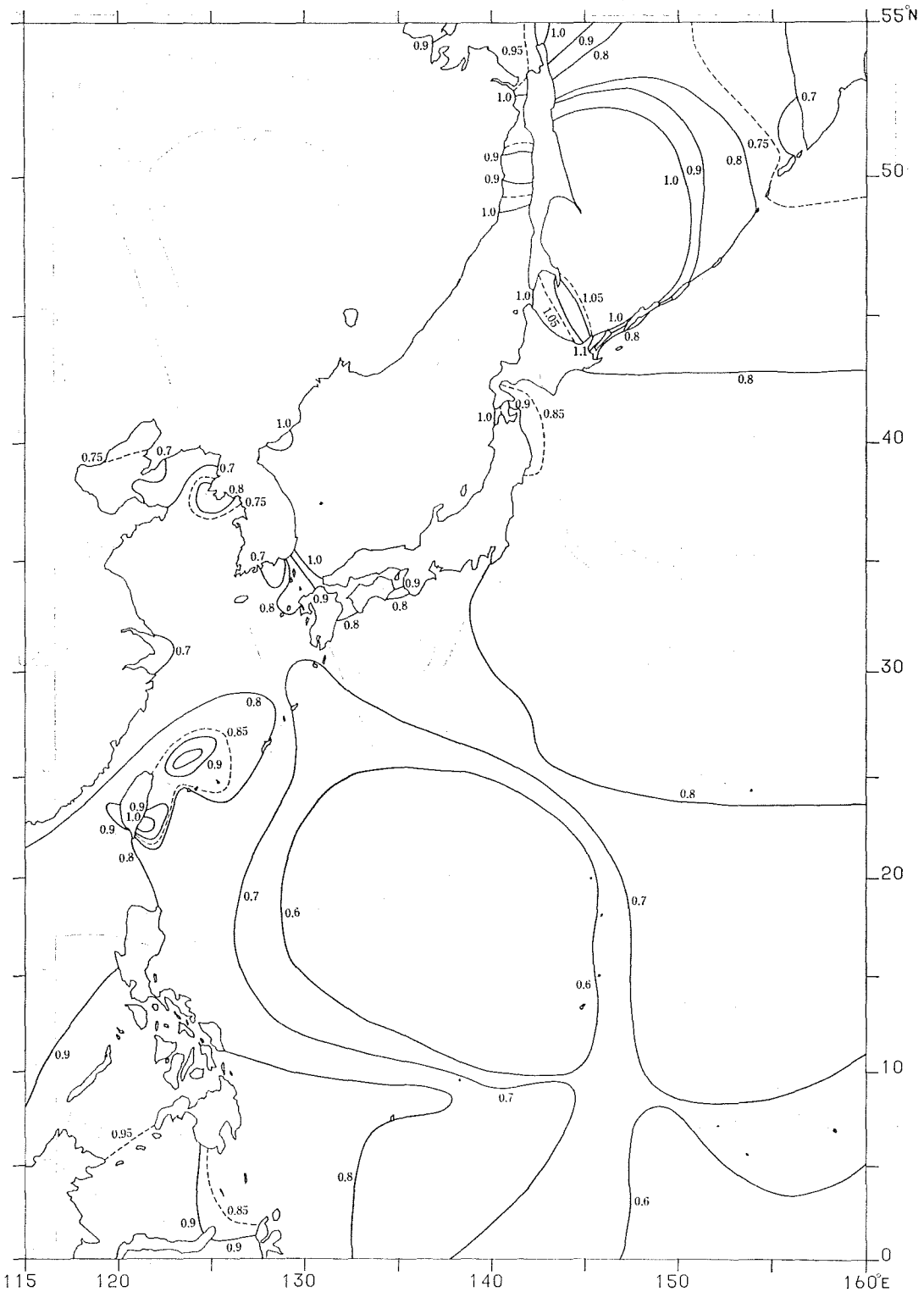

Figure 7 The ratio chart of O_1/K_1.

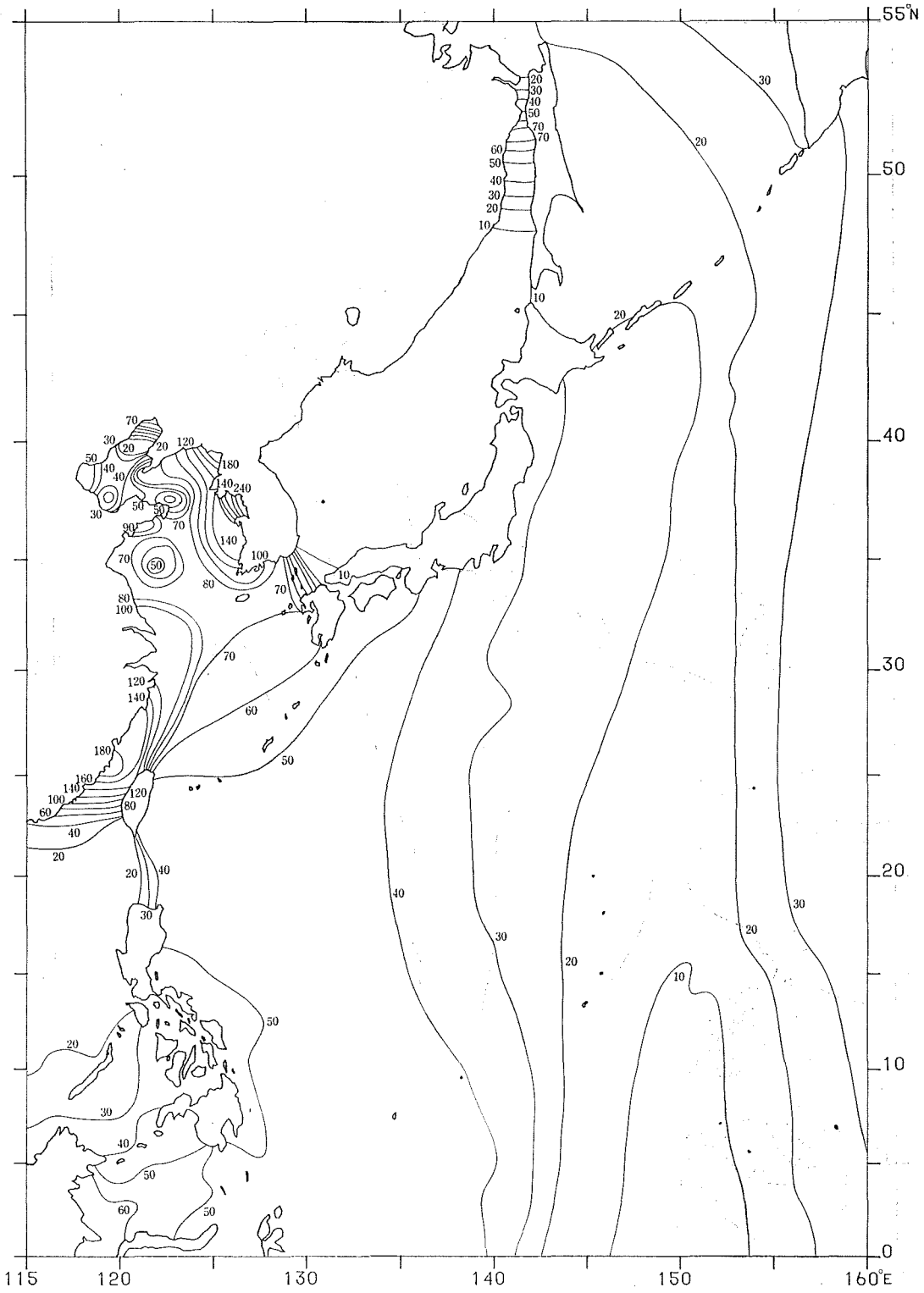

Figure 8 The amplitude chart of M_2 (unit ; centi-metres).

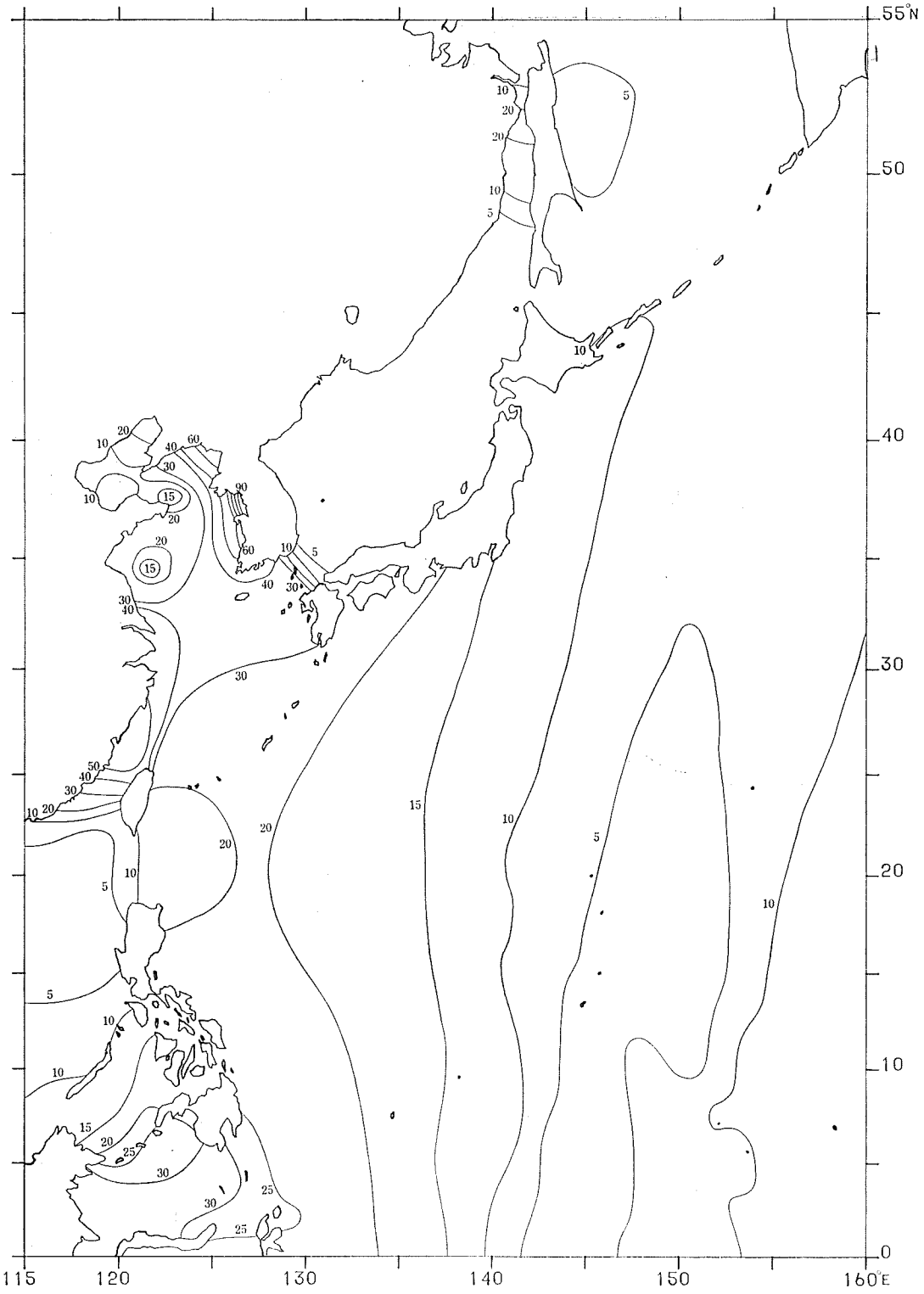

Figure 9 The amplitude chart of S_2 (unit ; centi-metres).

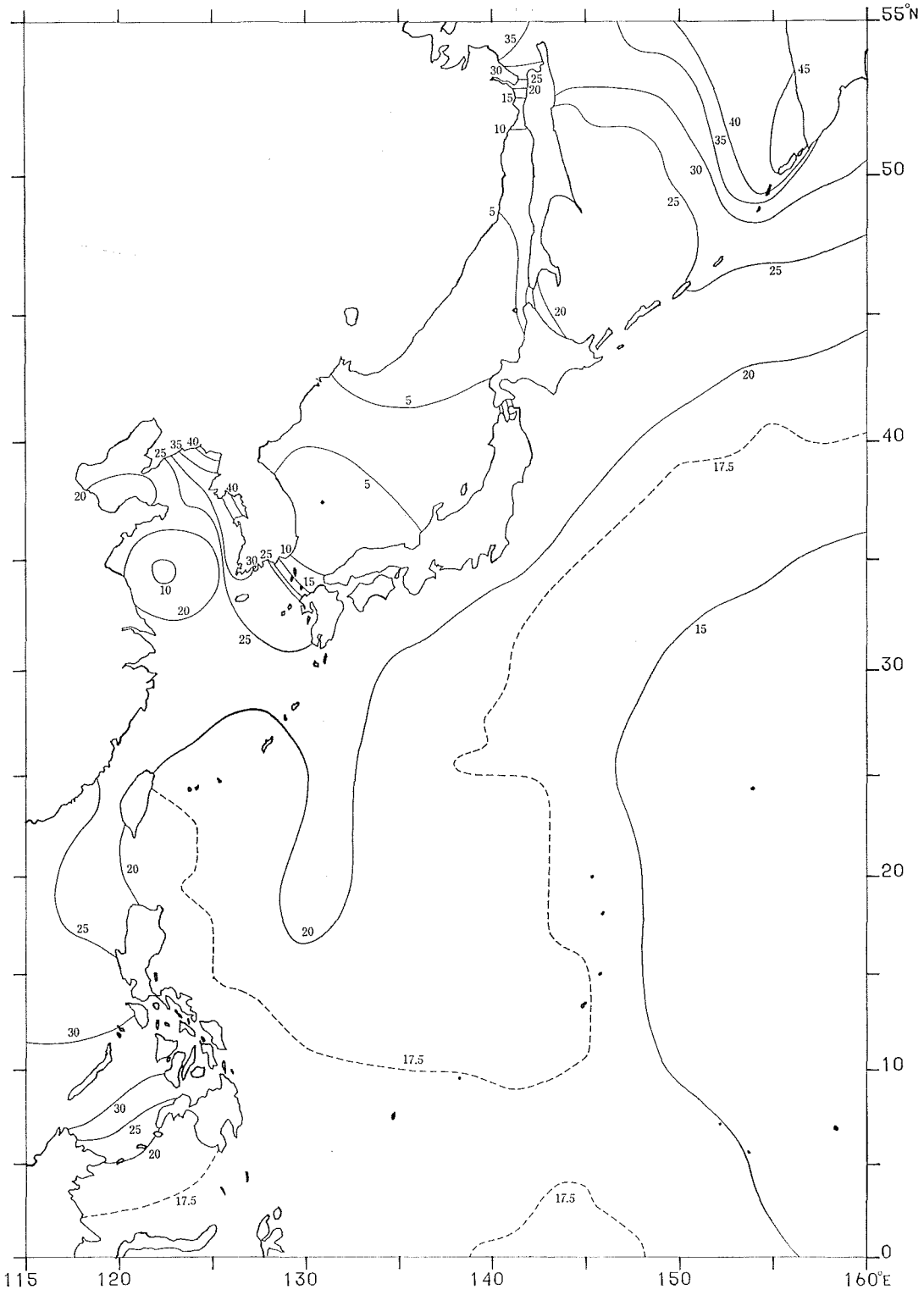

Figure 10 The amplitude chart of K_1 (unit ; centi-metres).

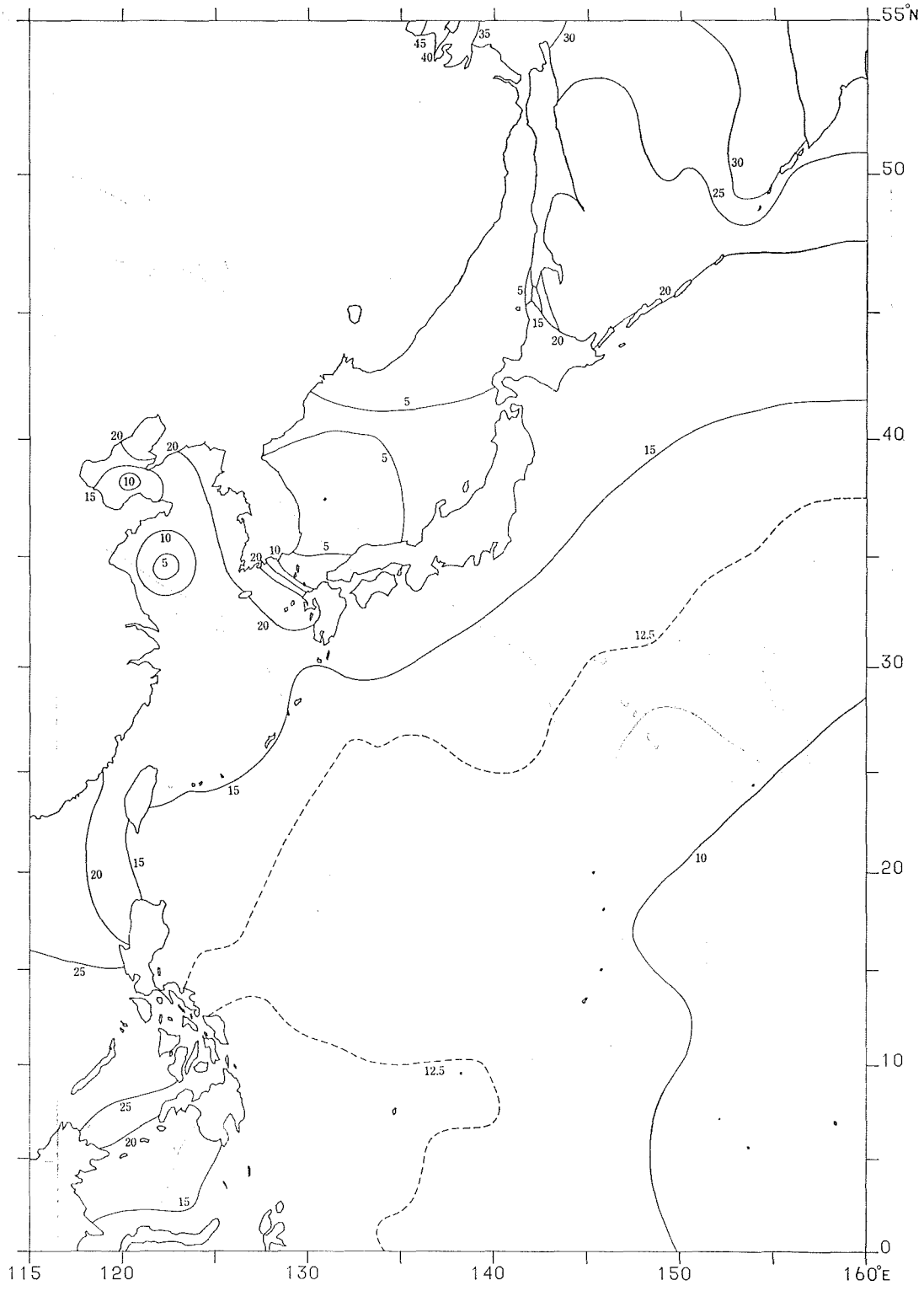

Figure 11 The amplitude chart of O_1 (unit ; centi-metres).

REPORT OF HYDROGRAPHIC RESEARCHES No. 15, March, 1980

NEW DETERMINATION OF A MARINE GEOID AROUND JAPAN

Yasuhiro Ganeko

Received 1979 September 10

Abstract

A marine geoid around Japan is computed on the basis of 30′×30′ and 1°×1° block mean gravity anomalies. The 30′×30′ block data are prepared by reading out the block-averaged gravity anomalies from the published gravity anomaly maps around Japan. The 1°×1° block data are prepared by taking averages of DMAAC's 1°×1° global gravity data and Watts and Leeds' 1°×1° block means. The geoidal heights are computed from the above terrestrial gravity data in combination with the GEM-10 satellite-derived global anomaly field. The GEM-10 model comprises a geopotential coefficient set which is complete up to degree and order 22. The radius of the circular cap area of the numerical Stokes' integration is taken to be 20°. The marked features of the computed geoid are the dents over trench areas. The dents amount occasionally to more than 20 meters relative to the GEM-10 global geoid. The general geoidal high along island arcs is another marked feature of the calculated geoid. Geoid undulations on the land areas of Japan are compared with an astro-geodetic geoid of Japan (Ganeko, 1976). The standard deviation of the undulation diflerences is 1.4 m, while the standard deviation decreases to 0.8 m if the Hokkaido area is excluded. The astrogeodetic geoid in the Hokkaido area seems to have a tilt downward to the north relative to the gravimetric geoid.

The gravimetric geoid is compared with the Geos-3 altimetric sea surface heights. Altimeter data taken along 12 revolutions of the satellite passing over the region of the gravimetric geoid are used, and the comparison figures for each revolution are presented. The r.m.s. values of differences between altimetric sea surface heights and the gravimetric geoidal heights for each revolution vary within the range from 0.6 to 1.9m except for tilts and constant biases. The total r.m.s. difference is around 1.3m. Differences seem to be large in the region where terrestrial gravity data are sparse and consequently gravimetric geoidal heights are poorly determined.

Detailed investigations are carried out concerning the error sources involved in the procedure of computation of a gravimetric geoid by means of numerical integration of Stokes' formula. The results of the investigations estimate the accuracy of the calculated gravimetric geoid to be around 1.3m in the area near Japan and to be around 1.8m in the gravity data-sparse areas. Terrestrial gravity data errors form the biggest error source under the present availability of the surface gravity data around Japan. The estimated accuracy of the gravimetric geoid is compatible with the comparison results between Geos-3 altimeter data and the gravimetric geoid. The accuracy of the geoidal height difference is also investigated. This kind of error estimation is meaningful because some of the error sources have long correlation distances, so that such error sources

* Astronomical Division

hardly affect the accuracy of the geoidal height difference. As for the calculated geoid, the accuracy of relative geoid undulations over 100km distance is estimated to be around one meter.

Detailed investigations concerning various error sources enable us to get a perspective of the geoid computation of the future. After an investigation of the statistical characteristics of the gravity anomaly field around Japan, we derive requirements for marine gravity surveys to achieve a 10cm geoid. 10′ block mean gravity anomalies with an accuracy better than 5 mGals must be prepared in the inner area of Stokes' integration, i. e. inside and outside to 2° around the area where a 10cm geoid is computed. These block data can be derived from profile gravity observations carried out along parallel ship tracks located every 10 nautical miles. Moreover, we need additional gravity surveys by profile observations made every 15 or 30 nautical miles depending on the roughness of the gravity anomaly field in the outer area extending to a distance of 20 to 30 degrees from the boundary of the inner area. Systematic errors larger than 0.1 mGals in gravity observations must be avoided though a few mGals random errors of point gravity observations are acceptable. Stokes' integration should be carried out in combination with a satellite-derived global gravitational field because long wavelength components of the geopotential field are well determined by the satellite trackings. The flattening of the earth and the sea surface topography must be taken into consideration in the computation of a 10cm marine geoid.

Contents

1. Introduction

The determination of the figure of the earth has been one of the most important problems of the geodetical sciences, and not a few people have made great efforts in this subject. The figure of the earth is formed by the topographic reliefs at land areas and by the quasi-stationary sea surface (mean sea surface). Under the assumption that the mean sea surface realizes a equipotential surface in the earth's gravitational field, and then the mean sea surface is equivalent to the geoid, which is elemental in the expression of the figure of the earth as a reference surface of the topographical heights at land and as a realization of the figure of the earth itself at sea.

The three dimensional rectangular coordinates (X, Y, Z) of the earth's surface in the geocentric coordinate system are obtained from the geographic coordinates (φ, λ), the geometric parameters of the earth ellipsoid a (semimajor axis) and b (semiminor axis), and the ellipsoidal height h of the earth's surface which is the sum of the topographical height H and the geoidal height N (see Figure 1):

$$h=H+N=H^*+\zeta, \tag{1-1}$$

where H^* and ζ are so called normal height and height anomaly whose further explanation will be found in the next chapter. The explicit expressions of X, Y and Z are given by (2-7). It should be noted that equation (2-7) is based on the assumptions that the center of the reference ellipsoid coincides with the center of the earth's gravity and the potential of the geoid is equal to the normal geopotential at the surface of the reference ellipsoid.

The three dimensional geometrical relations of points located on the earth's surface can be determined by the geometrical satellite geodesy (e. g. Yamazaki, 1971), but the positions in the geocentric coordinate system cannot be given by such a geometrical method. The world-wide networks of the satellite tracking stations determined by the geometrical method are translated to the geocentric coordinate expressions by knowing ellipsoidal heights, i. e. geoidal heights, at each satellite tracking station. The least-squares adjustment provides us with the translation parameters and the geometrical parameters of the best-fitting earth ellipsoid (e. g. Schmid, 1974; Mueller, 1974; Gaposchkin, 1974). The long wave-length components of the geoid undulations can be determined by the observations of orbit changes of artificial satellites (e. g. Caputo, 1967), and this method can provide us with geopotential coefficients up to degree 20 (Lerch et al., 1977). A geopotential coefficient set comprising coeffi-cients up to degree 20 can express geoid undulations with an accuracy of ± 4 m on the world-wide average basis (see Figure 30). In other words, on the world-wide average basis, geoid undulations of shorter wave-length components than degree 20 amount to ± 4 m and the satellite-derived global geoid undulations commit errors of ± 4 m even if the low degree harmonics are determined without errors. As we will see in Chapter 3, the differences between detailed geoid and the satellite-derived global geoid sometimes reach 20 meters at a specific area such as trench area. Therefore, the satellite-derived global geoid is insufficient for the use of deriving three dimensional positions of the earth's surface by using equation (2-7). The determination of accurate three demensional positions are necessary for satellite tracking stations whose positions affect the determination of satellite positions directly and for observation sites of the

position astronomy, and also the map projections require accurate geoid undulations.

The detailed structures of the geoid undulations can be computed by applying Stokes' formula to terrestrial gravity data. The recent accumulation of sea gravity observations by surface ship gravity meters has made it possible to compute detailed gravimetric geoid not only at land areas but also at ocean areas by the combination of terrestrial gravity data with the satellite-derived gravity anomaly field. The recent works concerning the world-wide detailed gravimetric geoid were made by Marsh and Vincent (1974) and Marsh and Chang (1976a). The Northwest Atlantic area, off east coasts of the United States, is the area where various satellite tracking stations are located and geodetical and geophysical surveys have been carried out with high density. This area has also been selected as the calibration area of the satellite altimetry experiments (Leitao et al., 1975), and much efforts have been concentrated there to obtain an accurate geoid (e. g. Talwani et al., 1972; Marsh and Chang, 1976b).

Detailed geoid undulations at land areas can also be computed by Helmert's formula:

$$N_Q - N_P = -\int_P^Q (\xi \cos A + \eta \sin A)\, ds \tag{1-2}$$

from deflections of the vertical, where ξ and η are the deflection components in the meridian and prime vertical, respectively, and A is the azimuth of the direction of the tangential at a point on the integral path from point P to point Q. We call a geoid computed from deflection observations an "astrogeodetic geoid". The numerical values of deflections of the vertical depend on the adopted deflection of the vertical at the geodetic datum station and the geometric parameters of the reference ellipsoid of the geodetic system, so that the astrogeodetic geoid depends on the geodetic system. Since it is impossible to determine the deflection at the geodetic datum station and the geometric parameters of the best-fitting earth ellipsoid from the geodetic observations made in a restricted land area, astrogeodetic geoids suffer some amount of systematic tilting and distortion against the geocentric coordinate system. On the contrary, the gravimetric geoid computed by Stokes' formula is automatically expressed in the geocentric coordinate system, so that the gravimetric geoid can be of use as a calibration field of astrogeodetic geoids.

Various geodetic systems can be interrelated with each other on the basis of satellite geodesy, and we know the positions of each geodetic datum in a global geodetic coordinate system. In other words, we know translation values of each geodetic datum relative to the global geodetic coordinate system or the deflection values at each geodetic detum station. SAO-SE3 solution (Gaposchkin et al., 1973) estimated the shift of the Tokyo datum station to the global coordinate system as $\Delta\varphi = 11.7''$ and $\Delta\lambda = -12.3''$. After applying these shifts to the Tokyo datum, the Japanese astrogeodetic geoid is expressed in the same coordinate system as gravimetric geoid. There have been made several investigations to determine the Japanese astrogeodetic geoid, i. e. Atumi (1933); Kawabata (1939); Okuda (1951); Fischer (1960); Ono (1974); Ganeko (1976). Hagiwara (1967) computed a gravimetric geoid on the land of Japan for the first time from restricted gravity data around

Japan available at that time. Watts and Leeds (1977) drew a gravimetric geoid in the Northwest Pacific area including the adjacent seas of Japan based on $1^\circ \times 1^\circ$ block mean gravity anomalies of their own surface gravity data. Ganeko (in press) made a test calculation of a detailed gravimetric geoid around Japan based on $30' \times 30'$ block mean gravity anomalies, the present paper is a further extension of his preliminary investigations.

Japan is located in a geophysically specific area such as trench and islands-arc system, and moreover the Kuroshio Current, which is one of the strongest ocean currents of the world, is passing by along the south coasts of Japan. So the area around Japan is one of the quite interesting areas in the field not only of geophysics but also of oceanography. It may be surely expected that much more satellite techniques will be applied in these scientific fields, and that the Japan area will necessarily become one of the calibration areas of satellite trackings. In this sense, it may be quite useful to obtain an accurate geoid in this area.

The satellite altimetry has opened a new page of the physical geodesy, for the satellite altimetry provides us with a direct solution concerning the determination of the figure of the earth at ocean areas. This situation may give a new physical meaning to the determination of the marine geoid, an equipotential surface at sea. The sea surface topography ascribes to real existences of various oceanographic phenomena accompanied with motions of sea water, and inversely the observed topography is taken to be a constraint condition for the ocean dynamics.

The test observations of the satellite altimetry by Skylab and Geos-3 have been successfully carried out (e. g. Mourad et al., 1975; Kearsley, 1977). Leitao et al. (1978) succeeded for the first time in relating the differences between altimetric sea surface heights and gravimetric geoidal heights with the sea surface topography due to a strong ocean current of the Gulf Stream. To use both the altimeter data and gravimetric geoid for the oceanographic purpose, 10 cm accuracy may be required for the determination of the satellite positions and for the geoid undulations. The achievement of such accuracy may be one of the main objects of the geometrical and physical geodesy at present.

The present paper attempts to compute a gravimetric geoid around Japan based on the current availability of the terrestrial gravity data in the area and to make detailed investigations to realize the reliability of the computed geoid. The detailed investigations of various error sources involved in the geoidal height computation procedures will tell us what kind of effort should be made to achieve a 10 cm geoid.

2. Procedure of Gravimetric Geoidal Height Comutation

(1) Stokes' Integral

The geoid undulation are computed from terrestrial gravity data by using the conventional Stokes' integral on a unit sphere (Heiskanen and Moritz, 1967, p. 94), which is

$$N=\frac{R}{4\pi G}\iint_{\sigma} \Delta g\, S(\psi)\, d\sigma, \tag{2-1}$$

where R is the mean radius of the earth, G the mean gravity on the whole surface of the earth, Δg so-called free-air gravity anomaly defined on the geoid, and $S(\psi)$ well-known Stokes' function written by

$$S(\psi)=\sum_{l=2}^{\infty}\frac{2l+1}{l-1}P_l(\cos\psi)$$

$$=\operatorname{cosec}\frac{\psi}{2}-6\sin\frac{\psi}{2}+1-5\cos\psi-3\cos\psi l_n\left(\sin\frac{\psi}{2}+\sin^2\frac{\psi}{2}\right) \tag{2-2}$$

(ibid., p. 94). ψ is a parameter of the spherical distance. Equation (2-1) is varid if the reference ellipsoid has the same potential as the geoid and the same mass as the earth (ibid., p. 101). On the other hand, (2-1) is based on approximations such as neglection of the flattening of the earth and approximate treatings of the topographic mass between the geoid and the physical surface of the earth. The spherical approximation causes errors of the order fN, where f is the geometrical flattening of the earth ellipsoid (see 4-(6)).

The geoidal height is computed more accurately by

$$N=\frac{R}{4\pi\gamma}\iint_{\sigma}\Delta g\,S(\psi)\,d\sigma+\frac{R}{4\pi\gamma}\iint_{\sigma}G_1\,S(\psi)\,d\sigma+\frac{\bar{g}-\bar{\gamma}}{\gamma}H \tag{2-3a}$$

or

$$N=\zeta+\frac{\bar{g}-\bar{\gamma}}{\gamma}H \tag{2-3b}$$

(ibid., p. 326) on the basis of Molodenskii's theory for the determination of the figure of the earth (Molodenskii et al., 1962). In the equations (2-3a, b), γ is the normal gravity on the telluroid which is defined as a surface where the normal gravitational potential of the reference ellipsoid is the same as the actual potential on the ground (see Figure 1), G_1 the first order correction term of the Molodenskii series solution of the geodetic boundary value problem (ibid., p. 122), $\bar{g}$ the mean gravity along the plumb line between the geoid and the ground, $\bar{\gamma}$ the mean normal gravity along the normal plumb line between the ellipsoid and the telluroid, H the topographic height from the geoid, and ζ the height anomaly which is the distance between the ground and the telluroid (see Figure 1). Then Δg is the ground level gravity anomaly which is defined by

$$\Delta g=g_P-\gamma=g_P-\left(\gamma_0+\frac{\partial\gamma}{\partial h}H^*\right), \tag{2-4}$$

where g_P is the gravity at a point P on the ground, γ the normal gravity on the telluroid, γ_0 the normal gravity at P_0 where P is projected onto the reference ellipsoid, $\partial\gamma/\partial h$ the vertical gradient of the normal gravity, and H^* the normalheight (see Figure 1). Then the potentinl difference between the ground and the geoid is defined by using H^* as follows:

$$\Delta W=-\int_0^{H^*}\gamma\,dh.$$

It is clear that (2-4) differs from the definition of the conventionally and widely-used free-air gravity anomaly:

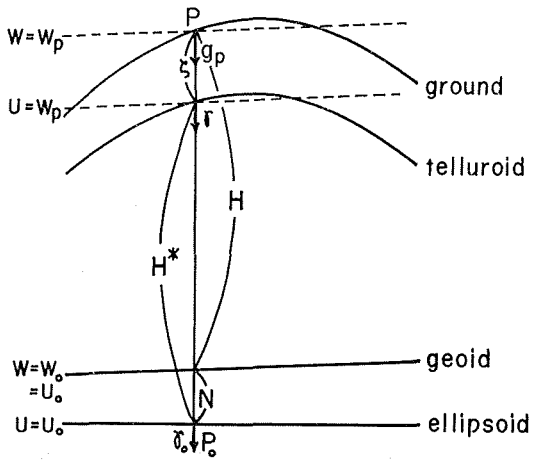

Figure 1 Normal height H^* and height anomaly ζ.

$$\Delta g = g_P - \frac{\partial \gamma}{\partial h} H - \gamma_0,$$

only by the amount

$$\Delta = \frac{\partial \gamma}{\partial h}(H^* - H). \tag{2-5}$$

The difference H^*-H is equivalent to the difference between geoidal height and height anomaly (see Figure 1), that is,

$$H^* - H = N - \zeta = \frac{\bar{g}-\bar{\gamma}}{\bar{\gamma}} H. \tag{2-6}$$

The difference is approximated to Bouguer anomaly Δg_B (in Gals) $\times H$ (in km) meters (Heiskanen and Moritz, 1967, p. 328). The difference is estimated to be 1.1 m in a specific case as at the top of Mt. Fuji (H=3776 m), Japan, and may in general be much less than the case. Therefore, (2-5) is as small as the order of 0.1 mGals, and it is negligible in ocean areas because the sea surface topography is estimated to be the order of 1 m (e. g. Lisitzin, 1974).

The second term in the right-hand side of (2-3a) is as small as or less than one meter (Heiskanen and Moritz, 1967, p. 329). Hagiwara (1972a) obtained the term as about 6 cm at the mountanous area of Tanzawa, Japan, and Hagiwara (1973) ascertained by using a model topographic relief that the term is small even in areas of rugged terrain.

We thus can consider that Stokes' integral (2-1) is a good approximation to height anomaly as far as Δg is understood as the ground level gravity anomaly (2-4), and that (2-1) is also a good approximation to geoidal height especially in ocean areas.

It should be noted that zero-th and first degree terms of the spherical harmonic expansion of geoidal heights automatically vanish in the performance of Stokes' integral over the whole surface of the earth, even if such terms are included in the gravity anomaly data, because of the characteristics of Stokes' function (see (2-2)), so that the computed geoidal heights are free from the ambiguity of the actual size of the earth

ellipsoid. Consider the computation formulas of three dimensional coordinates of the earth's surface by using parameters a (semimajor axis) and f (geometrical flattening) of the reference ellipsoid, geoidal height N by Stokes' integral and topographic height H. Then we can write the three dimensional coordinates by the formulas:

$$\left.\begin{aligned} X&=(\bar{N}+N+H)\cos\varphi\cos\lambda,\\ Y&=(\bar{N}+N+H)\cos\varphi\sin\lambda,\\ Z&=\left(\frac{b^2}{a^2}\bar{N}+N+H\right)\sin\varphi, \end{aligned}\right\} \tag{2-7}$$

where the origin of the rectangular coordinate (x, y, z) is located at the center of gravity of the earth, x-axis is in the meridian plane of Greenwich, z-axis coincides with the earth's mean axis of rotation, and y-axis is so chosen as to obtain a right-handed coordinate system. b is the semiminor axis of the ellipsoid calculated by $b=(1-f)$ a, φ and λ are geographic latitude and longitude, and $\bar{N}$ is defined by

$$\bar{N}=\frac{a^2}{(a^2\cos^2\varphi+b^2\sin^2\varphi)^{\frac{1}{2}}}. \tag{2-8}$$

Equation (2-7) may not give an actual position of the earth's surface, because zero degree term of geoidal heights N_0 cannot be determined by Stokes' integral. N_0 is evaluated by

$$N_0=-\frac{R}{2G}\Delta g_0+\frac{k\delta M}{2GR}, \tag{2-9a}$$

or

$$N_0=-\frac{R}{G}\Delta g_0+\frac{\delta W}{G}, \tag{2-9b}$$

where Δg_0 is the mean gravity anomaly over the whole surface of the earth, k the gravitational constant, δM the difference between the masses of the actual earth and the reference ellipsoid, and δW the difference between the potential of the geoid and the normal potential on the surface of the reference ellipsoid (Heiskanen and Moritz, 1967, p. 102). Therefore, in (2-7) N should be replaced by $N+N_0$ to obtain accurate coordinates of the earth's surface. We cannot evaluate N_0 term here because we do not have gravity data of world-wide coverage, so that we assume the term to be zero. Then the geoidal heights evaluated in the present paper are understood to be ones referred to an ellipsoid which has the same potential as the geoid on its surface and the same mass as the earth.

(2) Satellite-Derived Gravity Anomaly and Geoid Undulations

The geopotential outside the earth, except for the potential of centrifugal force by the rotation of the earth, is expressed in a series of Laplace harmonics as follows:

$$V=\frac{kM}{r}\left\{1+\sum_{l=2}^{\infty}\sum_{m=0}^{l}\left(\frac{a}{r}\right)^l\left[\bar{C}_{lm}\,\bar{R}_{lm}(\bar{\varphi},\lambda)+\bar{D}_{lm}\,\bar{S}_{lm}(\bar{\varphi},\lambda)\right]\right\}, \tag{2-10}$$

where r is the distance from the center of gravity of the earth, kM the product of the gravitational constant and the mass of the earth, $\bar{\varphi}$ and λ the geocentric latitude and longitude, and $\bar{R}_{lm}(\bar{\varphi},\lambda)$ and $\bar{S}_{lm}(\bar{\varphi},\lambda)$ are defined by using a fully normalized associated Legendre function $\bar{P}_{lm}$ as follows:

$$\left.\begin{aligned} \bar{R}_{lm}(\bar{\varphi},\lambda)&=\bar{P}_{lm}(\sin\bar{\varphi})\cos m\lambda,\\ \bar{S}_{lm}(\bar{\varphi},\lambda)&=\bar{P}_{lm}(\sin\bar{\varphi})\sin m\lambda. \end{aligned}\right\} \tag{2-11}$$

$\bar{R}_{lm}$ and $\bar{S}_{lm}$ are normalized so that the average squares of them over the unit sphere is unity :

$$\frac{1}{4\pi}\iint_{\sigma}\bar{R}_{lm}^{2}\,d\sigma=\frac{1}{4\pi}\iint_{\sigma}\bar{S}_{lm}^{2}\,d\sigma=1.$$

The geopotential coefficients $\bar{C}_{lm}$, $\bar{D}_{lm}$ can be determined by observing the orbit changes of artificial satellites moving in the gravitational field of the earth. But the contributions of high degree terms in (2-10) to orbit changes are too small to be detected by satellite trackings. Let L be the highest degree of the geopotential coefficients derivable from satellite trackings. We write the satellite-derived geopotential V_s as

$$V_s=\frac{kM}{r}\left\{1+\sum_{l=2}^{L}\sum_{m=0}^{l}\left(\frac{a}{r}\right)^{l}[\bar{C}_{lm}\,\bar{R}_{lm}(\bar{\varphi},\lambda)+\bar{D}_{lm}\,\bar{S}_{lm}(\bar{\varphi},\lambda)]\right\}. \tag{2-12}$$

The gravitational potential U of the reference ellipsoid is uniquely defined by Stokes' constants, kM, a, f and ω (angular velosity of the earth's rotation). U is written in a series expression of Laplace harmonics of even degrees and order zero :

$$U=\frac{kM}{r}\left\{1+\sum_{n=1}^{\infty}\left(\frac{a}{r}\right)^{2n}\bar{C}_{2n}^{\circ}\,\bar{R}_{2n\,0}(\bar{\varphi},\lambda)\right\} \tag{2-13}$$

which does not include the potential of centrifugal force. The coefficients $\bar{C}_{2n}^{\circ}$ are computed from the given Stokes' constants (Heiskanen and Moritz, 1967, p. 73). We define the satellite-derived disturbing potential T_s by

$$T_s=V_s-U=\frac{kM}{r}\sum_{l=2}^{L}\sum_{m=0}^{l}\left(\frac{a}{r}\right)^{l}[\bar{C}_{lm}^{*}\,\bar{R}_{lm}+\bar{D}_{lm}\,\bar{S}_{lm}], \tag{2-14}$$

where negligibly small high degree terms in (2-13) are omitted, and $\bar{C}_{lm}^{*}$ are differences between coefficients in (2-12) and those of corresponding degree terms in (2-13).

In an approximation of the spherical earth, we write the satellite-derived disturbing potential T_s as

$$T_s=RG\sum_{l=2}^{L}\sum_{m=0}^{l}[\bar{C}_{lm}^{*}\,\bar{R}_{lm}+\bar{D}_{lm}\,\bar{S}_{lm}], \tag{2-15}$$

and the satellite-derived gravity anomaly Δg_s as

$$\Delta g_s=G\sum_{l=2}^{L}(l-1)\sum_{m=0}^{l}[\bar{C}_{lm}^{*}\,\bar{R}_{lm}+\bar{D}_{lm}\,\bar{S}_{lm}]. \tag{2-16}$$

The satellite-derived geoid undulations are computed from (2-15) by Bruns formula :

$$N_s=\frac{T_s}{G} \tag{2-17}$$

which expresses the global feature of the geoid undulations.

(3) Performance of Stokes' Integral in Combination with Satellite-Derived Gravitational Field

Stokes' integral (2-1) requires gravity anomalies distributed over whole surface of the earth. However, it cannot be expected at present to have terrestrial gravity data coverage over the whole surface of the earth. On the other hand, the terrestrial gravity data exist densely in some areas, by using which we can compute geoid undulatios gravimetrically. When we perform Stokes' integral only over a restricted area, say a

spherical cap area whose angular radius is ϕ_0 centered at the geoidal height computation point (see Figure 2), the error of the computed geoidal height caused by omitting gravities outside the cap is called truncation error.

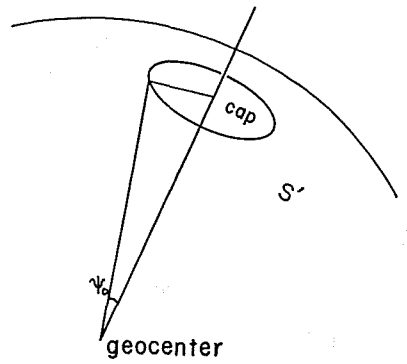

Figure 2 Spherical cap area.

Molodenskii et al. (1962), de Witte (1967) and Hagiwara (1970) evaluated this kind of error. Figure 3 shows the truncation errors evaluated around Japan when cap radius is 10°. To obtain Figure 3, the SAO-SE3 satellite-derived geopotential model (Gaposchkin et al., 1973) is used as the gravitational field outside the cap. Truncation errors are evaluated by the formula:

$$\delta N(\bar{\varphi}, \lambda) = \frac{R}{2G} \sum_{l=2}^{L} Q_l(\phi_0)\, \Delta g_l(\bar{\varphi}, \lambda), \tag{2-18}$$

where $Q_l(\phi_0)$ is Molodenskii truncation function when cap size is ϕ_0 (Molodenskii et al., 1962, p. 147) and Δg_l is $l-$th degree Laplace spherical harmonics of gravity anomaly which is evaluated by

$$\Delta g_l = \Delta g_{sl} = G(l-1) \sum_{m=0}^{l} [\bar{C}_{lm}^{*}\, \bar{R}_{lm} + \bar{D}_{lm}\, \bar{S}_{lm}]. \tag{2-19}$$

The SAO-SE3 geopotential model is composed of a complete geopotential coefficients set up to degree and order 18, then we put $L=18$ in equation (2-18). Hagiwara (1970) obtained the same kind of figure as Figure 3. There exist some numerical differences between two figures since Hagiwara took a different gravity model. Although Figure 3 does not include the effects of more detailed structures of the gravity anomaly field than degree 18, Figure 3 is approximately varid. Because the effects are estimated to be only around one meter (see the curves for $\phi_0=10°$ in Figures 30a, b in Chapter 4). The detailed discussions concerning with truncation error problems will be found in Chapter 4.

As seen in Figure 3, the truncation errors are quite large even in a relative sense, 10 m error difference over Japan area. Therefore, Stokes' integral should be performed by adopting some gravity anomaly informations outside the cap, where terrestrial gravity data do not exist. In this case we adopt satellite-derived gravity anomaly field as the additional gravity data. Though the satellite derived gravity anomaly field includes only low degree terms, a great improvement in diminishing the truncation errors is expected because there will be left the truncation effects only of higher degree terms

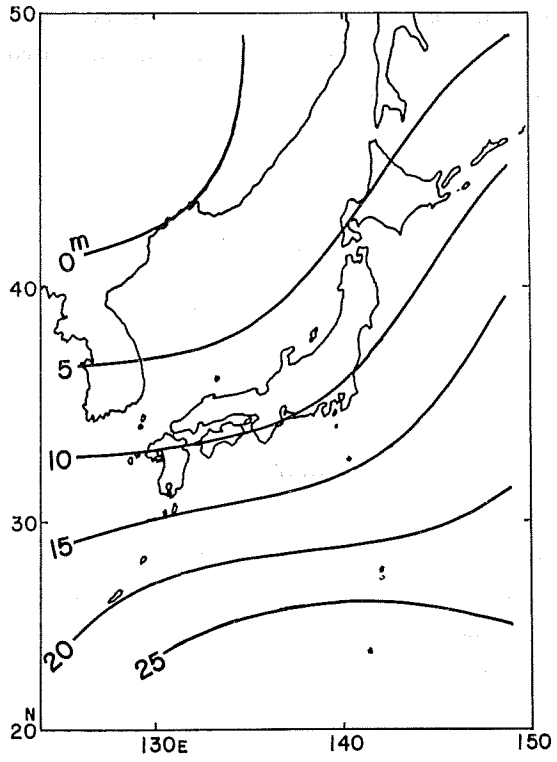

Figure 3 Geoidal height truncation errors for $\psi_0=10°$ evaluated by using SAO-SE3 geopotential coefficient set (18, 18).

than the satellite-derived gravitational field which are the order of one meter as mentioned before.

Let S' be the remaining area of the earth's surface outside the cap (see Figure 2), and we reform Stokes' integral as follows:

$$N=N_{in}+N_{out}, \tag{2-20a}$$

where

$$N_{in}=\frac{R}{4\pi G}\iint_{cap}\Delta g\, S(\psi)\, d\sigma, \tag{2-20b}$$

$$N_{out}=\frac{R}{4\pi G}\iint_{S'}\Delta g_s\, S(\psi)\, d\sigma, \tag{2-20c}$$

and Δg_s is the satellite-derived gravity anomaly given by (2-16). From (2-20a, b, c) we obtain another expression of Stokes' integral:

$$N=N_R+N_S \tag{2-21a}$$

where

$$N_R=\frac{R}{4\pi G}\iint_{cap}(\Delta g-\Delta g_s)\, S(\psi)\, d\sigma, \tag{2-21b}$$

$$N_S=\frac{R}{4\pi G}\iint_{\sigma}\Delta g_s\, S(\psi)\, d\sigma. \tag{2-21c}$$

N_S is equivalent to the satellite derived long wave-length components of geoid undulations

which can be evaluated by (2-17), and N_R is the residual short wave-length components of geoid undulations which can be evaluated by integration of residual gravity anomaly $\Delta g - \Delta g_s$ over the cap. Accordingly, numerical integration is necessary only for N_R. We know the undulation of the geoid reaches up to ± 100 m and the average height of the undulation is arouad ± 30 m on the world-wide basis. The total effect of the short wave-length components on the geoid undulation of higher degrees than 20 is estimated to be around ± 4 m on the world-wide average basis (see Chapter 4). Since N_R takes a value much smaller than N_S, some approximation techniques may be applicable to the evaluation of N_R.

3. Computation of a Gravimetric Geoid Around Japan

(1) Numerical Integration of Stokes' Formula

When we perform numerical integration (2-21b), we replace the integral by a summation by using average values of gravity anomalies over certain sized blocks, such as

$$N_R = \frac{R}{4\pi G} \sum_i \overline{\delta g}_i \, q_i, \tag{3-1}$$

where $\overline{\delta g}_i$ is the block mean of the residual gravity anomaly over the i-th block inside the cap area, which is computed from block mean surface gravity anomaly $\overline{\Delta g}_i$ and block mean satellite-derived gravity anomaly $\overline{\Delta g}_{si}$ as follows:

$$\overline{\delta g}_i = \overline{\Delta g}_i - \overline{\Delta g}_{si}. \tag{3-2}$$

In (3-1) q_i is the integration of Stokes' function over the i-th block σ_i, i. e.

$$q_i = \iint_{\sigma_i} S(\psi) \, d\sigma_i \,. \tag{3-3}$$

In the numerical integration of q_i, a block is divided into some subblocks, and the number of subblocks is chosen correspondingly to the size of the block and relative distance between the geoidal height computation point and the block. $\overline{\Delta g}_{si}$ is calculated from (2-16), in the spherical approximation, as

$$\begin{aligned} \overline{\Delta g_{si}} &= \frac{1}{S_i} \iint_{\sigma_i} \Delta g_s \, d\sigma_i \\ &= G \sum_{l=2}^{L} (l-1) \sum_{m=0}^{l} \left[\bar{C}^*_{lm} \frac{1}{S_i} \iint_{\sigma_i} \bar{R}_{lm} \, d\sigma_i + \bar{D}_{lm} \frac{1}{S_i} \iint_{\sigma_i} \bar{S}_{lm} \, d\sigma_i \right] \end{aligned} \tag{3-4}$$

where S_i is the area of block σ_i. Since the satellite-derived gravity anomaly is composed of long wave-length components of the gravity anomaly field, $\overline{\Delta g}_{si}$ is replaceable by a point anomaly Δg_{si} given at the center of block σ_i.

(2) Terrestrial Block Mean Gravity Anomalies

The main problem in the computation of geoidal heights is the preparation of terrestrial gravity anomaly data. The block mean gravity anomalies are read from gravity anomaly maps, or estimated from observed point gravities in and around blocks. The gravity measurements on land and at sea around Japan have been made by various institutions not only in Japan but also in other countries, and gravity anomaly maps have been published. The author prepares block mean gravity anomalies in the land

area of Japan and the adjacent seas of Japan on the basis of gravity anomaly maps: GSI (1970), Tomoda and Segawa (1971), Segawa and Bowin (1976), Segawa (1970b, 1976), JHD's gravity anomaly maps (1970—1977), published as a part of series of the Basic Map of the Sea), Stroev (1971), and Ganeko et al. (1978). In reading the block mean gravity anomalies, the basic block size is selected in accordance with the estimated accuracy and the reduced scale of each gravity anomaly map, i. e. equiangular blocks $5' \times 5'$, $10' \times 10'$, $15' \times 15'$ and $30' \times 30'$ are taken. A block bordered by meridians of latitude $S°$ and parallels of longitude $S°$ is called equiangular "$S° \times S°$ block". On the other hand, we nominate "$S°$ block" for a block formed by partitioning the earth's surface into near-equal areas as an area of $S° \times S°$ block at the equator.

The block gravity anomaly means obtained from the gravity anomaly maps are reduced to $30' \times 30'$ and $1° \times 1°$ block means for the geoidal height computations. The reductions are made by taking averages of smaller blocks included in each $30' \times 30'$ and $1° \times 1°$ blocks. Area A in Figure 4 indicates the area where $30' \times 30'$ block mean gravity anomalies are estimated. The accuracy of the $30' \times 30'$ block means is estimated to be $\pm 10 \sim \pm 18$ mGals from the gravity data density on the assumptions of 10 mGals contouring error of gravity anomaly maps, 10 mGals reading error of $10' \times 10'$ block means

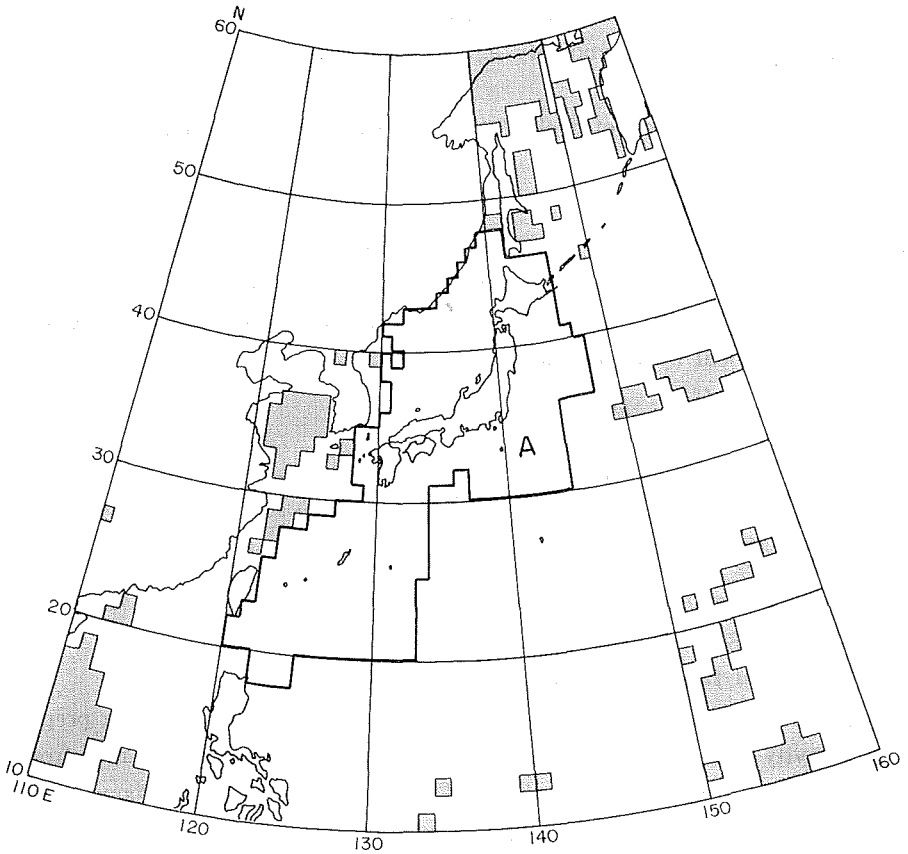

Figure 4 JHDGF-1 gravity anomaly file area: area A. The shaded areas include no gravity data in the world-wide $1° \times 1°$ block mean gravity data files.

and 15 mGals reading error of 15′×15′ and 30×30′ block means. Although the contouring error may bring about some amount of error correlations among block means located near each other, we neglect the effects because of difficulties in evaluating the effects and consider the contouring errors are random in each block. The reading errors are also considered to be random. Some systematic errors are possibly included in the blocks near and along the coasts of USSR. Fortunately, the possible systematic errors may not cause large geoidal height errors near Japan and in the Pacific area.

The read and reduced block means, i. e. 10′×10′, 15′×15′, 30′×30′ and 1°×1° block means, are compiled into a machine readable magnetic tape file named as JHDGF-1 (Japan Hydrographic Department Gravity File). The gravity anomalies are based on the JGSN 75 System (Suzuki, 1976) and the Geodetic Reference System 1967 (IAG, 1971). 30′×30′ block mean gravity anomalies compiled into JHDGF-1 are listed in Appendix B.

Since the surface gravity data included in JHDGF-1 file are not sufficient to compute geoid undulations around Japan, other gravity data have to de introduced. We use 1°×1° block mean anomalies of DMAAC* and Watts and Leeds (1977, referred as LAMONT from now on in this paper) for the area outside the JHDGF-1 region of Figure. 4. The weighted means are taken over the comon 1°×1° blocks of DMAAC and LAMONT data sets by using the accuracy estimates in DMAAC data and ±8 mGals equal accuracy assigned to LAMONT data for convenience' sake to produce higher weights than DMAAC data because of high reliability of LAMONT data in the Northwest Pacific area (Watts, private communication). DMAAC data are used on the continental areas where there are no LAMONT data coverage. All the 1°×1° block means are referred to the Geodetic Reference System 1967. The 1°×1° blocks which have no gravity anomaly means are indicated by the shaded blocks in Figure 4.

A data file is produced by weighted means of DMAAC and LAMONT. The differences of 1°×1° block means between JHDGF-1 and this data file is examined over the common blocks, and the histogram of the differences is shown in Figure 5. The total number of common 1°×1° blocks amounts to 354, the mean difference is −1.1 mGals, and the r. m. s. difference is 13.6 mGals. We find no large systematic difference between these two data files. From the 13.6 mGals r. m. s. difference, we may conclude that the average accuracy of 1°×1° block means in JHDGF-1 is less than 10 mGals. Other statistical characteristics of JHDGF-1 will be investigated in Chapter 5.

(3) Satellite-Derived Gravity Anomalies and Global Geoid Undulations

GEM-9 geopotential model (Lerch et al., 1977) is one of the most recent geopotential coefficient sets derived from satellite tracking data including accurate laser tracking data of high density satellites such as Peole, Starlette and Lageos. GEM-9 model is composed of a complete geopotential coefficient set up to degree and order 20 and some coefficients of resonance terms up to degree 30.

GEM-10 model (Lerch et al., ibid.) was derived by combination of GEM-9 solution and 5° block surface mean gravity anomalies. The model is composed of a complete

* Defence Mapping Agency/Aerospace Center 1°×1° mean freeair gravity anomaly set (1976)

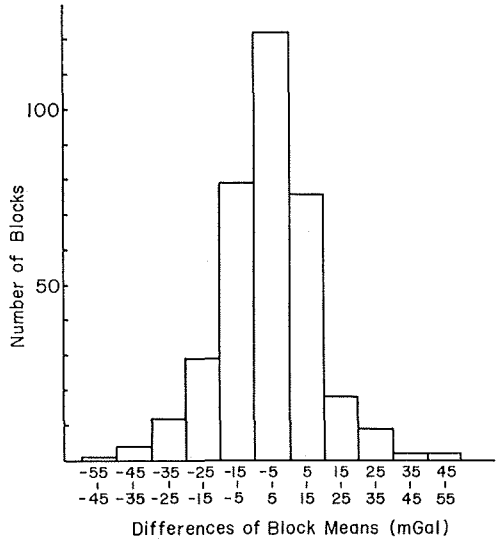

Figure 5 Histogram of the differences of $1°\times1°$ block mean gravity anomalies between JHDGF-1 and the weighted means of DMAAC's and LAMONT's.

geopotential coefficient set up to degree and order 22 and some coefficients of resonance terms up to degree 30. GEM-9 and GEM-10 solutions recomended to use the following physical constants of the earth ellipsoid:

$$\left.\begin{aligned} kM &= 398600.64 && \text{km}^3/\text{sec}^2, \\ a &= 6378140 && \text{m}, \\ f &= 1/298.255. \end{aligned}\right\} \tag{3-5}$$

The estimated possible errors of the constants are $\pm0.02\,\text{km}^3/\text{sec}^2$ for kM and ±1 m for a. The accuracies of the geopotential coefficients are estimated to be 1.9 m and 1.5 m respectively for GEM-9 and GEM-10 solutions on the global basis. We adopt the geopotential coefficient set of GEM-10 solution for the satellite-derived gravity anomaly field in the computation of a detailed gravimetric geoid around Japan. Figure 6 is the long wave-length geoid undulations around Japan computed by (2-17) from the geopotential coefficients of GEM-10 solution.

We need one more physical constant ω (angular velocity of the earth's rotation) of the reference ellipsoid to compute the normal gravitational field (2-13), adopting

$$\omega = 7.2921151\times10^{-5} \quad 1/\text{sec}. \tag{3-6}$$

In order to make the surface gravity data compatible with the satellite-derived gravity anomalies, the block mean gravity anomalies based on JGSN 75 and the Geodetic Reference System 1967 must be converted into a new system with adopted Stokes' constants (3-5) and (3-6). The conversions are made by using the equation:

$$\Delta g_{new} = \Delta g_{JGSN75} + \gamma_{1967} - \gamma_{new}, \tag{3-7}$$

where γ_{1967} and γ_{new} are normal gravities on the reference ellipsoids with Stokes' constants of the Geodetic Reference System 1967, i. e. $kM=398603\,\text{km}^3/\text{sec}^2$, $a=6378160$ m, $f=1/298.247167$, $\omega=7.29211515\times10^{-5}$ 1/sec, and newly adopted Stokes' constants (3-5) and

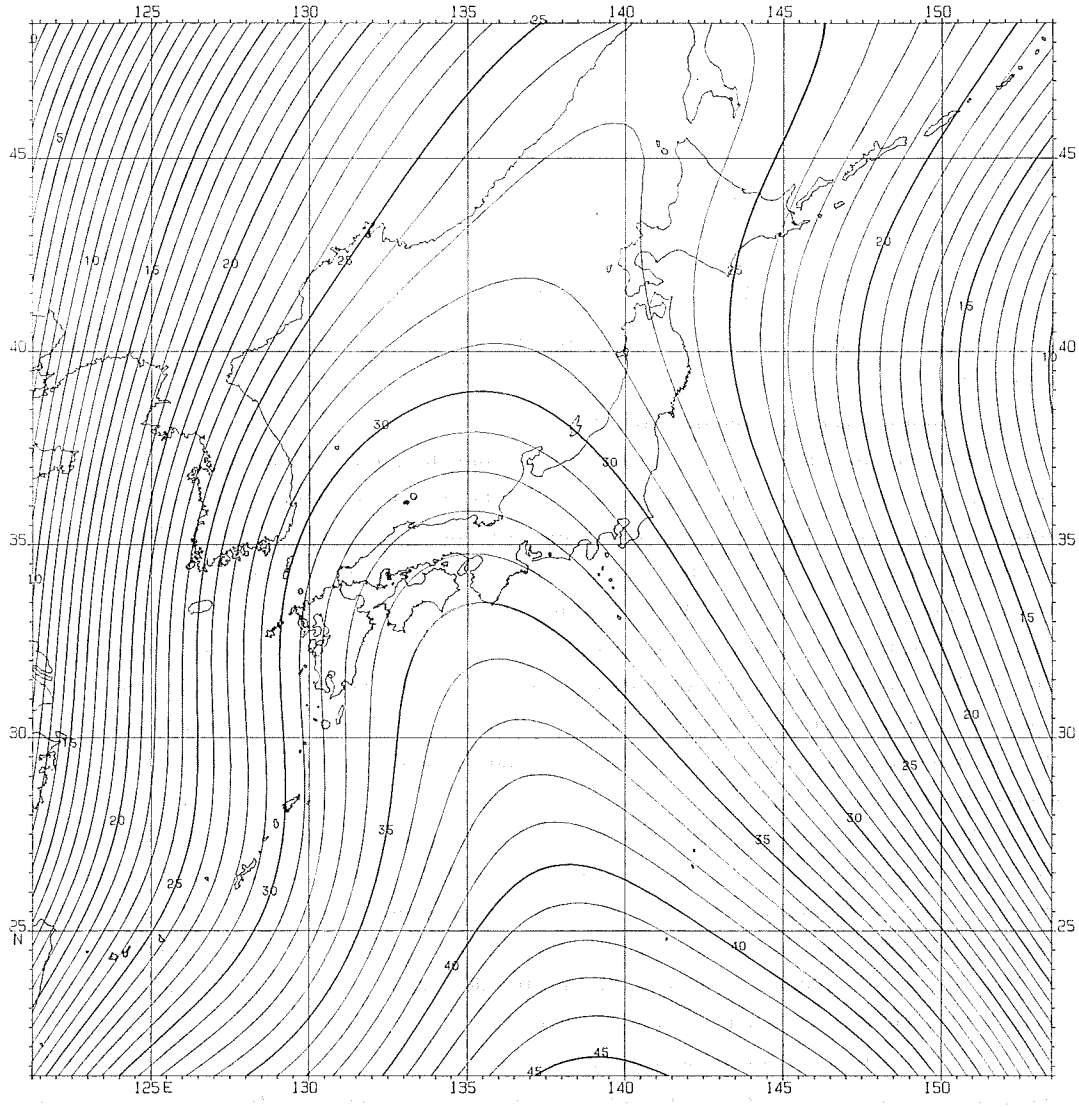

Figure 6 GEM-10 global geoid around Japan. Contour interval: 1 m.

(3-6). Normal gravity on the ellipsoid is given by

$$\gamma=\frac{a\gamma_a\cos^2\varphi+b\gamma_b\sin^2\varphi}{(a^2\cos^2\varphi+b^2\sin^2\varphi)^{\frac{1}{2}}} \tag{3-8}$$

(Heiskanen and Moritz, 1967, p. 70), where φ is geographic latitude and $b=a(1-f)$. γ_a (normal gravity at the equator) and γ_b (normal gravity at the pole) are computed by the formulas (ibid., p. 67):

$$\left.\begin{aligned}\gamma_a&=\frac{kM}{ab}\left(1-m-\frac{m}{6}\frac{e'q'_0}{q_0}\right),\\ \gamma_b&=\frac{kM}{a^2}\left(1+\frac{m}{3}\frac{e'q'_0}{q_0}\right),\end{aligned}\right\} \tag{3-9}$$

where

$$\left.\begin{aligned} m &= \frac{\omega^2 a^2 b}{kM}, \\ e' &= \left(\frac{a^2-b^2}{b^2}\right)^{\frac{1}{2}}, \end{aligned}\right\} \tag{3-10}$$

and

$$\left.\begin{aligned} q_0 &= \frac{1}{2}\left[\left(1+\frac{3}{e'^2}\right)\tan^{-1}e' - \frac{3}{e'}\right], \\ q'_0 &= 3\left(1+\frac{1}{e'^2}\right)\left(1-\frac{1}{e'}\tan^{-1}e'\right)-1. \end{aligned}\right\} \tag{3-11}$$

Ae we see in equations (3-8), (3-9), (3-10) and (3-11), the normal gravity is uniquely defined by Stokes' constants.

(4) Computation of Geoidal Heights

We have finished the preparation for geoidal height computations in the previous sections, and we perform the computation actually in this section. We adopt the cap radius $\psi_0=20°$ and divide the cap area into two parts at $\psi=10°$. $30'\times30'$ block mean gravity anomalies are used in the area of $\psi=0°$ to $10°$ (inner cap), and $1°\times1°$ block mean gravity anomalies are used in the remaining area of the cap from $\psi=10°$ to $20°$ (outer cap). When a $1°\times1°$ block in the inner cap has no $30'\times30'$ block means in it, the $1°\times1°$ block is considered to be composed of four $30'\times30'$ blocks which have the same values of gravity anomaly means as the $1°\times1°$ block. 26 mGals error is assigned to such $30'\times30'$ block means. Zero gravity anomaly and 30 mGals error are assigned to $1°\times1°$ blocks of no gravity data.

At the centers of each $30'\times30'$ block, satellite-derived gravity anomalies are evaluated and they are adopted as the $30'\times30'$ block means of the satellite-derived gravity anomaly instead of evaluating (3-4) strictly. $1°\times1°$ block means of satellite-derived anomaly are given by the average values of four $30'\times30'$ block means. These approximations seem to be plausible because the satellite-derived gravity anomaly changes almost linearly in a small area such as $30'\times30'$ block.

The computations of geoidal heights are carried out at the center of each $30'\times30'$ block, i. e. at every $30'\times30'$ mesh point. q_i in (3-3) is calculated by dividing block σ_i into subblocks. $30'\times30'$ block is divided into 25 subblocks when the distance between the geoidal height computation point and the center of the block is less than 1.5°, i. e. when $\psi\leqq1.5°$. On the other hand, we take 9 subblocks when $1.5°<\psi\leq3°$. No subdivisions are made for the $30'\times30'$ blocks when $\psi>3°$ and for $1°\times1°$ blocks in the outer cap area. The residual geoid undulations N_R are computed around Japan using (3-1). Figure 7 shows thus computed residual geoid undulations. We see much detailed features of geoid undulations than satellite-derived ones (cf. Figure 6). It is matter of course that the shorter wave-length undulations than $30'\times30'$ block size, the smallest block size adopted, are not included in this residual geoid. Deep geoidal valleys are found along the trenches and shallow geoidal basins are extending in Japan Sea, Philippine Sea and the Northwest Pacific area. Geoidal highs exist along the island arcs, Korea Peninsula and the continental coast.

We obtain the final results of geoidal height computation by adding the residual geoid Figure 7 to the satellite-derived global geoid Figure 6. The produced final results, i. e. $30' \times 30'$ detailed gravimetric geoid around Japan, are shown in Figure 8. Figure 7 and Figure 8 include a wider area than the JHDGF-1 region (see Figure 4), so that Figures 7 and 8 are for $1° \times 1°$ geoids outside the JHDGF-1 region. Watts and Leeds (1977) computed a gravimetric geoid in the Northwest Pacific Ocean based on their own $1° \times 1°$ block gravity means, and their geoid map includes the area of Figure 8. Comparing these two geoid maps, more detailed geoid undulations can be seen in Figure 8 than Watts and Leeds' because of detailed informations of the gravity anomaly field brought into by smaller block-size.

One of the marked features of the present geoid undulations is over the trench areas characterized by large negative gravity anomalies. Figure 9 shows the geoid section along the parallel at latitude 35° 15′. 22 meters geoidal dent relative to GEM-10 global geoid is seen along the axis of the negative gravity anomalies over the trench. If the geoidal dent is compared with the geoidal high at the mountainous area of the central Japan, the relative undulation of the geoid reaches 26 m within 400 km horizontal distance. The steep geoidal slopes in the land areas accompanied by the geoidal dents over the trench areas are seen at Kanto District and at the southern half of Hokkaido.

Ganeko (1976) obtained an astrogeodetic geoid of Japan by applying a statistical interpolation technique to deflections of the vertical. The relative geoid undulation on the land areas of Japan are compared between the astrogeodetic geoid, converted into SAO-SE3 global geodetic system and shown in Figure 10, and the gravimetric geoid shown in Figure 8. The comparisons are made at every $30' \times 30'$ grid point inside the land areas of Japan, and the standard deviation of 1.4 m is obtained while the standard deviation decreases to 0.8 m when Hokkaido area is excluded. The agreement between two kinds of geoid is fairly good. The geoidal slope to the south in Hokkaido is not so marked in the astrogeodetic geoid as in the gravimetric geoid. On the other hand, we see some amount of geoidal slope to the north in the astrogeodetic geoid at the northern half of Hokkaido, which is not seen in the gravimetric geoid. It is, therefore, considered that there may exist a tilt in the astrogeodetic geoid at Hokkaido probably because of sparse deflection observations at Hokkaido. It may be noted that the geoidal slope at Kanto District seems to have caused a shift of Tokyo Datum to the southeast relative to the global geodetic system.

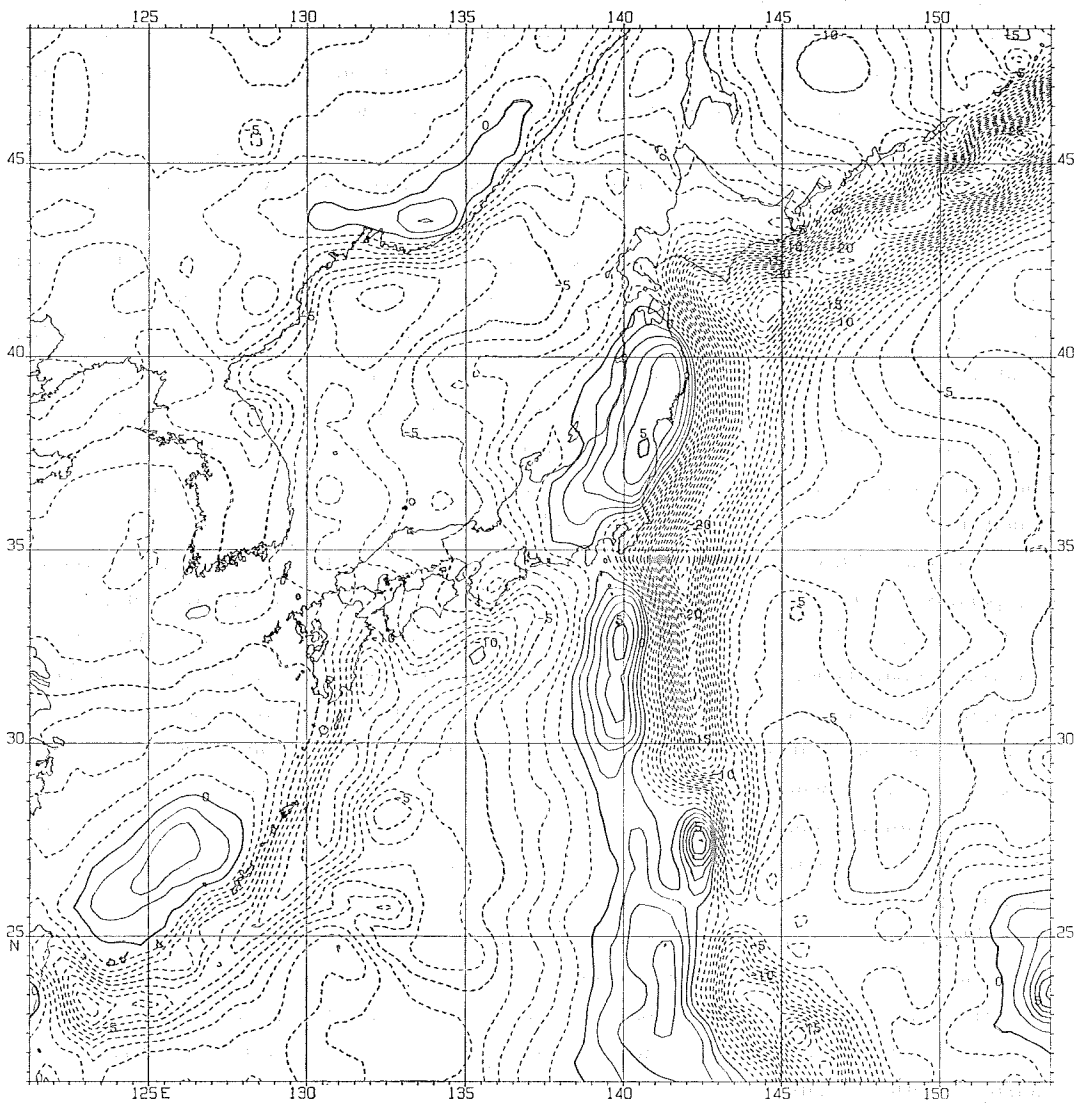

Figure 7 30′×30′ residual geoid on the reference surface: GEM-10 global geoid. Contour interval: 1 m. Broken lines are for negative geoid equiundulation.

Figure 8 30′×30′ detailed gravimetric geoid computed in combination with GEM -10 geopotential coefficient set and surface gravities of 30′×30′ and 1°×1° block means. Contour interval : 1 m.

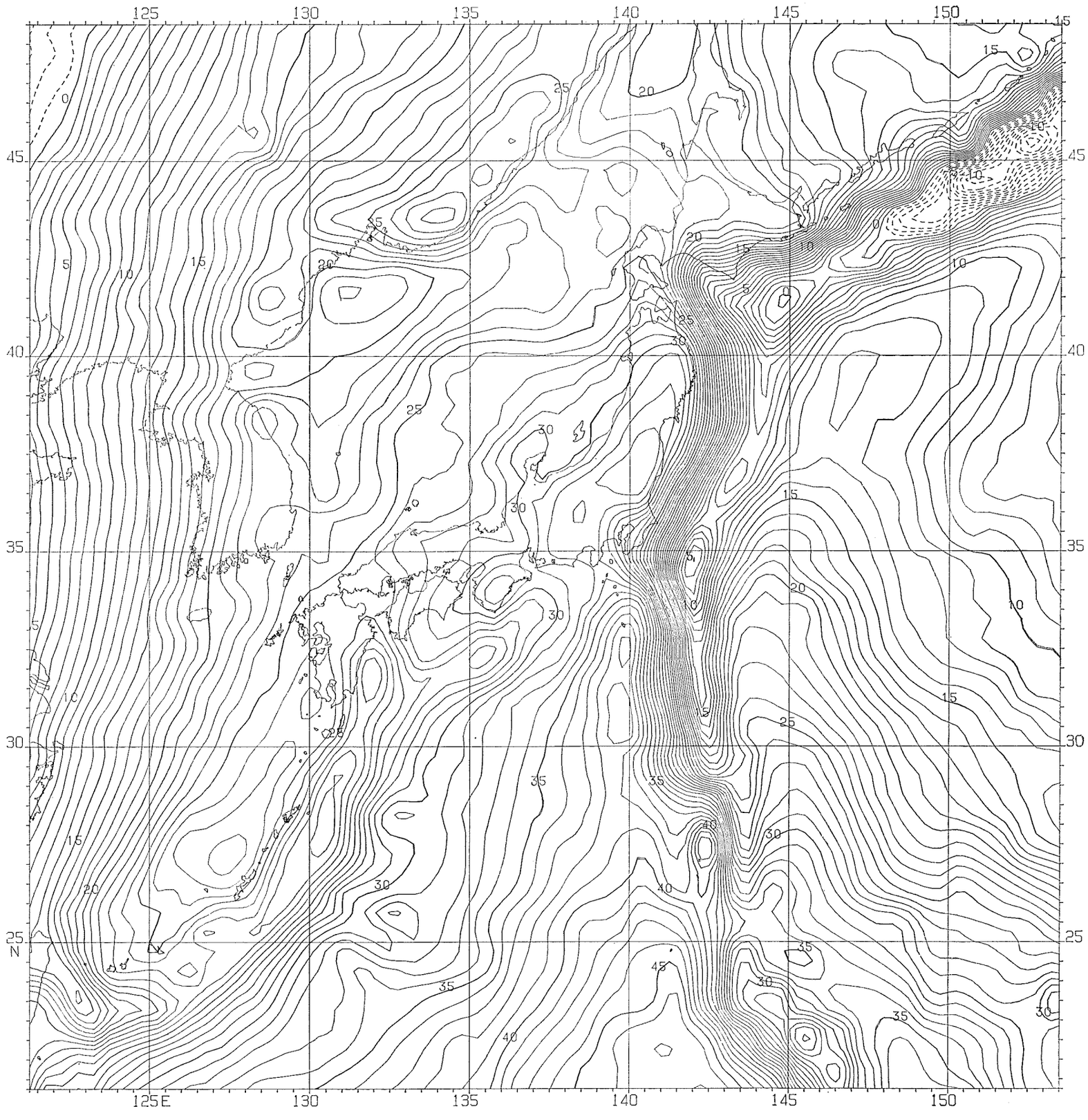

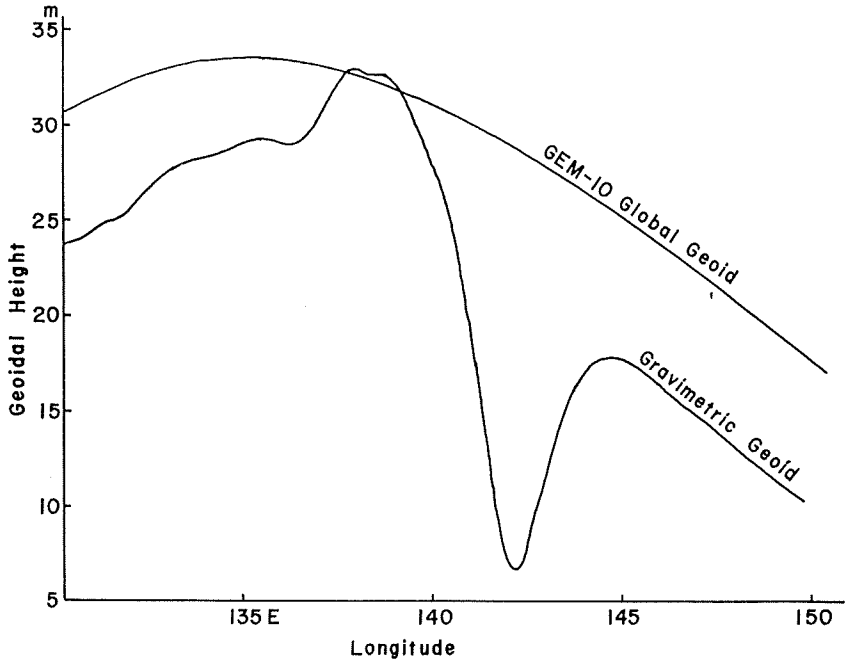

Figure 9 Sections of the GEM-10 global geoid and the 30′×30′ gravimetric geoid along the parallel at latitude 35° 15′ N.

(5) Comparisons Between Computed Gravimetric Geoid and Geos-3 Altimeter Data

Geos-3 satellite launched in April, 1975, has made a great deal of altimeter observations of the sea surface heights (e. g. Kearsley, 1977; Rapp, 1977a; Marsh et al., 1978). In addition, there are some altimeter data in the region of Figure 8. It is quite interesting and valuable to compare the altimeter data and the gravimetric geoid, so that we use altimeter data taken along the subsatellite tracks shown in Figure 11, which have been supplied from NASA (Stanley, 1978, private eommunication). The numbers attached to each track in Figure 11 are the revolution numbers of Geos-3. The tracks with four digits revolution numbers are the data taken at the early stage of the satellite, i. e. from July, 1975 to September, 1975, and those with five digits revolution numbers are the data at later stage, i. e. from August, 1977 to September, 1977. In the former revolutions, large errors exceeding 20 m are occasionally included in the radial component of the satellite positions (Stanley, 1978, private communication). That is seen in revolutions 1411 (see Figure 13) and 2051 (see Figure 17). In the latter revolutions, the accuracy of satellite positions has been improved (ibid.) (see Table 1).

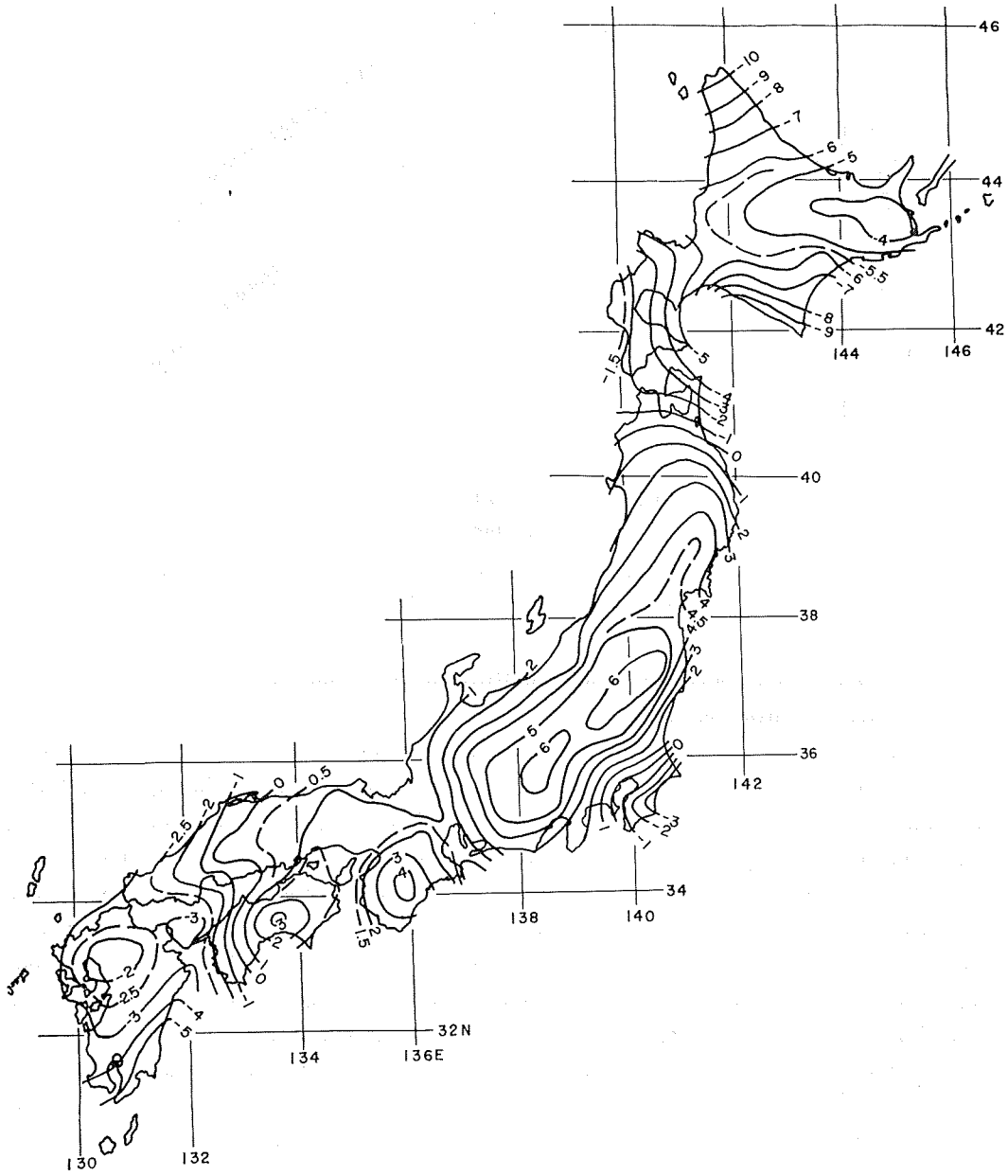

Figure 10 Astrogeodetic geoid of Japan converted into SAO-SE3 global geodetic system (Ganeko, 1976). Contour interval : 1 m.

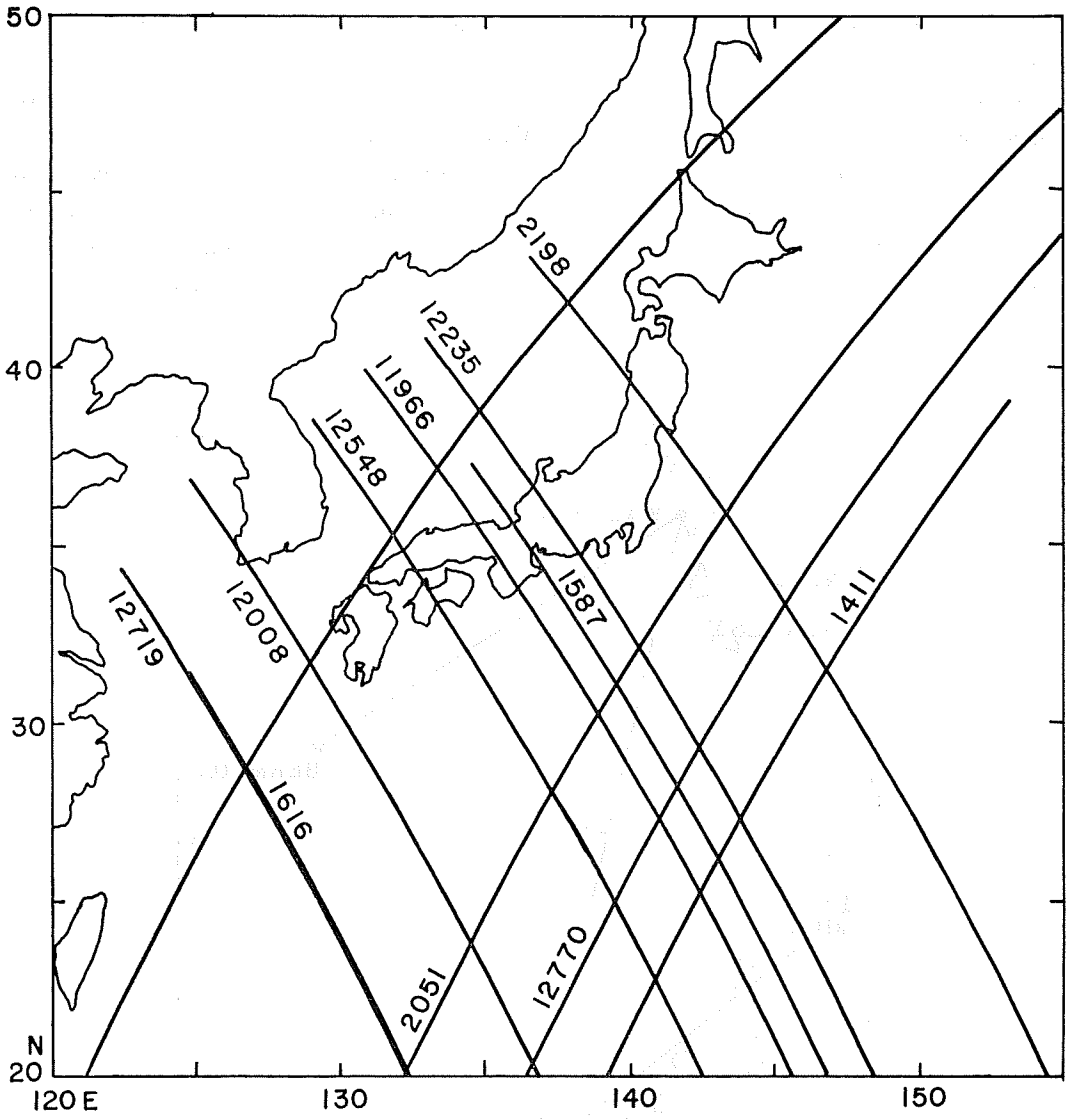

Figure 11 Geos-3 altimetry subsatellite tracks with revolution numbers of the satellite.

The sea surface height determined by the Geos-3 altimeter is the distance between sea surface and the reference ellipsoid whose parameters are $a=6378145$ m and $f=1/298.255$. Altimeter data were calibrated by using laser tracking data obtained at the satellite tracking stations located in the Geos-3 calibration area which is shown in Figure 12 (Leitao et al., 1975).

Figures 13~24 show altimetric sea surface heights, gravimetric geoid profiles along the subsatellite tracks and the differences between altimetric sea surface heights and gravi metric geoidal heights for each revolution in Figure 11. All the altimeter data used here are observations by the short pulse mode (ibid.), and altimeter data rate is 0.1 sec. Altimeter data form a unit data set, called "frame", with 32 or 20 observations corresponding to the adopted telemeter system of high or low data rate. Hence, the period of one frame is 3.276964 sec. or 2.048102 sec., and the period is corresponding to a subsatellite track length of about 22 km or 14 km, respectively. The individual sea surface heights plotted in Figures 13~24 are the average values of altimeter data included in each frame. Distinctions of telemeter systems adopted in each revolution are tabulated in Table 1.

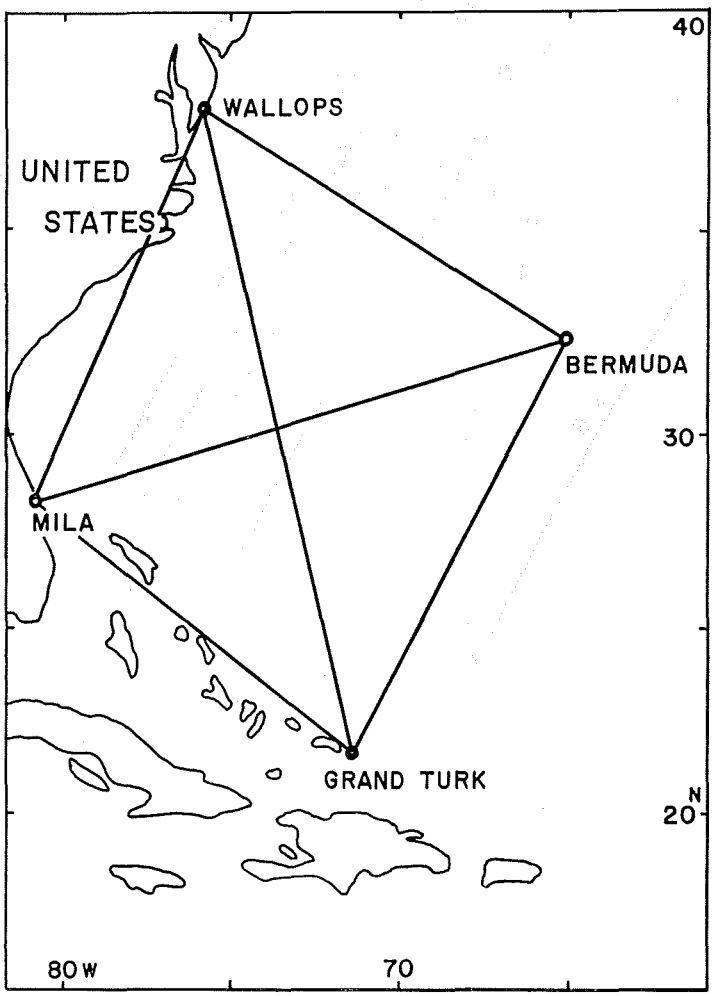

Figure 12 Geos-3 altimeter calibration area (Leitao et al., 1975).

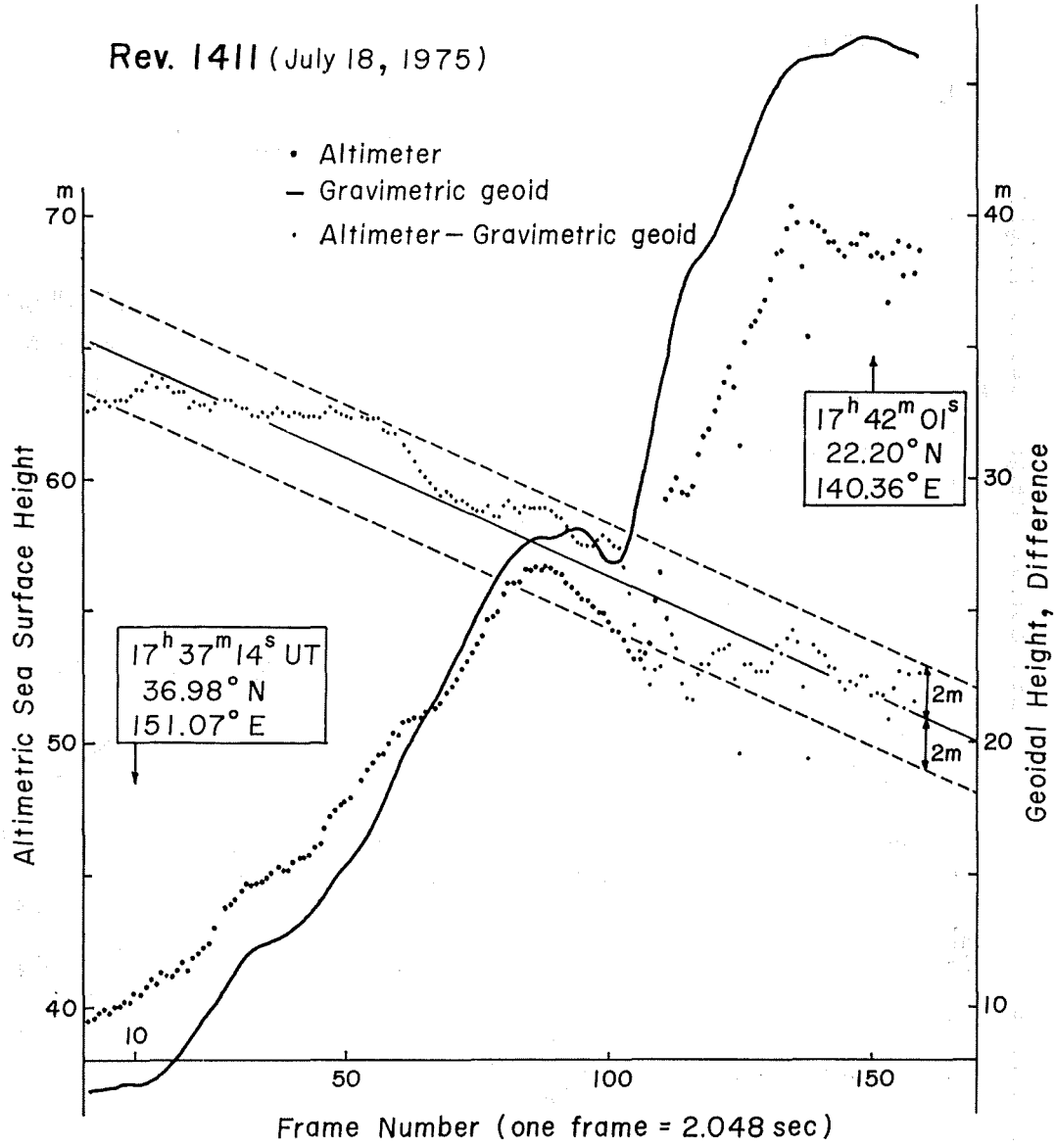

Figure 13 Comparison between Geos-3 altimetric profile (Rev. 1411) and the gravimetric geoid.

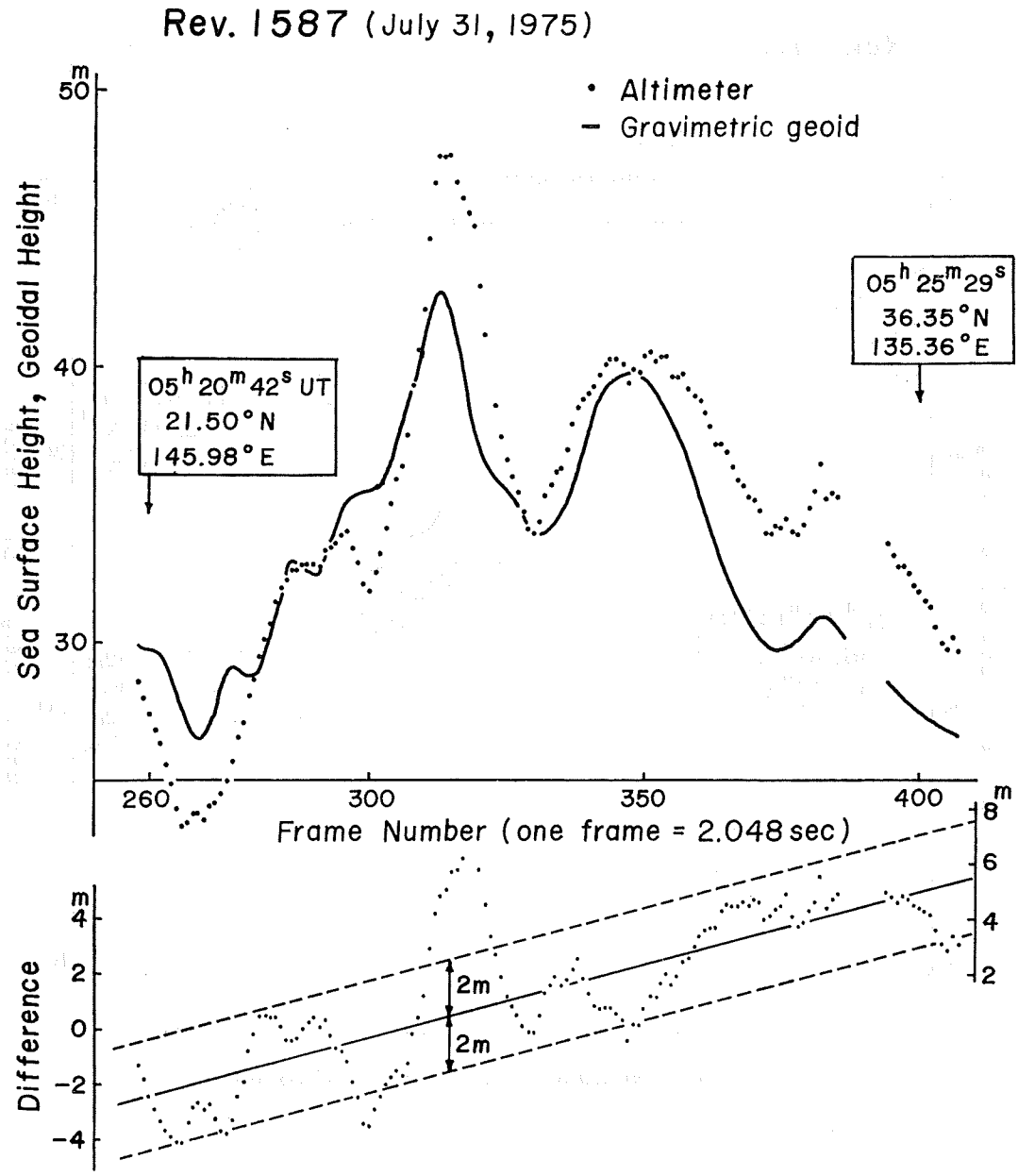

Figure 14 Comparison between Geos-3 altimetric profile (Rev. 1587) and the gravimetric geoid.

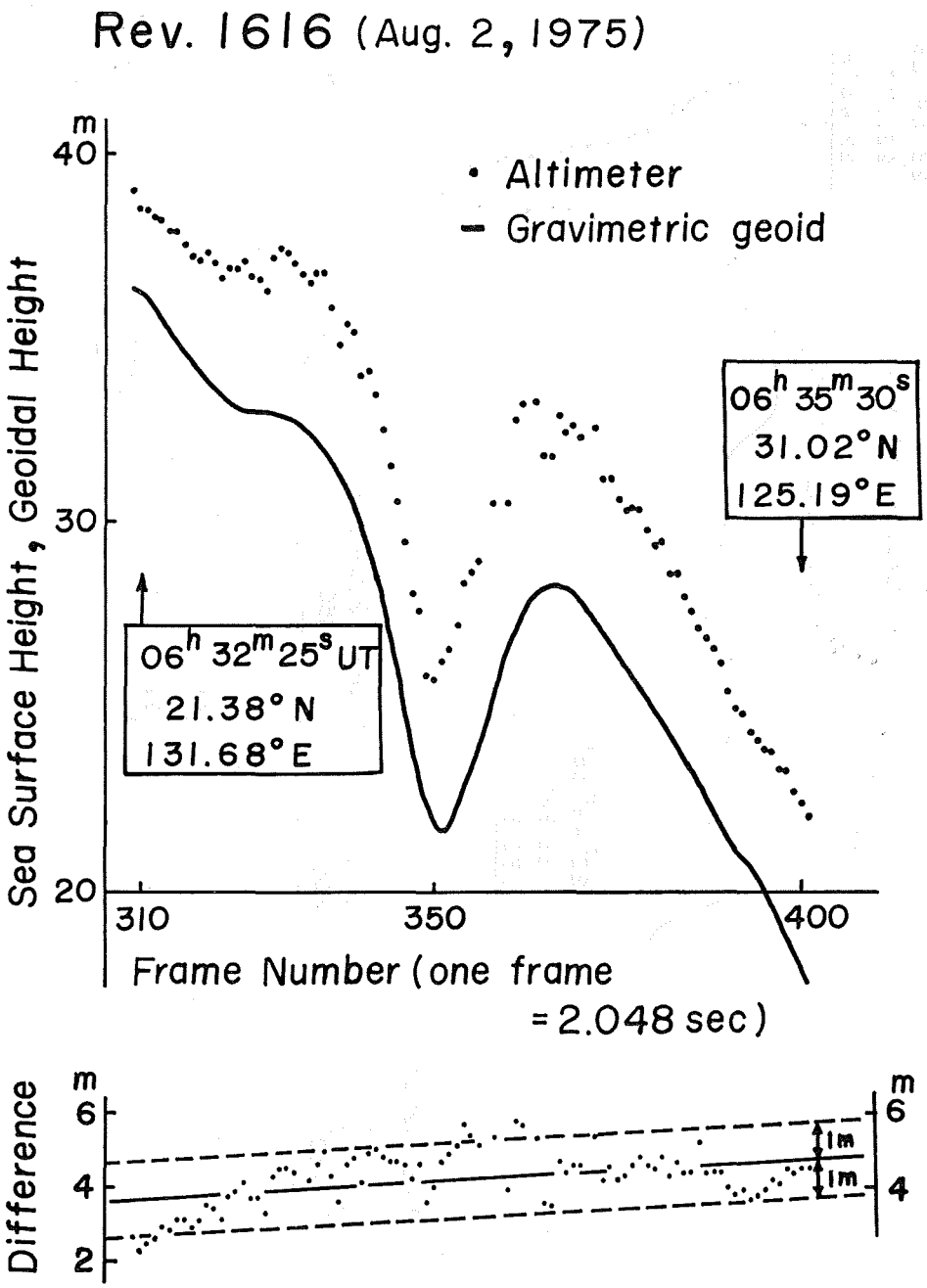

Figure 15 Comparison between Geos-3 altimetric profile (Rev. 1616) and the gravimetric geoid.

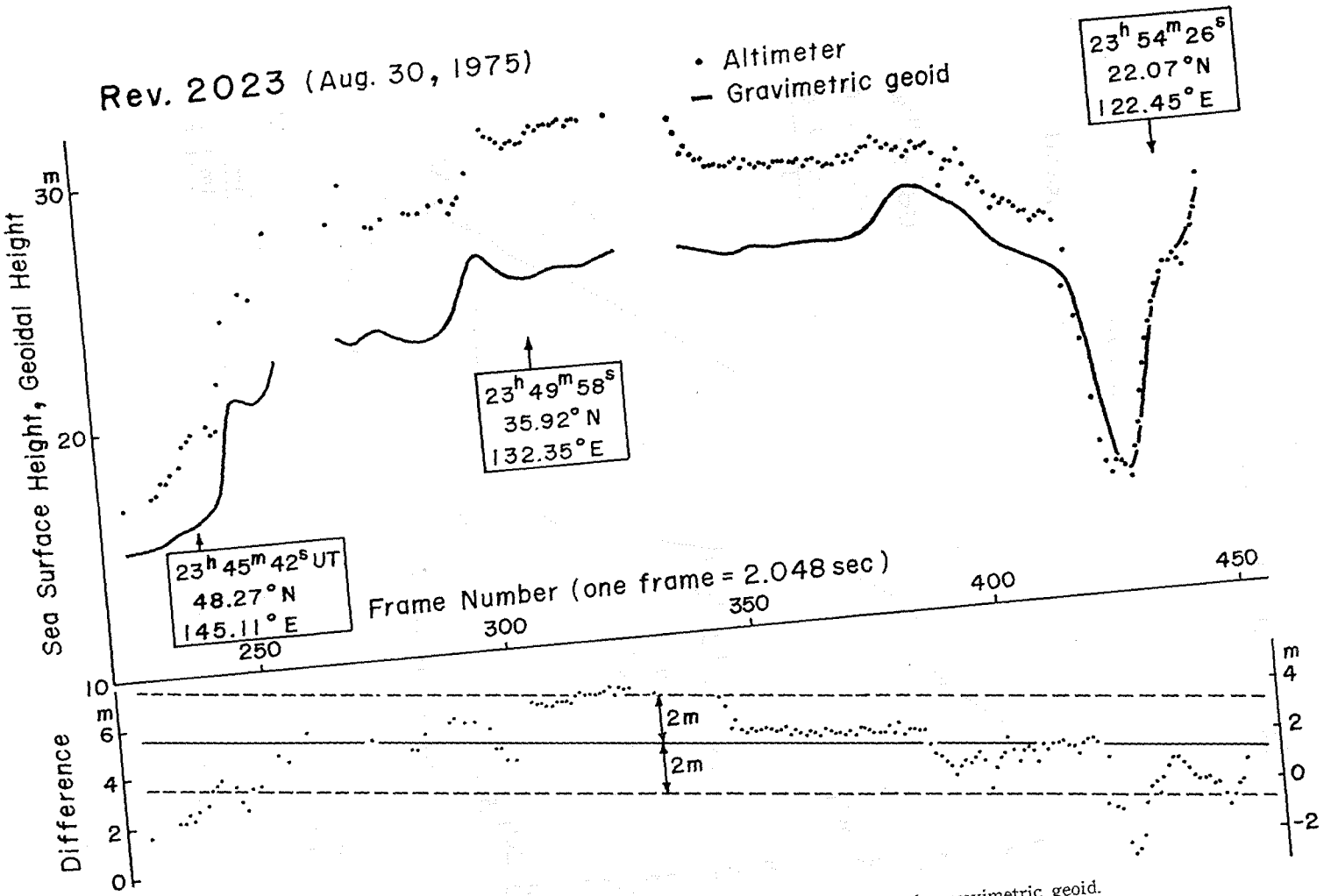

Figure 16 Comparison between Geos-3 altimetric profile (Rev. 2023) and the gravimetric geoid.

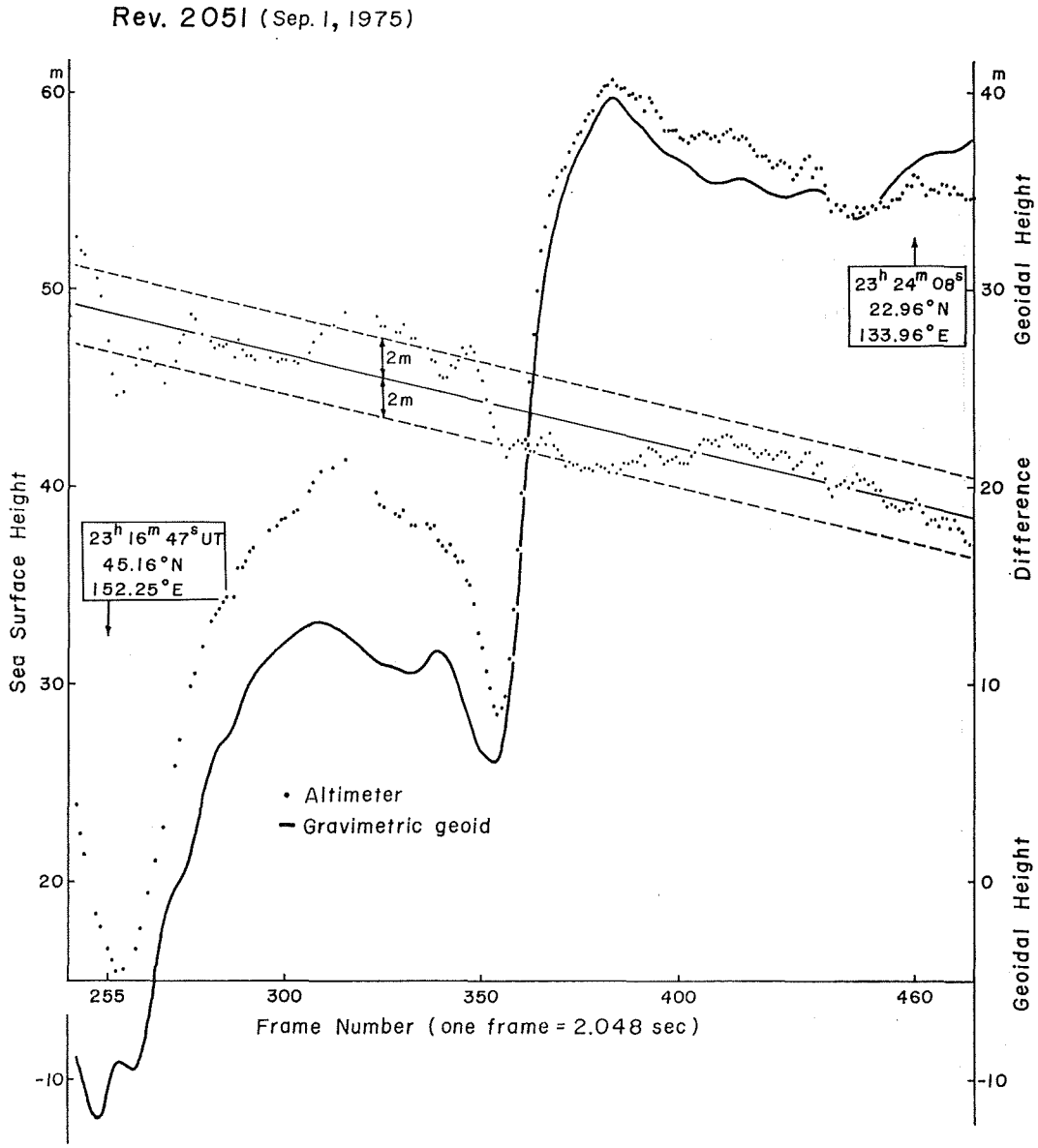

Figure 17 Comparison between Geos-3 altimetric profile (Rev. 2051) and the gravimetric geoid.

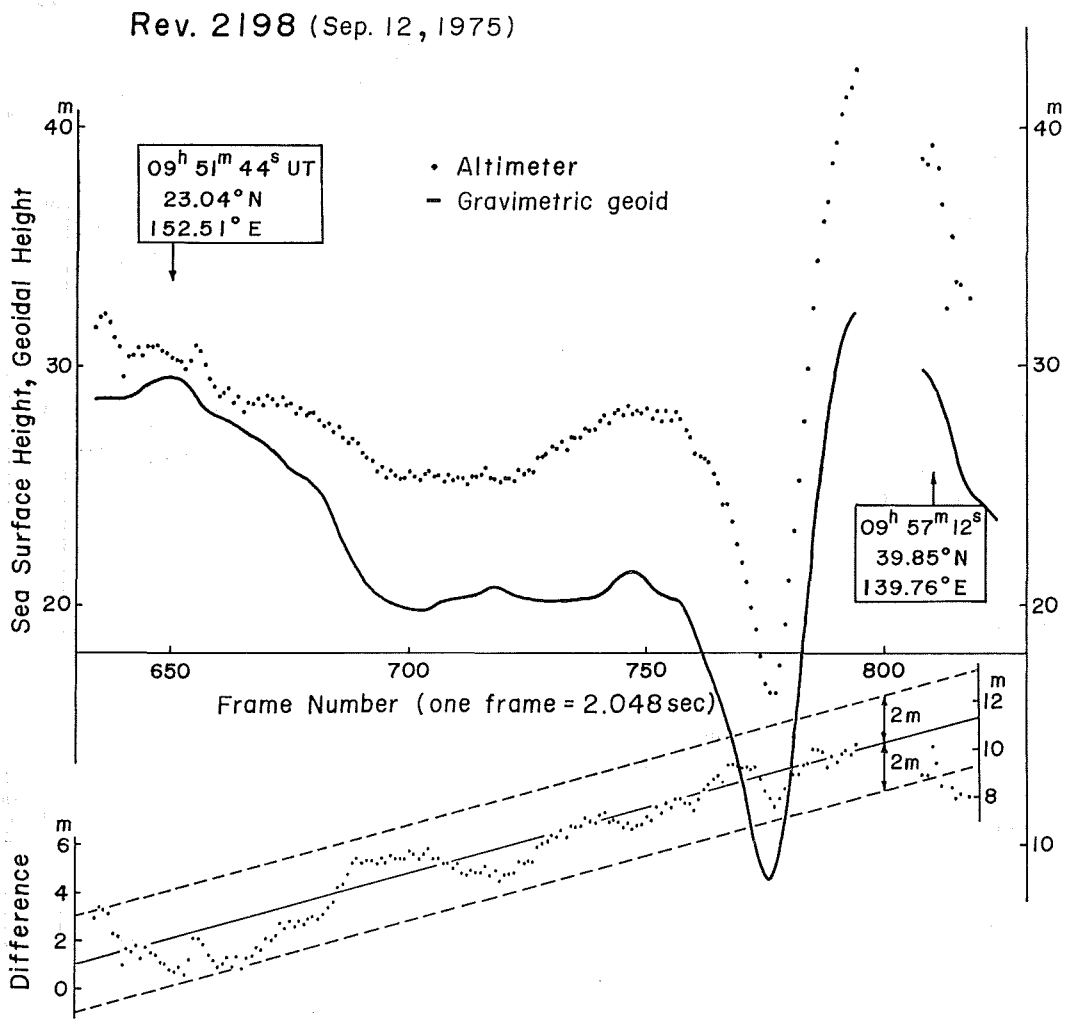

Figure 18 Comparison between Geos-3 altimetric profile (Rev. 2198) and the gravimetric geoid.

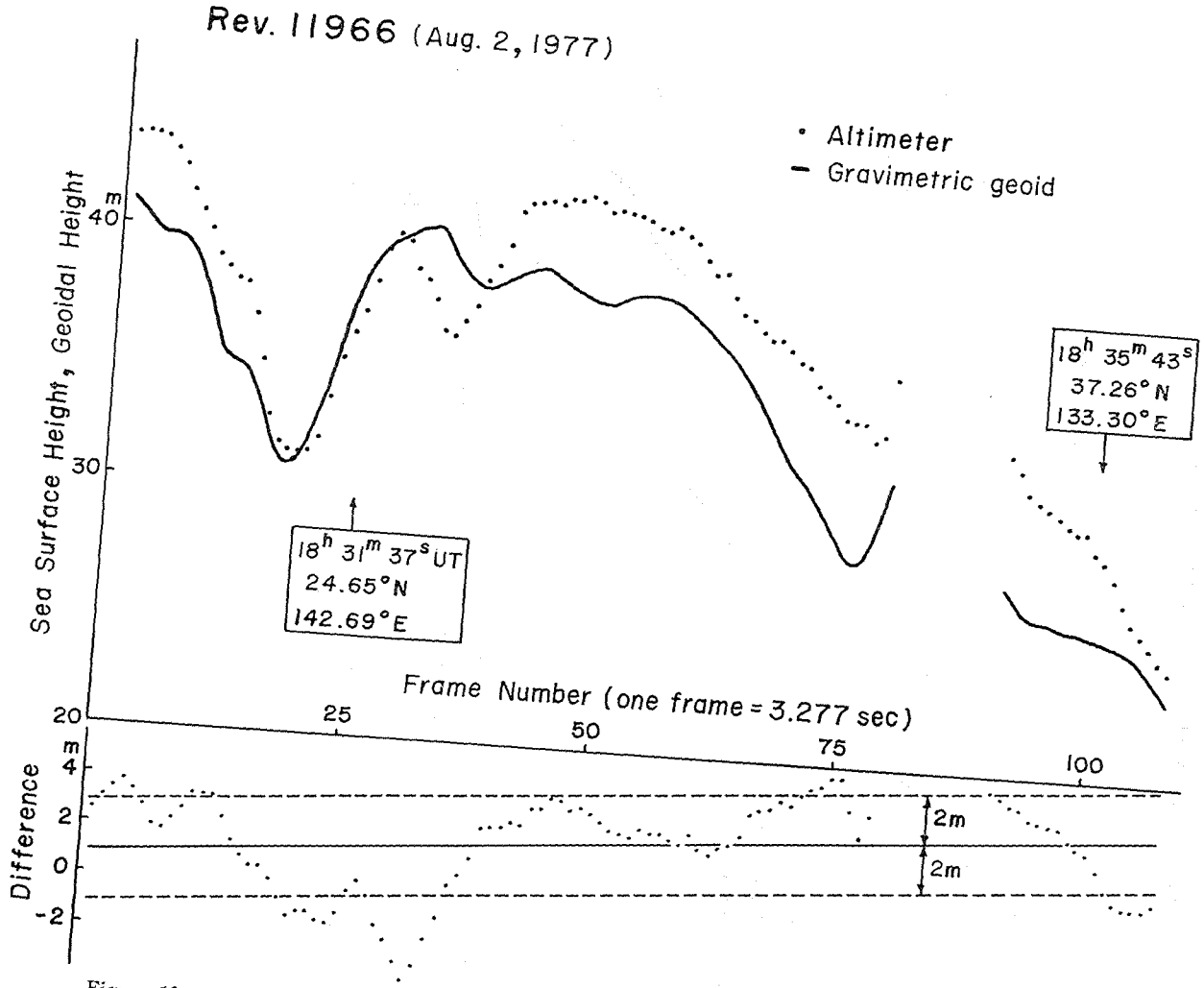

Figure 19 Comparison between Geos-3 altimetric profile (Rev. 11966) and the gravimetric geoid.

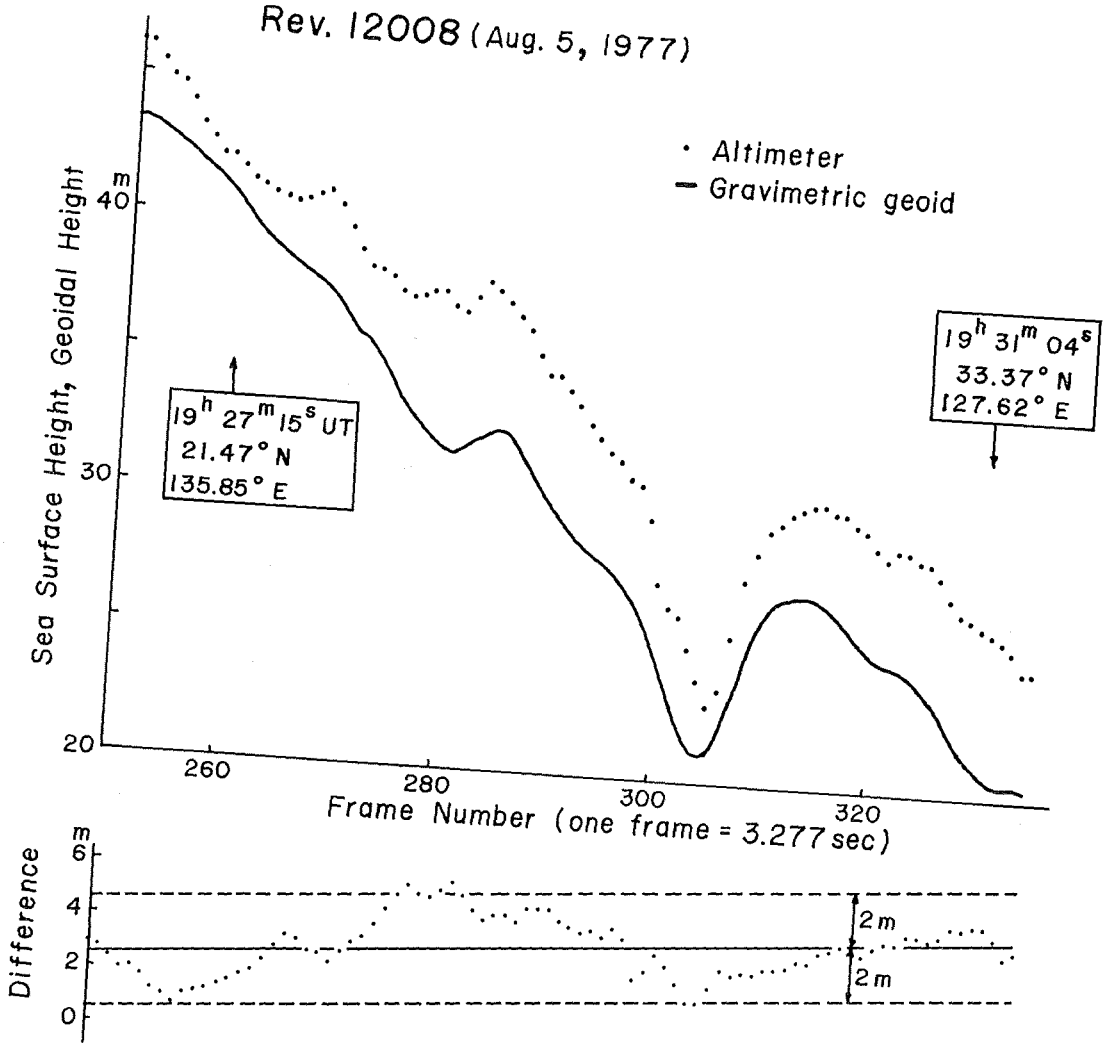

Figure 20 Comparison between Geos-3 altimetric profile (Rev. 12008) and the gravimetric geoid.

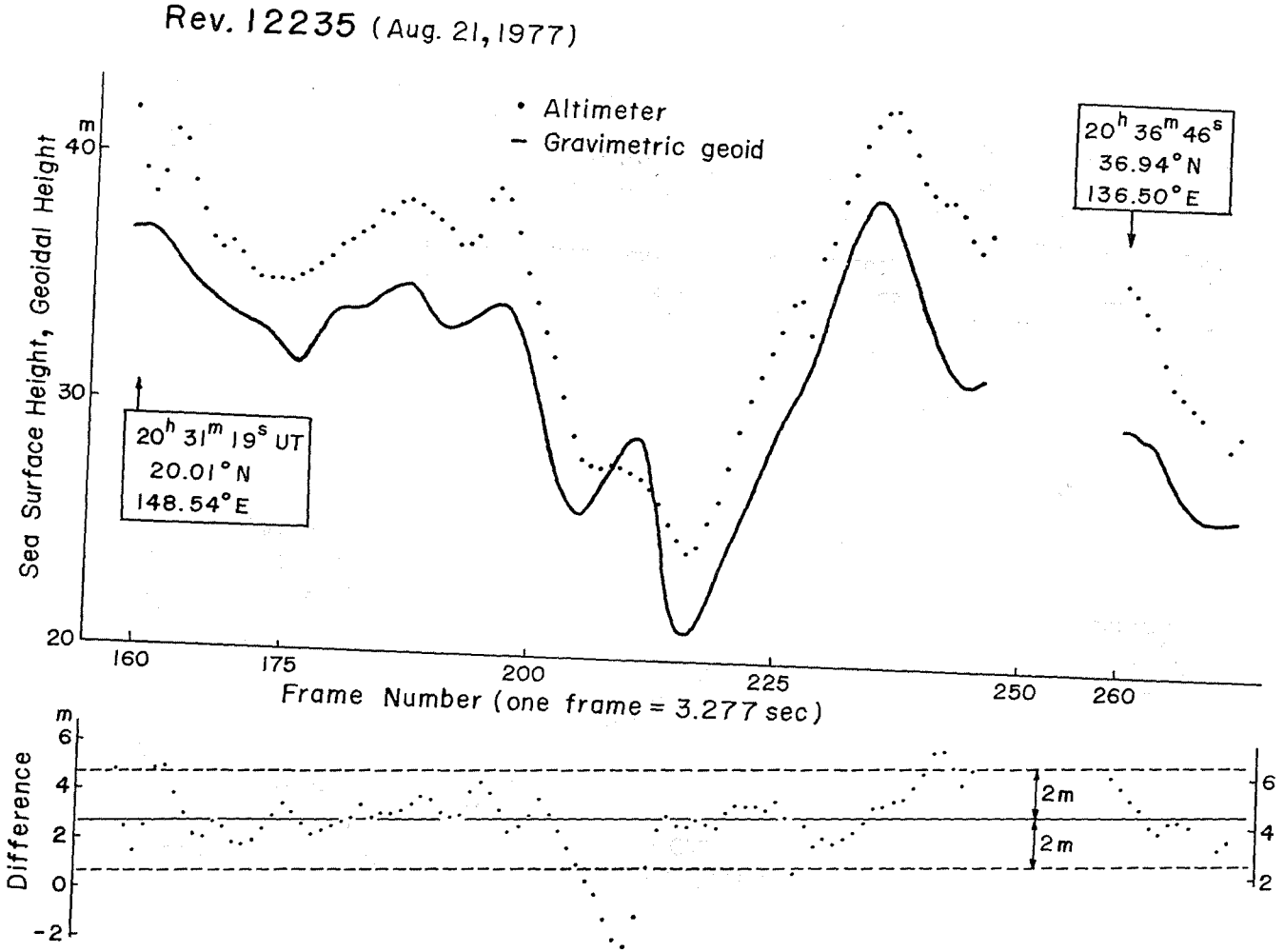

Figure 21 Comparison between Geos-3 altimetric profile (Rev. 12235) and the gravimetric geoid.

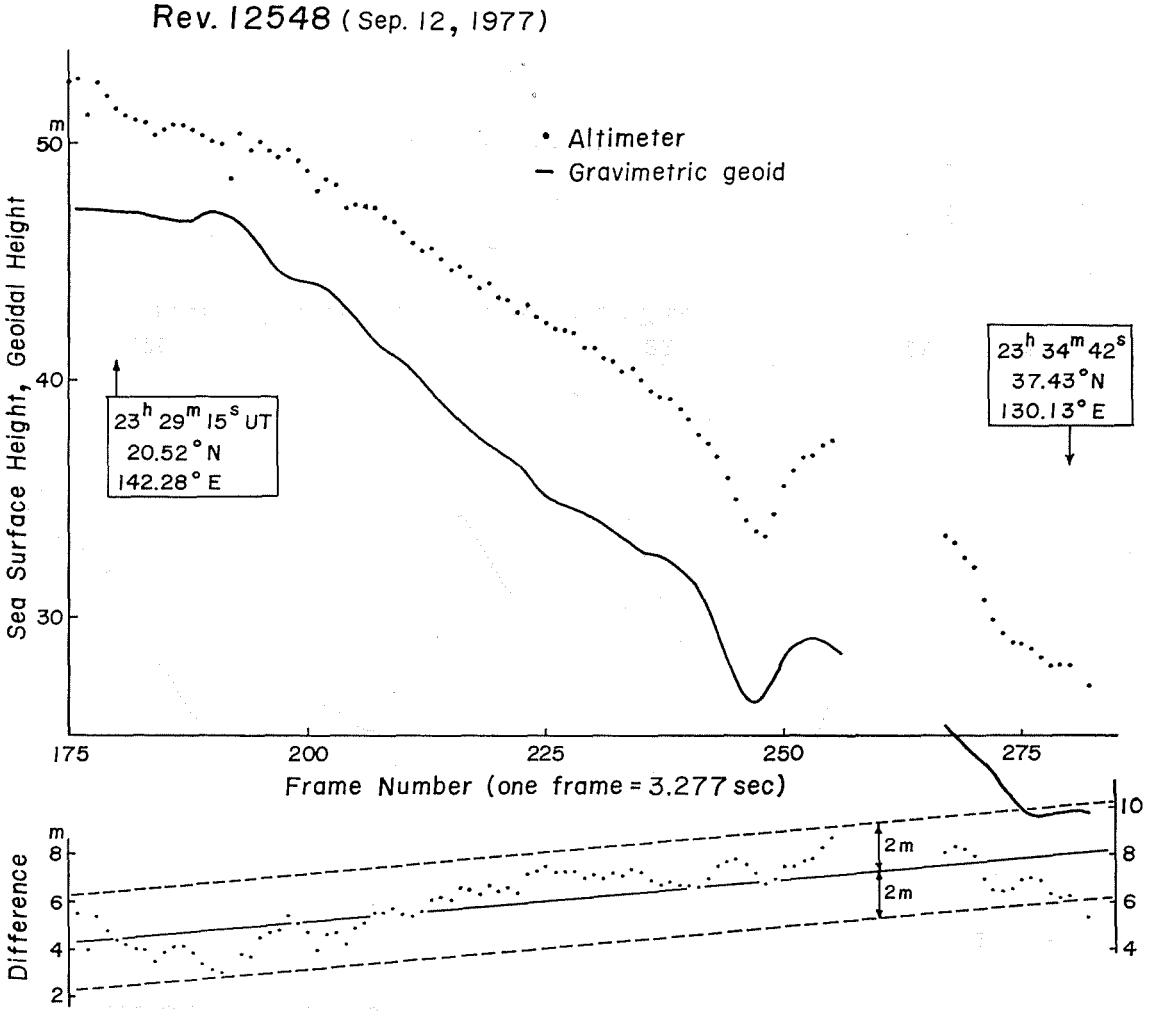

Figure 22 Comparison between Geos-3 altimetric profile (Rev. 12548) and the gravimetric geoid.

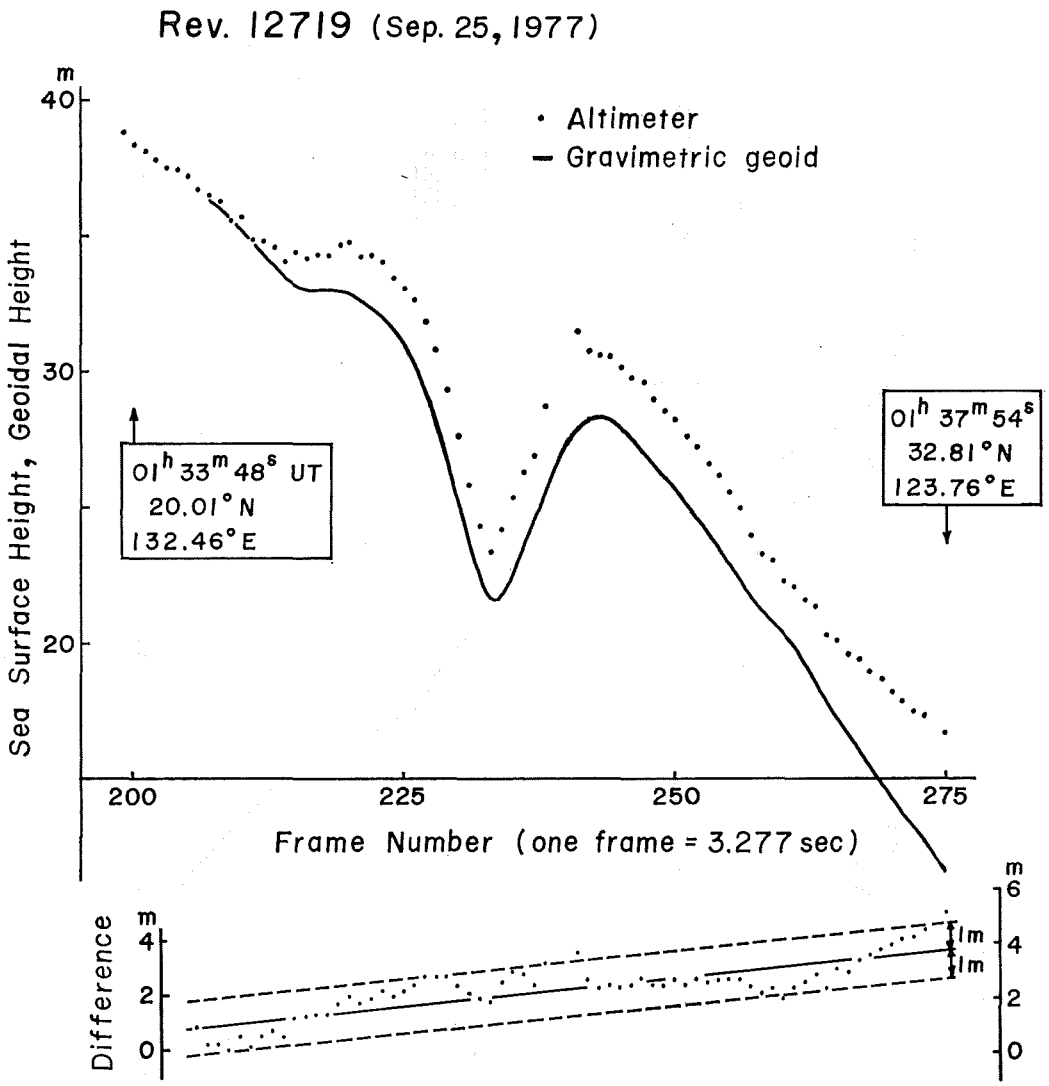

Figure 23 Comparison between Geos-3 altimetric profile (Rev. 12719) and the gravimetric geoid.

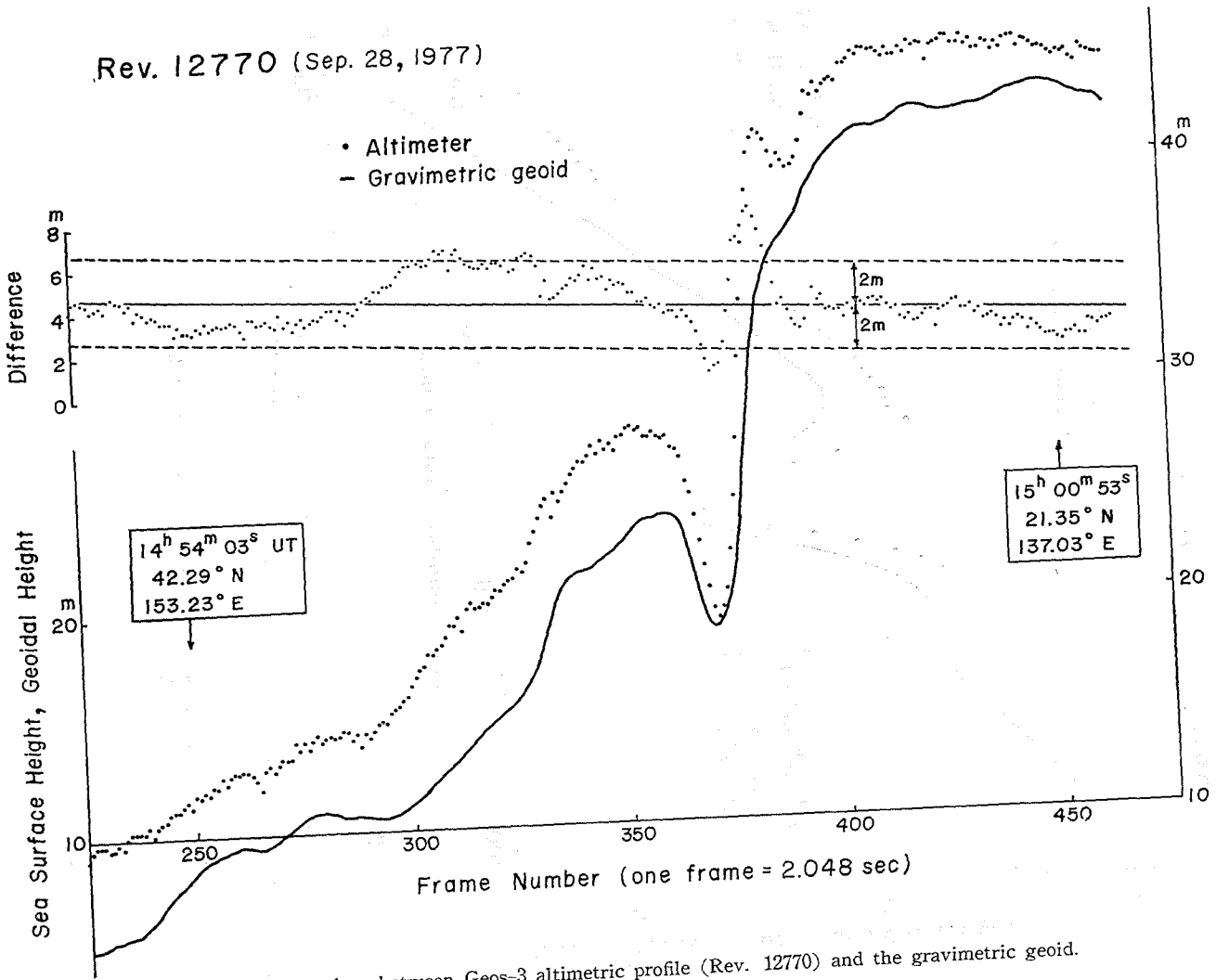

Figure 24 Comparison between Geos-3 altimetric profile (Rev. 12770) and the gravimetric geoid.

Since the altimetric sea surface heights are not corrected by ocean tidal heights and sea surface topographical heights, there may exist differences amounting to about one meter between plotted sea surface heights and geoidal heights. Detailed procedures of the altimeter data processing of Geos-3 are found in Leitao et al. (1975; its revised version, 1976).

As we see in Figures 13~24, the altimetric sea surface heights agree fairly well with the gravimetric geoidal heights except for tiltings and large differences in some parts. To eliminate long wave-length errors included in both profiles, a linear model difference

$$d=bt+a, \tag{3-12}$$

where t is the parameter of time, is fitted to the differences of each revolution by using a least-squares method. The fitted linear model differences are shown along the difference profiles in Figures 13~24. We can see deviations from linear difference amounting to ± 1 to ± 2 m. The parameters of the fitted linear model differences and standard deviations from linear differences are listed in Table 1 for each revolution with some other data of the revolutions. In the least-squares fitting procedures, unreasonable and spikelike sea surface heights, which are apparently wrong data, are omitted, and such data are not protted in the figures.

We find a systematic sign difference among fitted b parameters in Table 1, i.e. b has positive sign for the satellite tracks of south to north direction and vice versa. This implies the facts that geoidal heights become higher than altimetric sea surface heights to the south, and the tilt may be ascribed mainly to the disagreement between the origin of the coordinate system of the satellite altimetry and that of the gravimetric geoid. According to the physical oceanography, the sea surface topographical heights near Japan become higher to the south across the Kuroshio area (e.g. Lisitzin, 1974; Sugimori, 1978). The fact that large bias parts appear in revolutions 1411 and 2051 may be caused by large position errors of Geos-3 satellite as mentioned before, although we have not enough informations to discuss the bias parts further. Standard deviations from the linear model difference of the recent revolutions are generally smaller than those of the early revolutions.

Table 1 Comparisons between altimetric sea surface heights and the gravimetric geoidal heights

Revolution Number	Date	Track Direction	a (m)	b (cm/sec)	S.D. (m)	Frames	Data Rate
1411	1975. 7. 18	South	35. 1	-4. 362	1. 3	158	Low
1587	7. 31	North	-2. 5	2. 572	1. 7	140	L
1616	8. 02	N	3. 6	0. 596	0. 7	90	L
2023	8. 30	S	5. 5	-0. 736	1. 6	161	L
2051	9. 01	S	29. 7	-2. 176	1. 4	192	L
2198	9. 12	N	1. 2	2. 387	1. 0	174	L
11966	1977. 8. 02	N	0. 8	0. 872	1. 9	97	High
12008	8. 05	N	2. 5	0. 822	1. 1	86	H
12235	8. 21	N	2. 6	0. 513	1. 2	97	H
12548	9. 12	N	4. 3	1. 074	0. 9	95	H
12719	9. 25	N	0. 6	1. 275	0. 6	67	H
12770	9. 28	S	4. 8	-0. 442	1. 2	235	L

That may come from the improvements in the altimeter data processing and the satellite trackings. Revolution 11966 has the biggest standard deviation, which is resulted from large differences around the area of Bonin Islands. Large differences around the area of Bonin Islands are also found in revolutions 1587 and 2051. The gravimetric geoid may be inaccurate around there. We see large differences at the north parts of tracks of revolutions 2023 and 2051, which may indicate that the gravimetric geoid has not correctly determined in the north part of the region of Figure 8 because of sparse gravity data around there. It is noted that revolutions 2198, 11966 and 12548 include large differences in Japan Sea region.

On the basis of the results of comparison between altimetric sea surface heights and gravimetric geoidal heights, we may conclude that the relative undulation of the gravimetric geoid is determined in the accuracy of one to two meters. Other detailed error estimations of geoidal height computation by using Stokes' integral will be made in the next chapter.

4. Error Sources Involved in the Practical Performance of Stokes' Integral and Evaluation of the Computed Gravimetric Geoid

In this chapter we will make detailed investigations concerning with error sources involved in the practical computation of a gravimetric geoid based on Stokes' integral. Such investigation will make a contribution to the evaluation of the gravimetric geoid, which has been presented in the last chapter, and furthermore to the computation of a more accurate gravimetric geoid, i.e. geoid of 10 cm accuracy. A 10 cm geoid will play an important role not only in the geodetical science but also in other earth sciences, e.g. ocean dynamics.

(1) Statistical Characteristics of the Gravity Anomaly Field

The knowledge of the characteristics of the gravity anomaly field is indispensable for the error estimation of geoidal height computation, especially for the estimation of omission errors (see (2) in the present chapter). The characteristics are given mathematically in the statistical expressions. The knowledge of the statistical characteristics of the gravity anomaly field is also useful in the interpolation of gravity anomalies and estimation of block mean gravity anomalies (see Chapter 5). So we study the statistical characteristics of the gravity anomaly field for the conveniences of later sections.

The disturbing potential which is harmonic outside a sphere with a radius R is written in the form:

$$T=\frac{kM}{R}\sum_{l=2}^{\infty}\left(\frac{R}{r}\right)^{l+1}T_l, \tag{4-1}$$

where r is the radial distance and T_l is $l-$th degree Laplace surface harmonics. Let P and Q be points in the space outside the sphere, r_P and r_Q be radial distances of P and Q from the geocenter, and the geocentric angular distance between P and Q be ψ (see Figure 25). The rotationally symmetric spacial covariance function of the disturbing potential is given by

$$K(P, Q) = M\{T_P T_Q\}$$
$$= \left(\frac{kM}{R}\right)^2 \sum_{l=2}^{\infty} \sum_{l'=2}^{\infty} \left(\frac{R}{r_p}\right)^{l+1} \left(\frac{R}{r_Q}\right)^{l'+1} M\{T_l(P)\, T_{l'}(Q)\}, \tag{4-2}$$

where $M\{\ \}$ indicates the average taken over the possible combinations of points P and Q under the condition: ψ=constant. Then, we get

$$K(P, Q) = \sum_{l=2}^{\infty} \left(\frac{R^2}{r_P\, r_Q}\right)^{l+1} \sigma_l^2\, P_l\, (\cos\psi) \tag{4-3}$$

(Moritz, 1972, p. 88), where P_l is l−th degree unnormalized Legendre function and σ_l^2 is the degree variance of the disturbing potential. When we use a similar expression for the disturbing potential to (2-15), we can write

$$T_l = \frac{kM}{R} \sum_{m=0}^{l} [\bar{C}_{lm}^{*}\, \bar{R}_{lm} + \bar{D}_{lm}\, \bar{S}_{lm}] \tag{4-4}$$

and σ_l^2 is written as follows:

$$\sigma_l^2 = \left(\frac{kM}{R}\right)^2 \sum_{m=0}^{l} (\bar{C}_{lm}^{*2} + \bar{D}^2{}_{lm}). \tag{4-5}$$

R is chosen as the radius of a sphere included completely inside the earth (the sphere is called Bjerhammar sphere, (see Figure 25)) so that the disturbing potential T is harmonic on and outside the earth. Consider the case that both of P and Q are located on the surface of the earth. We put approximately $r_P\, r_Q = R_0^2$, where R_0 is the mean

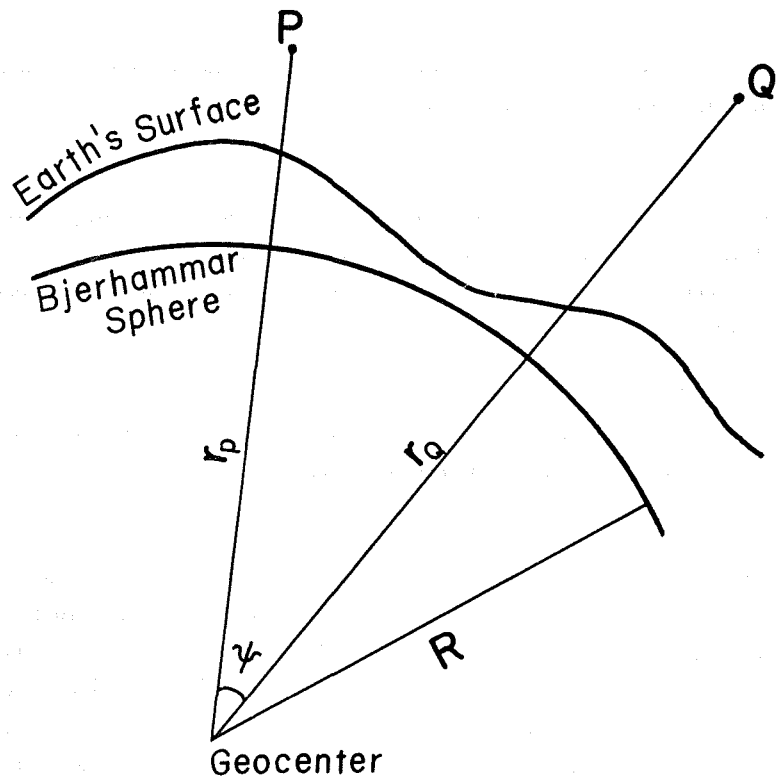

Figure 25 Explanation figure for the derivation of the spacial covariance functions.

radius of the earth, and introduce a parameter $s=(R/R_0)^2$. From (4-3) we get

$$K(\psi)=\sum_{l=2}^{\infty}\sigma_l^2\ s^{l+1}\ P_l(\cos\psi) \tag{4-6}$$

as the covariance function of the disturbing potential on the surface of the earth.

By using the relation between gravity anomaly and disturbing potential:

$$\Delta g=-\frac{\partial T}{\partial r}-\frac{2}{r}\ T$$

(Heiskanen and Moritz, 1967, p. 89), we obtain the covariance function of the gravity anomaly on the earth's surface as follows:

$$C(\psi)=\sum_{l=2}^{\infty}\sigma_l^2(\Delta g)\ s^{l+2}\ P_l(\cos\psi) \tag{4-7}$$

(Moritz, 1972, p. 89), where $\sigma_l^2(\Delta g)$ is the degree variance of gravity anomaly called "anomaly degree variance". Then σ_l^2 in (4-6) is given by

$$\sigma_l^2=\frac{R^2}{(l-1)^2}\,\sigma_l^2(\Delta g). \tag{4-8}$$

From (4-5) and (4-8), $\sigma_l^2(\Delta g)$ is expressed by geopotential coefficients as follows:

$$\sigma_l^2(\Delta g)=G^2(l-1)^2\sum_{m=0}^{l}(\bar{C}_{lm}^{*2}+\bar{D}^2{}_{lm}), \tag{4-9}$$

where

$$G^2=\left(\frac{kM}{R^2}\right)^2.$$

On the other hand, we can compute anomaly degree variances from (4-7) when we know the covariance function of gravity anomaly, i.e.

$$\sigma_l^2(\Delta g)=\frac{2l+1}{2}\ s^{-(l+2)}\int_0^{\pi}C(\psi)P_l(\cos\psi)\sin\psi\ d\psi. \tag{4-10}$$

The statistical characteristics of the gravity anomaly field are thus expressed by the covariance function or degree variances of gravity anomaly.

Kaula (1966) proposed an equation to estimate sizes of the fully normalized geopotential coefficients:

$$\sigma_l(\bar{C}_{lm},\ \bar{D}_{lm})=\frac{10^{-5}}{l^2}, \tag{4-11}$$

and it is called Kaula's rule of thumb. From (4-9) and (4-11), the anomaly degree variance based on Kaula's rule of thumb is written as

$$\sigma_l^2(\Delta g)=G^2(l-1)(2l+1)\,\frac{10^{-10}}{l^4},\quad l\geq 3. \tag{4-12}$$

Figure 26a shows the anomaly degree variances expressed by (4-12) and ones based on the satellite-derived geopotential coefficients: GEM-7 (Wagner et al., 1976); GEM-9 (Lerch et al., 1977). As seen in this figure, (4-12) is a fairly good model of the anomaly degree variances at least up to a degree of several tens. Geopotential coefficients are also derived from the combination of satellite tracking data and surface gravity data, or solely from surface gravity data. Figure 26b includes anomaly degree variances based on such geopotential coefficients: GEM-10 (Lerch et al., 1977, combination solution); Rapp's results (Rapp, 1977b, surface gravity data).

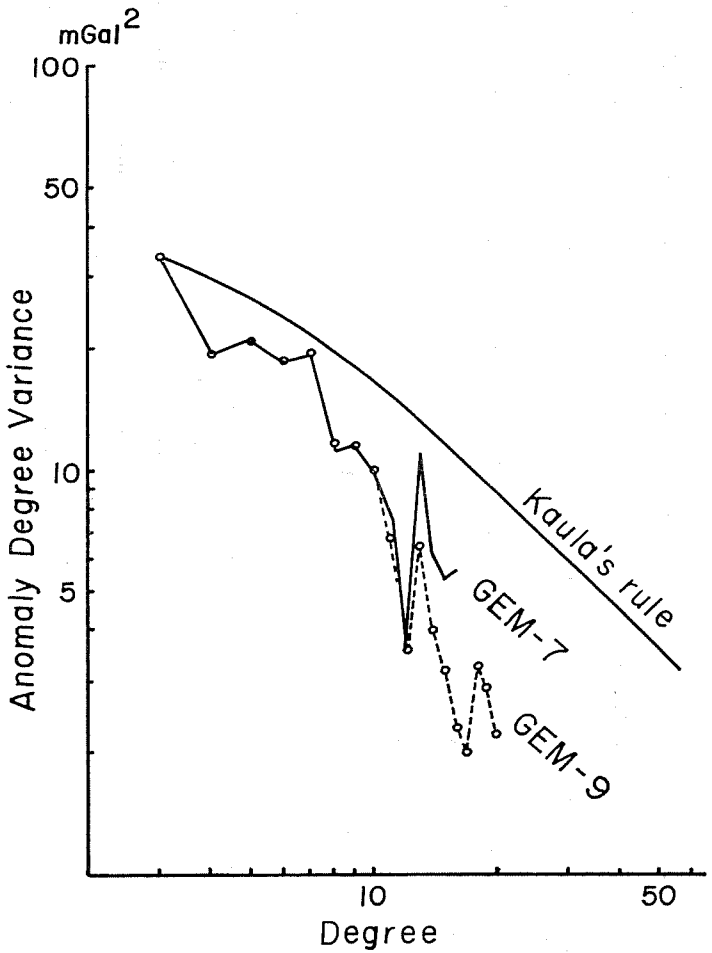

Figure 26a Anomaly degree variances based on Kaula's rule of thumb, GEM-7 and GEM-9 solutions.

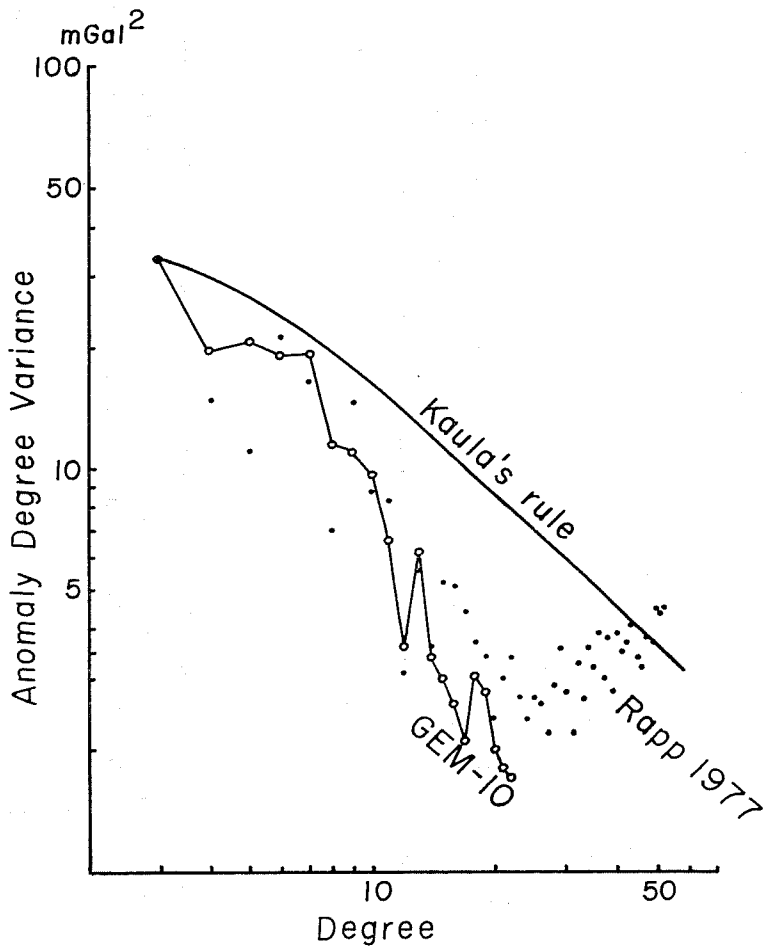

Figure 26b Anomaly degree variances based on Kaula's rule of thumb, GEM-10 and Rapp's solution.

Equation (4-7) is the covariance function of point gravity anomaly, and we can compute covariance functions of block mean gravity anomalies by using the point covariance function. Let σ_P and σ_Q be two blocks whose areas are S_P and S_Q, and ψ be the angular distance between centers of the blocks. The covariance function $\bar{\bar{C}}$ of the block mean gravity anomalies is derived by

$$\bar{\bar{C}}(\psi)=\frac{1}{S_P S_Q}\iint_{\sigma P}\iint_{\sigma Q} C(\psi')\,d\sigma_P\,d\sigma_Q, \tag{4-13}$$

where ψ' is the angular distance between $d\sigma_P$ (in σ_P) and $d\sigma_Q$ (in σ_Q). Approximating a square B° block to a circular area with radius $\psi_0=B^\circ/\sqrt{\pi}$ and using (4-7), we obtain the covariance function of mean gravity anomalies of B° block as follows:

$$\bar{\bar{C}}(\psi)=\sum_{l=2}^{\infty}\sigma_l^2(\Delta g)\,s^{l+2}\,\beta_l^2\,P_l(\cos\psi), \tag{4-14}$$

where

$$\beta_l=\cot\frac{\psi_0}{2}\cdot\frac{P_{l1}(\cos\psi_0)}{l(l+1)} \tag{4-15}$$

(see Appendix A). β_l is called smoothing parameter introduced by Pellinen (1966) and Meissl (1971). Rapp (1977b) tabulated the numerical values of β_l up to degree 52 for $B=5^\circ$. Note $\beta_l\to 1$ when $\psi_0\to 0$. The variance of block mean gravity anomalies is given by putting $\psi=0$ in (4-14), and it is written as

$$\bar{r}=\sum_{l=2}^{\infty}\sigma_l^2(\Delta g)\,s^{l+2}\,\beta_l^2. \tag{4-16}$$

Tscherning and Rapp (1974) obtained a model anomaly degree variance:

$$\sigma_l^2(\Delta g)=\frac{A(l-1)}{(l-2)(l+B)} \tag{4-17}$$

with $A=425.28$ mGal^2, $B=24$, and $s=0.999617$. They obtained the model by using actual degree variances up to degree 20 adopting $\sigma_2^2(\Delta g)=7.5$ mGal^2, $_r=C(0)=\sum_{l=2}^{\infty}\sigma_l^2(\Delta g)s^{l+2}=1795$ mGal^2, and variances of 1° and 5° block mean gravtiy anomalies 920 and 302 mGal^2, respectively.

We adopt notations $C_G(\psi)$ for the long wave-length component of the gravity anomaly covariance function:

$$C_G(\psi)=\sum_{l=2}^{L}\sigma_l^2(\Delta g)\,s^{l+2}\,P_l(\cos\psi), \tag{4-18}$$

and $C_L(\psi)$ for the local anomaly covariance function:

$$C_L(\psi)=\sum_{l=L+1}^{\infty}\sigma_l^2(\Delta g)\,s^{l+2}\,P_l(\cos\psi). \tag{4-19}$$

Consequently, $C(\psi)=C_G(\psi)+C_L(\psi)$. Figure 27 shows $C(\psi)$ and $C_L(\psi)$ based on the anomaly degree variance model (4-17) when $L=20$. The correlation distance (the distance where the covariance value is a half of the variance) of $C_L(\psi)$ is much shorter than that of $C(\psi)$, because $C_L(\psi)$ expresses only the statistical characteristics of short wave-length component of the gravity anomaly field. Since the covariances in Figure 27 corresponds to the world-wide average statistical characteristics of the gravity anomaly field, they may differ from covariance functions derived from gravity anomaly distribution in a

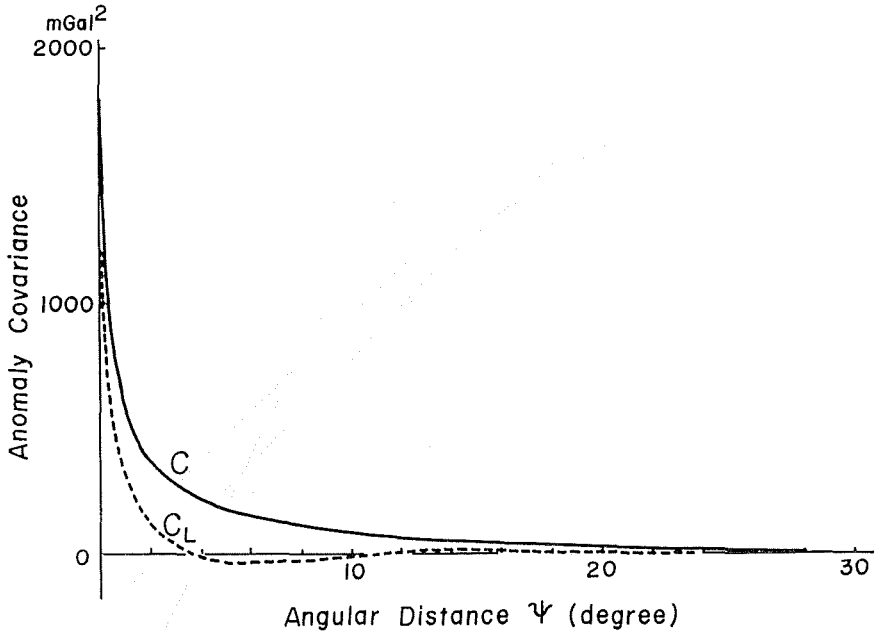

Figure 27 Anomaly covariance function $C(\psi)$ and local anomaly covariance function $C_L(\psi)$ based on the anomaly degree variance model (equation (4-17))by Tscherning and Rapp (1974).

restricted area. Ganeko (1976) obtained a local anomaly covariance function from observations of the deflections of the vertical distributed in Japan. It is approximated by an analytical function as follows:

$$C_L(\psi) = C_0 \exp\left(-\frac{r}{D}\right), \tag{4-20}$$

where $C_0 = 2809$ mGal², $D = 55$ km, and r is the parameter of distance in kirometers. (4-20) is based on the residual anomaly field of SAO-SE3 geopotential model (Gaposchkin et al., 1973) up to degree and order 18. The residual variance C_0 in (4-20) is larger than that of world-wide average, 1795 mGal², obtained by Tscherning and Rapp (1974). This is probably due to the fact that Japan is located in a geophysically active area and the gravity anomaly field around Japan is rougher than the world-wide average. If we assume the local covariance function (4-20) to be the world-wide average one, we can compute anomaly degree variance of a high degree by using (4-10). The computed anomaly degree variances for $s=1$ are shown by curve c in Figure 28. This figure also includes the degree variances based on Kaula's rule of thumb (curve a), degree variance model (4-17) (curve d) and another degree variance model by Rapp (1973a) (curve b):

$$\sigma_l^2(\Delta g) = \frac{B(l-1)}{(l-2)(l+D+\varepsilon l^2)} \tag{4-21}$$

where $B = 246.5556$ mGal², $D = 12.6755$ and $\varepsilon = 0.000657$. Rapp determined the parameters so that (4-7) and (4-16) fitted the actual gravity anomaly field by putting $s=1$ in both equations. In other words, the anomaly degree variance model (4-21) may be approximated

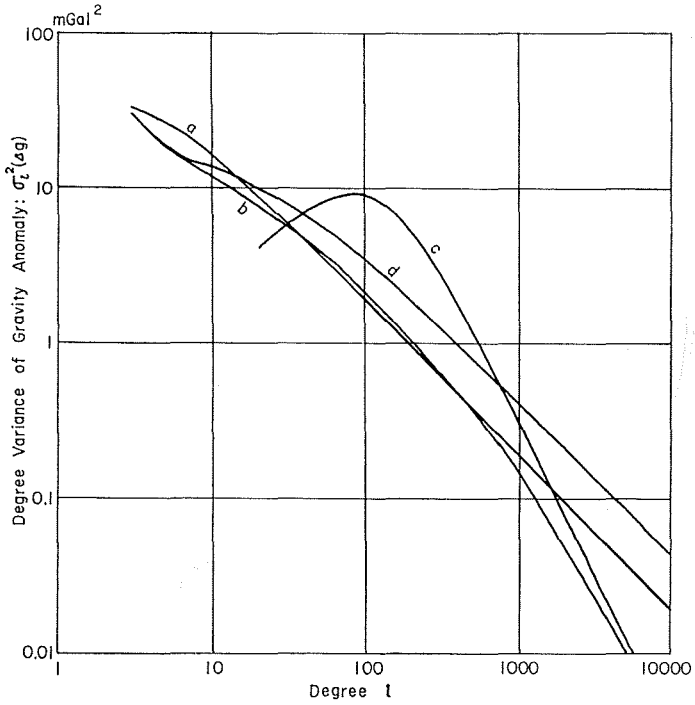

Figure 28 Anomaly degree variance models: (a) based on Kaula's rule of thumb; (b) Rapp (1973), equation (4-21); (c) Ganeko (1976), based on anomaly covariance function (4-20); (d) (d) Tscherning and Rapp (1974), equation (4-17).

by the degree variance model (4-17) multiplied by s^{l+2}, i. e.

$$\sigma_l^2(\Delta g)\ [\text{equation (4-21)}] \approx s^{l+2}\,\sigma_l^2(\Delta g)[\text{equation (4-17)}]$$

The anomaly degree variance model c shown in Figure 28 is characterized by a peak around degree 90, and the possibility of such peak seems to be supported by the anomaly degree variances by Rapp (1977b) derived from surface gravity data (see Figure 26b). However, if we take the difficulties of determination of the geopotential coefficients of high degrees into cosideration, it is not so firmly supported by the Rapp's results that such a peak exists on an anomaly degree variance curve as the global average. Degree 90 corresponds to about 400 km wave-length.

We compute covariance functions of block mean gravity anomalies included in JHDGF-1 gravity file obtained in the previous chapter. The obtained covariance functions are shown in Figure 29a (for $30' \times 30'$ and $1^\circ \times 1^\circ$ blocks) and in Figure 29b (for $10' \times 10'$ block). It is assumed that each block has the same area as far as they are located in the JHDGF-1 region (see Figure 4), and the block covariance functions are computed by

$$\bar{C}_L(r_k) = \frac{\sum_{i,j} (\bar{\Delta g} - \bar{\Delta g}_s)_i \, (\bar{\Delta g} - \bar{\Delta g}_s)_j}{N_k}, \tag{4-22a}$$

where $\bar{\Delta g} - \bar{\Delta g}_s$ is the block residual mean gravity anomalies based on the satellite-derived gravity anomaly of GEM-8 geopotential model (Wagner et al., 1976). The summation is taken over N_k paires of blocks σ_i and σ_j whose centers are separated by the distance

$r_{ij,k}$, which satisfies the condition:

$$r_k \leq r_{ij,k} \leq r^k + \Delta r, \quad k=0,1,2,\cdots, \tag{4-22b}$$

in which we assume $r^\circ=0$. Δr is taken as 20 km for $10'\times10'$ block, 30 km for $30'\times30'$ block and 60 km for $1^\circ\times1^\circ$ block. The distance parameter of the covariance function is computed by

$$r_k=\sum_{i,j} r_{ij,k}/N_k$$

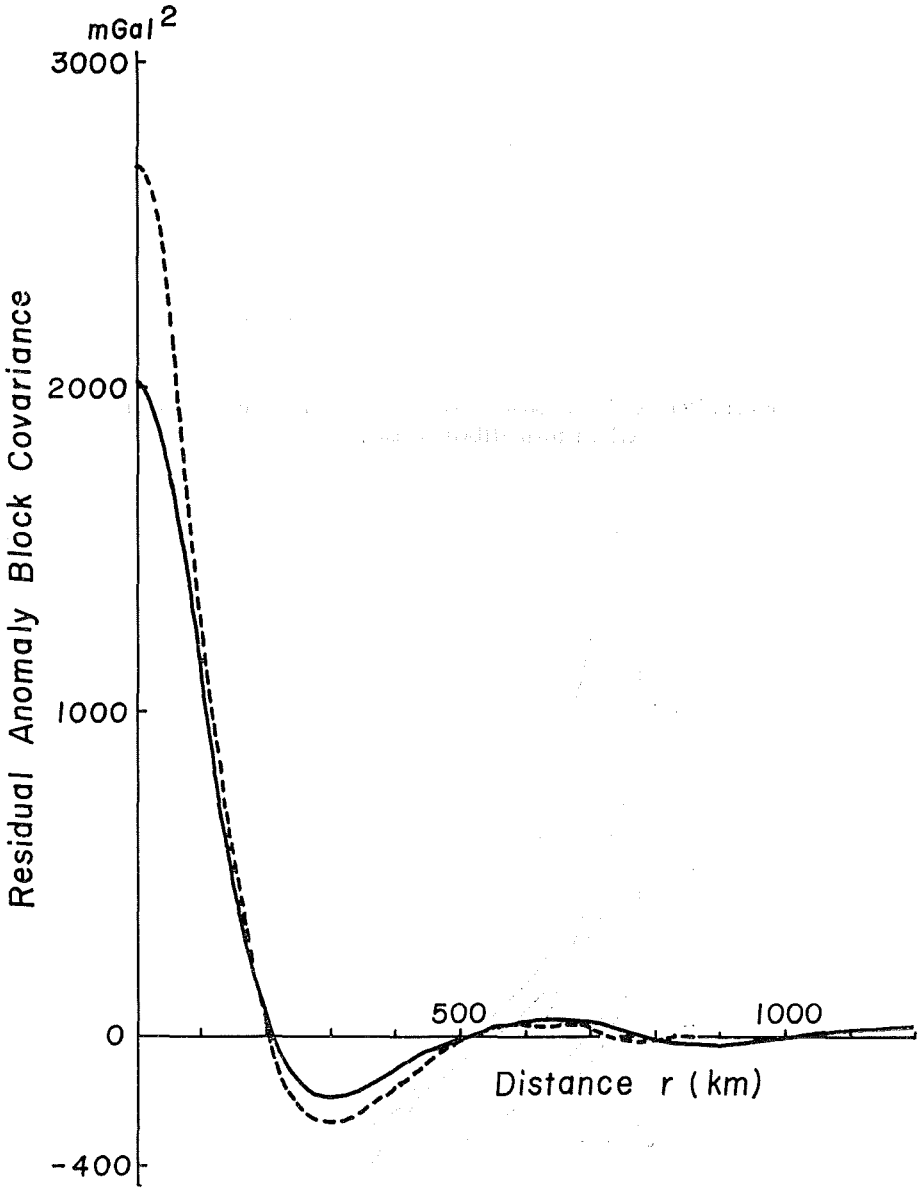

Figure 29a Residual anomaly block covariances of $30'\times30'$ blocks (broken line) and $1^\circ\times1^\circ$ blocks (full line) derived from JHDGF-1 data. Residual anomalies are referred to GEM-8 global anomaly field.

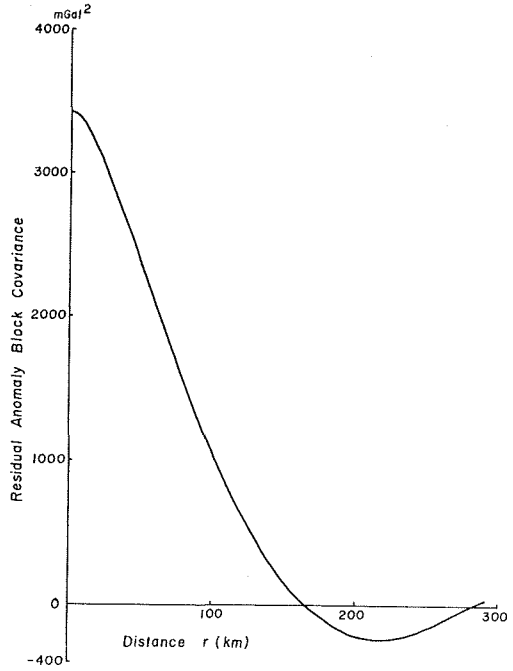

Figure 29b Residual anomaly block covariance of 10′×10′ blocks derived from JHDGF-1 data.

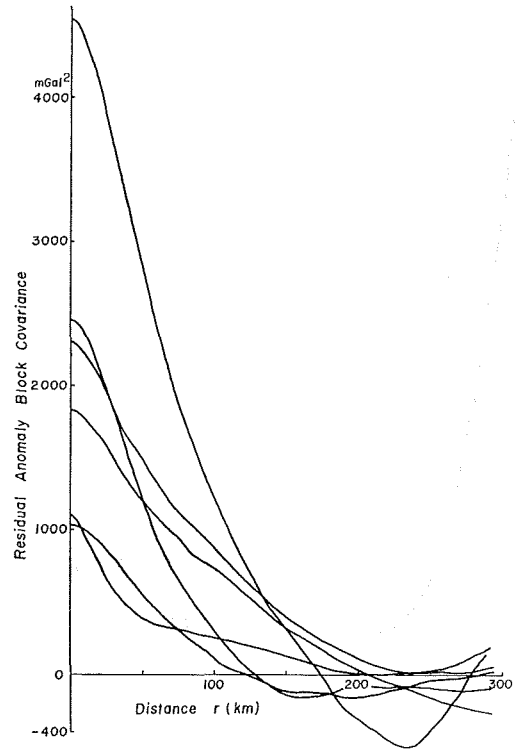

Figure 29c Residual anomaly block covariances of 10′×10′ blocks included in 5°×5° blocks.

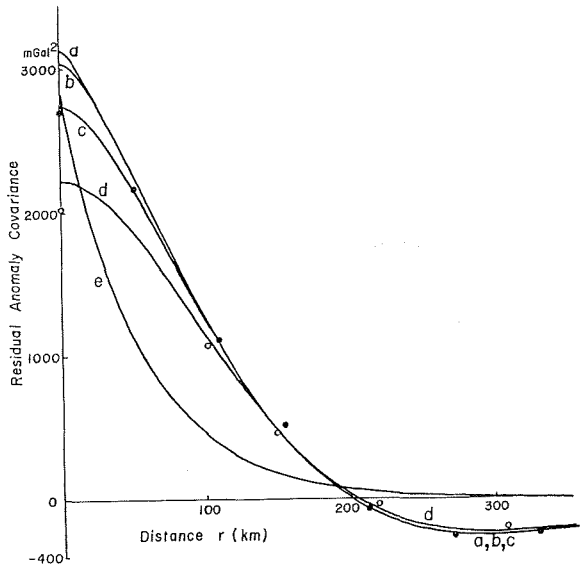

Figure 29d Residual anomaly covariance functions based on the analytical function model (4-23): (a) point covariance; (b) 10′×10′ block covariance; (c) 30′×30′ block covariance; (d) 1°×1° block covariance. (e) is the point covariance (4-20). Full and open circles are actual covariances for 30′×30′ and 1°×1° blocks, respectively.

It should be noted that the covariance function of 10′×10′ block shown in Figure 29b is an average of covariance functions derived from 10′×10′ blocks in every 5°×5° block area of JHDGF-1 region, and the number of pairs (N_k) is used as the weight in taking an average of 10′×10′ block covariance functions. Some examples of individual 10′×10′ block covariance functions are seen in Figure 29c. As we see in the figure, there are not any rules among the curves of covariance functions. This fact may indicates that the features of the short wavelength components of the gravity anomaly field largely depend on the local geophysical structures.

Adopting a model analytical expression of covariance function:

$$C_L(r)=C_0 \exp\left[-(r/D)^p\right]\cos kr \qquad (4\text{-}23)$$

for the residual gravity anomaly around Japan, the parameters are determined as follows: $C_0=3133$ mGal²; $D=161.2$ km; $k=0.007854$ 1/km; $p=1.227$. In the determinations of the parameters, 10′×10′ block covariances are not taken into consideration because of instabilities of 10′×10′ block covariances. Figure 29d shows the analytical covariance function (4-23) and the analytical block covariance functions derived from (4-13) and (4-23), comparing with the other type of covariance function (4-20).

(2) Omission Errors in the Numerical Evaluation of Stokes' Integral

Omission errors involved in the numerical evaluation of Stokes' integral come from the following situations.

(A) When the terrestrial gravity data are given by average value over a certain sized block area, the shorter wave-length components of the anomaly field than the size of the block area are omitted in the performance of numerical integration of Stokes'

integral.

(**B**) Outside the cap area, we adopt a satellite-derived geopotential coefficient set, so that we consequently omit the more detailed informations of the gravity anomaly field than the satellite-derived gravitational field.

These kinds of omission error were discussed in detail by Christodoulidis (1976) and Ganeko (1977). We summarize the methods of omission error estimations and apply them to the gravimetric geoid obtained in Chapter 3.

1) Basic equations of omission errors

We can write the geoidal height error due to the truncation of higher degree components of gravity anomaly than degree L outside the cap area as follows:

$$\delta N=\frac{R}{2G}\sum_{l=L}^{\infty}Q_l(\psi_0)\Delta g_l\,, \tag{4-24}$$

where Q_l is Molodenskii's truncation function (Molodenskii et al., 1962), ψ_0 the radius of the cap, and Δg_l l−th degree Laplace surface harmonics of gravity anomaly. R and G are the mean radius of the earth and the mean gravity on the earth's surface, respectively. We call usually (4-24) "truncation error" of geoidal height. The truncation error covariance is defined by

$$C_{\delta N}(\Theta, L, \psi_0)=M\{\delta N_P\,\delta N_Q\}\,, \tag{4-25}$$

where Θ is the angular distance between P and Q, and the average operator $M\{\ \}$ works as an average of possible pairs P and Q with a constant angular distance Θ over the whole earth. Inserting (4-24) into (4-25), and using orthogonality relations among spherical harmonics and an equation

$$\sigma_l^2(\Delta g)=M\{\Delta g_l^2\}\,,$$

we get (Ganeko, 1977)

$$C_{\delta N}(\Theta, L, \psi_0)=\left(\frac{R}{2G}\right)^2\sum_{l=L}^{\infty}Q_l^2(\psi_0)\,\sigma_l^2(\Delta g)\,P_l(\cos\Theta), \tag{4-26}$$

where P_l is l−th degree unnormalized Legendre function, and $\sigma_l^2(\Delta g)$ is the anomaly degree variance already discussed in the previous section.

2) Point truncation error

When $\Theta=0$ in (4-26), the equation is reduced to

$$\sigma^2_{\delta N}(L,\psi_0)\equiv C_{\delta N}(0, L, \psi_0)=\left(\frac{R}{2G}\right)^2\sum_{l=L}^{\infty}Q_l^2(\psi_0)\,\sigma_l^2(\Delta g) \tag{4-27}$$

which defines the variance of truncation error. (4-27) is evaluated when the anomaly degree variances are given. The definition of Molodenskii's truncation function is

$$Q_l(\psi_0)=\int_{\psi_0}^{\pi}P_l(\cos\psi)\,S(\psi)\,\sin\psi\,d\psi, \tag{4-28}$$

where $S(\psi)$ is Stokes' function (see (2-2)). The analytical evaluation equations of Q_l were investigated by Molodenskii et al. (1962), Hagiwara (1972, 1976) and Paul (1976). Ganeko (1977) obtained a simple asymptotic analytical expression of Q_l applicable at high degrees. Figure 30a shows the evaluated truncation errors of geoidal heights, $\sigma_{\delta N}(L, \psi_0)$, given by (4-27) for various cap sizes on the basis of the anomaly degree variance model (4-21) (curve b in Figure 28, and it is called "anomaly degree variance model b" in this

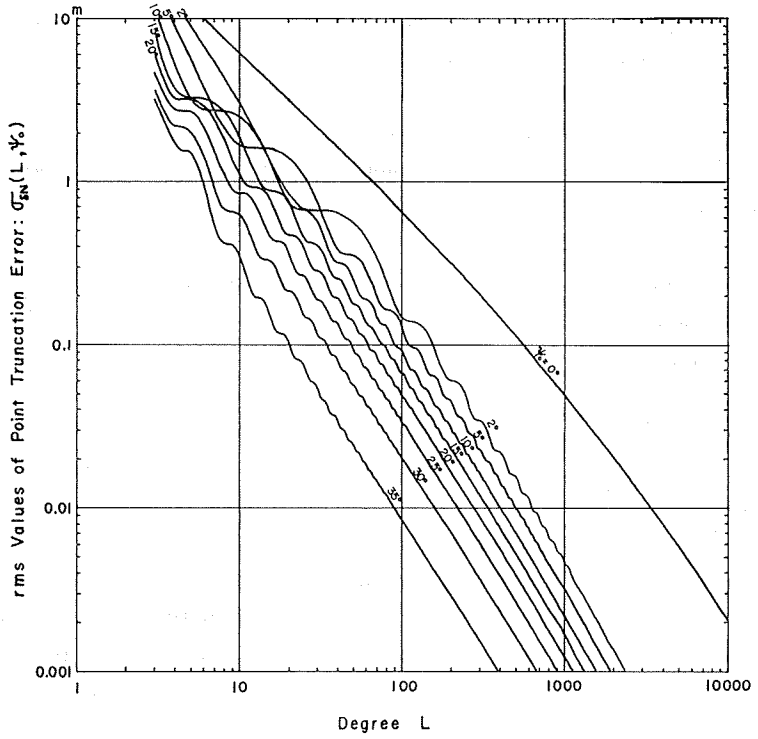

Figure 30a Point truncation errors based on the anomaly degree variance model *b*.

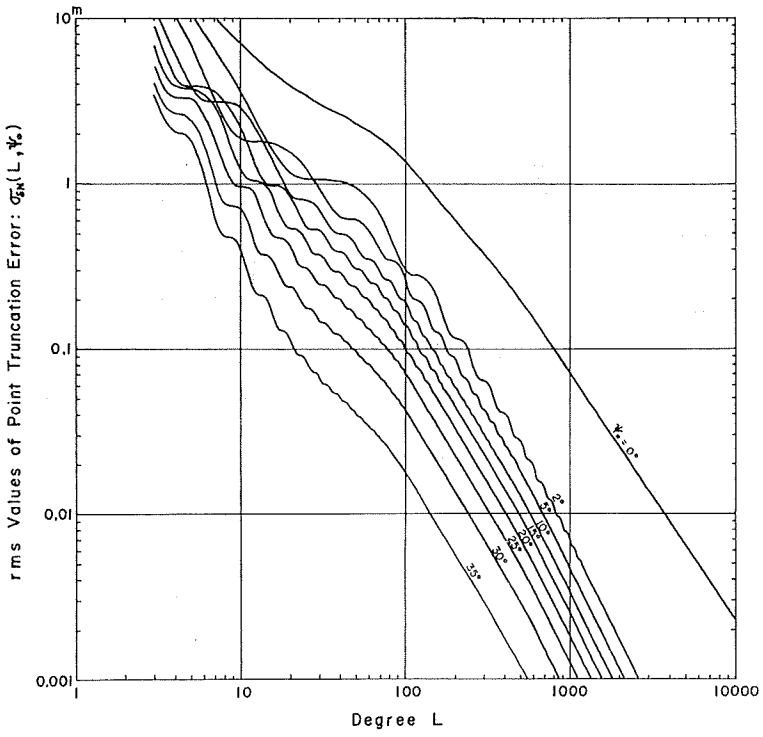

Figure 30b Point truncation errors based on the anomaly degree variance model *c*.

paper). Figure 30b shows truncation errors based on another anomaly degree variance model which is a combination of curve a for degrees lower than 30 and curve c for degrees higher than 30 (the combined degree variance model is called "anomaly degree variance model c" in this paper). The truncation error defined by (4-27) is called "point truncation error". We may be able to consider Figure 30a and Figure 30b as the lower bound and the upper bound of point truncation errors, respectively, due to the adopted anomaly degree variance models.

As for situation (A), L in (4-27) is derived by following equation for θ° block mean gravity anomalies:

$$L \fallingdotseq \frac{180^\circ}{\theta^\circ}\ , \tag{4-29}$$

and as for situation (B), L is corresponding to $l_{max}+1$, where l_{max} is the highest degree of the available satellite-derived geopotential coefficient set. Furthermore, let us consider the point truncation error of geoidal height computed under conditions shown in Figure 31. A cap area is divided into k zones which are numbered as 1, 2,..., k from inner to outer as seen in Figure 31. The radius of the outer boundary of $i-$th zone is ψ_i, and ψ_k is the radius of the outer-most boundary that coincides with the conventional cap size formerly denoted as ψ_0. It is assumed that s_i° $(i=1\sim k)$ block mean gravity anomalies are available in each zone. We consider s_i° block mean gravity anomalies can represent the gravity anomaly field up to degree $[180^\circ/s_i^\circ]$, and we put

$$L_i=\left[\frac{180^\circ}{s_i^\circ}\right]+1, \quad i=1\sim k.$$

Let L_{k+1} be the maximum degree of the satellite-derived geopotential coefficient set. By using (4-27), we can estimate

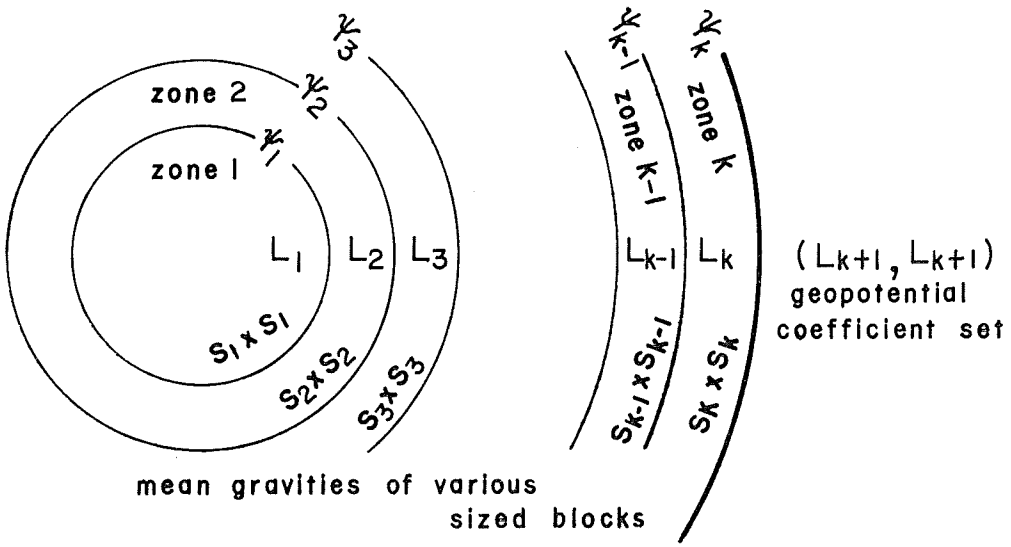

Figure 31 Zone divisions of a cap area.

Table 2 Individual point truncation error terms evaluated on the basis of anomaly degree variance models *b* and *c*

	Anomaly degree variance model *b*	Anomaly degree variance model *c*
$\sigma_{\delta N}(181, 0)$	0.36 m	0.69 m
$\sigma_{\delta N}(361, 0)$	0.17	0.31
$\sigma_{\delta N}(181, 5°)$	0.05	0.10
$\sigma_{\delta N}(361, 5°)$	0.02	0.03
$\sigma_{\delta N}(23, 20°)$	0.45	0.51
$\sigma_{\delta N}(181, 20°)$	0.02	0.04
$\sigma_{\delta N}(361, 20°)$	0.01	0.01

the point truncation error of geoidal height according to the zone divisions of Figure 31. It is evaluated by

$$\sigma_{\delta N}^2 = \sum_{i=1}^{k+1} \sigma_{\delta N}^2(L_i, \phi_{i-1}) - \sum_{i=1}^{k} \sum_{j=1}^{i} \sigma_{\delta N}^2(L_j, \phi_i) \tag{4-30}$$

(Ganeko, 1977), where ϕ_0 is zero.

We have computed the geoid undulations around Japan in Chapter 3 under the following data conditions:

$$\left.\begin{array}{rl} 0 \leq \phi \leq 5° & 30' \times 30' \text{ block mean gravity anomalies} \\ 5° < \phi \leq 20° & 1° \times 1° \text{ block mean gravity anomalies} \\ \phi > 20° & l_{max} = 22 \text{ satellite-derived geopotential coefficient set} \end{array}\right\} \tag{4-31}$$

To apply (4-30) to the data conditions (4-31), we put $k=2$, $\phi_1=5°$, $\phi_2=20°$, $L_1=361$, $L_2=181$ and $L_3=23$, and then the point truncation error is given by

$$\begin{aligned} \sigma_{\delta N}^2 = {} & \sigma_{\delta N}^2(361, 0) + \sigma_{\delta N}^2(181, 5°) + \sigma_{\delta N}^2(23, 20°) \\ & - \sigma_{\delta N}^2(361, 5°) - \sigma_{\delta N}^2(181, 20°) - \sigma_{\delta N}^2(361, 20°). \end{aligned} \tag{4-32}$$

Values of each term of (4-32) can be read from Figure 30a or Figure 30b depending on anomaly degree variance models. These values are listed in Table 2. Thus (4-32) is evaluated as

$$\left.\begin{array}{l} \sigma_{\delta N}^2 = (0.48 \text{ m})^2 \quad \text{for anomaly degree variance model } b \\ \quad = (0.60 \text{ m})^2 \quad \text{for anomaly degree variance model } c \end{array}\right\} \tag{4-33}$$

When geoidal heights are co mputed under the conditions:

$$\begin{array}{ll} 0 \leq \phi \leq 20° & 1° \times 1° \text{ block mean gravity anomalies} \\ \phi > 20° & l_{max} = 22 \text{ satellite-derived geopotential coefficient set} \end{array} \tag{4-34}$$

the point truncation error is evaluated by

$$\sigma_{\delta N}^2 = \sigma_{\delta N}^2(181, 0) + \sigma_{\delta N}^2(23, 20°) - \sigma_{\delta N}^2(181, 20°)$$

and using numerical values in Table 2, we get

$$\left.\begin{array}{l} \sigma_{\delta N}^2 = (0.58 \text{ m})^2 \quad \text{for anomaly degree variance model } b \\ \quad = (0.86 \text{ m})^2 \quad \text{for anomaly degree variance model } c \end{array}\right\} \tag{4-35}$$

3) Relative truncation error

The error of geoidal height difference between two points P and Q is written as

$$\delta\Delta N_{PQ}=\delta(N_Q-N_P)=\delta N_Q-\delta N_P,$$

and using (4-24) the mean square value of it is given by

$$\sigma^2_{\delta\Delta N}(\Theta, L, \psi_0)=M\{\delta\Delta N^2_{PQ}\}$$
$$=2\,[C_{\delta N}(0, L, \psi_0)-C_{\delta N}(\Theta, L, \psi_0)] \tag{4-36}$$

(Ganeko, 1977). Inserting (4-26) and (4-27) into (4-36), we obtain

$$\sigma^2_{\delta\Delta N}(\Theta, L, \psi_0)=2\left(\frac{R}{2G}\right)^2\sum_{l=L}^{\infty}Q_l^2(\psi_0)\sigma_l^2(\Delta g)[1-P_l(\cos\Theta)]. \tag{4-37}$$

(4-37) can be used to evaluate the error in geoidal height difference between two points separated by an angular distance Θ when the geoidal heights at both points are computed under the same data conditions. The error defined by (4-37) is called "relative truncation error" in this paper. It may be natural that the relative truncation error (4-37) amounts to twice the point truncation error (4-27) when two points are separated far enough each other.

Ganeko (1977) calculated (4-37) by adopting anomaly degree variance model *b*, and gave Figure 32a and Figure 32b. We find out some rules concerning relative truncation errors from his results. When the distance between two points is one sixth or one seventh of wave-length λ_{min} which corresponds to the highest degree of the gravity data, i.e. surface gravities or satellite-derived gravity anomalies outside the cap area, the relative truncation error amounts to the same quantity as the point truncation error. When the distance is less than the critical distance, the relative truncation error is smaller than the point truncation error, and when the distance is sufficiently larger than λ_{min}, the square relative truncation error amounts to twice the square point truncation error. By using the notations of (4-27) and (4-37), the above rules are summarized as follows:

$$\sigma^2_{\delta\Delta N}(0, L, \psi_0)=0, \qquad \Theta=0, \tag{4-38a}$$

$$\sigma^2_{\delta\Delta N}(\Theta, L, \psi_0)<\sigma^2_{\delta N}(L, \psi_0), \qquad \Theta<\frac{60^\circ}{L}, \tag{4-38b}$$

$$\sigma^2_{\delta\Delta N}(\Theta, L, \psi_0)\approx\sigma^2_{\delta N}(L, \psi_0), \qquad \Theta\approx\frac{60^\circ}{L}, \tag{4-38c}$$

$$\sigma^2_{\delta\Delta N}(\Theta, L, \psi_0)\approx 2\sigma^2_{\delta N}(L, \psi_0), \qquad \Theta>1.5\frac{60^\circ}{L}. \tag{4-38d}$$

We consider the case that θ° block mean gravity anomalies are available on the whole surface of the earth. Then we know the gravity anomaly field up to degree $L=180^\circ/\theta^\circ$. According to (4-38c), when the distance between two points is $\theta/3$, i.e. $\Theta=\theta/3$, the relative truncation error is as large as the point truncation error. Therefore, the geoidal heights computed at every θ° mesh point on the basis of θ° block mean gravtiy anomalies commit relative truncation errors in the geoidal height difference between neighbouring mesh points which are larger than point truncation errors at each mesh point.

Let us apply the rules of (4-38) to the data conditins of (4-31). On the analogy of (4-30) and (4-32), a relative truncation error is estimated by

$$\sigma^2_{\delta\Delta N}=\sigma^2_{\delta\Delta N}(\Theta, 361, 0)+\sigma^2_{\delta\Delta N}(\Theta, 181, 5^\circ)+\sigma^2_{\delta\Delta N}(\Theta, 23, 20^\circ)$$
$$-\sigma^2_{\delta\Delta N}(\Theta, 361, 5^\circ)-\sigma^2_{\delta\Delta N}(\Theta, 181, 20^\circ)-\sigma^2_{\delta\Delta N}(\Theta, 361, 20^\circ), \tag{4-39}$$

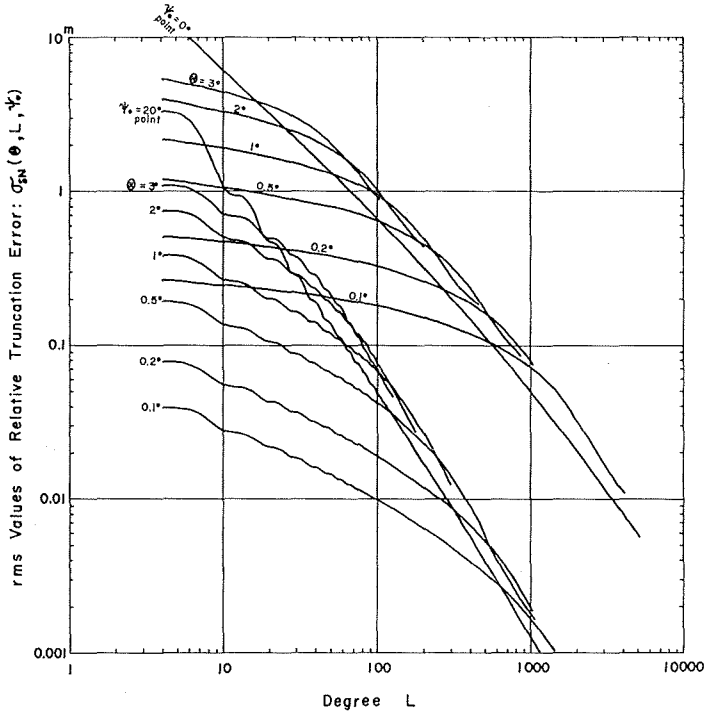

Figure 32a Relative truncation errors for $\psi_0=0°$ and 20° based on the anomaly degree variance model *b*.

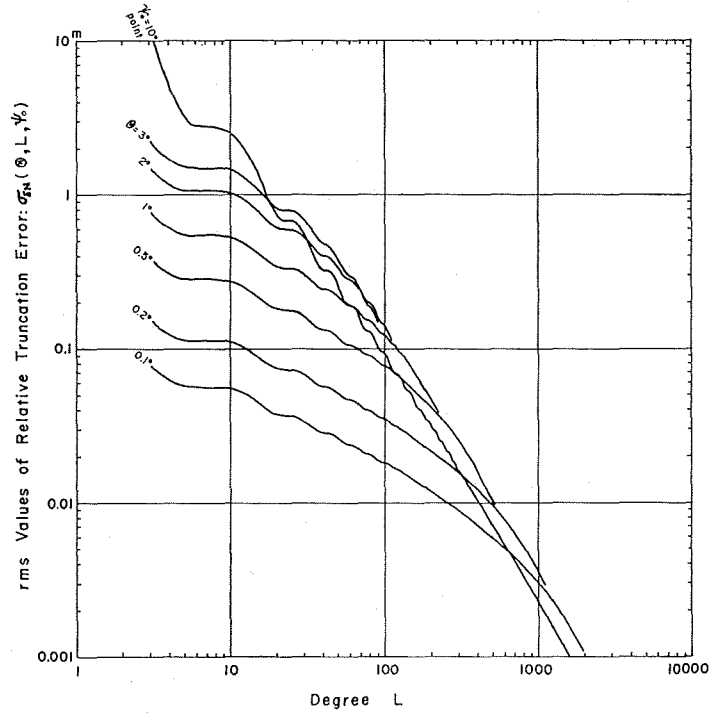

Figure 32b Relative truncation errors errors for $\psi_0=10°$ based on the anomaly degree variance model *b*.

and the critical distances of (4-38c) corresponding to each L in (4-39) are

$$\left.\begin{aligned}\Theta_1&=60^\circ/361=0.17^\circ,\\ \Theta_2&=60^\circ/181=0.33^\circ,\\ \Theta_3&=60^\circ/23=2.61^\circ.\end{aligned}\right\} \tag{4-40}$$

When $\Theta>1^\circ$ ($\approx$100 km), using (4-38) and (4-40), equation (4-39) is reduced to

$$\begin{aligned}\sigma^2_{\delta\Delta N}=&2\sigma^2_{N\delta}(361,0)+2\sigma^2_{\delta N}(181,5^\circ)+\sigma^2_{\delta\Delta N}(\Theta,23,20^\circ)\\ &-2\sigma^2_{\delta N}(361,5^\circ)-2\sigma^2_{\delta N}(181,20^\circ)-2\sigma^2_{\delta N}(361,20^\circ),\end{aligned} \tag{4-41}$$

and when $\Theta>4^\circ$, equation (4-39) is simply reduced to

$$\sigma^2_{\delta\Delta N}=2\sigma^2_{\delta N}. \tag{4-42}$$

Thus the relative truncation errors of the gravimetric geoid computed under the data conditions of (4-31) are estimated as shown in Table 3 on the basis of the anomaly degree variance model b given in Figure 32a (Table 4). When we compute geoidal heights under the data conditions of (4-34), a relative truncation error is estimated by

$$\begin{aligned}\sigma^2_{\delta\Delta N}=&\sigma^2_{\delta\Delta N}(\Theta,181,0)+\sigma^2_{\delta\Delta N}(\Theta,23,20^\circ)\\ &-\sigma^2_{\delta\Delta N}(\Theta,181,20^\circ).\end{aligned} \tag{4-43}$$

The estimated relative truncation errors are also listed in the third column of Table 3.

4) A numerical test of the truncation error

JHDGF-1 gravity data file includes $10'\times10'$ block mean gravity anomalies in some regions, and a $10'\times10'$ detailed gravimetric geoid is computed. Figure 33 is obtained under the data conditions: $10'\times10'$ block mean gravity anomalies for $\psi\leq2^\circ$; $30'\times30'$ block means for $2^\circ<\psi\leq10^\circ$; and GEM-8 geopotential model (Wagner et al., 1976, complete up to degree and order 25) for $\psi>10^\circ$. we see more detailed structures of geoid undulation than the $30'\times30'$ geoid previously shown in Figure 8. The geoidal dent seen from off Ensyu Nada toward Suruga Bay is due to the negative gravity anomalies along Nankai Trough (e.g. Segawa and Bowin, 1976). The contour lines change their directions as seen at the central part of Boso Peninsula. This is caused by the regional positive gravity anomalies at the tip of the peninsula. A $30'\times30'$ gravimetric geoid is computed in the same region of Figure 33 based on the data conditions: $30'\times30'$ block mean gravity anomalies for $\psi\leq10^\circ$ and GEM-8 geopotential model for $\psi>10^\circ$. The differences detween the $10'\times10'$ geoid and the $30'\times30'$ geoid are shown in Figure 34. Differences exceeding one meter occur in some regions. The numerical differences are also computed at $30'\times30'$ mesh points located in the region of Figure 34. The mean difference is -9 cm ($10'\times10'$ geoid$-30'\times30'$ geoid) and the r.m.s. difference is 54 cm. On the other hand, we can estimate the difference between two kinds of geoid by using the truncation error estimation technique described formerly. If we adopt the anomaly degree variance model c to be fitted to the gravity anomaly field around the region concerned, from Figure 30b, we obtain truncation error difference between two geoids as around 30 cm. This value is slightly smaller than the actual r.m.s. difference, but acceptable taking the rough gravity anomaly over the concerning region into consideration.

Table 3 Relative truncation errors involved in the computed gravimetric geoid (Figure 8) estimated on the basis of the anomaly degree variance model b

Distance Θ	Data condition (4-31)	Data condition (4-34)
0°	0 m	0 m
1	0.31	0.54
2	0.43	0.62
3	0.54	0.70
5	0.68	0.82

Table 4 Numerical values of a relative truncation error term $\sigma_{\delta AN}(\Theta, 23, 20°)$ based on the anomaly degree variance model b

Distance Θ	0.1°	0.2	0.5	1.0	2.0	3.0
$\sigma_{\delta AN}$	0.02 m	0.04	0.10	0.19	0.36	0.48

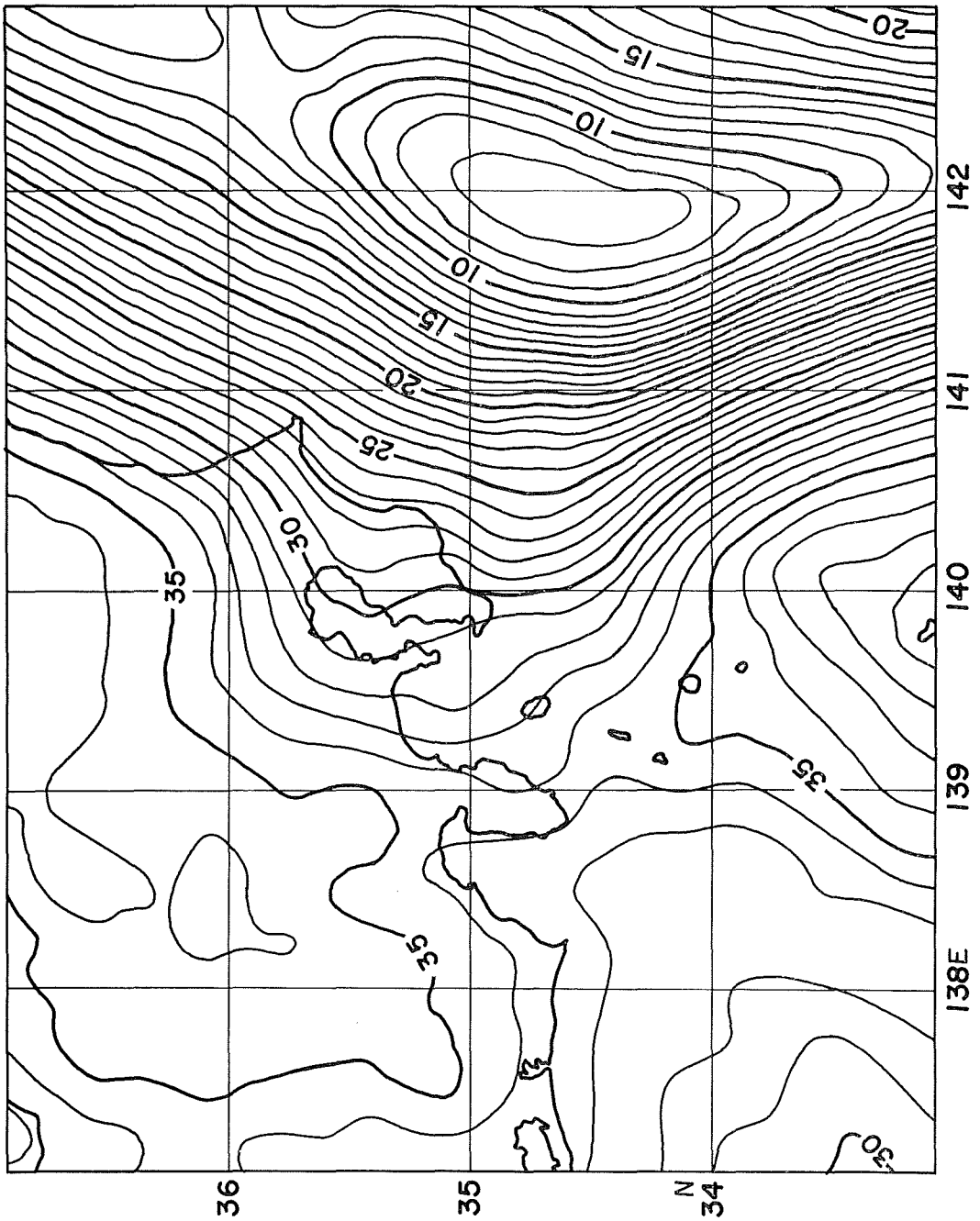

Figure 33 10′×10′ detailed gravimetric geoid computed in combination with GEM-8 geopotential coefficient set and 10′×10′ block surface mean gravity anomalies Cap size: $\psi_0=10°$, $a=6378145$m, $f=1/298.255$. Contour interval: 1 m.

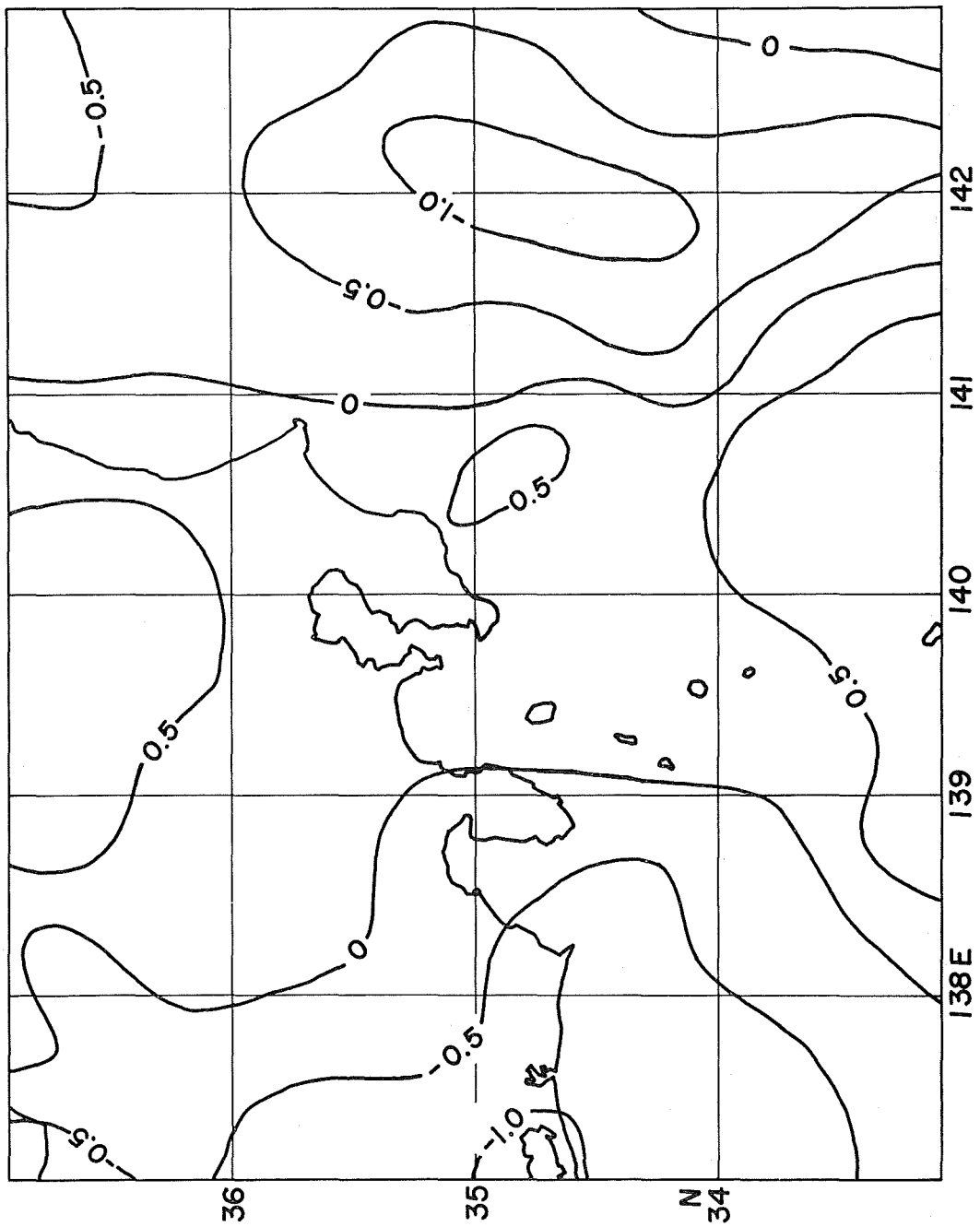

Figure 34 Differences between 10′×10′ geoid and 30′×30′ geoid. Contour interval: 0.5 m.

(3) Error Propagation from Geopotential Coefficient Errors

1) Error covariance

The satellite-derived geopotential field contributes to geoidal height computation from outside the cap area as much as equation (2-20c), and the contribution is evaluated by using Molodenskii's truncation function Q_l as follows (Molodenskii et al., 1962, p. 147):

$$N_{out}=\frac{R}{2G}\sum_{l=2}^{L}Q_l(\phi_0)\Delta g_l\,, \tag{4-44}$$

where R is the average radius of the earth, G the average gravity over the whole earth, L the maximum complete degree of a satellite-derived geopotential coefficient set, and ϕ_0 the radius of the cap area. (4-44) has a similar form to (4-24) which was used to estimate the truncation errors. Δg_l, l—th degree surface harmonics of satellite-derived gravity anomaly, is evaluated from the satellite-derived geopotential coefficients as follows:

$$\Delta g_l=G(l-1)\sum_{m=0}^{l}[\bar{C}^{*}_{ml}\bar{R}_{lm}+\bar{D}_{lm}\bar{S}_{lm}] \tag{4-45}$$

which has the same notation as (2-16). From (4-44), we write the error of N_{out} caused by geopotential coefficient errors as

$$\delta N_{out}=\frac{R}{2G}\sum_{l=0}^{L}Q_l(\phi_0)\delta\Delta g_l\,, \tag{4-46}$$

where $\delta\Delta g_l$ is the error of l—th degree harmonics due to geopotential coefficient errors $\delta\bar{C}^{*}_{lm}$ and $\delta\bar{D}_{lm}$:

$$\delta\Delta g_l=G(l-1)\sum_{m=0}^{l}[\delta\bar{C}^{*}_{lm}\bar{R}_{lm}+\delta\bar{D}_{lm}\bar{S}_{lm}]. \tag{4-47}$$

We define the covariance of δN_{out} by

$$\begin{aligned}K_{\delta N}(\Theta,\phi_0)&=M\{\delta N^{P}_{out}\delta N^{Q}_{out}\}\\&=\left(\frac{R}{2G}\right)^2\sum_{l=2}^{L}\sum_{l'=2}^{L}Q_l(\phi_0)Q_{l'}(\phi_0)M\{\delta\Delta g_l(P)\delta\Delta g_{l'}(Q)\}\,,\end{aligned} \tag{4-48}$$

where Θ is the angular distance between points P and Q on the surface of the earth. In the same way as we have obtained (4-26) from (4-25), (4-48) is reduced to

$$K_{\delta N}(\Theta,\phi_0)=\left(\frac{R}{2G}\right)^2\sum_{l=2}^{L}Q_l^2(\phi_0)\sigma_l^2(\delta\Delta g_s)P_l(\cos\Theta). \tag{4-49}$$

$\sigma_l^2(\delta\Delta g_s)$ is the error degree variance of satellite-derived gravity anomaly, which is evaluated from the geopotential coefficient errors:

$$\sigma_l^2(\delta\Delta g_s)=G^2(l-1)^2\sum_{m=0}^{l}(\delta\bar{C}^{*2}_{lm}+\delta\bar{D}^{2}_{lm}). \tag{4-50}$$

Here subscript s indicates "satellite-derived" again.

2) Point undulation error

The mean square error of geoidal height due to geopotential coefficient errors at an arbitrary point is given by putting $\Theta=0$ in (4-49), and it is written as

$$\varepsilon^2_{\delta N}(\phi_0)\equiv K_{\delta N}(0,\phi_0)=\left(\frac{R}{2G}\right)^2\sum_{l=2}^{L}Q_l^2(\phi_0)\,\sigma_l^2(\delta\Delta g_s). \tag{4-51}$$

To evaluate the above equation, we have to know the error degree variances (4-50), i.e. geopotential coefficient errors $\delta\bar{C}^{*}_{lm}$ and $\delta\bar{D}_{lm}$. It is not necessarily easy to get the geopotential coefficient errors actually. Some geopotential coefficient sets are accompanied with estimated errors of the coefficients. We can define % error of the coefficients by

$$(\%\ \text{error})_l=\left\{\frac{\sum_{m=0}^{l}(\delta\bar{C}_{lm}^{2}+\delta\bar{D}_{lm}^{2})}{\sum_{m=0}^{l}(\bar{C}_{lm}^{2}+\bar{D}_{lm}^{2})}\right\}^{\frac{1}{2}}\times 100 \tag{4-52}$$

which was used by Rapp and Rummel (1975). Figure 35 shows examples of % errors produced from GEM-8 and GEM-10 geopotential models. We see some accuracy improvements of the coefficients in GEM-10 model. The fact that % errors around degree 20 are almost 100 % or more shows that coefficients at high degrees were poorly determined, but not that those coefficients are meaningless. Another method of evaluating the accuracy of coefficients was adopted by Rapp (1973) and Rapp and Rummel (1975), which estimate coefficient errors from two different geopotential models, A and B for example. In this case coefficient errors are calculated by

$$\left.\begin{aligned}\left|\delta\bar{C}_{lm}\right|&=\frac{1}{\sqrt{2}}\left|\bar{C}_{lm}^{A}-\bar{C}_{lm}^{B}\right|,\\ \left|\delta\bar{D}_{lm}\right|&=\frac{1}{\sqrt{2}}\left|\bar{D}_{lm}^{A}-\bar{D}_{lm}^{B}\right|.\end{aligned}\right\} \tag{4-53}$$

Table 5 gives error degree variances derived from coefficient errors in geopotential models GEM-8 and GEM-10 and those evaluated based on (4-53) from coeffiicient differences between GEM-8 model and SAO-SE4. 3 model (Gaposchkin, 1976). The lowermost line in Table 5 indicates commission errors of gravity anomaly computed by $[\sum\sigma_l^2(\delta\Delta g_s)]^{\frac{1}{2}}$ on the basis of each error degree variance set.

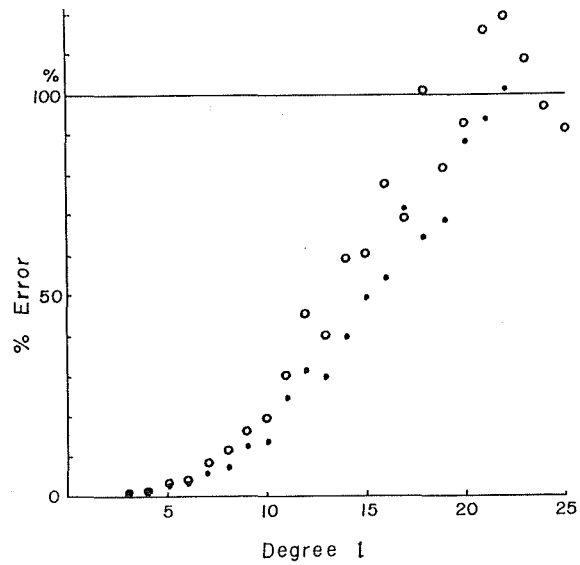

Figure 35 Percent errors of geopotential coefficients. Open and full circles are for GEM-8 and GEM-10 models, respectively.

Table 5 Error degree variances based on satellite-derived geopotential coefficient sets

Degree	GEM-8 -SAO-SE4. 3	GEM-8	GEM-10
	mGal²	mGal²	mGal²
3	0. 024	0. 003	0. 001
4	0. 067	0. 004	0. 001
5	0. 444	0. 028	0. 013
6	0. 355	0. 033	0. 014
7	0. 710	0. 123	0. 062
8	0. 916	0. 132	0. 057
9	1. 594	0. 308	0. 166
10	1. 342	0. 354	0. 169
11	2. 561	0. 681	0. 382
12	2. 095	0. 675	0. 349
13	1. 669	1. 042	0. 534
14	2. 814	1. 152	0. 527
15	2. 547	1. 645	0. 732
16	1. 712	2. 119	0. 762
17	2. 394	3. 296	1. 074
18	1. 970	5. 071	1. 283
19	2. 150	6. 277	1. 322
20	3. 001	7. 265	1. 553
21	2. 877	7. 960	1. 584
22	2. 946	8. 357	1. 740
23	2. 626	8. 374	
24	3. 147	8. 168	
	6. 3 mGal	8. 3 mGal	3. 5 mGal

When we know the errors of geopotential coefficients, a point undulation error is obtained by (4-51). The evaluated undulation errors are shown in Table 6 for cap radii $\psi_0=0$, 10°, 20° and 30°. When $\psi_0=0$, the tabulated undulation errors express the accuracies of satellite-derived geoid undulations in combination with omission errors due to the omissoin of higher degree terms of geoid undulation than those included in satellite-derived geopotential models. The omission errors have already discussed in detail in the previous section. Such omission error given as $\sigma_{\delta N}(L, 0)$ (see (4-27)) is read as 3 or 4 meters from Figure 30 in the case $L=20$. Then we can estimate the accuracy of the satellite-derived geoid undulations by

$$m^2=\varepsilon^2_{\delta N}(0)+\sigma^2_{\delta N}(L, 0).$$

As we see in Table 6, under the data condition (4-31) or (4-34) adopted in Chapter 3 to compute a gravimetric geoid, the mean point undulation error amounts to 0. 31 m due to uncertainties of geopotential coefficients of GEM-10 model.

3) Relative undulation error

The error of the difference between N_{out} components at points P and Q is written by

$$\delta\Delta N_{out}=\delta(N^Q_{out}-N^P_{out})=\delta N^Q_{out}-\delta N^P_{out},$$

and its mean square value is sxpressed by using the undulation error covariance (4-49) as follows:

$$\begin{aligned}\varepsilon^2_{\delta\Delta N}(\Theta, \psi_0)&=M\{\delta\Delta N^2_{out}\}\\&=2[K_{\delta N}(0, \psi_0)-K_{\delta N}(\Theta, \psi_0)],\end{aligned}\qquad (4\text{-}54)$$

Table 6 Point geoidal height errors due to errors of geopotential coefficients

Cap size ψ_0	GEM-8 −SAO-SE 4.3	GEM-8	GEM-10
°	m	m	m
0	3.46	3.02	1.53
10	1.26	0.95	0.59
20	0.82	0.52	0.31
30	0.44	0.27	0.15

where Θ is the angular distance between P and Q. Inserting the expression of (4-49) into (4-54), we obtain

$$\varepsilon^2_{\delta AN}(\Theta, \psi_0) = 2\left(\frac{R}{2G}\right)^2 \sum_{l=2}^{L} Q_l^2(\psi_0)\sigma_l^2(\delta Ag_s)\,[1-P_l(\cos\Theta)]. \tag{4-55}$$

Note that (4-55) is very similar to (4-37) which is obtained for the estimation of relative truncation error. Although (4-55) has been already discussed by Christodoulidis (1976) and Ganeko (1977), we here evaluate (4-55) by using error degree variances shown in Table 5. The obtained relative undulation errors due to geopotential coefficient errors are given in Table 7. We find that the relative undulation errors up to distance $\Theta=5°$ ($\approx$500 km) are less than the point undulation errors. As seen in Table 6 and Table 7, the GEM-10 model results in the smallest undulation errors.

Table 7 Relative geoidal height errors due to errors of geopotential coefficients

	GEM-8−SAO-SE4.3			GEM-8			GEM-10		
Cap size	ψ_0=10°	20°	30°	10°	20°	30°	10°	20°	30°
Distance Θ	m	m	m	m	m	m	m	m	m
0.2°	0.04	0.02	0.01	0.04	0.02	0.01	0.02	0.01	0.005
0.4	0.08	0.05	0.02	0.08	0.04	0.02	0.04	0.02	0.01
0.6	0.12	0.07	0.03	0.11	0.06	0.04	0.07	0.03	0.02
0.8	0.16	0.09	0.04	0.15	0.08	0.05	0.09	0.04	0.02
1.0	0.20	0.12	0.06	0.19	0.10	0.06	0.11	0.06	0.03
2.0	0.40	0.23	0.11	0.38	0.20	0.12	0.22	0.11	0.05
3.0	0.59	0.34	0.16	0.56	0.30	0.17	0.32	0.16	0.08
4.0	0.78	0.45	0.22	0.72	0.38	0.22	0.42	0.21	0.10
5.0	0.95	0.55	0.26	0.89	0.47	0.27	0.51	0.26	0.13
6.0	1.12	0.64	0.31	1.03	0.54	0.31	0.60	0.30	0.15
7.0	1.27	0.73	0.35	1.16	0.61	0.34	0.67	0.34	0.17
8.0	1.40	0.81	0.39	1.26	0.66	0.37	0.74	0.38	0.18
9.0	1.52	0.87	0.42	1.35	0.71	0.39	0.80	0.40	0.19
10.0	1.63	0.93	0.45	1.42	0.74	0.40	0.84	0.43	0.20
Point error	1.26	0.82	0.44	0.95	0.52	0.27	0.59	0.31	0.15

(4) Error Propagation from Terrestrial Gravity Data Errors

1) Point undulation error

When terrestrial gravity data are utilized for geoidal height computation through (2-20b), a geoidal height error can be written in the form:

$$\delta N_{in}=\frac{R}{4\pi G}\iint_{cap}\delta\Delta g\, S(\phi)\,d\sigma, \tag{4-56}$$

where $\delta\Delta g$ is error of terrestrial gravity anomaly. When the terretrial gravities are given in the form of block means, (4-56) is rewritten as

$$\delta N_{in}=\frac{R}{4\pi G}\sum_{i=1}^{k}\delta\overline{\Delta g}_i\cdot q_i, \tag{4-57}$$

where $\delta\overline{\Delta g}_i$ is the error of the mean gravity anomaly over block σ_i. q_i is given by (3-3), and k is the number of blocks included in a cap area with radius ϕ_0. The mean square value of (4-57) is given by

$$\begin{aligned} m_{\delta N}^2(\phi_0)&=M\{\delta N_{in}^2\}\\ &=\left(\frac{R}{4\pi G}\right)^2\sum_{i=1}^{k}\sum_{j=1}^{k}M\{\delta\overline{\Delta g}_i\delta\overline{\Delta g}_j\}\,q_i\,q_j=\left(\frac{R}{4\pi G}\right)^2\sum_{i=1}^{k}\sum_{j=1}^{k}C_\delta(i,j)q_i\,q_j, \end{aligned} \tag{4-58}$$

where $C_\delta(i,j)$ is the error covariance of block mean gravity anomalies assuming to be a function of the distance between blocks σ_i and σ_j.

We consider first a specific case of the error covariance (called "Case A"):

$$\left.\begin{aligned} C_\delta(i,j)&=m_\theta^2 \quad \text{for } i=j,\\ &=0 \quad \text{for } i\neq j, \end{aligned}\right\}\ \text{Case A}, \tag{4-59}$$

which means that the errors of block mean gravity anomalies are completely independent of each other. m_θ^2 is the mean square error of θ° block mean gravity anomalies. When the error covariance satisfies (4-59), (4-58) is reduced to

$$m_{\delta N}^2(\phi_0)=\left(\frac{R}{4\pi G}\right)^2\sum_{i=1}^{k}m_\theta^2\,q_i^2. \tag{4-60}$$

In the evaluation of (4-60), we take a square cap area such as shown in Figure 36, and the square cap area is extended by adding square rings of θ° width. The evaluated undulation errors for block sizes $\theta=10'$, $30'$ and 1° are shown in Figure 37, and some of numerical values are given in the columns labeled as "Case A" in Table 8. m_θ has been taken to be 1 mGal for all block sizes. As we can read from Figure 37, the undulation errors increase steadily as cap size becomes larger, but they increase little even when cap size becomes larger than 10°. That may be due to the facts that the correlation distance of gravity anomaly data errors is short under the assumption of (4-59) and that distant short wave-length variations of gravity anomaly contribute little to the geoidal height computations as investigated in section 3-(2). We can derive a simple formula for estimating undulation errors due to terrestrial gravity errors when the cap is large enough, such as

$$m_{\delta N}(\text{cm})\fallingdotseq 12\times m_\theta(\text{mGal})\times\theta(\text{degree}).$$

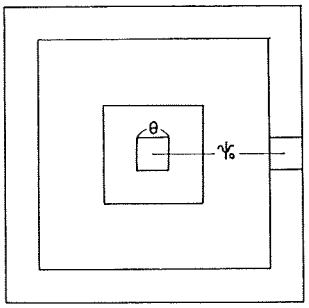

Figure 36 Square cap area.

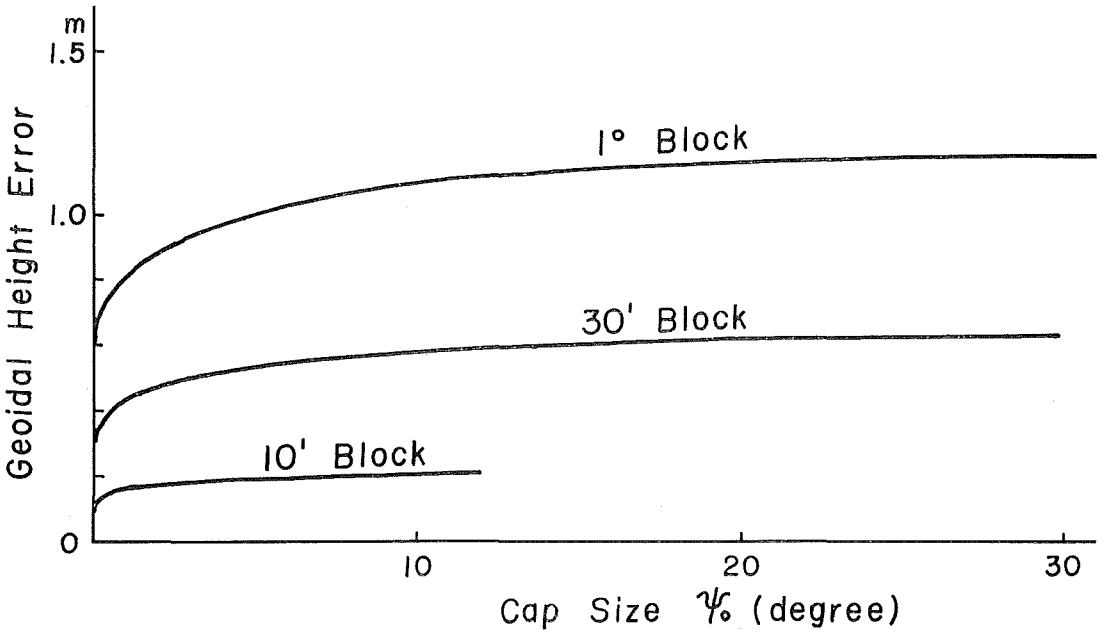

Figure 37 Point geoidal height errors due to errors of block mean gravity anomalies. For error covariance Case A, and $m_0^2=1$ mGal^2.

Table 8 Point geoidal height errors due to errors of block mean gravity anomalies ($m_\theta^2=1\,\mathrm{mGal}^2$)

Block size	$\theta=10'$			30′			1°		
Error covariance	Case A	Case B	Case C	A	B	C	A	B	C
Cap size ϕ_0									
β_0	m	m	m	m	m	m	m	m	m
	0.011			0.032			0.064		
2	0.018	0.024	0.040	0.048	0.065	0.092	0.089	0.120	0.189
5	0.020	0.027	0.045	0.054	0.074	0.122	0.101	0.139	0.226
10	0.021	0.029	0.049	0.059	0.081	0.135	0.110	0.152	0.252
20				0.062	0.085	0.144	0.117	0.162	0.270
30				0.062	0.086	0.145	0.118	0.163	0.274
35							0.118	0.163	0.274

Let us adopt another type of error covariance of gravity anomaly data instead of (4-59); i.e. an exponential type error covariance:

$$C_\delta(\psi)=m_\theta^2\exp(-D_\theta\psi),\quad D_\theta>0, \tag{4-61}$$

which has a long tail in the error correlation and was ever used by Christodoulidis (1976) to estimate the same kind of undulation error as treated in this section by a different method. Before applying (4-61) to (4-58), we rewrite (4-58) as follows:

$$m_{\delta N}^2(\psi_0)=\left(\frac{R}{4\pi G}\right)^2\left\{\sum_i{}'\sum_j{}' C_\delta(i,j)\,q_i\,q_j + 2q_p\sum_i{}' C_\delta(i,p)q_i + C_\delta(p,p)q_p^2\right\}, \tag{4-62}$$

where P is the center of block σ_P where computation of geoidal height is made, and $\sum'$ indicates the summation over all blocks in the cap area except for block σ_P. Since the correlation distance of gravity anomaly data errors is usually short, we approximately write the first term in the righthand side of (4-62) as

$$\sum_i{}'\sum_j{}' C_\delta(i,j)q_i\,q_j\fallingdotseq\sum_i{}' u^2\,q_j^2, \tag{4-63}$$

where

$$u^2=\sum_j{}' C_\delta(i,j). \tag{4-64}$$

It is noteworthy that (4-64) corresponds to the "error constant" introduced by Heiskanen and Moritz (1967, p. 273). Let the area of blocks be denoted by B, approximate (4-64) to

$$u^2=\sum_j{}' C_\delta(i,j)\fallingdotseq\frac{1}{B}\sum_j C_\delta(i,j)B\fallingdotseq\frac{1}{B}\iint_{cap} C_\delta(\psi_{ij})\,d\sigma, \tag{4-65}$$

and insert (4-61) into (4-65), then we obtain

$$\begin{aligned}Bu^2&\fallingdotseq m_\theta^2\int_{\alpha=0}^{2\pi}\int_{\psi=0}^{\pi}\exp(-D_\theta\psi)\sin\psi\,d\psi\,d\alpha\\&=2\pi m_\theta^2\frac{1}{D_\theta^2+1}\left[1+\exp(-D_\theta\pi)\right]\fallingdotseq 2\pi m_\theta^2/D_\theta^2.\end{aligned} \tag{4-66}$$

The last approximation in (4-66) is permissible because of short correlation distance of the gravity data errors. From (4-62), (4-63) and (4-66), we finally obtain

$$m_{\delta N}^2(\phi_0)=\left(\frac{R}{4\pi G}\right)^2\left[\frac{2\pi}{B}\frac{m_\theta^2}{D_\theta^2}\sum_i{}' q_i^2 + 2m_\theta^2 q_p\sum_i{}' \exp(-D_\theta\phi_{ip})q_i+m_\theta^2 q_p^2\right]. \tag{4-67}$$

We evaluate (4-67) for two cases of the parameter in the exponential error covariance, i.e.,

$$\left.\begin{aligned} &D_\theta=1/\beta_0\,,\quad \beta_0=\sqrt{B/\pi}: \text{ Case B,}\\ &D_\theta=1/\theta \qquad\qquad\quad : \text{ Case C,}\end{aligned}\right\} \tag{4-68}$$

where β_0 is the radius of a circular block whose area is equal to the area of θ° square block. Figure 38 and Table 8 include the results for block sizes $\theta=10'$, $30'$ and 1° when $m_\theta=1$ mGal. Case C gives a longer error correlation distance than Case B, so that Case C naturally results in larger undulation errors than Case B and, of course, than Case A.

2) Relative undulation error

The error of geoidal height difference due to errors of terrestrial gravity data is derived from (4-56) as follows:

$$\delta\Delta N=\delta\,(N_{in}^P-N_{in}^Q)=\frac{R}{4\pi G}\iint_{cap}\delta\Delta g\,[S(\phi_P)-S(\phi_Q)]\,d\sigma, \tag{4-69}$$

where ϕ_P is the angular distance between P and the surface element $d\sigma$, and ϕ_Q is the distance between Q and $d\sigma$. The cap area is taken to be large enough to include sufficient terrestrial data for computations of geoidal heights at both points P and Q (see Figure 39). If we rewrite (4-69) so as to make the equation fit the available terrestrial gravity data, we have

$$\delta\Delta N=\frac{R}{4\pi G}\sum_{i=1}^{k}\delta\bar{\Delta g}_i\,[q_{Pi}-q_{Qi}]. \tag{4-70}$$

The difinitions of q_{Pi} and q_{Qi} are derived from a generalized expression of q_{XY}

$$q_{XY}=\iint_{\sigma_Y} S(\phi_{Xy})\,d\sigma_y, \tag{4-71}$$

where ϕ_{Xy} is the angular distance between point X, the center of bloek σ_X, and the surface element $d\sigma_y$ in block σ_Y. Writing the block area as $B=\pi\beta_0^2$, we have approximate expressions of (4-71) as

$$\left.\begin{aligned} &q_{XX}=4B/\beta_0,\\ &q_{XY}=q_{YX}=S(\phi_{XY})\cdot B,\end{aligned}\right\} \tag{4-72}$$

where ϕ_{XY} is the angular distance between centers of blocks σ_X and σ_Y. Then we obtain from (4-70) and (4-72)

$$\delta\Delta N=\frac{R}{4\pi G}B\left\{\sum_i{}'\delta\bar{\Delta g}_i\,[S(\phi_{Pi})-S(\phi_{Qi})] + (\delta\bar{\Delta g}_P-\delta\bar{\Delta g}_Q)\left[\frac{4}{\beta_0}-S(\phi_{PQ})\right]\right\}. \tag{4-73}$$

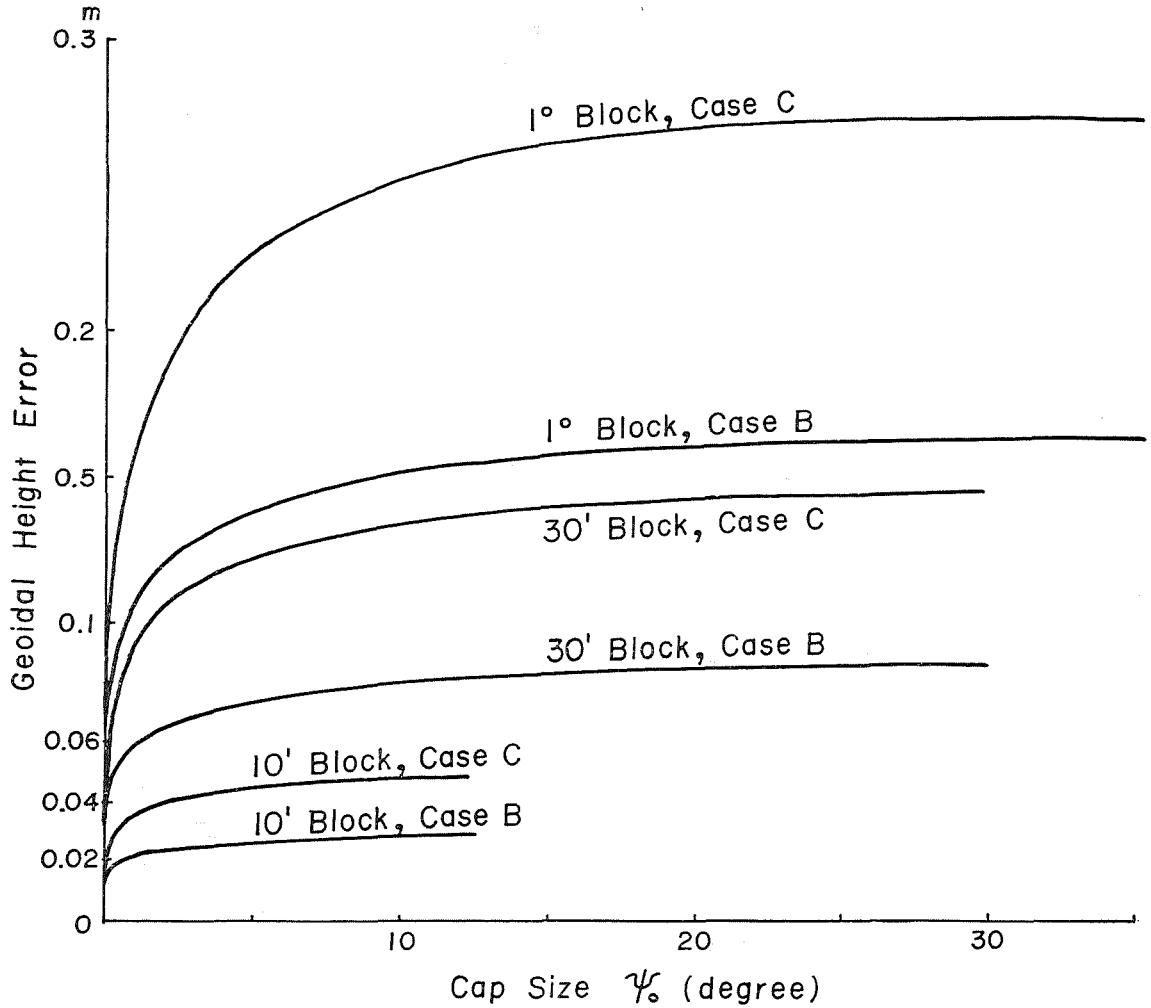

Figure 38 Point geoidal height errors due to errors of block mean gravity anomalies. For error covariance models Case B and C, and $m_0^2=1$ mGal^2.

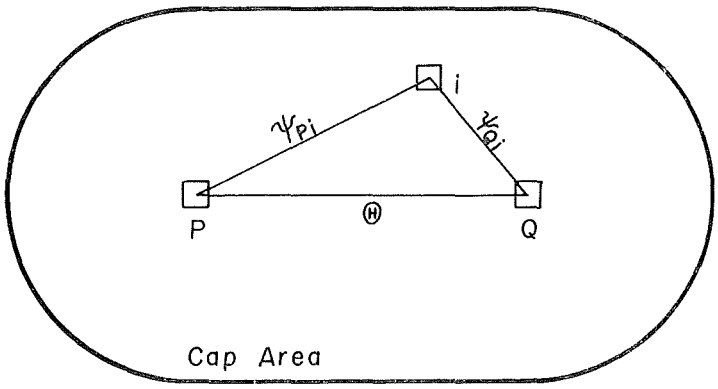

Figure 39 Common cap area for the computation of a geoidal height difference.

The summation $\sum'$ does not include $i=P$ and $i=Q$. Setting $A=RB/4\pi G$, the mean square value of (4-73) can be written in the form:

$$\begin{aligned} m^2_{\delta\Delta N}(\Theta) &= M\{\delta\Delta N^2\} \\ &= A^2\sum_i{}' \sum_j{}' M\{\delta\overline{\Delta g}_i\,\delta\overline{\Delta g}_j\}\,[S(\psi_{Pi})-S(\psi_{Qi})]\,[S(\psi_{Pj})-S(\psi_{Qj})] \\ &+2A^2\sum_i{}' M\left\{\delta\overline{\Delta g}_i\,(\delta\overline{\Delta g}_P-\delta\overline{\Delta g}_Q)\right\}\left[\frac{4}{\beta_0}-S(\Theta)\right] \\ &+A^2M\left\{(\delta\overline{\Delta g}_P-\delta\overline{\Delta g}_Q)^2\right\}\left[\frac{4}{\beta_0}-S(\Theta)\right]^2, \end{aligned} \tag{4-74}$$

where Θ is the distance between P and Q. Being assumed that the error covariance has a short correlation distance, (4-74) is reduced to

$$\begin{aligned} m^2_{\delta\Delta N}(\Theta) &= A^2\sum_i{}' \left[\sum_j{}' C_\delta(\psi_{ij})\right][S(\psi_{Pi})-S(\psi_{Qi})]^2 \\ &+2A^2\sum_i{}' \left[C_\delta(\psi_{Pi})-C_\delta(\psi_{Qi})\right]\left[\frac{4}{\beta_0}-S(\Theta)\right] \\ &+2A^2\left[C_\delta(0)-C_\delta(\Theta)\right]\left[\frac{4}{\beta_0}-S(\Theta)\right]^2. \end{aligned} \tag{4-75}$$

Note that the second term of the righthand side of (4-75) vanishes because of the symmetrical expressions at P and Q. Therefore, we can evaluate the relative undulation errors by a sum of the following two terms:

$$\left.\begin{aligned} I_1 &= A^2\sum_i{}' \left[\sum_j{}' C_\delta(\psi_{ij})\right][S(\psi_{Pi})-S(\psi_{Qi})]^2, \\ I_2 &= 2A^2\left[C_\delta(0)-C_\delta(\Theta)\right]\left[\frac{4}{\beta_0}-S(\Theta)\right]^2. \end{aligned}\right\} \tag{4-76}$$

Using (4-65) in I_1, i.e. $u^2=m_\theta^2$ for the error covariance Case A (see (4-59)) and $u^2=2\pi m_\theta^2/BD_\theta^2$ for the exponential type error covariances Cases B and C (see (4-68)), we evaluate (4-76) for block sizes $\theta=10'$, $30'$ and $1°$. And we take the common cap area (Fig. 39) to be large enough, i. e. the boundary of the cap area being located farther than $30°$ from both points P and Q. Some of evaluated results are shown in Table 9. The root mean square error m_θ is assumed to be 1 mGal in Table 9.

JHDGF-1 gravity file includes estimated errors of block mean gravity anomalies, and in these case we can compute a geoidal height error by

Table 9 Relative geoidal height errors due to errors of block mean gravity anomalies ($m_0^2=1\,\mathrm{mGal}^2$)

Block size	$\Theta=10'$			30′			1°		
Error covariance	Case A	Case B	Case C	A	B	C	A	B	C
Angular distance Θ °	m	m	m	m	m	m	m	m	m
1	0.018	0.021	0.031	0.042	0.046	0.058	0.067	0.066	0.076
2	0.020	0.025	0.038	0.050	0.058	0.082	0.085	0.092	0.118
3	0.021	0.027	0.042	0.055	0.065	0.096	0.095	0.107	0.148
5	0.023	0.029	0.047	0.060	0.073	0.113	0.107	0.126	0.186
10	0.025	0.033	0.054	0.068	0.086	0.138	0.125	0.154	0.240
15	0.027	0.035	0.058	0.074	0.094	0.153	0.136	0.171	0.275
20	0.028	0.037	0.062	0.078	0.100	0.165	0.145	0.185	0.301

$$m_1^2=\left(\frac{R}{4\pi G}\right)^2\sum_{i=1}^{k}\delta\bar{g}_i^2\,q_i^2 \tag{4-77}$$

from the given errors of block mean gravity anomalies under the assumption that the errors are independent of each other. From (4-77), m_1 is evaluated to be 0.8 to 1.0 meters in JHDGF-1 region under the data conditions of (4-31) and to be around 1.3 meters outside the JHDGF-1 region under the data conditions of (4-34). Then we assume the geoidal height error of one meter due to errors of terrestrial gravity data and also assume that all block mean gravity anomalies suffer the same amount of mean errors, written as m, independently. Under the data conditions of (4-31) and from Table 8, we can write

$$m_{\delta N}^2=m^2\,\{0.054^2+(0.117^2-0.101^2)\}=(1\text{ meter})^2.$$

The above equation yields $m=12.5$ mGal, and the value of m brings about a geoidal height error under the data conditions of (4-34) such as

$$m_{\delta N}^2=0.117^2\times 12.5^2=(1.46\text{ meter})^2. \tag{4-78}$$

Since the main contribution to the undulation error is made by $1^\circ\times1^\circ$ block data, we estimate a relative undulation error due to terrestrial gravity data errors included in the geoidal map obtained in Chapter 3 as follows:

$$\bar{m}_{\delta\Delta N}^2=m^2\times m_{\delta\Delta N}^2(\Theta,\,\theta=1^\circ).$$

From $m=12.5$ mGal and Table 9 for $\Theta=5^\circ$ ($\approx$500 km), we obtain

$$m_{\delta\Delta N}^2=0.107^2\times 12.5^2=(1.34\text{ meter})^2. \tag{4-79}$$

We should note here that it has been assumed that the error covariance satisfies the condition of Case A.

(5) Undulation Errors due to Neglection of Sea Surface Topography

1) Undulation errors due to sea gravity errors

Physical oceanographic theory predicts deviations of the mean sea surface from a equipotential surface (e. g. Lisitzin, 1974), and the deviations are computed from oceanographic data such as velocity of ocean currents and salinity and temperature of sea water. We call the deviations of the mean sea surface from a equipotential surface,

the geoid, "sea surface topography". Since the sea surface topographical heights are in order of one meter, they have been neglected in the theory of physical geodesy until recently. The recent developments in satellite altimetry have achieved an accuracy higher than one meter by Geos-3 satellite (e.g. Kearsley, 1977; Rapp, 1977), and a trial to achieve around 10 cm accuracy of altimeter observation has been made by SEASAT-1 satellite (NASA News, 78-77). The fact that the satellite altimetry provides us with the shape of sea surface with such a high accuracy forces the physical geodesy to enter a new age of 10 cm global geodesy. Therefore, it may be necessary to investigate the effects of sea surface topography on the computation of geoidal heights.

The gravity measurements at sea are generally made on the surface of the sea water, so that the measured gravities are not considered to be on a equipotential surface, i.e. on the geoid. We can apply the gravity reduction procedure (2-4) to sea gravities just as land gravities. Normal height H^* in (2-4) is almost equal to the sea surface topographical height t, and then gravity anomaly at sea is befined by

$$\Delta g = g_P - \gamma_0 + \frac{2\gamma_0}{a} t \,, \tag{4-80}$$

where g_P is real gravity on the sea surface, γ_0 the normal gravity on the reference ellipsoid and a the semi-major axis of the reference ellipsoid. In Chapter 3, we have used gravity data without the correction term concerning t. The geoidal height error due to the neglection of this term is estimated by

$$\delta N_t = \frac{R}{4\pi G} \iint_{\sigma} \alpha t \, S(\phi) \, d\sigma, \tag{4-81}$$

where $\alpha = 2\gamma_0/a$. Brennecke and Groten (1977) evaluated (4-81) by using a world-wide map of the sea surface topography by Lisitzin (1974). According to their results, the contribution from the long wave-length components of the sea surface topography, the components from degree 2 to degree 10 of the spherical harmonic expansion of the sea surface topography, is about 60 cm, and the contribution from the higher degree terms is as small as several centimeters. Since the effect of the long wave-length components of the sea surface topography is not negligible, we can check possible geoidal height errors due to the effect of the sea surface topography by using the computation method adopted in Chapter 3. The geoidal height error is evaluated as

$$\delta N_t = \frac{R}{4\pi G} \iint_{cap} \alpha t \, S(\phi) \, d\sigma. \tag{4-82}$$

In this case, we set t=constant ever the cap because of the long wave length characteristics of the sea surface topography, then we obtain

$$\delta N_t = \frac{R}{2G} \alpha t \, \Phi(\phi_0), \tag{4-83}$$

where

$$\Phi(\phi_0) = \int_0^{\phi_0} S(\phi) \sin\phi \, d\phi.$$

$\Phi(\phi_0)$ is easily evaluated from the definite integral of Stokes' function:

Table 10 Geoidal height errors due to neglection of sea surface topography (one meter topography over the cap area is assumed)

Cap size ϕ_0	5°	10°	15°	20°	25°	30°	35°
$\Phi(\phi_0)$	0.649	1.345	2.009	2.594	3.068	3.408	3.602
δN_t	m 0.20	0.42	0.62	0.80	0.95	1.05	1.11

$$\int_{\psi_1}^{\psi_2} S(\psi)\sin\psi\, d\psi=\left[-\cos\psi+\frac{7}{4}\cos^2\psi+2\sin\frac{\psi}{2}\left(\frac{3}{2}\cos\psi+\frac{1}{2}\right)\right.$$
$$\left.-\frac{3}{2}\sin^2\psi\, l_n\left(\sin\frac{\psi}{2}+\sin^2\frac{\psi}{2}\right)\right]_{\psi_1}^{\psi_2}$$

(Molodenskii et al., 1962, p. 168). Table 10 show δN_t for various cap sizes when t=1m. Under the data conditions used in Chapter 3 and from the feature of the sea surface topography around Japan (e.g. Sugimori, 1978), we can conclude that the geoidal height error of around 50 cm due to neglection of the sea surface topography possibly occurs, and that the error is a kind of systematic error in a small region because of the characteristics of the sea surface topography.

2) Undulation error due to land gravity errors

Every height system of land areas is based on the mean sea surface at certain tide stations. The mean sea surface at tide stations, of course, suffer sea surface topography, so that orthometric heights of the ground are not necessarily based on the geoid. In other words, heights systems suffer systematic errors as much as the sea surface topographic heights at the base tide stations. These systematic errors cause gravity reduction errors at land areas as much as at ocean areas and cause systematic geoidal height errors both at land and at ocean, especially at the transition areas from continent to ocean. The geoidal height errors may be in an order of errors shown in Table 10. These situation may be shown schematically by Figure 40, in which two height systems I and II are separated by the ocean lying between different height systems. The geopotential values on the mean sea surfaces at base tide stations T_1 and T_2 are not equal to each other due to the existence of the sea surface topography. We have to interrelate two height systems by knowing the potential difference or sea surface topographic heights over the ocean, and this kind of knowledges will make us possible to compute a more accurate gravimetric geoid, say a 10 cm geoid.

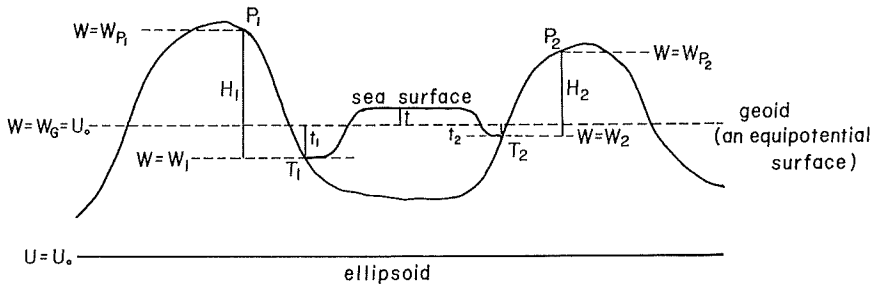

Figure 40 Sea surface topography and land height systems.

(6) Undulation Errors due to Theoretical Approximations

1) Spherical approximation

We have adopted the spherically approximated earth through this paper, as (2-1) and (2-3a) are based on the spherical approximation. Geoidal heights computed in the spherical approximation suffer errors of the same order as the flattening of the earth. The solution of the boundary value problem on a ellipsoidal reference surface was investigated by Molodenskii et al. (1962, p. 59), and the solution includes three times repetitions of integration. Lelgemann (1970) solved the problem in a simple form. We summarize his solution in a slightly changed form.

The disturbing potential on the reference ellipsoid is expanded in the series of the second eccentricity e'^2 $(\approx(a^2-b^2)/b^2)$ of the reference ellipsoid as follows:

$$T^*=T^\circ+e'^2\delta T+\cdots \tag{4-84}$$

(we use * on the shoulder for a quantity evaluated on the ellipsoid), where

$$T^\circ=\frac{R}{4\pi}\iint_\sigma \Delta g^* S(\psi)\,d\sigma. \tag{4-85}$$

The integration of (4-85) is carried out by using the geographical coordinates (φ, λ), then $d\sigma=\cos\varphi\, d\varphi\, d\lambda$. Δg^* is the gravity anomaly on the ellipsoid, which is derived from the ground level gravity anomaly, (2-4), by

$$\Delta g^*=\Delta g-h\frac{\partial \Delta g}{\partial h}+\cdots \tag{4-86}$$

(Moritz, 1971), where h is the height of the ground from the ellipsoid. The correction term δT is written as

$$\delta T=\frac{kM}{R}\sum_{l=2}^{\infty}\sum_{m=0}^{l}[\bar{A}_{lm}\bar{R}_{lm}+\bar{B}_{lm}\bar{S}_{lm}], \tag{4-87}$$

where $\bar{R}_{lm}$ and $\bar{S}_{lm}$ are fully normalized Laplace surface harmonics defined by (2-11), and coefficients $\bar{A}_{lm}$ and B_{lm} are derived from geopotential coe fficients in the spherical harmonic expansion of the disturbing potential:

$$T=\frac{kM}{R}\sum_{l=2}^{\infty}\sum_{m=0}^{l}[\bar{C}^*_{lm}\bar{R}_{lm}+\bar{D}_{lm}\bar{S}_{lm}]. \tag{4-88}$$

$\bar{A}_{lm}$ and $\bar{B}_{lm}$ are computed by the equations as follows:

$$\left.\begin{aligned}\bar{A}_{lm}&=\bar{C}^*_{l-2\,m}\bar{p}_{lm}+\bar{C}^*_{lm}\bar{q}_{lm}+\bar{C}^*_{l+2\,m}\bar{r}_{lm},\\ \bar{B}_{lm}&=\bar{D}_{l-2m}\bar{p}_{lm}+\bar{D}_{lm}\bar{q}_{lm}+\bar{D}_{l+2\,m}\bar{r}_{lm},\end{aligned}\right\} \tag{4-89}$$

where

$$\left.\begin{aligned}\bar{p}_{lm}&=\frac{3(l-3)}{2(l-1)(2l-1)}\left\{\frac{(l-m-1)(l-m)(l+m)(l+m-1)}{(2l-3)(2l+1)}\right\}^{\frac{1}{2}},\\ \bar{q}_{lm}&=\frac{-l^3+3lm^2+9l^2+10l+6m^2-9}{3(l-1)(2l+3)(2l-1)},\\ \bar{r}_{lm}&=\frac{3l+5}{2(l-1)(2l+3)}\left\{\frac{(l+m+2)(l+m+1)(l-m+2)(l-m+1)}{(2l+1)(2l+5)}\right\}^{\frac{1}{2}}.\end{aligned}\right\} \tag{4-90}$$

Note that we can use the disturbing potential (4-88) in the spherical approximation, because the expression is necessary only to evaluate a small correction term $e'^2\delta T$. Since we do not know the complete expression of the disturbing potential, we have to test the contribution of the terms of high degrees in (4-88) to $e'^2\delta T$. The correction of

geoidal height from $e'^2\delta T$ is

$$\delta N=\frac{e'^2\delta T}{G} \tag{4-91}$$

and the mean square value of (4-91) is written by using (4-87) in the form:

$$\varepsilon^2=M\{\delta N^2\}=e'^4R^4\sum_{l=2}^{\infty}\sum_{m=0}^{l}(\bar{A}_{lm}^{\ 2}+\bar{B}_{lm}^{\ 2}), \tag{4-92}$$

where the relation $G=kM/R^2$ has been used. Then the mean square contribution of the terms of higher degrees than L becomes

$$\varepsilon_L^2=e'^4R^4\sum_{l=L}^{\infty}\sum_{m=0}^{l}(\bar{A}_{lm}^{\ 2}+\bar{B}_{lm}^{\ 2}). \tag{4-93}$$

When $l\gg1$ in (4-90), we can set

$$max|\bar{p}_{lm}|\approx\frac{3}{8},\quad \max|\bar{q}_{lm}|\approx\frac{1}{6},\quad \max|\bar{r}_{lm}|\approx\frac{3}{8}$$

and the sizes of coefficients $\bar{A}_{lm}$ and $\bar{B}_{lm}$ are bounded as

$$\left.\begin{aligned}|\bar{A}_{lm}|&<\frac{3}{8}|\bar{C}^*_{l-2\,m}|+\frac{1}{6}|\bar{C}^*_{lm}|+\frac{3}{8}|\bar{C}^*_{l+2\,m}|\approx|\bar{C}^*_{lm}|,\\ |\bar{B}_{lm}|&<\frac{3}{8}|\bar{D}_{l-2\,m}|+\frac{1}{6}|\bar{D}_{lm}|+\frac{3}{8}|\bar{D}_{l+2\,m}|\approx|\bar{D}_{lm}|.\end{aligned}\right\} \tag{4-94}$$

From (4-93) and (4-94), we finally obtain

$$\varepsilon_L^2<e'^4R^4\sum_{l=L}^{\infty}\sum_{m=0}^{l}(\bar{C}^{*2}_{lm}+\bar{D}_{lm}^{\ 2}),\quad L\gg1. \tag{4-95}$$

If Kaula's rule of thumb, (4-11), is adopted to estimate the sizes of the geopotential coefficients at high degrees, (4-95) is reduced simply to

$$\varepsilon_L<\frac{0.43}{L}\ \text{(meter)} \tag{4-96}$$

in which we usually take $R=6371$ km and $e'^2=0.00674$. We thus conclude that (4-88) is safely replaced by a satellite-derived disturbing potential restricted within rather low degree terms. Lelgemann (1970) evaluated (4-92) by using actual geopotential coefficients of up to degree 14, and obtained r.m.s. value $\delta N=0.2$ m. He drew a world-wide distribution map of δN, and found that the contour paterns in the map are similar to the long wave-length components of the global geoid undulations. We read out δN around Japan as 20 to 30 cm from his map.

2) Neglection of higher order correction terms in Molodenskii's solution

We have neglected G_1 term in (2-3a) to compute a gravimetric geoid in Chapter 3. G_1 is evaluated at P on the ground by

$$G_1=\frac{R^2}{2\pi}\iint_{\sigma}\frac{h-h_p}{l_0^{\,3}}\,\Delta g\,d\sigma, \tag{4-97}$$

where h and h_p are heights at the surface element $d\sigma$ and at P, and

$$l_0=2R\sin\frac{\psi}{2},$$

in which ψ is the angular distance between $d\sigma$ and P. The gravity correction G_1 is not negligible because, for example, G_1 amounts to -34 mGals at the top of a conic mountain having the form $h(r)=H\cdot\exp(-r^2/4B^2)$, where $H=500$ m and $B=300$ m (Hagiwara, 1973). But the effect of G_1 term on geoidal height is small because G_1 behaves short

wave-length variations very similar to the short wave-length components of topographic relief (see Figure 4 of Hagiwara, 1972a). Therefore, we may conclude that the geoidal height errors included in the geoid obtained in Chapter 3 due to the neglection of G_1 are negligibly small, i.e. less than 10 cm.

The geoidal heights computed in Chapter 3 are actually height anomalies. Height anomalies in ocean areas are almost equal to geoidal heights, but not in land areas. The difference between geoidal height and height anomaly, which is given by (2-6), is estimated to be around a few tens centimeters at the mountainous region in the central part of Japan.

(7) Summary of Error Sources

We have investigated various error sources in the geoidal height computation, and the error sources are relisted below:

(a) omission of detailed structures of the gravity anomaly field;
(b) uncertenties of the satellite derived geopotential coefficients;
(c) terrestrial gravity data errors;
(d) omission of sea surface topography;
(e) spherical approximation in Stokes' integral;
(f) omission of higher correction terms in Molodenskii's solution.

The geoidal height error due to (a) largely depends on the behavior of the anomaly degree variances at high degrees, and the error decreases as the cap size becomes larger and as the sizes of blocks, by which mean gravity anomalies are given, becomes smaller. The recent developments of the satellite trackings have made the error source (b) less important. The main error source is still due to errors of the terrestrial gravity data caused by lack of density of gravity observations and lack of accuracy of sea gravity observations ever made. We have to make great efforts in avoiding the error source (c) to produce a more accurate geoid. The existence of the sea surface topography brings about a complicated problem in the definition of the geoid and in the gravity reduction procedures. We cannot neglect the sea surface topography (d) to compute an accurate geoid. The error sources (e) and (f) have almost been solved theoretically, and they should be taken into consideration in the computation of a 10 cm geoid.

In Table 11, we summarize the point undulation errors accompanied with the gravimetric geoid obtained in Chapter 3 under the data conditions of (4-31) and (4-34). The total error is based on the assumption that the error sources are independent of each other. We may conclude the accuracy of the gravimetric geoid (Figure 8) is around 1.5 m or, in other words, in a range of 1 m to 2 m except for N_0 term given by (2-9). N_0 term is in an order of ambiguity of the semimajor axis of the earth ellipsoid. The estimated errors of the gravimetric geoid are compatible with the comparison results between the gravimetric geoid and Geos-3 altimeter data (Table 1).

We have also investigated the error of geoidal height difference. This kind of error depends largely on the correlation distance of the error source. For the geoidal height difference over 500 km distance, we can summarize the errors due to various error sources as shown in Table 12. We find the total error of the geoidal height difference to

Table 11 Point geoidal height errors due to various error sources involved in the gravimetric geoid obtained in Chapter 3

Error source	Data condition (4-31)	Data condition (4-34)	Note
	m	m	
a	0.60	0.86	Anomaly degree variance model *c*
b	0.31	0.31	GEM-10 model
c	1.0+	1.5*	
d	0.5	0.5	From Table 10, estimated
e	0.2	0.2	World-wide average
f	0.1	0.1	Estimated
Total	1.3	1.8	Independent error sources

+ based on the assigned errors in JHDGF-1
* based on 12.5 mGals error of 1°×1° block means

Table 12 Relative geoidal height errors due to various error sources for 500 km distance

Error source	Relative geoidal height error	Note
		Anomaly degree variance model *c*
	m	
a	0.85	Data condition (4-31)
	1.22	Data condition (4-34)
b	0.26	GEM-10 model
c	1.34	12.5 mGals error of 1°×1° block mean
d	0.2	Table 10, estimted
e	0.1	Due to a long correlation distance
f	0.1	Estimated
		Independent error sources
Total	1.6	Data condition (4-31)
	1.8	Data condition (4-34)

be as large as the point geoidal height error, i.e. 1.6 m for the data condition (4-31) and 1.8 m for the data condition (4-34). When the distance is 100 km, the error will decrease to around one meter.

5. Surface Data Requirements for the Computation of an Accurate Geoid

In Chapter 3, we have used block mean gravity anomalies read out from various kinds of gravity anomaly maps of different accuracy to obtain a gravimetric geoid. Since it is difficult for us to estimate the accuracies of such block gravity data, the accuracy of the computed geoid is ambiguous. When we know the errors of block mean gravity

anomalies, we can estimate the error of the geoid on the basis of the gravity data errors (see 4-(4)). To obtain accurate block mean gravity anomalies and to estimate the accuracy of the obtained block data properly, we had better consider to use some mathematical procedures to derive block mean gravity anomalies from raw gravity observations. On the basis of the mathematical treatings, we can consider the problem that what kind of gravity survey is suitable and effective to compute a more accurate geoid, say a geoid with an accuracy of the order of ± 10 cm.

(1) Estimation of Block Mean Gravity Anomalies by Using Least-squares Collocation

1) Least-squares collocation

Least-squares collocation is one of the most efficient statistical techniques for dealing with physical observations. Least-squares collocation has three functions of interpolation, prediction and filtering simultaneously, and besides it can deal with not only homogeneous measurements but also heterogeneous measurements relating functionally to the physical measurements concerned. Moritz (1972) discussed the mathematical frameworks of least-squares collocation in detail. We summarize briefly the mathematical procedures of least-squares collocation for the conveniences of the later sections.

The fundumental equation of least-squares collocation is

$$x=AX+s'+n \tag{5-1}$$

(ibid., p. 7). x expresses "observations", and when we deal with gravity anomaly, the observations are all kinds of observations having some relations with gravity anomaly, i.e. gravity anomaly itself, deflection of the vertical, geoidal height, topographic height, bottom topography at sea, underground crustal structures, etc. When there are q observations, x is a column vector composed of q elements. s' is the signal part (information relating to gravity anomaly) included in x, and s' is assumed to satisfy the condition of "random" such as

$$M\{s'\}=0, \tag{5-2}$$

where the operator M indicates a procedure "mean". n is the random noise included in the observations, then

$$M\{n\}=0 \tag{5-3}$$

is assumed. s' and n are column vectors comprising q elements each.

The term AX expresses the systematic part included in observations x, where X is a column vector which comprises r unknown parameters and A is a known $q\times r$ matrix which is equivalent to the design matrix appearing in the conventional least-squares adjustment. To compute p signals: $s=[s_1, s_2, \ldots, s_p]^T$, from q observations, we define vector v by

$$v=[s, s'+n]^T=[s_1, s_2, \ldots, z_1, z_2, \ldots, z_q]^T, \tag{5-4}$$

where $s'+n$ is simply written as z, and T on the shoulder denotes the operation of transposition. We use a minimum codition:

$$v^TQ^{-1}v=\text{minimum}, \tag{5-5}$$

where Q is the covariance matrix, $(p+q)\times(p+q)$ matrix, of v, which comprises covariances

of signal and covariances between signal and noise. Q is written by a partitioned matrix such as

$$Q=\begin{pmatrix} C_{ss} & C_{sz} \\ C_{zs} & C_{zz} \end{pmatrix}, \tag{5-6}$$

where C_{ss} is the covariance matrix of the signal s, $C_{ss}=cov(s, s)$, and C_{sz} and C_{zs} are covariance matrices between s and z, which are

$$C_{sz}=C_{zs}^{T}=cov(s, z)=M\{s\,z^{T}\}=M\{s(s'+n)^{T}\}=M\{s\,s'^{T}\}+M\{s\,n^{T}\}.$$

Since n and s are independent of each other, we can write

$$C_{sz}=C_{zs}^{T}=M\{s\,s'^{T}\}=C_{ss'}. \tag{5-7}$$

In the same way, we have

$$C_{zz}=cov(z, z)=M\{(s'+n)(s'+n)^{T}\}=C_{s's'}+C_{nn}, \tag{5-8}$$

where C_{nn} is the covariance matrix of the noise. We can solve the unknown signal vector s and the unknown parameter vector X under the condition (5-5) with the constraint equation (5-1) by using the method of Lagrangian multipliers (e.g. Brandt, 1970, p. 176-178). The solutions are written as follows:

$$X=(A^{T}\bar{C}^{-1}A)^{-1}A^{T}\bar{C}^{-1}x, \tag{5-9}$$

$$s=C_{ss'}\bar{C}^{-1}(x-AX), \tag{5-10}$$

where

$$\begin{aligned}\bar{C}&=cov(x, x)=M\{x-AX)(x-AX)^{T}\}\\&=M\{z\,z^{T}\}=\bar{C}_{s's'}+C_{nn}\end{aligned} \tag{5-11}$$

(Moritz, 1972, p. 15). The error covariances of obtained X and s are given by

$$E_{XX}=(A^{T}\bar{C}^{-1}A)^{-1}, \tag{5-12}$$

and by

$$E_{ss}=C_{ss}-C_{sx}\bar{C}^{-1}C_{xs}+HAE_{XX}A^{T}H^{T}, \tag{5-13}$$

where

$$\begin{aligned}C_{sx}&=C_{xs}^{T}=cov(s, x)=M\{s(x-AX)^{T}\}\\&=M\{s\,z^{T}\}=C_{ss'},\\H&=C_{sx}\bar{C}^{-1}\end{aligned} \tag{5-13}$$

(ibid., p. 32-33).

When we apply least-squares collocation actually, the covariances of the signal and the noise should be known in advance. To our convenience, the computed signals are not so affected by slight changes of the covariance functions (Moritz, 1972; Smith, 1974). Although there is a disadvantage that least-squares collocation requires to invert matrices of the same dimension as the number of observations, such a problem has become less important in the modern electronic computer era.

2) Estimation of block mean gravity anomalies from gravity measurements

One of simple applications of least-squares collocation is the estimation of block mean gravity anomalies from point gravity measurements. In this case, we understand equation (5-1) in the following way : x comprises q point gravity anomalies distributed inside and around the block area ; s' is the signal part relating to the block mean gravity anomaly included in point gravity anomalies ; n is the random noise of the gravity measurements. If we use centered gravity anomalies which satisfy $M\{\Delta g\}=0$, we may put the systematic part AX to be zero. The signal s required to be computed is a block mean gravity anomaly, and then from (5-10) the block mean gravity anomaly, written as $\overline{\Delta g}$, is estimated by

$$\overline{\Delta g}=C^{T}_{\Delta g\,\overline{\Delta g}}\,\overline{C}^{-1}\Delta g, \tag{5-14}$$

where $C_{\overline{\Delta g}\,\Delta g}$ is a column vector composed of q covariances between the block mean gravity anomaly and q point gravity anomalies, Δg is a column vector composed of q point gravity anomalies : $\Delta g=(\Delta g_1, \Delta g_2, \ldots, \Delta g_q)^T$, and $\overline{C}$ is a rectangular $q\times q$ matrix whose elements are covariances of point gravity anomalies: i.e. (i, j)-th element of $\overline{C}$ is given by

$$[\,\overline{C}\,]_{ij}=C_{\Delta g}(\Delta g_i, \Delta g_j)+C_n(n_i, n_j). \tag{5-15}$$

The covariance function of gravity anomaly, $C_{\Delta g}$, and the covariance function of noise included in gravity observations, C_n, are functions of the distance between points i and j when the statistical characteristics of Δg and n are isotropic. The covariances between block mean gravity anomaly and point gravity anomaly can be obtained if the covariance function of point gravity anomaly is known (Heiskanen and Moritz, 1967, p. 277). The error of the computed block mean gravity anomaly is estimated from (5-13) as

$$\varepsilon^2=C_{\overline{\Delta g}\,\overline{\Delta g}}-C^{T}_{\Delta g\,\overline{\Delta g}}\,\overline{C}^{-1}C_{\Delta g\,\overline{\Delta g}}, \tag{5-16}$$

where $C_{\overline{\Delta g}\,\overline{\Delta g}}$ is the variance of block mean gravity anomalies. The solutions (5-14) and (5-16) are equivalent to the solutions by a least-squares estimation approach to estimate a block mean gravity anomaly in the form of linear combination of point gravity anomalies (Heiskanen and Moritz, ibid., p. 277 ; Ganeko, 1978).

The same expressions as (5-14) and (5-16) can be used to estimate a block mean gravity anomaly from mean gravity anomalies of smaller block only by replacing Δg_i and $\overline{\Delta g}$ by $\overline{\Delta g_i}$ (mean gravity anomaly of smaller block) and $\overline{\overline{\Delta g}}$ (mean gravity anomaly of larger block). Smith (1974) made detailed test calculations of estimating 5° and 1° block mean gravity anomalies from available 1° block mean gravity anomalies.

3) Estimation of gravity anomaly from other data

Least-squares collocation may possibly be applied to estimate gravity anomaly from topographic heights, sea bottom topography and other geophysical data if the relation between such data and gravity anomaly are given numerically, i.e. by covariance functions. We know the fact that free-air gravity anomalies are in most cases well correlated to topographic heights at land, and for example in Japan area, the fact was tested by some authors, e.g. Yokoyama and Tajima (1957) ; Rikitake et al. (1965) ; Hagiwara (1967). Hagiwara (1965) found good correlations between Bouguer gravity

anomalies and the geological structures in Japan. A tendency that the sea bottom topography has also some relations with free-air gravity anomaly was pointed out by Watts (1976), Mckenzie and Bowin (1976) and Cochran and Talwani (1977). The relations between geophysical structures at sea and gravity anomaly were investigated by Marsh and Marsh (1976), Khan (1977) and Jordan (1978). Although we find some correlations between gravity anomaly and geophysical and geographical structures, the correlations are not necessarily well applicable to interpolating gaps of gravity anomaly. The use of geophysical and geographical data for interpolating gravity anomaly may be limitted to specific areas where strong correlations exist between gravity anomaly and such data.

On the other hand, geoidal heights and deflection of the vertical are mathematically interrelated to gravity anomaly by the geopotential theory, and then we can derive analytical covariance functions between arbitrary two quantities among gravity anomaly, geoidal height, deflection of the vertical and the differentials of them. Tscherning and Rapp (1974) obtained covariance functions such as gravity anomaly-gravity anomaly, gravity anomaly-geoid undulation, gravity anomaly-deflection of the vertical, undulation-undulation, deflection-deflection and deflection-undulation from a model anomaly degree variance (4-17). When we know these covariance functions, least-squares collocation is well applied to estimate gravity anomaly from geoid undulations and deflections of the vertical. Smith (1974) and Rapp (1974) made simulation studies concerning the estimation of gravity anomaly from satellite altimeter data by least-squares cllocation assuming that the sea surface heights from the ellipsoid (=altimetric sea surface heights) are approximately equal to geoidal heights. Rummel and Rapp (1977) and Rapp (1977a) applied the method actually to Geos-3 altimeter data, and ± 3 mGals accuracy of 5° block mean gravity anomaly and ± 6 mGals accuracy of $1° \times 1°$ block mean gravity anomaly were obtained (Rapp, 1977a). Such applications of the satellite altimetry for estimating gravity anomalies in the gravity data sparse areas will make us possible to get geopotential coefficients up to high degrees, and the detailed gravity anomaly field will be of use to compute an accurate gravimetric geoid as seen in the last chapter.

(2) Requirements for a 10 cm Geoid

1) Requirements for block sizes of terrestrial gravity data

The fundumental requirement for the block size of mean gravity anomalies is obtained from the curves for $\psi_0=0$ in Figures 30a and 30b. Truncation errors less than 10 cm are achieved at around degree $L=1000$ which corresponds to the following block size by equation (4-29) :

$$\theta=\frac{180°}{1000}\fallingdotseq 11',$$

i.e., we need at least 10′ block mean gravity anomalies in the inner-most cap area. We test the truncation errors caused by two data conditions A and B in Table 13. The truncation errors are estimated by using (4-30) for each data condition, and the estimated truncation errors are shown in Table 14 for both anomaly degree variance models *b* and *c* which have been often used in the previous chapters. According to (4-38), we can

Table 13 Proposed data conditions for the computation of a gravimetric geoid with an accuracy of the order of ±10cm

Data condition A		Data condition B	
Area	Data	Area	Data
$\psi \leq 2°$	10′ block gravity anomaly	$\psi \leq 2°$	10′ blok gravity anomaly
$2° < \psi \leq 10°$	30′ block gravity anomaly	$2° < \psi \leq 10°$	30′ block gravity anomaly
$10° < \psi \leq 35°$	1° block gravity anomaly	$10° < \psi \leq 20°$	1° block gravity anomaly
$\psi > 35°$	$l_{max}=30$ global geo-potential model	$\psi > 20°$	$l_{max}=100$ global geo-potential model

Table 14 Point truncation errors of the geoidal heights computed under the proposed data conditions A and B

Anomaly degree variance model*	Data condition A	Data condition B
	m	m
b	0.08	0.07
c	0.12	0.12

* Shown in Figure 28.

estimate the errors of relative geoid undulation due to the truncation effects under the data conditions A and B to be $\sqrt{2}$ times the values in Table 14 for a distance farther than 300 km. So far as we consider the truncation errors, we can compute geoidal heights as accurate as 10 cm under the data conditions listed in Table 13. We may expect that global geopotential models comprising geopotential coefficients up to degree 100 or 2° block mean gravity anomalies all over the surface of the earth will become available in the near future if we take the successful results of the satellite altimetry by Geos-3 into consideration.

2) Requirements for accuracies of gravity data

a. Data condition A

Along the discussions made in 4-(4), we can estimate the point undulation error due to gravity bata errors as follows:

$$m^2_{\delta N,A} = m^2_{\delta N}(2°, \theta_1) + m^2_{\delta N}(10°, \theta_2) - m^2_{\delta N}(2°, \theta_2) + m^2_{\delta N}(35°, \theta_3) - m^2_{\delta N}(10°, \theta_3), \tag{5-17}$$

where $\theta_1=10'$, $\theta_2=30'$ and $\theta_3=1°$. Let us adopt the error covariances of the type of Case A (4-58) for all block mean gravity anomalies, and put the r. m. s. errors of gravity data for each block size as m_{θ_1}, m_{θ_2} and m_{θ_3} (in mGals). From the listed values in

Table 8, (5-17) is given numerically as

$$m^2_{\delta N,A}=0.018^2 m^2_{\theta_1}+0.034^2 m^2_{\theta_2}+0.043^2 m^2_{\theta_3}\ (\text{meter}^2) \tag{5-18}$$

When we can set $m_{\theta 1}=m_{\theta 2}=m_{\theta 3}=m_\theta$, (5-18) is reduced to

$$m_{\delta N,A}=0.058 m_\theta\ (\text{meter}) \tag{5-19}$$

which shows that the error of 10 cm level can be achieved by $m_\theta=1\sim2$ mGals. As we see in (5-18), the contribution of 10′ block data is smaller than other sized block data, and then larger errors of 10′ block data than the errors of other sized block data are acceptable. For example, when $m_{\theta 1}=5$ mGals, $m_{\theta 2}=m_{\theta 3}=2$ mGals, we obtain

$$m_{\delta N,A}=0.14\ \text{meters}. \tag{5-20}$$

Concerning the relative undulation error between 300 km distance, we assume the main error source to be due to 30′ block data errors, and we estimate the relative undulation error from Table 9 as follows:

$$m^2_{\delta\Delta N,A}=0.055^2 m^2_{\theta_2}.$$

If we set $m_{\theta 2}=2$ mGals, we obtain $m_{\delta\Delta N,A}=0.11$ meters.

For other types of error covariance such as exponential error covariances of Case B and Case C (4-68), we can estimate point undulation errors from Table 8 under the same assumptions as (5-19);

$$\left.\begin{aligned} m_{\delta N,A}&=0.080 m_\theta\ (\text{meter})\ \text{for Case B},\\ &=0.152 m_\theta\ (\text{meter})\ \text{for Case C}.\end{aligned}\right\} \tag{5-21}$$

(5-21) results in rather large undulation errors, so that we should bear in mind not to bring any systematic errors in the terrestrial gravity data.

b. Data condition B

Under the data condition of B in Table 13, the point truncation error is estimated as

$$m^2_{\delta N,B}=0.018^2 m^2_{\theta_1}+0.034^2 m^2_{\theta_2}+0.040^2 m^2_{\theta_3} \tag{5-22}$$

for the error covariances of Case A. (5-22) estimates almost the same undulation errors as (5-19), and this comes from the fact that the undulation errors due to gravity data errors little increase even when the cap size becomes larger than 20° (see Figure 37). Therefore, so far as concerning the undulation errors due to gravity data errors, the data condition B is equivalent to the data condition A.

(3) Accurate Surface Gravity Surveys to be Required

In this section, we will study what kind of gravity surveys can derive block mean gravity anomalies as accurate as those required in the previous section to compute a geoid with a 10 cm accuracy. We have studied how to compute block mean gravity anomalies from point gravity observations in 5-(1), i.e. the least-squares collocation method. Block mean gravity anomalies are estimated by (5-14) and the errors of the estimated block means are given by (5-16) on the basis of the known covariance function of gravity anomaly. Let us make a simulation study based on (5-16) for various distri-

butions of gravity observation sites. When we apply least-squares collocation, the average of the signal, i.e. gravity anomaly in our case, should be zero. In other words, gravity anomaly should satisfy the condition (5-2) by taking it into consideration that a block mean is estimated from the gravity observations being inside and near around the block. Then it should be recommended toapply least-squares collocation to both the residual gravity anomaly derived by subtracting a satellite derived global gravity anomaly and its block means, because the global gravity anomaly is considered to be a kind of bias term of gravity anomaly in a restricted region.

The covariance function of the gravity anomaly around Japan has already been obtained in 4-(1), and an analytical function model (4-23) of the point residual gravity anomalies has been proposed. Covariance functions being necessary for (5-16) are easily obtained numerically by using the model function of the point anomaly covariance (Heiskanen and Moritz, 1967, p. 277 ; Ganeko, 1978). The errors (5-16) depends only upon the distribution paterns of gravity observation sites. They are independent of the gravity anomalies. But the errors of gravity measurements contribute to (5-16) through the error covariance C_n (see (5-15)). Table 15 includes the estimation errors of block mean gravity anomalies for 5′, 10′, 30′ and 1° blocks on the basis of the model residual anomaly covariance function (4-23). The adopted blocks are square ones which have the same areas as equiangular blocks of $5'\times5'$, $10'\times10'$, $30'\times30'$ and $1^\circ\times1^\circ$ located at latitude 33°. Three cases that gravity measurement errors fall on 0, 3 and 5 mGals are tested on the assumption that the errors are independent of site of measurement; i.e. the error covariance matrix C_{nn} comprises only diagonal elements. The second column of Table 15 shows variances of block mean residual gravity anomalies for each block size. The estimated errors of block means are listed in the column from the third to the sixth for four kinds of distribution paterns of gravity observation sites. The third column includes the average estimation errors (called representation errors) for the case that there is only one gravity observation site in the block. The fourth column is for the case that one observation site is located at the center of the block. The fifth and the sixth columns are for the case that gravity measurements are carried out along lines, and such a case is actually realistic in the sea gravity observations. The fifth column is for the case that there is one series of gravity observation sites (we call it a profile observation) along the ship's track crossing the block at the center of it (see Figure 41a), and the sixth column is for the case that there are two profile observations crossing the block as shown in Figure 41b. T.S.S.G. (Tokyo Surface Ship Gravimeter) (Tomoda and Kanamori, 1962; Tomoda et al., 1968; Segawa, 1970a, b; Fujimoto, 1976) provides us with gravity data with an interval of 2 or 4 km at the normal velocity of survey ships. If we take the functional shape of the anomaly covariance near origin into consideration, we may note that 2 km spacing of sites in a profile observation is sufficient for estimating 5′ block means, and 4 km spacing is sufficient for larger blocks.

Table 15 Estimation errors of block mean gravity anomalies computed by using the least-squares collocation method under various distribution conditions of gravity observation sites

Block size $B\times B$	Block anomaly variance	Representation error	One obs. site at the block center	One profile observation	Two profile observations	Random obs. error
km	mGal^2	mGal	mGal	mGal	mGal	mGal
B=8.5	3093	6.4	3.7	1.7	0.7	0
5′ block		7.1	4.7	2.1	1.2	3
		8.1	6.2	2.6	1.7	5
B=17.0	3036	9.9	5.6	2.7	1.0	0
10′ block		10.3	6.3	2.9	1.2	3
		11.1	7.4	3.2	1.5	5
B=50.9	2518	19.9	10.5	5.2	1.9	0
30′ block		20.1	10.8	5.2	2.0	3
		20.5	11.4	5.3	2.2	5
B=101.8	2215	30.3	14.8	8.2	3.0	0
1° block		30.4	15.0	8.3	3.0	3
		30.7	15.3	8.3	3.1	5

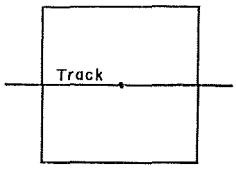

Figure 41a One profile gravity observation along the track crossing a block at its center.

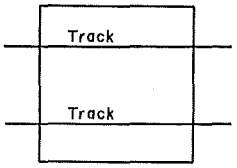

Figure 41b Two profile gravity observations along tracks crossing a block.

Teble 15 shows that when we require the estimation error less than ±5 mGals for 10′ block and ±2 mGals error for 30′ and 1° blocks, one profile observation is necessary for 10′ blocks, two profile observations are necessary for 30′ blocks, and more than two profile observations are necessary for 1° blocks. In other words, parallel profile gravity observations are to be carried out every 10 naut. miles in an area where 10′ block mean gravity anomalies are desired, and profile observations are necessary every 15 naut. miles in the remaining area where surface gravity data are desired. Random gravity measurement errors up to ±5 mGals may be acceptable. The gravity surveys at sea like above mentioned will make us possible to compute a marine gravimetric geoid with a decimeter accuracy.

The performance of the gravity surveys described here requires a little time, cost and effort. It should be noted that Table 15 is based on the anomaly covariance functions derived from gravity anomalies in the region including rough gravity anomaly areas such as trenches and islands-arcs. If we adopt the variance of world-wide average residual gravity anomaly, 1620 mGal^2 (Table 11 of Tscherning and Rapp, 1974) in place of 3133 mGal^2 in (4-23). Each value listed in Table 15 decreases by 30%. In this case, parallel profile gravity observations carried out every 30 naut. miles can yield 1° block mean gravity anomalies with a sufficient accuracy, ±2 mGals, for our present purpose. When

we carry out gravity surveys actually, it may be necessary for efficient surveys that we examine beforehand the roughness of the gravity anomaly field in the areas to be surveyed.

6. Summary and Conclusions

We have obtained a gravimetric geoid around Japan based on $30' \times 30'$ and $1° \times 1°$ block mean gravity anomalies. The $30' \times 30'$ block data have been read from the published gravity anomaly maps around Japan, and the $1° \times 1°$ block data have been prepared by taking averages of DMAAC global gravity data and LAMONT data. The gravimetric geoidal heights have been computed from the terrestrial gravity data in combination with a satellite-derived geopotential field: GEM-10 model. GEM-10 model is one of the recent geopotential models and it comprises a geopotential coefficient set which is complete up to degree and order 22. The radius of the cap area of Stokes' integration where terrestrial gravity data are used has been taken to be 20°. The most marked features in the computed geoid (Figure 8) are seen along trenches, where there are geoidal dents of more than 20 meters relative to GEM-10 global geoid. The geoidal highs along islands-arcs are other marked features in the geoid.

We have made detailed investigations concerning various error sources accompanied with our computation method of geoidal heights, and the reliability of the computed geoid has been investigated from various points of view. Some of the altimeter data taken by Geos-3 satellite have been compared with the gravimetric geoid, and the results are seen in Table 1 and Figures 13~24. The r.m.s. difference of relative undulations between altimetric sea surface heights and the gravimetric geoid is around 1.3 m, which scatters in a range from 0.6 m to 1.9 m depending on the locations of the satellite tracks and the dates of the satellite revolutions; i.e. at the early stage of the satellite, the satellite positions were a little poorly determined.

Chapter 4 has been devoted to the investigations of error sources accompanied with the geoidal height computation procedures in the former chapters and evaluations of the actual possible errors of the computed geoid. The r.m.s. error of the computed geoid undulations has been estimated to be 1.3 m in JHDGF-1 region (see Figure 4) and to be 1.8 m outside the region. These error estimates are compatible with the comparison results between Geos-3 altimeter data and the gravimetric geoid. The accuracy of geoidal height differences (relative undulation error) has also been investigated. Such relative undulation errors have a little meaning because some of error sources have long correlation distances, and the relative undulation errors are differently evaluated from the conventional point undulation errors.

Concerning the computed gravimetric geoid, we have estimated a relative undulation error over 500 km distance to be about 1.6 m or 1.8 m depending on the data conditions (see Table 12). The relative undulation error decreases to around one meter when the distance is 100 km. As we see in Tables 11 and 12, the errors of terrestrial gravity data still form the biggest error source. The second big error source is formed by the omission errors, and the third one is due to existence of the sea surface topography.

We may conclude from the error investigations as made above that it is difficult for us to obtain geoid undulations with an accuracy of one meter or less around Japan under the current availability of the terrestrial gravity data near Japan. The geoidal map obtained in the pressnt paper shows a general features of the geoid undulations around Japan, especially at trenches and islands-arcs, and the geoid will be of use not only as the first step to compute an accurate geoid but also in the better evaluations of three dimensional positions of the satellite tracking stations and other astronomical observation sites located in the region of the geoidal map, and moreover it will be of use as a calibration field of other geoids, e.g. astrogeodetic geoids (Ono, 1974; Ganeko, 1976) and Doppler results (Mori and Kanazawa, 1979).

There is a strong ocean current near Japan, which is called Kuroshio, and oceanographers are very interested in deviations of the sea surface from the geoid (an equipotential surface) over the Kuroshio area. Unfortunately, the accuracy of the obtained gravimetric geoid is insufficient at all to detect such deviations from the obtained geoidal map. We understand some difficulties in the determination of the sea surface topography over the Kuroshio area because of rougher geoid undulations over the area than the Gulf Stream area, off east coasts of the United States.

Our second object in computation of gravimetric geoid consists in a 10 cm marine geoid which can afford to make use of the satellite altimetry with the same order of accuracy. In Chapter 5, we have obtained the data conditions for the terrestrial gravity data to get a geoid (marine geoid) with an accuracy of 10 cm level, and we have known that much more additional gravity surveys are necessary to get such an accurate geoid. Inside and near the region (see Table 13) where a 10 cm geoid is desired, 10′ block mean gravity anomalies with an accuracy of 5 mGals or better are necessary, and such a condition will be fulfilled at sea by profile gravity observations along parallel ship tracks located every 10 naut. miles. In the region where 30′ or 1° block mean gravity anomalies are prepared (see Table 13), profile gravity observations should be carried out every 15 or 30 naut. miles depending on the roughness of the gravity anomaly field. The satellite altimeter data (sea surface heights) can be used in the geoidal height computations directly (Mather, 1973, 1974) or indirectly, i.e. in the form of gravity anomalies derived from altimetric geoidal heights (Rapp, 1977a), and then the satellite altimetry may take the place of the conventional gravity surveys at sea to some extent.

The existence of the sea surface topography causes difficulties in the definition and the realization of the geoid, as an equipotential surface in the earth's gravitational field is not realized by the mean sea surface (schematically explained by Figure 40). The gravity reduction errors both at sea and at land caused by the sea surface topography result in geoidal height errors which are are not negligible(5-(5), Table 10). This situation comes from the characteristics of the long wave-length variations of the sea surface topography and the systematic errors of the land height systems caused by the sea surface topographic heights at the base tide stations of the height systems. Physical oceanography predicts relative sea surface undulations from an equipotential surface on the basis of oceanographic data, but the oceanographic sea surface undulations do not

necessarily agree well with the geodetic levelling observations along the coasts of continents (Sturges, 1967; Hammon and Greig, 1972). Therefore we cannot put too much reliance upon the oceanographic sea surface topography at present, however we may be able to use the oceanographic sea surface topography as the first approximation of the true sea surface topography in the better gravity reductions. The gravimetric geoid computed from the gravity anomalies reduced by using the oceanographic sea surface heights will provide us with another sea surface topography in combination with 10 cm satellite altimetry. Consequently it may be a new definition of the geoid. The new sea surface topography and the new definition of the geoid will be used in the gravity reductions again to compute a more accurate geoid which will provide us with more accurate sea surface topography and geoid.

Acknowledgments

The author wishes to express his cordial gratitude to Prof. Y. Hagiwara for his encouragement and advice during the preparation of this work. He also wishes to thank Dr. E. M. Gaposchkin and Dr. H. R. Stanley for providing him with DMAAC's $1^\circ \times 1^\circ$ block mean gravity anomalies and Geos-3 altimeter data, respectively, and to thank Dr. A. B. Watts for his advice concerning the reliability of $1^\circ \times 1^\circ$ gravity anomaly data in the Northwest Pacific area. The author's thanks are also due to Dr. A. M. Sinzi, Dr. A. Yamazaki, Mr. T. Mori and Mr. A. Senda of JHD for providing him with conveniences in the performance of computations by using an electronic computer. The author is also indebted to Mr. K. Koyama of the Astronomical Division, JHD, for his help in computing geoidal heights and drawing geoidal maps by using a machine.

This paper in based on the author's dissertation, submitted to the University of Tokyo, in partial fulfillment of the requirements for the doctorate.

Refesences

Atumi, K., 1933: "La deviation de la verticale au Japon", *Japan. J. Astron. Geophys., 10*, 305-312.

Brennecke, J. and E. Groten, 1977: "The deviation of the sea surface from the geoid and their effect on geoid computation" *Bull. Geod., 51*, 47—51.

Brandt, S., 1970: *Statistical and Computational Methods in Data Analysis*, North-Holland Publishing Company, Amsterdam-London, pp. 322.

Caputo, M., 1967: *The Gravity Field of the Earth*, International Geophysics Series, Vol. 10, Academic Press, New York, pp. 202.

Christodoulidis, D. C., 1976: "On the realization of a 10 cm relative oceanic geoid", *Rep. 247, Dep. Geod. Sci.*, Ohio State Univ. Res. Found., Ohio State Univ. Columbus, Ohio, pp. 96.

Cochran, J. R. and M. Talwani, 1977: "Free-air gravity anomalies in the world's oceans and their relationship to residual elevation", *Geophys. J. R. astr. Soc., 50*, 495—552.

De Witte, L., 1967: "Truncation error in the Stokes and Vening Meinesz formula for different order spherical harmonic gravity terms", *Geophys. J. R. astr. Soc., 12,* 449—464.

DMAAC, Defence Mapping Agency/Aerospace Center, 1°×1° mean free-air gravity anomaly set 1976.

Fischer, I., 1960: "An astrogeodetic world datum from geoidal heights based on the flattening $f=1/298.3$", *J. Geophys. Res., 65,* 2067—2076.

Fujimoto, H., 1976: "Processing of gravity data at sea and their geophysical interpretation in the region of the Western Pacific", *Bull. Ocean Res. Inst.,* Univ. of Tokyo, No. 3, 1—81.

Geneko, Y., 1976: "Astrogeodetic geoid of Japan", *Spec. Rep. 372,* Smithsonian Astrophysical Observ., Cambridge, Mass., pp. 34.

Ganeko, Y., 1977: "The errors of geoidal height computation due to the omission of detailed information of the anomaly field", *J. Geod. Soc. Japan, 23,* 140—155.

Ganeko, Y., 1979: "Detailed gravimetric geoid around Japan based on 30′×30′ block gravity means", *Marine Geodesy,* 2, 297—312.

Ganeko, Y., 1978: "A statistical method for estimation of block gravity means", *Rep. Hydrographic Researches,* No. 13, Japan Hydrographic Department, 67—82.

Ganeko, Y., T. Yanagi and K. Kubo, 1978: "Gravity measurement at sea in 1973, 1974 and 1976", *Data Report of Hydrographic Observations,* Series of Astronomy and Geodesy, No. 12, Japan Hydrographic Department, 55—80.

Gaposchkin, E. M., editor, 1973: "1973 Smithsonian Standard Earth (III)", *Spec. Rep. 353,* Smithsonian Astrophys. Observ., Cambridge, Mass., pp. 388.

Gaposchkin, E. M., 1974: "Earth's gravity field to the eighteenth degree and geocentric coordinates for 104 stations from satellie and terrestrial data", *J. Geophys. Res., 79,* 5377—5411.

Gaposchkin, E. M., 1976: "Gravity-field determination using laser observations", presented at the Royal Society Discussion Meeting, London, *Preprint Series No. 548,* Center for Astrophysics, Cambridge, Mass., pp. 33.

Geographycal Survey Institute, 1970: *Free-air Anomalies in Japan,* the gravity anomaly map in the reduced scale of 1/2000000.

Hagiwara, Y., 1967: "Analyses of gravity values in Japan", *Bull. Earthq. Res. Inst., 45,* Univ. of Tokyo, Tokyo, 1091—1228.

Hagiwara, Y., 1970: "Truncation errors in the Stokes formula integration", *J. Geod. Soc. Japan, 16,* 190—198.

Hagiwara, Y., 1972a: "Practical computation of G_1-G_1 over Tanzawa Mountains", *J. Geod. Soc. Japan, 18,* 161—171.

Hagiwara, Y., 1972b: "Truncation error formulas for the geoidal height and the deflection of the vertical", *Bull. Geod., No. 106,* 453—466.

Hagiwara, Y., 1973: "G_1 distribution over models of topographic relief", *J. Phys. Earth, 21,* 305—311.

Hagiwara, Y., 1976: "A new formula for evaluating the truncation error coefficient", *Bull. Geod., 50,* 131—135.

Hamon, B. and M. A. Greig, 1972: "Mean sea level in relation to geodetic leveling around Australia", *J. Geophys. Res., 77,* 7157—7162.

Heiskanen, W. and H. Moritz, 1967: *Physical Geodesy,* W. H. Freeman, San Francisco, Calif., pp. 364.

International Association of Geodesy, 1971: "Geodetic Reference System 1967", Publ. Spec., 3, Bull. Geod., pp. 116.

Japan Hydrographic Department, 1970—1977: *Gravity Anomaly Chart*, in the series of the Basic Map of the Sea, Nos. 6321G—6331G, 6333G, 6334G, 6336G, 6337G, 6345G, 6350G, 6351G, 6353G—6357G, 6370G, 6372G—6377G, 6379G—6382G.

Jordan, S. K., 1978: "Statistical model for gravity, topography, and density contrasts in the earth", *J. Geophys. Res.*, *83*, 1816—1824.

Kaula, W. M., 1966: *Theory of Satellite Geodesy*, Blaisdell, Waltham, Mass.

Kawabata, Y., 1939, Bull. of the Central Meteorological Observatory, Tokyo, 7, No. 2.

Kearsley, W., 1977: "The prediction and mapping of geoidal undulations from Geos-3 altimetry", *Rep. 267, Dep. Geod. Sci.*, Ohio State Univ. Res. Found., Ohio State Univ., Columbus, Ohio, pp. 68.

Khan, M. A., 1977: "Depth of sources of gravity anomalies", *Geophys. J. R. astr. Soc.*, *48*, 197—209.

Leitao, C. D., C. L. Purdy and R. L. Brooks, 1975, Wallops Geos-c Altimeter Processing Report, *NASA Technical Memorandum. TMX-69357*, Wallops Flight Center, Wallops Island, VA.

Leitao, C. D., N. E. Huang and C. C. Parra, 1978: "Remote sensing of Gulf Stream using Geos-3 rader altimeter", *NASA Technical Paper 1209*, pp. 31.

Lelgemann, D., 1970: "Untersuchungen zu einer genaueren Losung des Problems von Stokes", *No. C155*, German Geodetic Commission, pp. 30.

Lerch, F. J., S. M. Klosko, R. E. Laubscher and C. A. Wagner, 1977: "Gravity model improvement using Geos-3 (GEM 9 & 10)", *Rep. X—921—77—246*, Goddard Space Flight Center, Greenbelt, Maryland, pp. 121.

Lisitzin, E., 1974, Sea level changes, p. 143, Elsevier, Amsterdam-Oxford-New York.

Marsh, J. G. and S. Vincent, 1974: "Global detailed geoid computation and model analysis", *Geophys. Surveys*, *1*, 481—511.

Marsh, J. G. and E. S. Chang, 1976a: "Global detailed gravimetric geoid", paper presented at AGU Fall Meeting, San Francisco, California.

Marsh, J. G. and E. S. Chang, 1976b: "5′ detailed gravimetric geoid in the North Western Atlantic Ocean", paper presented at AGU Fall Meeting, San Francisco, California.

Marsh, J. G., T. V. Martin, J. J. McCarthy and P. J. Chovitz, 1978: "Estimation of mean sea surface in the North Atlantic, the Pacific and the Indian Ocean using Geos-3 altimeter data", paper presented at the Second International Symposium on the Uses of Artificial Satellites for Geodesy and Geodynamics, Lagonissi, Greece.

Marsh, B. D. and J. G. Marsh, 1976: "On global gravity anomalies and two-scale mantle convection", *J. Geophys. Res.*, *81*, 5267—5280.

Mather, R., 1973: "A solution of the geodetic boundary value problem to order e^3", *Doc. X—592—73—11*, NASA/Goddard Space Flight Center, Greenbelt, Maryland, pp. 128.

Mather, R., 1974: "On the solution of the geodetic boundary value problem for the determination of sea surface topography", *Geophys. J. R. astr. Soc.*, *39*, 87—109.

Mckenzie, D. and C. Bowin, 1976: "The relationship between bathymetry and gravity in the Atlantic Ocean", *J. Geophys. Res.*, *81*, 1903—1915.

Meissle, P., 1971: "A study of covariance functions related to the earth's disturbing potential", *Rep. 151, Dep. Geod. Sci.*, Ohio State Univ. Res. Found., Ohio State Univ., Columbus, Ohio, pp. 87.

Molodensii, M. S., V. F. Eremeev and M. I. Yukina, 1962: *Methods for Study of the External Gravitational Field and Figure of the Earth*, Translated from the Russian by the Israel Program for Scientific Translations, Ierusalem.

Mori, T. and T. Kanazawa, 1979: "Doppler positioning of off-lying islands", *Data Report of Hydrographic Observations*, Series of Astronomy and Geodesy, No. 13, Japan Hydrographic Department, Tokyo, 64—103.

Moritz, H., 1971: "Series solution of Molodenskii problem", *Publ. No. A70*, German Geodetic Commission, pp. 92.

Moritz, H., 1972: "Advanced least-squares method", *Rep. 175. Dep. Geod. Sci.*, Ohio State Univ. Res. Found., Ohio State Univ., Columbus, Ohio, pp. 133.

Mourad, A. G., S. Gopalapillai, M. Kuhner, D. M. Fubara and Z. H. Byrns, 1975: "The application of Skylab altimetry to marine geoid determination", report prepared for NASA, TF6-NASA/JSC, pp. 93.

Mueller, I. I., 1974: "Global satellite triangulation and trilateration results", *J. Geophys. Res.*, *79*, 5333—5347.

Okuda, K., 1951: "On the change of local geoid in the southwestern part of Japan", *Bull. Geogr. Surv. Inst.*, *2*, Part 4, 239—275.

Ono, K., 1974: "On the astrogeodetic deflections of the vertical in Japan", *J. Phys. Earth*, *22*, 25—69.

Paul, M. K., 1973: "A method of evaluating the truncation error coefficients for geoidal height", *Bull. Geod., No. 110*, 413—425.

Pellinen, L. P., 1966: "A method for expanding the gravity potential of the earth in spherical functions", Translations of the Central Scientific Research Institute of Geodesy, Aerial Survey and Cartography, Issue 171, (translation ACIC-TC-1282, available: NTIS, Springfield, VA, AD661810).

Rapp, R. H., 1973a: "Improved models for potential coefficients and anomaly degree variances", *J. Geophys. Res.*, *78*, 3497—3500.

Rapp, R. H,, 1973b: "Accuracy of geoid undulation computations", *J. Geophys. Res.*, *78*, 7589—7595.

Rapp, R. H., 1974: "Gravity anomaly recovery from satellite altimeter data using least-squares collocation techniques", *Rep. 220, Dep. Geod. Sci.*, Ohio State Univ. Res. Found., Ohio State Univ., Columbus, Ohio, pp. 25.

Rapp, R. H., 1977a: "Mean gravity anomalies and sea surface heights derived from Geos-3 altimeter data", *Rep. 268, Dep. Geod. Sci.*, Ohio State Univ. Res. Found., Ohio State Univ., Columbus, Ohio, pp. 116.

Rapp, R. H., 1977b: "Potential coefficient determinations from 5° terrestrial gravity data", *Rep. 251, Dep. Geod. Sci.*, Ohio State Univ. Res. Found., Ohio State univ., Columbus, Ohio, pp. 77.

Rapp, R. H. and R. Rummel, 1975: "Methods for the computation of detailed geoids and their accuracy", *Rep. 233, Dep. Geod. Sci.*, Ohio State Univ. Res. Found., Ohio State Univ., Columbus, Ohio, pp. 36.

Rikitake, T., H. Tajima, S. Izutsuya, Y. Hagiwara, K. Kawada and Y. Sasai, 1965: "Gravimetric and geomagnetic studies of Onikobe area", *Bull. Earthq. Res. Inst.*, *43*, Univ. of Tokyo, Tokyo, 241—267.

Rummel, R. and R. H. Rapp, 1977: "Undulation and anomaly estimation using Geos-3 altimeter data without precise satellite orbits, *Bull. Geod.*, *51*, 73—88.

Schmid, H. H., 1974; "Worldwide geometric satellite triangulation", *J. Geophys. Res.*, *79*, 5349—5376.

Segawa, J., 1970a: "Gravity measurement at sea by use of the T. S. S. G., Part 1" *J. Phys. Earth*, *18*, 19—49.

Segawa, J., 1970b: "Gravity measurement at sea by use of the T.S.S.G., Part 2", *J. Phys. Earth, 18*, 203—284.

Segawa, J., 1976: "Gravity in the Ryukyu Arc", *J. Geod. Soc. Japan, 22*, 23—39.

Segawa, J. and C. Bowin, 1976: "Gravity in the junction between the Japanese and the Izu-Bonin Islands", *J. Phys. Earth, 24*, 275—311.

Smith, G. N., 1974: "Mean anomaly prediction from terrestrial gravity data and satellite altimeter data", *Rep. 214, Dep. Geod. Sci.*, Ohio State Univ. Res. Found., Ohio State Univ., Columbus, Ohio, pp. 139.

Stanley, H. R., 1978, private communication.

Stroev, P. A., 1971: "Gravity anomalies in the Sea of Japan", in Islands Arc and Marginal Sea, Proceeding of the first Japan-USSR symposium on solid earth sciences, S. Asano and G. B. Udintsev, editors, 245—255.

Sturges, W., 1967: "Slopes of sea level along the Pacific coast of the United States", *J. Geophys. Res., 72*, 3267—3637.

Sugimori, Y., 1978: "宇宙から海を測る", 自然, 33, No. 11, 26—38.

Suzuki, H., 1976: "The International Gravity Standardization Net 1971 and the Japan Gravity Standardization Net 1975", *J. Geod. Soc. Japan, 22*, 112—129.

Talwani, M., H. Poppe and P. Rabinowitz, 1972: "Gravimetrically determined geoid in the Western North Atlantic", in *Sea Surface Topography from Space, Vol. 2*, NOAA Technical Report, ERL-228-AOML 7—2, John Apel, editor, 1—34.

Tomoda, Y. and H. Kanamori, 1962: "Tokyo Surface Ship Gravity Meter −1", *J. Geod. Soc. Japan, 7*, 116—145.

Tomoda, Y.' K. Ozawa and J. Segawa, 1968: "Measurement of gravity and magnetic field on board a cruising vessel", *Bull. Ocean Res. Inst.*, 3, Univ. of Tokyo, Tokyo, 1—170.

Tscherning, C. C. and R. H. Rapp, 1974: "Closed covariance expressions for gravity anomalies, geoid undulations, and deflection of the vertical implied by anomaly degree variance models", *Rep. 208, Dep. Geod. Sci.*, Ohio State Univ. Res. Found., Ohio State Univ., Columbus, Ohio, pp. 89.

Wagner, C. A., F. J. Lerch, J. E. Bround and J. A. Richardson, 1976: "Improvement in the geopotential derived from satellite and surface data (GEM 7 & 8)", *Rep. X—921—76—20*, NASA/Goddard Space Flight Center, Greenbelt, Maryland, pp. 11.

Watts, A. B., 1976: "Gravity and bathymetry in the central Pacific Ocean", *J. Geophys. Res., 81*, 1533—1553.

Watts, A. B. and A. R. Leeds, 1977; "Gravimetric geoid in the Northwest Pacific Ocean", *Geophys. J. R. astr. Soc., 50*, 249—277.

Yamazaki, A., 1971: "Determination of relative geodetic position from simultaneous observations of artificial satellite", *Rep. Hydrographic Researches, No. 7*, Japan Hydrographic Department, 1—22.

Yokoyama, I. and H. Tajima, 1957: "A gravity survey in Volcano Mihara, Ooshima Island by means of a Worden gravimeter", *Bull. Earthq. Res. Inst.*, 35, Univ. of Tokyo, Tokyo, 23—33.

APPENDIX A

Derivation of the Smoothing Parameter

The covariance between block mean gravity anomalies of blocks σ_P and σ_Q is given by

$$\bar{\bar{C}}(\psi)=\frac{1}{S_P S_Q}\iint_{\sigma_P}\iint_{\sigma_Q} C(\psi')\,d\sigma_P\,d\sigma_Q, \tag{A-1}$$

where S_P and S_Q are the areas of σ_P and σ_Q, ψ' is the angular distance between surface elements $d\sigma_P$ and $d\sigma_Q$ which are located in each block (see figure), and $C(\psi')$ is the anomaly covariance function which can be expanded into the series of Legendre functions as equation (4-7). First, we perform a surface integration over block σ_Q. Let P_1 be an arbitrary point in block σ_P, and let ψ_1 and r be what shown in the figure, and we use (4-7). Then we write

$$\begin{aligned}\bar{C}(\psi_1)&=\frac{1}{S_Q}\iint_{\sigma_Q} C(r)\,d\sigma_Q\\ &=\sum_{l=2}^{\infty}\sigma_l^2(\Delta g)\,s^{l+2}\frac{1}{S_Q}\iint_{\sigma_Q} P_l(\cos r)\,d\sigma_Q.\end{aligned} \tag{A-2}$$

Applying a relation among Legendre functions

$$\begin{aligned}P_l(\cos r)&=P_l(\cos\psi_1)P_l(\cos t)\\ &\quad+2\sum_{m=1}^{l}(-1)^m P_{lm}(\cos\psi_1)P_{l-m}(\cos t)\cos m\alpha\end{aligned}$$

and a equation for the surface element $d\sigma_Q=\sin t\,dt\,d\alpha$ (all notations of parameters are self-explanatory in the figure) to the surface integration in (A-2) for a circular block with the radius ψ_0, we obtain

$$\begin{aligned}\frac{1}{S_Q}\iint_{\sigma_Q} P_l(\cos r)\,d\sigma_Q&=\frac{2\pi}{S_Q}\int_0^{\psi_0} P_l(\cos\psi)P_l(\cos t)\sin t\,dt\\ &=P_l(\cos\psi_1)\frac{2\pi}{S_Q}\int_0^{\psi_0} P_l(\cos t)\sin t\,dt.\end{aligned}$$

Using $S_Q=2\pi(1-\cos\psi_0)$, and setting

$$\beta_l=\frac{1}{1-\cos\psi_0}\int_0^{\psi_0} P_l(\cos t)\sin t\,dt, \tag{A-3}$$

we get

$$\bar{C}(\psi_1)=\sum_{l=2}^{\infty}\sigma_l^2(\Delta g)s^{l+2}\,\beta_l\,P_l(\cos\psi_1).$$

Meanwhile we integrate $\bar{C}(\psi_1)$ over block σ_P as

$$\bar{\bar{C}}(\psi)=\frac{1}{S_P}\iint_{\sigma_P}\bar{C}(\psi_1)\,d\sigma_P,$$

and we can repeat the same procedure as the integration over block σ_Q. Then we finally obtain

$$\bar{\bar{C}}(\psi)=\sum_{l=2}^{\infty}\sigma_l^2(\Delta g)s^{l+2}\,\beta_l^2\,P_l(\cos\psi)$$

which is equivalent to (4-14). The smoothing parameter (A-3) is expressed by analytical functions as follows:

$$\beta_l = \frac{P_{l1}(\cos\psi_0)}{l(l+1)} \cot\frac{\psi_0}{2}$$
$$= \frac{1}{2l+1}[P_{l-1}(\cos\psi_0) - P_{l+1}(\cos\psi_0)] \frac{1}{1-\cos\psi_0}.$$

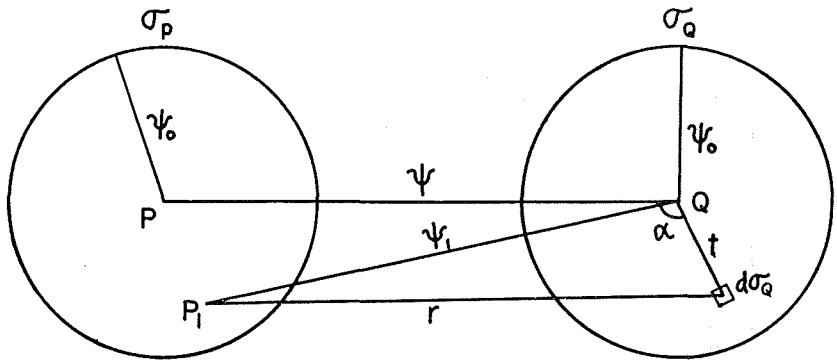

APPENDIX B

JHDGF-1 block mean gravity anomaly data for 1°×1° blocks and for four 30′×30′ blocks included in each 1°×1° block (see the figure shown below). Mean anomalies are listed in the following order: $\overline{\Delta g}_0$ (1°×1° block); $\overline{\Delta g}_1$, $\overline{\Delta g}_2$, $\overline{\Delta g}_3$, $\overline{\Delta g}_4$ (30′×30′ blocks). Anomalies are given in mGals based on JGSN 75 system. Listed positions are those of the center points of 1°×1° blocks.

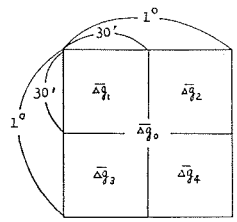

LAT. ° ′	LONG. ° ′	1°×1° mGal	30′×30′ mGal	30′×30′ mGal	30′×30′ mGal	30′×30′ mGal
47 30	139 30	− 1	2	− 3	2	− 3
46 30	138 30	− 2	7	2	− 3	−13
46 30	139 30	− 9	− 3	−13	−13	− 8
45 30	137 30	2	7	7	7	−13
45 30	138 30	−10	− 3	−13	−13	−13
45 30	139 30	19	− 4	21	22	37
42 30	132 30	8	48	48	−22	−42
42 30	133 30	11	48	48	−32	−22
42 30	134 30	− 4	28	− 2	−22	−22

LAT. ° ′	LONG. ° ′	1°×1° mGal	30′×30′ mGal	30′×30′ mGal	30′×30′ mGal	30′×30′ mGal
41 30	130 30	−21	−12	−42	−12	−17
41 30	131 30	−24	−42	−32	−12	−12
41 30	132 30	−22	−32	−32	−12	−12
41 30	133 30	−13	−27	−17	−12	3
41 30	134 30	− 2	− 7	−12	8	3
40 30	131 30	− 3	− 2	− 7	− 2	− 2
40 30	132 30	− 4	− 7	− 5	− 4	0
40 30	133 30	5	2	− 2	4	16
40 30	134 30	22	− 2	0	46	44
44 30	136 30	15	28	8	18	8
44 30	137 30	25	21	26	24	28
44 30	138 30	33	45	39	54	− 7
44 30	139 30	44	41	58	18	58
43 30	135 30	− 2	28	8	−12	−32
43 30	136 30	−17	− 7	−22	−22	−17
43 30	137 30	24	23	32	20	23
43 30	138 30	20	39	5	23	13
43 30	139 30	1	− 1	23	9	−28
42 30	135 30	−13	−12	−12	−17	−12
42 30	136 30	2	8	− 2	8	− 7
42 30	137 30	6	3	8	3	8
42 30	138 30	18	26	16	16	17
42 30	139 30	8	− 8	− 5	− 7	52
41 30	135 30	3	− 7	3	8	8
41 30	136 30	3	8	3	3	− 2
41 30	137 30	− 7	− 2	− 8	−11	− 7
41 30	138 30	14	− 4	13	12	36
41 30	139 30	13	− 1	5	29	18
40 30	135 30	23	4	10	44	35
40 30	136 30	13	9	− 5	29	20
40 30	137 30	4	− 7	1	9	11
40 30	138 30	5	9	− 3	10	6
40 30	139 30	23	0	19	13	59
47 30	140 30	−11	− 8	−13	− 8	−13
47 30	141 30	1	− 3	7	− 8	7
46 30	140 30	1	−13	− 3	7	12
46 30	141 30	12	7	7	37	− 3
45 30	140 30	23	30	20	26	14
45 30	141 30	11	31	− 7	31	−13
45 30	142 30	27	37	16	36	20
45 30	143 30	26	33	26	12	31
45 30	144 30	12	2	12	9	26
45 30	145 30	5	− 4	12	0	12
44 30	140 30	36	55	33	26	31
44 30	141 30	18	39	−17	34	17
44 30	142 30	39	33	32	47	44
44 30	143 30	28	12	29	34	36
44 30	144 30	24	31	−11	49	27
43 30	140 30	34	25	17	39	55
43 30	141 30	37	36	40	42	31
43 30	142 30	51	43	57	34	69
43 30	143 30	54	50	64	30	71
43 30	144 30	99	60	86	113	137
42 30	140 30	58	61	67	62	44
42 30	141 30	23	77	5	45	−37
42 30	142 30	−31	−12	47	−131	−30
42 30	143 30	− 8	32	22	9	−96
42 30	144 30	−11	48	92	−105	−80
41 30	140 30	76	82	76	68	76

LAT. ° ′	LONG. ° ′	1°×1° mGal	30′×30′ mGal	30′×30′ mGal	30′×30′ mGal	30′×30′ mGal
41 30	141 30	47	66	−26	97	50
41 30	142 30	−122	−164	−133	−56	−134
41 30	143 30	−105	−55	−63	−164	−139
41 30	144 30	−153	−127	−167	−148	−172
40 30	140 30	67	57	73	64	73
40 30	141 30	116	90	107	111	157
40 30	142 30	18	32	−53	84	7
40 30	143 30	−58	−60	−93	−22	−57
40 30	144 30	−125	−173	−130	−127	−72
44 30	145 30	28	20	20	35	35
43 30	145 30	122	87	73	175	154
42 30	145 30	−41	35	−33	−83	−81
41 30	145 30	−110	−134	−137	−126	−43
40 30	145 30	−14	−48	− 4	−12	7
40 30	146 30	36	30	50	31	35
34 30	128 30	18	26	11	26	11
34 30	129 30	18	− 2	33	25	14
33 30	128 30	9	7	10	7	10
33 30	129 30	26	20	26	29	29
32 30	128 30	25	22	25	29	26
32 30	129 30	23	25	28	17	21
31 30	128 30	21	30	5	31	18
31 30	129 30	29	11	33	27	44
30 30	129 30	34	30	34	35	37
39 30	130 30	8	− 1	19	19	− 6
39 30	132 30	5	− 1	5	4	11
39 30	133 30	26	16	49	23	16
39 30	134 30	35	35	15	34	56
38 30	130 30	− 9	−11	−21	−11	9
38 30	131 30	9	− 1	3	9	24
38 30	132 30	23	12	18	30	30
38 30	133 30	19	14	12	27	25
38 30	134 30	15	14	13	20	13
37 30	131 30	6	8	13	1	4
37 30	132 30	22	21	32	17	19
37 30	133 30	24	32	24	27	12
37 30	134 30	− 1	4	− 7	− 6	7
36 30	131 30	5	5	5	7	5
36 30	132 30	5	1	11	− 3	10
36 30	133 30	21	25	7	28	23
36 30	134 30	0	18	4	−14	− 6
35 30	130 30	17	25	26	10	9
35 30	131 30	11	20	− 2	17	10
35 30	132 30	22	0	21	25	41
35 30	133 30	27	27	5	40	36
35 30	134 30	21	13	12	33	25
39 30	135 30	30	35	48	30	5
39 30	136 30	25	33	28	14	24
39 30	137 30	25	25	23	26	25
39 30	138 30	25	18	28	10	45
39 30	139 30	31	30	46	27	20
38 30	135 30	9	18	19	5	− 5
38 30	136 30	17	12	15	4	37
38 30	137 30	31	33	28	55	9

LAT. ° ′	LONG. ° ′	1°×1° mGal	30′×30′ mGal	30′×30′ mGal	30′×30′ mGal	30′×30′ mGal
38 30	138 30	33	28	37	40	29
38 30	139 30	41	32	42	27	62
37 30	135 30	22	− 2	18	33	39
37 30	136 30	51	47	58	48	51
37 30	137 30	12	64	− 8	10	−20
37 30	138 30	15	22	9	10	19
37 30	139 30	52	27	46	66	70
36 30	135 30	− 2	0	− 2	6	−11
36 30	136 30	27	21	24	19	45
36 30	137 30	31	− 3	49	29	47
36 30	138 30	59	50	71	58	57
36 30	139 30	69	72	87	44	75
35 30	135 30	8	16	− 9	23	0
35 30	136 30	0	14	21	−19	−18
35 30	137 30	45	25	53	36	67
35 30	138 30	54	56	62	44	55
35 30	139 30	26	44	9	38	13
34 30	130 30	6	− 5	− 3	9	22
34 30	131 30	15	10	18	24	8
34 30	132 30	9	27	23	−14	− 1
34 30	133 30	17	22	17	7	20
34 30	134 30	19	21	15	21	17
33 30	130 30	25	32	29	23	16
33 30	131 30	10	24	9	16	− 7
33 30	132 30	3	− 9	− 6	5	20
33 30	133 30	29	18	31	43	25
33 30	134 30	36	43	25	41	34
32 30	130 30	31	33	27	41	23
32 30	131 30	−17	26	−22	− 8	−64
32 30	132 30	−10	−17	32	−54	− 2
32 30	133 30	42	45	36	43	46
32 30	134 30	3	36	7	4	−34
31 30	130 30	36	38	31	44	33
31 30	131 30	−41	3	−92	− 3	−71
31 30	132 30	−28	−64	0	−35	−14
31 30	133 30	−13	− 7	−30	−19	−10
31 30	134 30	−12	−31	−32	6	9
30 30	130 30	37	37	38	35	39
30 30	131 30	−41	−18	−51	−60	−35
30 30	132 30	− 4	4	−19	5	− 8
30 30	133 30	13	− 2	18	12	24
34 30	135 30	32	7	20	29	71
34 30	136 30	37	33	4	75	36
34 30	137 30	24	36	33	7	19
34 30	138 30	23	31	43	13	7
34 30	139 30	60	47	46	79	67
33 30	135 30	52	52	102	9	46
33 30	136 30	−15	47	−36	−42	−27
33 30	137 30	−13	−12	− 7	−28	− 3
33 30	138 30	14	22	− 5	− 8	47
33 30	139 30	85	55	91	64	128
32 30	135 30	−52	−34	−50	−61	−64
32 30	136 30	−18	−34	− 5	−37	5
32 30	137 30	5	8	6	17	−10
32 30	138 30	16	− 7	25	15	30
32 30	139 30	103	73	143	62	135
31 30	135 30	− 4	−38	−26	19	31
31 30	136 30	24	8	26	31	31
31 30	137 30	16	9	10	20	27
31 30	138 30	43	30	63	32	47

LAT. ° ′	LONG. ° ′	1°×1° mGal	30′×30′ mGal	30′×30′ mGal	30′×30′ mGal	30′×30′ mGal
31 30	139 30	94	64	100	88	122
30 30	137 30	31	30	31	31	31
30 30	138 30	37	31	39	34	44
30 30	139 30	89	64	112	73	106
39 30	140 30	64	55	75	56	70
39 30	141 30	130	125	148	103	145
39 30	142 30	53	106	5	99	1
39 30	143 30	−67	−45	−71	−55	−98
39 30	144 30	−74	−99	−35	−130	−34
38 30	140 30	70	62	75	60	84
38 30	141 30	115	108	124	110	120
38 30	142 30	52	88	18	78	25
38 30	143 30	−72	−30	−112	−24	−124
38 30	144 30	−69	−132	−25	−105	−15
37 30	140 30	105	82	113	89	135
37 30	141 30	96	99	106	86	92
37 30	142 30	− 9	57	− 2	− 6	−83
37 30	143 30	−122	−83	−132	−150	−122
37 30	144 30	−41	−73	−28	−50	−13
36 30	140 30	115	112	122	130	96
36 30	141 30	7	55	12	17	−57
36 30	142 30	−116	−68	−133	−98	−164
36 30	143 30	−92	−158	−88	−102	−22
36 30	144 30	4	−24	27	6	8
35 30	140 30	32	38	52	35	3
35 30	141 30	−80	− 3	−76	−76	−168
35 30	142 30	−125	−134	−66	−210	−91
35 30	143 30	−10	−29	− 1	−20	9
35 30	144 30	21	22	17	25	20
39 30	145 30	0	−14	9	− 1	6
39 30	146 30	20	24	29	13	14
39 30	147 30	15	25	15	13	5
38 30	145 30	4	4	7	0	4
38 30	146 30	9	10	12	7	7
38 30	147 30	− 1	9	− 5	4	−11
37 30	145 30	− 9	−12	− 3	−15	− 5
37 30	146 30	− 1	2	3	− 2	− 6
37 30	147 30	−16	− 3	−13	−21	−25
36 30	145 30	2	6	− 9	6	5
36 30	146 30	2	5	5	− 1	− 1
36 30	147 30	− 1	3	1	− 3	− 3
34 30	140 30	13	−31	−21	81	22
34 30	141 30	−205	−136	−247	−159	−279
34 30	142 30	−104	−207	−48	−148	−13
34 30	143 30	7	−11	3	2	33
34 30	144 30	30	27	23	45	24
33 30	140 30	138	167	104	148	135
33 30	141 30	−107	−33	−257	52	−186
33 30	142 30	−101	−185	−18	−204	6
33 30	143 30	34	22	27	56	31
33 30	144 30	23	34	20	23	14
32 30	140 30	102	143	105	111	48
32 30	141 30	−55	80	−143	27	−184
32 30	142 30	−92	−176	−30	−154	− 9
32 30	143 30	31	37	28	34	24
32 30	144 30	13	16	10	14	10
31 30	140 30	60	79	30	91	40
31 30	141 30	−29	39	−116	42	−81

LAT. ° ′	LONG. ° ′	1°×1° mGal	30′×30′ mGal	30′×30′ mGal	30′×30′ mGal	30′×30′ mGal
31 30	142 30	−147	−214	−45	−238	−89
31 30	143 30	35	38	28	40	33
31 30	144 30	13	14	11	16	11
30 30	140 30	87	99	66	117	65
30 30	141 30	15	51	−51	60	1
30 30	142 30	−146	−216	−80	−168	−121
30 30	143 30	37	40	42	18	49
30 30	144 30	22	24	13	31	19
27 30	123 30	5	0	1	10	10
27 30	124 30	13	7	15	12	17
26 30	123 30	28	25	25	32	32
26 30	124 30	35	24	26	37	55
25 30	122 30	24	39	38	3	16
25 30	123 30	38	43	47	35	26
25 30	124 30	22	44	17	11	16
29 30	127 30	21	20	24	20	20
29 30	128 30	27	20	31	21	38
29 30	129 30	29	46	31	33	8
28 30	125 30	19	11	15	21	29
28 30	126 30	31	19	22	53	31
28 30	127 30	24	17	18	26	34
28 30	128 30	38	38	42	47	24
28 30	129 30	14	9	21	38	−14
27 30	125 30	46	28	50	42	63
27 30	126 30	44	58	33	47	38
27 30	127 30	49	38	44	56	56
27 30	128 30	33	52	26	43	10
27 30	129 30	−45	−13	−61	−66	−42
26 30	125 30	38	61	33	43	14
26 30	126 30	32	38	43	29	19
26 30	127 30	45	58	45	43	35
26 30	128 30	− 9	34	−36	3	−38
26 30	129 30	−62	−48	−68	−72	−61
25 30	125 30	26	11	20	32	42
25 30	126 30	−16	42	4	−25	−86
25 30	127 30	−35	−51	−29	−34	−26
25 30	128 30	−58	− 7	−86	−81	−58
25 30	129 30	−17	−65	−16	−11	24
24 30	122 30	−27	−27	33	−79	−34
24 30	123 30	47	40	30	49	71
24 30	124 30	36	38	49	46	9
23 30	122 30	−64	−29	−124	− 3	−101
23 30	123 30	−58	−43	− 2	−111	−74
23 30	124 30	−54	−18	−31	−74	−94
22 30	121 30	2	8	5	1	− 5
22 30	122 30	4	9	−41	19	27
22 30	123 30	−29	−101	−30	−14	31
22 30	124 30	0	−17	−19	21	15
21 30	120 30	−10	− 3	− 5	−29	− 3
21 30	121 30	12	− 3	13	−18	56
21 30	122 30	11	0	34	−10	18
21 30	123 30	3	− 6	21	−25	22
21 30	124 30	22	23	27	18	21
20 30	120 30	−26	−28	−12	−24	−40
20 30	121 30	38	−45	105	−16	109
20 30	122 30	− 6	13	−15	2	−23
20 30	123 30	3	−22	21	− 8	21
20 30	124 30	20	23	14	28	13

LAT. ° ′	LONG. ° ′	1°×1° mGal	30′×30′ mGal	30′×30′ mGal	30′×30′ mGal	30′×30′ mGal
24 30	125 30	8	48	−22	−13	19
24 30	126 30	− 1	−30	9	54	−37
24 30	127 30	−53	−27	−70	−84	−31
24 30	128 30	− 9	−34	− 7	− 5	13
24 30	129 30	26	16	34	23	30
23 30	125 30	−50	−25	−18	−93	−63
23 30	126 30	−39	−56	−57	−31	−10
23 30	127 30	1	−21	− 1	6	19
23 30	128 30	8	− 7	15	13	11
23 30	129 30	21	21	22	17	25
22 30	125 30	2	−19	−10	20	17
22 30	126 30	8	2	6	10	15
22 30	127 30	9	5	9	5	17
22 30	128 30	16	14	11	23	17
22 30	129 30	10	17	14	9	0
21 30	125 30	19	24	18	17	15
21 30	126 30	14	14	11	16	14
21 30	127 30	15	11	13	17	18
21 30	128 30	20	17	12	27	25
21 30	129 30	4	7	− 1	9	1
20 30	125 30	17	12	17	21	18
20 30	126 30	14	13	10	21	10
20 30	127 30	10	10	10	10	10
20 30	128 30	11	12	12	10	10
20 30	129 30	9	10	10	9	6
29 30	130 30	−33	19	−43	−14	−93
29 30	131 30	−56	−76	−41	−65	−41
29 30	132 30	− 1	2	2	−11	3
29 30	133 30	21	11	16	5	53
28 30	130 30	−71	−61	−72	−64	−87
28 30	131 30	− 5	−30	−10	−19	40
28 30	132 30	46	17	29	63	74
28 30	133 30	11	1	− 1	44	1
27 30	130 30	−72	−61	−85	−81	−61
27 30	131 30	−10	−22	18	−32	− 6
27 30	132 30	16	48	23	− 1	− 5
27 30	133 30	1	13	− 7	− 2	− 3
26 30	130 30	− 8	−57	−16	1	42
26 30	131 30	22	2	8	58	20
26 30	132 30	− 1	− 4	− 4	1	2
26 30	133 30	− 1	3	− 1	− 2	− 5
25 30	130 30	11	− 8	−10	30	31
25 30	131 30	8	16	32	14	−29
25 30	132 30	28	67	67	−29	7
25 30	133 30	0	22	−13	22	−32
24 30	130 30	35	40	55	25	21
24 30	131 30	43	62	12	47	51
24 30	132 30	− 6	−29	−36	21	19
23 30	130 30	11	23	−13	28	6
23 30	131 30	10	5	19	6	9
23 30	132 30	7	16	9	2	1
22 30	130 30	− 4	4	− 7	− 4	− 8
22 30	131 30	− 1	− 1	1	− 4	0
22 30	132 30	6	2	10	3	10
21 30	130 30	2	− 3	2	4	5
21 30	131 30	5	3	7	5	5
21 30	132 30	5	6	4	4	4
20 30	130 30	5	5	5	5	5

LAT. ° ′	LONG. ° ′	1°×1° mGal	30′×30′ mGal	30′×30′ mGal	30′×30′ mGal	30′×30′ mGal
20 30	131 30	5	5	5	5	4
20 30	132 30	5	5	5	5	5
19 30	122 30	4	23	−18	39	−30
19 30	123 30	8	3	12	3	16
19 30	124 30	17	13	12	24	19
18 30	122 30	−25	19	−61	7	−67
18 30	123 30	1	−13	27	−31	23
18 30	124 30	32	39	27	36	28

REPORT OF HYDROGRAPHIC RESEARCHES No. 15, March, 1980

TRIGONOMETRIC SERIES FOR THE COORDINATES OF THE OBJECTS IN THE SOLAR SYSTEM

Yoshio Kubo*

Received 1979 September 10

Abstract

Trigonometric series for approximate positions of some objects in the solar system are developed. These give geocentric positions of the Sun and the Moon and heliocentric and geocentric positions of the inner planets with a precision of 0.1, which corresponds to the precision in the *Nautical Almanac*.

Key Words : trigonometric series-coordinates of celestial objects

1. Introduction

The spread of electronic calculators has made it quite easy to carry out some astronomical calculations such as obtaining the altitude and azimuth of a celestial object from its right ascension and declination. In that case, the right ascension and declination still have to be obtained from an almanac, interpolated if necessary and put into the calculator as data. Some calculators, however, have an ability of programmed calculation as well as a fairly large number of memories. With such calculators, if a proper formula giving the position of the celestial object is available and programmed, the user will be able to obtain the position by himself. And if it is combined with the program calculating the horizontal coordinates, the altitude or the azimuth will be obtained only by giving the time for which the user desires to calculate them.

In order to provide users of such calculators or mini or personal computers with compact formulas giving approximate coordinates of the objects in the solar system, some trigonometric series have been developed. They consist of the series for geocentric positions of the Sun and the Moon both in ecliptic and equatorial coordinate systems and the heliocentric ecliptic and the geocentric equatorial coordinates of the inner planets.

The formulas are intended to be correct for the years 1970 to 2030, to the precision of 0.1 which is the same as in the *Nautical Almanac* published by the Hydrographic Department of Japan.

As for the outer planets, the present ephemerides are computed by a numerical integration and there exists no analytical formula to represent the result of the integration. This makes the derivation of similar trigonometric series for the outer planets somewhat difficult. However, a new method valid in such a case is being developed and the series will appear in a coming volume of this report.

* Astronomical Division

2. Method of Derivation of the Series

Series for the geocentric longitude, latitude and distance of the Sun and the heliocentric longitudes, latitudes and radius vectors of the inner planets are first derived, based on the respective *Tables* by Newcomb (1895a, 1895b, 1895c, 1898) amended by Ross (1917) for the elements of Mars. Also those for the longitude, latitude and horizontal parallax of the Moon are derived from *Improved Lunar Ephemeris* (Eckert, Jones, Clark, 1954), etc. In deriving the series only the terms of the perturbations greater than 1″ or the equivalent amount for radius vector are taken into consideration. The results are Fourier series with numerical coefficients and arguments consisting of linear combinations of the mean anomalies of planets and so on.

Then, the transformations from heliocentric to geocentric coordinates for the planets and from ecliptic to equatorial coordinates are carried out. Further the effects of nutation and aberration are considered. Throughout these procedures, all the calculations are carried out retaining the form of Fourier series, thus giving apparent geocentric equatorial coordinates also as Fourier series. The operations have been performed using a Fourier series processor for computer developed by the author. At the final stage the arguments are reduced to the form of $aT+b$ by substituting numerical values for the mean anomalies and so on.

3. Structure of the Series

i) General

The formulas give the coordinates of the celestial objects at any time referred to the ecliptic or equator and the equinox *of date*. As for the rectangular coordinates of the Sun, those referred to the equator and equinox of any epoch can be also obtained.

T is the desired time for which the position is to be calculated, measured from J2000.0 in Julian ephemeris centuries, or

$$T=\frac{\mathrm{JED}-2451545.0}{36525},$$

JED being the Julian ephemeris date of the desired time.

In the terms with coefficient multiplied by T, the cosine function is not printed but replaced with double commas (,,) to show it is the cosine function having the same arguments as immediately above.

ii) Sun

The series for geocentric ecliptic coordinates are given in Table 1. They are referred to the mean equinox and do not undergo aberratoin. The latitude is zero with the present precision. In order to get apparent longitude, $-0\overset{\circ}{.}0057+0\overset{\circ}{.}0048\cos(1934^\circ T+145^\circ)$ must be added to the mean longitude.

In Table 2, the series for apparent right ascension and declination are shown. Related to the right ascension of the Sun, Greenwich mean and apparent sidereal times are given by

$$\mathrm{GMST}=12^{\mathrm{h}}+\mathrm{UT}+\alpha_{\mathrm{m}}$$

and

$$\mathrm{GAST}=12^{\mathrm{h}}+\mathrm{UT}+\alpha_{\mathrm{m}}+p$$

respectively, where UT is the universal time,

$$\alpha_m = 18^h.69735 + 2400^h.05130\ T$$

and

$$p = 0^h.00029 \cos\ (1934^\circ\ T + 145^\circ).$$

Table 1. Sun: Mean longitude and geocentric distance (Latitude is zero)

LONGITUDE

$$\begin{aligned}
&280.4659^\circ + 36000.7695^\circ\ T \\
&+ 1.9147 \cos (35999.050^\circ\ T + 267.520^\circ) \\
&- 48T'' \\
&+ 0.0200 \cos (71998.1^\circ\ T + 265.1^\circ) \\
&+ 20 \cos (32964^\circ\ T + 158^\circ) \\
&+ 18 \cos (19^\circ\ T + 159^\circ) \\
&+ 18 \cos (445267^\circ\ T + 208^\circ) \\
&+ 15 \cos (45038^\circ\ T + 254^\circ) \\
&+ 13 \cos (22519^\circ\ T + 352^\circ) \\
&+ 7 \cos (65929^\circ\ T + 45^\circ) \\
&+ 7 \cos (3035^\circ\ T + 110^\circ) \\
&+ 7 \cos (9038^\circ\ T + 64^\circ) \\
&+ 6 \cos (33718^\circ\ T + 316^\circ) \\
&+ 5 \cos (155^\circ\ T + 118^\circ)
\end{aligned}$$

$$\begin{aligned}
&+ 0.0005 \cos (2281^\circ\ T + 221^\circ) \\
&+ 4 \cos (29930^\circ\ T + 48^\circ) \\
&+ 4 \cos (31557^\circ\ T + 161^\circ)
\end{aligned}$$

DISTANCE

$$\begin{aligned}
&1.000140\ \text{AU} \cos (0^\circ\ T + 0^\circ) \\
&+ 0.016706 \cos (35999.05^\circ\ T + 177.53^\circ) \\
&- 42T'' \\
&+ 139 \cos (71998^\circ\ T + 175^\circ) \\
&+ 31 \cos (445267^\circ\ T + 298^\circ) \\
&+ 16 \cos (32964^\circ\ T + 68^\circ) \\
&+ 16 \cos (45038^\circ\ T + 164^\circ) \\
&+ 5 \cos (22519^\circ\ T + 233^\circ) \\
&+ 5 \cos (33718^\circ\ T + 226^\circ)
\end{aligned}$$

Table 2. Sun: Apparent right ascension and declination

RIGHT ASCENSION

$$\begin{aligned}
&18.69735^h + 2400.05130^h\ T \\
&+ 0.16419^h \cos (72001.539^\circ\ T + 290.920^\circ) \\
&- 19T'' \\
&+ 12764 \cos (35999.050^\circ\ T + 267.520^\circ) \\
&- 32T'' \\
&+ 549 \cos (36002.5^\circ\ T + 113.4^\circ) \\
&- 2T'' \\
&+ 549 \cos (108000.6^\circ\ T + 288.5^\circ) \\
&- 2T'' \\
&+ 353 \cos (144003.1^\circ\ T + 311.9^\circ) \\
&+ 133 \cos (71998.1^\circ\ T + 265.1^\circ) \\
&+ 32 \cos (1934^\circ\ T + 145^\circ) \\
&+ 24 \cos (108004^\circ\ T + 134^\circ) \\
&+ 24 \cos (180002^\circ\ T + 309^\circ) \\
&+ 15 \cos (144000^\circ\ T + 286^\circ) \\
&+ 13 \cos (32964^\circ\ T + 158^\circ) \\
&+ 12 \cos (19^\circ\ T + 159^\circ) \\
&+ 12 \cos (445267^\circ\ T + 208^\circ) \\
&+ 10 \cos (45038^\circ\ T + 254^\circ) \\
&+ 10 \cos (216005^\circ\ T + 333^\circ) \\
&+ 9 \cos (22519^\circ\ T + 352^\circ) \\
&+ 5 \cos (65929^\circ\ T + 45^\circ) \\
&+ 5 \cos (3035^\circ\ T + 110^\circ) \\
&+ 5 \cos (9038^\circ\ T + 64^\circ) \\
&+ 4 \cos (33718^\circ\ T + 316^\circ) \\
&+ 3 \cos (155^\circ\ T + 118^\circ) \\
&+ 3 \cos (73936^\circ\ T + 166^\circ) \\
&+ 3 \cos (2281^\circ\ T + 221^\circ)
\end{aligned}$$

$$\begin{aligned}
&+ 0.00003^h \cos (3^\circ\ T + 296^\circ) \\
&+ 3 \cos (29930^\circ\ T + 48^\circ) \\
&+ 3 \cos (31557^\circ\ T + 161^\circ)
\end{aligned}$$

DECLINATION

$$\begin{aligned}
&+ 23.2643^\circ \cos (36000.7696^\circ\ T + 190.4602^\circ) \\
&- 127T'' \\
&+ 0.3888^\circ \cos (1.72^\circ\ T + 12.94^\circ) \\
&- 12T'' \\
&+ 3886 \cos (71999.82^\circ\ T + 187.99^\circ) \\
&- 12T'' \\
&+ 1646 \cos (108002.3^\circ\ T + 211.4^\circ) \\
&- 3T'' \\
&+ 82 \cos (72003^\circ\ T + 34^\circ) \\
&+ 82 \cos (144001^\circ\ T + 209^\circ) \\
&+ 73 \cos (107999^\circ\ T + 186^\circ) \\
&+ 31 \cos (180004^\circ\ T + 232^\circ) \\
&+ 22 \cos (37935^\circ\ T + 65^\circ) \\
&+ 8 \cos (35997^\circ\ T + 345^\circ) \\
&+ 4 \cos (68965^\circ\ T + 78^\circ) \\
&+ 4 \cos (3036^\circ\ T + 123^\circ) \\
&+ 3 \cos (481268^\circ\ T + 128^\circ) \\
&+ 3 \cos (35982^\circ\ T + 121^\circ) \\
&+ 3 \cos (36020^\circ\ T + 80^\circ) \\
&+ 3 \cos (409266^\circ\ T + 287^\circ) \\
&+ 3 \cos (13482^\circ\ T + 293^\circ) \\
&+ 3 \cos (9037^\circ\ T + 332^\circ) \\
&+ 3 \cos (180000^\circ\ T + 206^\circ)
\end{aligned}$$

In Table 3, the series for equatorial rectangular coordinates are shown. The coordinates are free from aberration and are referred to the mean equator and equinox of date. However, the series give those referred to the equator and equinox of any epoch, if $-1^\circ.3963\,\tau$ is added to the arguments of cosine functions, τ being the time interval from the epoch to the desired time in Julian ephemeris centuries.

Table 3. Sun: Equatorial rectangular coordinates

X

AU °

+ 0.999860 COS (36000.7696T + 280.4659)
+ 25063 COS (1.720 T + 102.941)
- 63T ″
+ 8354 COS (71999.82 T + 277.99)
- 21T ″
+ 105 COS (107999 T + 276)
+ 35 COS (35997 T + 75)
+ 31 COS (481268 T + 218)
+ 26 COS (3036 T + 213)
+ 21 COS (9037 T + 244)
+ 16 COS (35982 T + 211)
+ 16 COS (36020 T + 170)
+ 14 COS (13482 T + 23)
+ 10 COS (58520 T + 9)
+ 9 COS (68965 T + 168)
+ 7 COS (2282 T + 54)
+ 7 COS (101930 T + 56)
+ 7 COS (29928 T + 35)
+ 6 COS (32966 T + 261)
+ 6 COS (39035 T + 120)
+ 6 COS (26962 T + 306)
+ 6 COS (45039 T + 75)
+ 6 COS (81038 T + 265)
+ 5 COS (36156 T + 128)
+ 5 COS (35846 T + 253)
+ 4 COS (33720 T + 149)
+ 4 COS (38281 T + 232)
+ 4 COS (6071 T + 323)
+ 4 COS (65931 T + 58)
+ 4 COS (67558 T + 172)
+ 4 COS (4444 T + 209)

Y

AU °

+ 0.917354 COS (36000.7696T + 190.4659)
+ 91T ″
+ 22995 COS (1.720 T + 12.941)
- 56T ″
+ 7664 COS (71999.82 T + 187.99)
- 19T ″
+ 3324 COS (107999 T + 186)
+ 1147 COS (35997 T + 165)
+ 544 COS (481268 T + 128)
+ 169 COS (3036 T + 123)
+ 139 COS (9037 T + 334)
+ 93 COS (35982 T + 121)
+ 71 COS (36020 T + 80)
+ 55 COS (13482 T + 293)
+ 32 COS (58520 T + 279)
+ 31 COS (68965 T + 78)
+ 23 COS (2282 T + 324)
+ 19 COS (29928 T + 125)
+ 18 COS (101930 T + 326)
+ 16 COS (39035 T + 30)
+ 16 COS (32966 T + 171)
+ 14 COS (45039 T + 345)
+ 12 COS (26962 T + 216)
+ 11 COS (81038 T + 175)
+ 10 COS (36156 T + 38)
+ 9 COS (35846 T + 163)
+ 8 COS (33720 T + 59)
+ 8 COS (38281 T + 142)

Z

AU °

+ 0.397721 COS (36000.7696T + 190.4659)
- 208T ″
+ 9970 COS (1.72 T + 12.94)
- 30T ″
+ 3323 COS (71999.82 T + 187.99)
- 10T ″
+ 42 COS (107999 T + 186)
+ 14 COS (35997 T + 165)
+ 12 COS (481268 T + 128)
+ 10 COS (3036 T + 123)
+ 8 COS (9037 T + 334)
+ 6 COS (35982 T + 121)
+ 6 COS (36020 T + 80)
+ 6 COS (13482 T + 293)
+ 4 COS (58520 T + 279)
+ 4 COS (68965 T + 78)
+ 4 COS (2282 T + 324)
+ 4 COS (29928 T + 125)
+ 4 COS (101930 T + 326)
+ 4 COS (39035 T + 30)
+ 4 COS (32966 T + 171)
+ 4 COS (45039 T + 345)
+ 4 COS (26962 T + 216)
+ 4 COS (81038 T + 175)
+ 4 COS (36156 T + 38)
+ 4 COS (35846 T + 163)
+ 4 COS (33720 T + 59)
+ 4 COS (38281 T + 142)

iii) Moon

The series for the Moon are given in Tables 4 and 5. Both the ecliptic and equatorial coordinates are referred to the true equinox of date and suffer aberration, though it is very small.

iv) Mercury, Venus and Mars

The series for these planets are listed in Tables 6 through 11. The heliocentric coordinates are referred to the mean equinox of date and do not suffer aberration. Series for apparent right ascension, declination and geocentric distance are not given for these planets because they are too lengthy. Instead, the series giving the geocentric equatorial rectangular coordinates are shown. They are referred to the true equator and equinox of date and suffer aberration. Therefore the apparent right ascension and declination are obtained directly by

$$\text{R.A.} = \tan^{-1}\frac{Y}{X} \quad \text{and} \quad \text{Dec.} = \tan^{-1}\frac{Z}{\sqrt{X^2+Y^2}}.$$

Also,

$$d = \sqrt{X^2+Y^2+Z^2}$$

gives the geocentric distance, though it is not the true distance but suffering aberration.

Table 4. Moon: Apparent longitude, latitude and horizontal parallax

LONGITUDE

$$218.3162 + 481267.8809\,T$$

$$+ 6.2888 \cos(477198.868\,T + 44.963)$$
$$+ 1.2740 \cos(413335.35\,T + 10.74)$$
$$+ 0.6583 \cos(890534.22\,T + 145.70)$$
$$+ 2136 \cos(954397.74\,T + 179.93)$$
$$+ 1851 \cos(35999.05\,T + 87.53)$$
$$+ 1144 \cos(966404.0\,T + 276.5)$$
$$+ 588 \cos(63863.5\,T + 124.2)$$
$$+ 571 \cos(377336.3\,T + 13.2)$$
$$+ 533 \cos(1367733.1\,T + 280.7)$$
$$+ 458 \cos(854535.2\,T + 148.2)$$
$$+ 409 \cos(441199.8\,T + 47.4)$$
$$+ 347 \cos(445267.1\,T + 27.9)$$
$$+ 304 \cos(513197.9\,T + 222.5)$$
$$+ 154 \cos(75870\,T + 41)$$
$$+ 125 \cos(1443603\,T + 52)$$
$$+ 110 \cos(489205\,T + 142)$$
$$+ 107 \cos(1303870\,T + 246)$$
$$+ 100 \cos(1431597\,T + 315)$$
$$+ 85 \cos(826671\,T + 111)$$
$$+ 79 \cos(449334\,T + 188)$$
$$+ 68 \cos(926533\,T + 323)$$
$$+ 52 \cos(31932\,T + 107)$$
$$+ 50 \cos(481266\,T + 205)$$
$$+ 40 \cos(1331734\,T + 283)$$
$$+ 40 \cos(1844932\,T + 56)$$
$$+ 40 \cos(133\,T + 29)$$
$$+ 38 \cos(1781068\,T + 21)$$
$$+ 37 \cos(541062\,T + 259)$$
$$+ 28 \cos(1934\,T + 145)$$
$$+ 27 \cos(918399\,T + 182)$$
$$+ 26 \cos(1379739\,T + 17)$$
$$+ 24 \cos(99863\,T + 122)$$
$$+ 23 \cos(922466\,T + 163)$$
$$+ 22 \cos(818536\,T + 151)$$
$$+ 21 \cos(990397\,T + 357)$$
$$+ 21 \cos(71998\,T + 85)$$
$$+ 21 \cos(341337\,T + 16)$$
$$+ 18 \cos(401329\,T + 274)$$
$$+ 16 \cos(1856938\,T + 152)$$
$$+ 12 \cos(1267871\,T + 249)$$
$$+ 11 \cos(1920802\,T + 186)$$
$$+ 9 \cos(858602\,T + 129)$$
$$+ 8 \cos(1403732\,T + 98)$$
$$+ 7 \cos(790672\,T + 114)$$
$$+ 7 \cos(405201\,T + 50)$$
$$+ 7 \cos(485333\,T + 186)$$
$$+ 7 \cos(27864\,T + 127)$$
$$+ 6 \cos(111869\,T + 38)$$
$$+ 6 \cos(2258267\,T + 156)$$
$$+ 5 \cos(1908795\,T + 90)$$
$$+ 5 \cos(1745069\,T + 24)$$
$$+ 5 \cos(509131\,T + 242)$$
$$+ 4 \cos(39871\,T + 223)$$
$$+ 4 \cos(12006\,T + 187)$$
$$+ 3 \cos(958465\,T + 340)$$
$$+ 3 \cos(381404\,T + 354)$$
$$+ 3 \cos(349472\,T + 337)$$
$$+ 3 \cos(1808933\,T + 58)$$
$$+ 3 \cos(549197\,T + 220)$$
$$+ 3 \cos(4067\,T + 70)$$
$$+ 3 \cos(2322131\,T + 191)$$

LATITUDE

$$+ 5.1281 \cos(483202.019\,T + 3.273)$$
$$+ 0.2806 \cos(960400.89\,T + 138.24)$$
$$+ 2777 \cos(6003.15\,T + 48.31)$$
$$+ 1733 \cos(407332.20\,T + 52.43)$$
$$+ 554 \cos(896537.4\,T + 104.0)$$
$$+ 463 \cos(69866.7\,T + 82.5)$$
$$+ 326 \cos(1373736.2\,T + 239.0)$$
$$+ 172 \cos(1437599.8\,T + 273.2)$$
$$+ 93 \cos(884531\,T + 187)$$
$$+ 88 \cos(471196\,T + 87)$$
$$+ 82 \cos(371333\,T + 55)$$
$$+ 43 \cos(547066\,T + 217)$$

$$+ 0.0042 \cos(1850935\,T + 14)$$
$$+ 34 \cos(443331\,T + 230)$$
$$+ 25 \cos(860538\,T + 106)$$
$$+ 22 \cos(481268\,T + 308)$$
$$+ 22 \cos(1337737\,T + 241)$$
$$+ 21 \cos(105866\,T + 80)$$
$$+ 19 \cos(924402\,T + 141)$$
$$+ 18 \cos(820668\,T + 153)$$
$$+ 18 \cos(519201\,T + 181)$$
$$+ 18 \cos(1449606\,T + 10)$$
$$+ 15 \cos(42002\,T + 46)$$
$$+ 15 \cos(928469\,T + 121)$$
$$+ 15 \cos(996400\,T + 316)$$
$$+ 14 \cos(29996\,T + 129)$$
$$+ 13 \cos(447203\,T + 6)$$
$$+ 13 \cos(37935\,T + 65)$$
$$+ 11 \cos(1914799\,T + 48)$$
$$+ 10 \cos(1297866\,T + 288)$$
$$+ 9 \cos(1787072\,T + 340)$$
$$+ 8 \cos(972407\,T + 235)$$
$$+ 7 \cos(1309873\,T + 205)$$
$$+ 6 \cos(559072\,T + 134)$$
$$+ 6 \cos(1361730\,T + 322)$$
$$+ 5 \cos(848532\,T + 190)$$
$$+ 5 \cos(419339\,T + 149)$$
$$+ 5 \cos(948395\,T + 222)$$
$$+ 4 \cos(2328134\,T + 149)$$
$$+ 4 \cos(1024264\,T + 352)$$
$$+ 3 \cos(932536\,T + 282)$$
$$+ 3 \cos(1409735\,T + 57)$$
$$+ 3 \cos(2264270\,T + 115)$$
$$+ 3 \cos(1814936\,T + 16)$$
$$+ 3 \cos(335334\,T + 57)$$

PARALLAX

$$+ 0.950725 \cos(0\,T + 0)$$
$$+ 51820 \cos(477198.868\,T + 134.963)$$
$$+ 9530 \cos(413335.35\,T + 100.74)$$
$$+ 7842 \cos(890534.22\,T + 235.70)$$
$$+ 2824 \cos(954397.74\,T + 269.93)$$
$$+ 858 \cos(1367733.1\,T + 10.7)$$
$$+ 531 \cos(854535.2\,T + 238.2)$$
$$+ 400 \cos(377336.3\,T + 103.2)$$
$$+ 319 \cos(441199.8\,T + 137.4)$$
$$+ 271 \cos(445267\,T + 118)$$
$$+ 263 \cos(513198\,T + 312)$$
$$+ 197 \cos(489205\,T + 232)$$
$$+ 173 \cos(1431597\,T + 45)$$
$$+ 167 \cos(1303870\,T + 336)$$
$$+ 111 \cos(35999\,T + 178)$$
$$+ 103 \cos(826671\,T + 201)$$
$$+ 84 \cos(63864\,T + 214)$$
$$+ 83 \cos(926533\,T + 53)$$
$$+ 78 \cos(1844932\,T + 146)$$
$$+ 73 \cos(1781068\,T + 111)$$
$$+ 64 \cos(1331734\,T + 13)$$
$$+ 63 \cos(449334\,T + 278)$$
$$+ 41 \cos(481266\,T + 295)$$
$$+ 34 \cos(918399\,T + 272)$$
$$+ 33 \cos(541062\,T + 349)$$
$$+ 31 \cos(922466\,T + 253)$$
$$+ 30 \cos(75870\,T + 131)$$
$$+ 29 \cos(990397\,T + 87)$$
$$+ 26 \cos(818536\,T + 241)$$
$$+ 23 \cos(553069\,T + 266)$$
$$+ 19 \cos(1267871\,T + 339)$$
$$+ 13 \cos(1403732\,T + 188)$$
$$+ 13 \cos(341337\,T + 106)$$
$$+ 13 \cos(401329\,T + 4)$$
$$+ 12 \cos(2258267\,T + 246)$$
$$+ 11 \cos(1908795\,T + 180)$$
$$+ 11 \cos(858602\,T + 219)$$
$$+ 10 \cos(1745069\,T + 114)$$
$$+ 9 \cos(790672\,T + 204)$$
$$+ 7 \cos(2322131\,T + 281)$$
$$+ 7 \cos(1808933\,T + 148)$$
$$+ 6 \cos(485333\,T + 276)$$
$$+ 6 \cos(99863\,T + 212)$$
$$+ 5 \cos(405201\,T + 140)$$

Table 5. Moon: Apparent right ascension and declination

RIGHT ASCENSION

H H
14,55441 + 32084,52539 T

```
H                °                °
+ 0.41925 COS ( 477198,868 T +  44,963 )
+   16358 COS ( 962535,762 T + 166,633 )
-     19T                 ''
+    8494 COS ( 413335,35  T +  10,74  )
+    7104 COS (   1934,14  T + 324,96  )
-      4T                 ''
+    7048 COS ( 964469,90  T +  41,59  )
-      4T                 ''
+    4389 COS ( 890534,22  T + 145,70  )
+    1818 COS ( 485336,89  T + 211,67  )
-      2T                 ''
+    1795 COS (1439734,63  T + 301,60  )
-      2T                 ''
+    1424 COS ( 954397,74  T + 179,93  )
+    1235 COS (  35999,05  T +  87,53  )
+     778 COS ( 487271,0   T +  86,6   )
+     773 COS (1441668,8   T + 176,6   )
+     763 COS ( 966404,0   T + 276,5   )
+     392 COS (  63863,5   T + 124,2   )
+     383 COS ( 549200,4   T + 245,9   )
+     381 COS ( 377336,3   T +  13,2   )
+     355 COS (1367733,1   T + 280,7   )
+     348 COS (1925071,5   T +  63,3   )
+     345 COS (1375871,1   T + 267,4   )
+     306 COS ( 960601,6   T + 291,7   )
+     305 COS ( 854535,2   T + 148,2   )
+     295 COS (1927005,7   T + 298,2   )
+     273 COS ( 441199,8   T +  47,4   )
+     268 COS (  73935,7   T + 345,9   )
+     232 COS ( 445267,1   T +  27,9   )
+     223 COS (1853070,0   T +  42,3   )
+     203 COS ( 888600,1   T +  90,7   )
+     203 COS ( 513197,9   T + 222,5   )
+     160 COS (1916933,5   T +  76,6   )
+     159 COS ( 551134,5   T + 120,9   )
+     154 COS (  72001,5   T + 110,9   )
+     149 COS (1377805,3   T + 142,3   )
+     102 COS (  75870     T +  41     )
+      97 COS (1855004     T + 277     )
+      96 COS (1928940     T + 173     )
+      83 COS (1443603     T +  52     )
+      79 COS (1447873     T + 108     )
+      78 COS (2402270     T + 198     )
+      73 COS ( 489205     T + 142     )
+      71 COS (1303870     T + 246     )
+      69 COS (1918868     T + 312     )
+      68 COS (1431597     T + 315     )
+      67 COS (1449807     T + 343     )
+      66 COS (2404205     T +  73     )
+      59 COS (1026399     T +  21     )
+      57 COS ( 826671     T + 111     )
+      53 COS ( 449334     T + 188     )
+      53 COS ( 998535     T + 344     )
+      52 COS ( 926537     T + 169     )
+      45 COS ( 926533     T + 323     )
+      40 COS (2330269     T + 177     )
+      38 COS (   8138     T + 257     )
+      34 COS (  31932     T + 107     )
+      34 COS ( 483403     T + 337     )
+      34 COS (1437800     T +  67     )
+      34 COS (   3868     T + 200     )
+      33 COS ( 481266     T + 205     )
+      28 COS ( 411401     T + 136     )
+      27 COS (1331734     T + 283     )
+      27 COS (1844932     T +  56     )
+      26 COS (    133     T +  29     )
+      26 COS (1781068     T +  21     )
+      25 COS ( 541062     T + 259     )
+      24 COS ( 898672     T + 312     )
+      23 COS (1028333     T + 256     )
+      23 COS (1365799     T + 226     )
+      22 COS (2406139     T + 308     )
+      18 COS ( 918399     T + 182     )
+      18 COS (1403736     T + 304     )
+      17 COS (2332203     T +  52     )
+      17 COS (1511736     T + 143     )
+      16 COS ( 585199     T + 243     )
+      16 COS (  99863     T + 122     )
+      16 COS (1339872     T + 270     )
+      16 COS (1379739     T +  17     )
+      16 COS ( 922466     T + 163     )
+      15 COS (1513670     T +  17     )
+      15 COS (1817071     T +  45     )
+      15 COS ( 818536     T + 151     )
+      15 COS (1451741     T + 218     )
+      15 COS (1475734     T + 119     )
+      14 COS (2338407     T + 164     )
+      14 COS ( 990397     T + 357     )
+      14 COS (1930874     T +  48     )
```

```
H                °                °
+ 0.00014 COS (  71998     T +  85     )
+      14 COS ( 341337     T +  16     )
+      14 COS (1000469     T + 219     )
+      13 COS (1036471     T + 243     )
+      13 COS (2394132     T + 212     )
+      13 COS (1923137     T + 188     )
+      13 COS ( 109935     T + 343     )
+      13 COS ( 928471     T +  44     )
+      12 COS (2889541     T + 195     )
+      12 COS (2340341     T +  39     )
+      11 COS ( 401329     T + 274     )
+      11 COS (2815606     T + 299     )
+      11 COS (2879469     T + 333     )
+      11 COS ( 108001     T + 108     )
+      11 COS (1856938     T + 152     )
+      10 COS (2887607     T + 320     )
+      10 COS ( 517269     T + 229     )
+      10 COS (1407803     T + 284     )
+      10 COS (2881403     T + 208     )
+      10 COS ( 900606     T + 187     )
+      10 COS ( 952464     T + 125     )
+      10 COS (2817540     T + 174     )
+      10 COS (  34065     T + 213     )
+       9 COS (  37933     T + 322     )
+       8 COS ( 852601     T +  93     )
+       8 COS ( 886666     T + 216     )
+       8 COS ( 475265     T + 170     )
+       8 COS (1373937     T +  32     )
+       8 COS (1267871     T + 249     )
+       8 COS (1920802     T + 186     )
+       7 COS (2266405     T + 143     )
+       7 COS ( 587134     T + 118     )
+       7 COS (2891476     T +  70     )
+       7 COS ( 547266     T +  11     )
+       7 COS (  10072     T + 132     )
+       7 COS ( 473331     T + 115     )
+       7 COS (1341806     T + 145     )
+       6 COS (1405670     T + 179     )
+       6 COS (1503598     T + 156     )
+       6 COS (1819005     T + 280     )
+       6 COS ( 970674     T + 153     )
+       6 COS (1789206     T +   8     )
+       6 COS ( 858602     T + 129     )
+       6 COS ( 521336     T + 209     )
+       6 COS (2396067     T +  86     )
+       5 COS (1477668     T + 354     )
+       5 COS (1403732     T +  98     )
+       5 COS ( 405197     T + 204     )
+       5 COS (2807468     T + 312     )
+       5 COS ( 405201     T +  50     )
+       5 COS ( 485333     T + 186     )
+       5 COS (  37937     T + 168     )
+       5 COS (1301935     T + 191     )
+       5 COS (  27864     T + 127     )
+       5 COS ( 972608     T +  28     )
+       5 COS (1034537     T +   8     )
+       5 COS ( 790672     T + 114     )
+       4 COS ( 958667     T +  57     )
+       4 COS (1409737     T + 159     )
+       4 COS ( 924599     T + 268     )
+       4 COS (2342275     T + 274     )
+       4 COS (2412343     T + 240     )
+       4 COS (3366740     T + 330     )
+       4 COS (1988935     T + 277     )
+       4 COS ( 519203     T + 104     )
+       4 COS (1851136     T + 347     )
+       4 COS (1411870     T +  85     )
+       4 COS (1515604     T + 252     )
+       4 COS (2408073     T + 183     )
+       3 COS (2268339     T +  18     )
+       3 COS (2410408     T +   5     )
+       3 COS (3364806     T +  95     )
+       3 COS (1908795     T +  90     )
+       3 COS ( 111869     T +  38     )
+       3 COS (1445939     T + 233     )
+       3 COS ( 523270     T +  84     )
+       3 COS (2400336     T + 323     )
+       3 COS (2743604     T + 278     )
+       3 COS (1791141     T + 243     )
+       3 COS (1914999     T + 202     )
+       3 COS (2258267     T + 156     )
+       3 COS ( 994468     T +   4     )
+       3 COS ( 449338     T +  34     )
+       3 COS (1745069     T +  24     )
+       3 COS (1861208     T + 209     )
+       3 COS (2294270     T + 180     )
+       3 COS ( 349472     T + 337     )
+       3 COS (1779134     T + 326     )
+       3 COS (1990869     T + 152     )
+       3 COS (1961071     T + 241     )
+       3 COS (1889072     T +  66     )
+       3 COS (1842998     T +   1     )
```

Table 5. Moon: Apparent right ascension and declination (Continued)

```
   H                                  °                                  °
+ 0.00002 COS (  12006      T + 187      )
+       2 COS (  451272     T + 269      )
+       2 COS (  509131     T + 242      )
+       2 COS (   70067     T + 236      )
+       2 COS ( 1880934     T +  79      )
+       2 COS ( 3368674     T + 205      )
+       2 COS ( 2893410     T + 305      )
+       2 COS ( 2883338     T +  83      )
+       2 COS (  381404     T + 354      )
+       2 COS (   39871     T + 223      )
+       2 COS ( 1889069     T + 220      )
+       2 COS ( 2819474     T +  49      )
+       2 COS ( 2414277     T + 115      )
+       2 COS (  549197     T + 220      )
+       2 COS (  958465     T + 340      )
+       2 COS (  135865     T + 325      )
+       2 COS (    4067     T +  70      )

   DECLINATION

   °                                  °                                  °
+ 23.1925 COS (  481267.8808T + 128.3163 )
-    127T                          ′′
+  4.9107 COS (  483202.019  T +   3.273  )
+  1.2789 COS (    4069.01   T + 173.35   )
-     7T                           ′′
+  1.2707 COS (  958466.75   T + 263.28   )
-     7T                           ′′
+  0.2686 COS (  960400.89   T + 138.24   )
+    2659 COS (    6003.15   T +  48.31   )
+    2646 COS (   67932.53   T + 207.58   )
+    2510 COS (  894603.23   T + 229.05   )
+    1657 COS (  407332.2    T +  52.4    )
+    1621 COS ( 1443803.6    T +  24.9    )
-      3T                          ′′
+    1470 COS ( 1371802.1    T +   4.0    )
+    1195 COS (  409266.3    T + 287.4    )
+    1060 COS (  479333.7    T + 253.4    )
+    1033 COS ( 1445737.8    T + 259.9    )
+     778 COS ( 1435665.6    T +  38.2    )
+     531 COS (  896537.4    T + 104.0    )
+     443 COS (   69866.7    T +  82.5    )
+     377 COS (  517266.9    T + 305.8    )
+     371 COS (  445268.8    T + 130.8    )
+     312 COS ( 1373736.2    T + 239.0    )
+     272 COS (  966604.8    T +  70.0    )
+     268 COS ( 1921002.5    T + 159.9    )
+     264 COS (  545131.4    T + 342.5    )
+     244 COS (  485136.2    T +  58.2    )
+     220 COS ( 1447671.9    T + 134.9    )
+     190 COS ( 1849001.0    T + 139.0    )
+     172 COS (  968538.9    T + 304.9    )
+     170 COS ( 1922936.6    T +  34.9    )
+     164 COS ( 1437600      T + 273      )
+     116 COS (  103932      T + 205      )
+     115 COS (  858604      T + 232      )
+     102 COS ( 1335803      T +   6      )
+     102 COS (  922468      T + 266      )
+      88 COS (  884531      T + 187      )
+      85 COS (  473130      T + 322      )
+      84 COS (  471196      T +  87      )
+      84 COS (  373267      T + 290      )
+      83 COS (  994466      T +  81      )
+      78 COS (  371333      T +  55      )
+      70 COS (  926535      T + 246      )
+      70 COS (   36001      T + 190      )
+      64 COS (   40068      T + 171      )
+      58 COS (  956533      T +  28      )
+      58 COS (    2135      T + 298      )
+      57 COS ( 1030468      T + 104      )
+      50 COS ( 1912864      T + 173      )
+      49 COS ( 1857139      T + 126      )
+      41 COS (  547066      T + 217      )
+      41 COS (  555204      T + 204      )
+      41 COS (   31930      T +   4      )
+      40 COS ( 1850935      T +  14      )
+      38 COS ( 1785137      T + 105      )
+      37 COS ( 1032402      T + 339      )
+      36 COS ( 2334338      T + 261      )
+      35 COS ( 1924871      T + 270      )
+      34 COS (  886465      T +  62      )
+      33 COS (    7937      T + 283      )
+      32 COS ( 1441870      T + 150      )
+      32 COS (  443331      T + 230      )
+      32 COS ( 1859073      T +   1      )
+      32 COS (  557138      T + 259      )
+      31 COS ( 2408274      T + 157      )
+      31 COS ( 2398201      T + 295      )
+      30 COS (  405398      T + 177      )
+      30 COS ( 1307939      T + 330      )
+      29 COS ( 2406339      T + 282      )
+      23 COS (  860538      T + 106      )

+  °                                  °                                  °
+ 0.0023 COS ( 1369868      T + 309      )
+      22 COS (  417404     T + 274      )
+      22 COS ( 2336272     T + 136      )
+      22 COS ( 1022330     T + 118      )
+      21 COS ( 1337737     T + 241      )
+      19 COS (  105866     T +  80      )
+      19 COS (  930602     T +  47      )
+      19 COS (  553269     T + 329      )
+      19 COS ( 2400136     T + 170      )
+      18 COS ( 2326200     T + 274      )
+      18 COS (  924402     T + 141      )
+      18 COS ( 1407801     T + 182      )
+      17 COS (  519201     T + 181      )
+      17 COS (  892669     T + 354      )
+      17 COS (  820668     T + 153      )
+      15 COS (  513200     T + 325      )
+      14 COS ( 2262336     T + 240      )
+      14 COS (   42002     T +  46      )
+      14 COS ( 1813002     T + 141      )
+      14 COS (  962335     T + 193      )
+      14 COS (  928469     T + 121      )
+      14 COS (  996400     T + 316      )
+      13 COS ( 1449606     T +  10      )
+      13 COS (  970473     T + 360      )
+      13 COS (   29996     T + 129      )
+      13 COS ( 2410208     T +  31      )
+      13 COS (  447203     T +   6      )
+      12 COS (   37935     T +  65      )
+      12 COS (  489406     T + 115      )
+      12 COS (   31933     T +  30      )
+      11 COS (   65998     T + 333      )
+      11 COS ( 1399667     T +  41      )
+      11 COS ( 1507667     T + 239      )
+      10 COS (  581130     T + 340      )
+      10 COS ( 1914799     T +  48      )
+      10 COS (  962534     T +  64      )
+      10 COS (       2     T +  13      )
+      10 COS (  445265     T + 105      )
+       9 COS ( 1297866     T + 288      )
+       9 COS ( 1471665     T + 216      )
+       9 COS ( 1403734     T +  21      )
+       9 COS (  972407     T + 235      )
+       8 COS ( 1929141     T + 327      )
+       8 COS ( 2883538     T +  57      )
+       8 COS (  481401     T + 248      )
+       8 COS (  481135     T + 189      )
+       7 COS ( 1787072     T + 340      )
+       7 COS ( 1931075     T + 202      )
+       7 COS ( 2885472     T + 292      )
+       7 COS ( 2811537     T +  36      )
+       7 COS ( 1479803     T + 202      )
+       7 COS ( 1407805     T +  27      )
+       6 COS ( 1509601     T + 114      )
+       6 COS (  822602     T +  28      )
+       6 COS (  559072     T + 134      )
+       6 COS ( 1309873     T + 205      )
+       6 COS (  491340     T + 350      )
+       6 COS ( 1861007     T + 236      )
+       6 COS (  449336     T + 111      )
+       6 COS ( 1379940     T + 171      )
+       6 COS ( 1361730     T + 322      )
+       5 COS (   79939     T + 304      )
+       5 COS ( 1299804     T +   9      )
+       5 COS (  411200     T + 162      )
+       5 COS (  848532     T + 190      )
+       5 COS (  964671     T + 195      )
+       5 COS ( 1919068     T + 285      )
+       5 COS (  409270     T + 133      )
+       4 COS ( 2813471     T + 271      )
+       4 COS (  419339     T + 149      )
+       4 COS ( 2338206     T +  11      )
+       4 COS ( 1749138     T + 107      )
+       4 COS (  337268     T + 292      )
+       4 COS (  139931     T + 203      )
+       4 COS (  822605     T + 234      )
+       4 COS (  948395     T + 222      )
+       4 COS ( 2328134     T + 149      )
+       4 COS ( 1024264     T + 352      )
+       4 COS (  553266     T + 303      )
+       3 COS ( 2402070     T +  45      )
+       3 COS ( 1847067     T +  84      )
+       3 COS (  477400     T +  18      )
+       3 COS ( 1381874     T +  46      )
+       3 COS (  932536     T + 282      )
+       3 COS ( 1481737     T +  77      )
+       3 COS ( 1409735     T +  57      )
+       3 COS ( 2390063     T + 308      )
+       3 COS ( 1409739     T + 262      )
+       3 COS ( 2264270     T + 115      )
+       3 COS ( 1885000     T + 317      )
+       3 COS (  898472     T + 159      )
+       3 COS ( 1814936     T +  16      )
```

Table 6. Mercury: Heliocentric longitude, latitude and radius vector

LONGITUDE

```
                  °                    °
  252.2502 + 149474.0714 T
                  °                    °                    °
+ 23.4405 COS ( 149472.5153T +  84.7947 )
+       23T                  ″
+  2.9818 COS ( 298945.031 T + 259.589  )
+        6T                  ″
+  0.5258 COS ( 448417.55  T +  74.38   )
+    1796 COS ( 298945.77  T + 137.84   )
+    1061 COS ( 597890.1   T + 249.2    )
+     850 COS ( 149473.3   T + 143.0    )
+     760 COS ( 448418.3   T + 312.6    )
+     256 COS ( 597890.8   T + 127.4    )
+     230 COS ( 747362.6   T +  64.0    )
+      81 COS ( 747363     T + 302      )
+      69 COS (      1     T + 148      )
+      52 COS ( 896835     T + 239      )
+      23 COS ( 896836     T + 117      )
+      19 COS (   6356     T +  85      )
+      11 COS (1046308     T +  54      )
+      10 COS (  32437     T + 234      )
+       9 COS ( 143403     T + 171      )
+       6 COS ( 155828     T + 268      )
+       5 COS (1046308     T + 292      )
+       4 COS ( 143117     T +  84      )
+       3 COS ( 181909     T +  63      )
+       3 COS ( 123392     T + 288      )
+       3 COS ( 448419     T +  11      )
```

LATITUDE

```
                  °                    °                    °
+  6.7057 COS ( 149472.886 T + 113.919  )
+       17T                  ″
+  1.4396 COS (      0.37   T + 119.12   )
+        5T                  ″
+  1.3643 COS ( 298945.40   T + 288.71   )
+        5T                  ″
+  0.3123 COS ( 448417.92   T + 103.51   )
+     753 COS ( 597890.4    T + 278.3    )
+     367 COS ( 149472.1    T +  55.7    )
+     187 COS ( 747362.9    T +  93.1    )
+      50 COS ( 298945      T + 230      )
+      47 COS ( 896835      T + 268      )
+      28 COS ( 448419      T + 342      )
+      23 COS ( 298946      T + 347      )
+      20 COS ( 597891      T + 157      )
+      12 COS (1046308      T +  83      )
+       9 COS ( 747364      T + 331      )
+       9 COS ( 448417      T +  45      )
+       5 COS ( 149474      T + 352      )
+       3 COS ( 896836      T + 146      )
```

RADIUS VECTOR

```
  AU                 °                    °
+ 0.395283 COS (      0      T +  0       )
+       2T                   ″
+   78341 COS ( 149472.515 T + 354.795  )
+       8T                   ″
+    7955 COS ( 298945.03  T + 169.59   )
+       2T                   ″
+    1214 COS ( 448417.55  T + 344.38   )
+     218 COS ( 597890.1   T + 159.2    )
+      42 COS ( 747363     T + 334      )
+       6 COS ( 896835     T + 149      )
```

Table 7. Mercury: Apparent geocentric equatorial rectangular coordinates

X

```
  AU                 °                    °
+ 0.999860 COS (  36000.7696T + 280.4583 )
+   377489 COS ( 149474.0714T + 252.2228 )
+   118956 COS (      1.5561T + 257.4522 )
+       12T                  ″
+    38402 COS ( 298946.587 T +  66.995  )
+    25063 COS (      1.720 T + 102.941  )
-       63T                  ″
+     8354 COS (  71999.82  T + 277.99   )
-       21T                  ″
+     5860 COS ( 448419.10  T + 241.77   )
+     2068 COS ( 149470.96  T +  97.34   )
+     1414 COS ( 149471.70  T + 155.59   )
+     1060 COS ( 597891.6   T +  56.6    )
+      446 COS (      0.8   T + 199.2    )
+      211 COS ( 747364.1   T + 231.4    )
+      144 COS ( 298944.2   T + 330.4    )
+      141 COS ( 298943.5   T + 272.1    )
+      105 COS ( 107999     T + 276      )
+       45 COS ( 896837     T +  46      )
+       42 COS (  34067     T + 226      )
+       42 COS (  37935     T + 155      )
+       35 COS (  35997     T +  75      )
+       31 COS ( 481268     T + 218      )
+       26 COS (   3036     T + 213      )
+       25 COS ( 262947     T + 134      )
+       22 COS ( 448417     T + 145      )
+       21 COS (   9037     T + 244      )
+       16 COS ( 448416     T +  87      )
+       16 COS (  77473     T + 141      )
+       16 COS ( 147540     T + 197      )
+       16 COS ( 151408     T + 127      )
+       16 COS (  35982     T + 211      )
+       16 COS (  36020     T + 170      )
+       14 COS (  13482     T +  23      )
+       10 COS (1046309     T + 221      )
+       10 COS (  58520     T +   9      )
+        9 COS (  68965     T + 168      )
+        9 COS ( 412420     T + 309      )
+        8 COS ( 113475     T + 139      )
+        8 COS ( 149473     T + 194      )
```

```
  AU                 °                    °
+ 0.000007 COS (   2282     T +  54      )
+        7 COS ( 101930     T +  56      )
+        7 COS (  29928     T +  35      )
+        7 COS ( 143118     T + 245      )
+        7 COS ( 155830     T +  80      )
+        6 COS (  32966     T + 261      )
+        6 COS (  39035     T + 120      )
+        6 COS (  26962     T + 306      )
+        6 COS (  45039     T +  75      )
+        6 COS (  81038     T + 265      )
+        5 COS (   1936     T + 132      )
+        5 COS (   1933     T + 158      )
+        5 COS (  36156     T + 128      )
+        5 COS (  35846     T + 253      )
+        4 COS (  72000     T + 213      )
+        4 COS (  33720     T + 149      )
+        4 COS (  38281     T + 232      )
+        4 COS ( 597889     T + 320      )
+        4 COS (  65931     T +  58      )
+        4 COS (   6071     T + 323      )
+        4 COS (  67558     T + 172      )
+        4 COS (   4444     T + 209      )
```

Y

```
  AU                 °                    °
+ 0.917354 COS (  36000.7696T + 190.4583 )
+       91T                  ″
+   346339 COS ( 149474.0714T + 162.2228 )
+       32T                  ″
+   109140 COS (      1.556 T + 167.452  )
+       21T                  ″
+    35233 COS ( 298946.587 T + 336.995  )
+        7T                  ″
+    22995 COS (      1.720 T +  12.941  )
-       56T                  ″
+    18380 COS ( 149472.886 T + 293.894  )
-        5T                  ″
+     7664 COS (  71999.82  T + 187.99   )
-       19T                  ″
+     5792 COS (      0.37  T + 299.12   )
+     5376 COS ( 448419.10  T + 151.77   )
```

Table 7. Mercury: Apparent geocentric equatorial rectangular coordinates (Continued)

```
   AU                    °          °
+ 0.001897 COS ( 149470.96   T + 187.34   )
+      1870 COS ( 298945.40   T + 108.71   )
+      1297 COS ( 149471.70   T + 245.59   )
+       973 COS ( 597891.6    T + 326.6    )
+       409 COS (      0.8    T + 109.2    )
+       285 COS ( 448417.9    T + 283.5    )
+       193 COS ( 747364.1    T + 141.4    )
+       132 COS ( 298944.2    T +  60.4    )
+       129 COS ( 298943.5    T +   2.1    )
+       101 COS ( 149472      T +  56      )
+        96 COS ( 107999      T + 186      )
+        52 COS ( 597890      T +  98      )
+        47 COS (  34067      T + 136      )
+        41 COS ( 896837      T + 316      )
+        32 COS (  35997      T + 165      )
+        29 COS (  37935      T +  65      )
+        28 COS ( 481268      T + 128      )
+        23 COS (   3036      T + 123      )
+        23 COS ( 262947      T +  44      )
+        20 COS ( 448417      T + 235      )
+        20 COS (   9037      T + 334      )
+        18 COS ( 147540      T + 107      )
+        15 COS ( 448416      T + 177      )
+        15 COS (  77473      T + 231      )
+        14 COS (  35982      T + 121      )
+        14 COS (  36020      T +  80      )
+        13 COS (  13482      T + 293      )
+        11 COS ( 151408      T +  37      )
+        10 COS ( 747363      T + 273      )
+         9 COS (1046309      T + 131      )
+         9 COS (  58520      T + 279      )
+         9 COS (  68965      T +  78      )
+         8 COS ( 113475      T +  49      )
+         8 COS ( 412420      T + 219      )
+         7 COS ( 149473      T + 104      )
+         7 COS ( 298945      T + 230      )
+         6 COS (   2282      T + 324      )
+         6 COS (  29928      T + 125      )
+         6 COS ( 101930      T + 326      )
+         6 COS ( 143118      T + 155      )
+         6 COS ( 155830      T + 350      )
+         6 COS (  39035      T +  30      )
+         6 COS (  32966      T + 171      )
+         6 COS (   1933      T + 248      )
+         6 COS (  45039      T + 345      )
+         6 COS (  26962      T + 216      )
+         5 COS (  81038      T + 175      )
+         4 COS (  36156      T +  38      )
+         4 COS (  35846      T + 163      )
+         4 COS (  72000      T + 123      )
+         4 COS (  33720      T +  59      )
+         4 COS (  38281      T + 142      )
+         4 COS ( 597889      T +  50      )
+         4 COS (   1936      T +  42      )
```

```
Z
   AU                    °          °
+ 0.397721 COS (  36000.7696T + 190.4583 )
-      208T                  ″
+   150156 COS ( 149474.0714T + 162.2228 )
-       80T                  ″
+    47318 COS (      1.556 T + 167.453  )
-       20T                  ″
+    42395 COS ( 149472.886 T + 113.894  )
+       15T                  ″
+    15275 COS ( 298946.587 T + 336.996  )
-        7T                  ″
+    13360 COS (      0.371 T + 119.124  )
+        6T                  ″
+     9970 COS (      1.72  T +  12.94   )
-       30T                  ″
+     4313 COS ( 298945.40  T + 288.66   )
+     3323 COS (  71999.82  T + 187.99   )
-       10T                  ″
+     2331 COS ( 448419.10  T + 151.77   )
+      823 COS ( 149471.0   T + 187.3    )
+      658 COS ( 448417.9   T + 103.5    )
+      562 COS ( 149471.7   T + 245.6    )
+      422 COS ( 597891.6   T + 326.6    )
+      232 COS ( 149472.1   T + 235.7    )
+      177 COS (      0.8   T + 109.2    )
+      119 COS ( 597890.4   T + 278.3    )
+       84 COS ( 747364     T + 141      )
+       57 COS ( 298944     T +  60      )
+       56 COS ( 298943     T +   2      )
+       42 COS ( 107999     T + 186      )
+       37 COS (  37935     T +  65      )
+       24 COS ( 747363     T +  93      )
+       18 COS ( 896837     T + 316      )
+       16 COS ( 298945     T +  50      )
+       14 COS ( 151408     T +  37      )
+       14 COS (  35997     T + 165      )
+       12 COS ( 481268     T + 128      )
+       11 COS ( 262947     T +  44      )
+       10 COS (   3036     T + 123      )
+        9 COS ( 448417     T + 235      )
+        8 COS (   9037     T + 334      )
+        7 COS (  77473     T + 231      )
+        6 COS ( 448416     T + 177      )
+        6 COS (  35982     T + 121      )
+        6 COS (  36020     T +  80      )
+        6 COS (  13482     T + 293      )
+        5 COS ( 896835     T + 268      )
+        4 COS (1046309     T + 131      )
+        4 COS (  58520     T + 279      )
+        4 COS (  34067     T + 316      )
+        4 COS (  68965     T +  78      )
+        4 COS ( 113475     T +  49      )
+        4 COS ( 412420     T + 219      )
```

Table 8. Venus: Heliocentric longitude, latitude and radius vector

```
   LONGITUDE
    °              °
 181.9793 +  58519.2125 T
    °          °              °
+  0.7761 COS (  58517.81   T + 320.41   )
-      54T                  ″
+     503 COS ( 117036.6    T + 300.6    )
+      33 COS ( 117036      T +  11      )
+      32 COS (  45038      T + 254      )
+      20 COS (  67556      T + 159      )
+      14 COS (  22519      T + 172      )
+      10 COS (   9038      T + 244      )
+       8 COS (  55483      T + 239      )
+       8 COS (    155      T + 303      )
+       7 COS (  58519      T +  70      )
+       7 COS ( 175554      T + 351      )
+       5 COS (   3035      T + 110      )
+       4 COS (  54076      T +  34      )
```

```
   LATITUDE
    °              °              °
+  3.3939 COS (  58518.312 T +  15.299  )
-      10T                  ″
+   0.0230 COS (      0.5   T + 144.9    )
+      230 COS ( 117036.1   T +  65.7    )
+        5 COS ( 175555     T +  46      )

   RADIUS VECTOR
   AU                    °          °
+ 0.723348 COS (      0     T +   0     )
+     4899 COS (  58517.81   T + 230.41  )
-       34T                  ″
+       17 COS ( 117036      T + 281     )
+       16 COS (  45038      T + 164     )
+       14 COS (  67556      T +  69     )
+        4 COS (  55483      T + 121     )
```

Table 9. Venus: Apparent geocentric equatorial rectangular coordinates

X

AU °

+ 0.999860 cos (36000.7696T + 280.4572)
+ 722680 cos (58519.2126T + 181.9661)
+ 25063 cos (1.720 T + 102.941)
- 63T ″
+ 8354 cos (71999.82 T + 277.99)
- 21T ″
+ 7342 cos (1.41 T + 311.57)
- 52T ″
+ 2447 cos (117037.02 T + 232.39)
- 17T ″
+ 635 cos (58517.4 T + 28.6)
+ 105 cos (107999 T + 276)
+ 42 cos (34067 T + 226)
+ 42 cos (37935 T + 155)
+ 40 cos (9037 T + 245)
+ 39 cos (13482 T + 335)
+ 35 cos (35997 T + 75)
+ 34 cos (81038 T + 353)
+ 31 cos (481268 T + 218)
+ 30 cos (56585 T + 127)
+ 30 cos (60453 T + 57)
+ 26 cos (3036 T + 213)
+ 16 cos (35982 T + 211)
+ 16 cos (36020 T + 170)
+ 14 cos (13482 T + 23)
+ 12 cos (175555 T + 283)
+ 12 cos (103557 T + 166)
+ 10 cos (58520 T + 9)
+ 9 cos (68965 T + 168)
+ 9 cos (81038 T + 84)
+ 9 cos (36000 T + 100)
+ 7 cos (3036 T + 42)
+ 7 cos (2282 T + 54)
+ 7 cos (101930 T + 56)
+ 7 cos (29928 T + 35)
+ 6 cos (0 T + 202)
+ 6 cos (32966 T + 261)
+ 6 cos (39035 T + 120)
+ 6 cos (26962 T + 306)
+ 6 cos (45039 T + 75)
+ 6 cos (67558 T + 156)
+ 6 cos (49481 T + 28)
+ 6 cos (126075 T + 71)
+ 6 cos (81038 T + 265)
+ 5 cos (58364 T + 329)
+ 5 cos (58674 T + 215)
+ 5 cos (103556 T + 75)
+ 5 cos (36156 T + 128)
+ 5 cos (35846 T + 253)
+ 4 cos (58516 T + 279)
+ 4 cos (33720 T + 149)
+ 4 cos (38281 T + 232)
+ 4 cos (6071 T + 323)
+ 4 cos (65931 T + 58)
+ 4 cos (67558 T + 172)
+ 4 cos (4444 T + 209)

Y

AU °

+ 0.917354 cos (36000.7696T + 190.4572)
- 91T ″
+ 663046 cos (58519.2126T + 91.9661)
- 65T ″
+ 22995 cos (1.720 T + 12.941)
- 56T ″
+ 17037 cos (58518.312 T + 195.289)
- 4T ″
+ 7664 cos (71999.82 T + 187.99)
- 19T ″
+ 6736 cos (1.41 T + 221.57)
- 47T ″
+ 2245 cos (117037.02 T + 142.39)
- 16T ″
+ 582 cos (58517.4 T + 118.6)
+ 173 cos (0.5 T + 324.9)
+ 96 cos (107999 T + 186)

AU °

+ 0.000058 cos (117036 T + 246)
+ 47 cos (34067 T + 136)
+ 38 cos (9037 T + 335)
+ 36 cos (13482 T + 245)
+ 34 cos (56585 T + 37)
+ 32 cos (35997 T + 165)
+ 31 cos (81038 T + 263)
+ 29 cos (37935 T + 65)
+ 28 cos (481268 T + 128)
+ 23 cos (3036 T + 123)
+ 21 cos (60453 T + 327)
+ 14 cos (36020 T + 80)
+ 14 cos (35982 T + 121)
+ 13 cos (13482 T + 293)
+ 11 cos (175555 T + 193)
+ 11 cos (103557 T + 76)
+ 9 cos (58520 T + 279)
+ 9 cos (68965 T + 78)
+ 8 cos (81038 T + 354)
+ 8 cos (36000 T + 10)
+ 7 cos (3036 T + 312)
+ 6 cos (2282 T + 324)
+ 6 cos (29928 T + 125)
+ 6 cos (101930 T + 326)
+ 6 cos (0 T + 112)
+ 6 cos (39035 T + 30)
+ 6 cos (32966 T + 171)
+ 6 cos (45039 T + 345)
+ 6 cos (26962 T + 216)
+ 6 cos (67558 T + 66)
+ 6 cos (49481 T + 298)
+ 5 cos (126075 T + 341)
+ 5 cos (81038 T + 175)
+ 4 cos (58674 T + 125)
+ 4 cos (58364 T + 239)
+ 4 cos (103556 T + 345)
+ 4 cos (36156 T + 38)
+ 4 cos (35846 T + 163)
+ 4 cos (58516 T + 9)
+ 4 cos (38281 T + 142)
+ 4 cos (33720 T + 59)

Z

AU °

+ 0.397721 cos (36000.7696T + 190.4572)
- 208T ″
+ 287466 cos (58519.2126T + 91.9661)
- 151T ″
+ 39295 cos (58518.312 T + 15.289)
+ 15T ″
+ 9970 cos (1.72 T + 12.94)
- 30T ″
+ 3323 cos (71999.82 T + 187.99)
- 10T ″
+ 2921 cos (1.41 T + 221.57)
- 22T ″
+ 974 cos (117037.0 T + 142.4)
- 7T ″
+ 399 cos (0.5 T + 144.9)
+ 252 cos (58517.4 T + 118.6)
+ 133 cos (117036.1 T + 65.7)
+ 42 cos (107999 T + 186)
+ 37 cos (37935 T + 65)
+ 27 cos (60453 T + 327)
+ 16 cos (9037 T + 335)
+ 16 cos (13482 T + 245)
+ 14 cos (35997 T + 165)
+ 13 cos (81038 T + 263)
+ 12 cos (481268 T + 128)
+ 10 cos (3036 T + 123)
+ 6 cos (35982 T + 121)
+ 6 cos (36020 T + 80)
+ 6 cos (13482 T + 293)
+ 5 cos (175555 T + 193)
+ 5 cos (103557 T + 76)
+ 4 cos (58520 T + 279)
+ 4 cos (34067 T + 316)
+ 4 cos (68965 T + 78)

Table 10. Mars: Heliocentric longitude, latitude and radius vector

```
    LONGITUDE

                  °                  °
 355.4472 +  19141.6999 T

    °                  °                  °
+ 10.6919 COS (  19139.859 T + 289.388  )
+     105T                 ″
+  0.6227 COS (  38279.71  T + 308.78   )
+      12T                 ″
+     504 COS (  57419.6   T + 328.2    )
+     147 COS (     19     T + 336      )
+     144 COS (  38282     T + 342      )
+     140 COS (      0     T + 180      )
+      37T                 ″
+      70 COS (  16105     T +  48      )
+      60 COS (  13071     T + 168      )
+      47 COS (  76559     T + 348      )
+      45 COS (  32211     T + 191      )
+      38 COS (   2281     T +  21      )
+      28 COS (  19142     T + 142      )
+      28 COS (  57422     T +   1      )
+      23 COS (  16859     T +  13      )
+      19 COS (  14579     T +  95      )
+      18 COS (   1098     T +  50      )
+      13 COS (   4561     T + 290      )
+      10 COS (   3035     T +  39      )
+       9 COS (  35245     T +  67      )
+       9 COS (  10036     T + 167      )
+       7 COS (  29176     T + 208      )
+       7 COS (  12298     T + 166      )
+       6 COS (  51350     T + 205      )
+       5 COS (  16696     T + 137      )
+       5 COS (  21421     T +  53      )
+       4 COS (    895     T + 229      )
+       4 COS (   6069     T + 220      )
+       4 COS (  17918     T +  28      )
+       3 COS (  10017     T + 256      )

    °                  °                  °
+ 0.0003 COS (  76562     T +  21      )
+       3 COS (  48316     T + 179      )
+       3 COS (   6842     T + 214      )

    LATITUDE

    °                  °                  °
+ 1.8334 COS (  19140.925 T + 215.876  )
-       7T                 ″
+ 0.1727 COS (     1.07    T +  16.50   )
+    1709 COS (  38280.79  T + 235.28   )
+     179 COS (  57420.6   T + 254.7    )
+      21 COS (  19139     T +   3      )
+      20 COS (  76561     T + 274      )

    RADIUS VECTOR

    AU                 °                  °
+ 1.530339 COS (      0     T +   0      )
+       13T                  ″
+ 0.141850 COS (  19139.859 T + 199.388  )
+      139T                 ″
+     6606 COS (  38279.72  T + 218.78   )
+       13T                 ″
+      455 COS (  57419.6   T + 238.2    )
+       80 COS (  16105     T + 317      )
+       72 COS (  32211     T + 103      )
+       55 COS (  13071     T +  77      )
+       35 COS (  76559     T + 258      )
+       24 COS (  16859     T + 284      )
+       23 COS (  14579     T +   3      )
+       13 COS (  29176     T + 118      )
+       10 COS (  35245     T + 338      )
+        9 COS (  48316     T +  89      )
+        8 COS (   2281     T + 311      )
```

Table 11. Mars: Apparent geocentric equatorial rectangular coordinates

```
    X

    AU                 °                  °
+ 1.516648 COS (  19141.6961T + 355.4263 )
-       13T                  ″
+ 0.999860 COS (  36000.7696T + 280.4541 )
+   213424 COS (      1.8372T + 156.0424 )
+      210T                 ″
+    70678 COS (  38281.555 T +  14.812  )
+       69T                 ″
+    25063 COS (      1.720 T + 102.941  )
-       63T                 ″
+     8354 COS (  71999.82  T + 277.97   )
-       21T                 ″
+     4940 COS (  57421.42  T +  34.22   )
+       10T                 ″
+     1666 COS (  19138.02  T +  43.33   )
+      410 COS (  76561.3   T +  53.6    )
+      395 COS (  19140.2   T + 256.3    )
+      194 COS (  19122.8   T + 109.5    )
+      194 COS (  19160.6   T +  61.4    )
+      134 COS (   3036.4   T +  37.0    )
+      114 COS (   6071.0   T + 277.8    )
+      105 COS ( 107999     T + 276      )
+       83 COS (  13069     T + 108      )
+       63 COS (  17208     T + 300      )
+       63 COS (  21076     T + 230      )
+       56 COS (      0     T +  57      )
+       53 COS (  35247     T + 134      )
+       53 COS (  16861     T +  61      )
+       52 COS (  38278     T +  63      )
+       49 COS (  32212     T + 255      )
+       48 COS (   2283     T +  31      )
+       47 COS (  21422     T + 104      )
+       42 COS (  34067     T + 226      )
+       42 COS (  37935     T + 155      )

    AU                 °                  °
+ 0.000041 COS (  52860     T + 115      )
+       37 COS (  95701     T +  73      )
+       36 COS (   4563     T + 351      )
+       35 COS (  35997     T +  75      )
+       31 COS ( 481268     T + 218      )
+       27 COS (     21     T + 222      )
+       27 COS (     17     T +  90      )
+       26 COS (   3036     T + 213      )
+       23 COS (  20240     T + 135      )
+       23 COS (  18043     T +  36      )
+       23 COS (  51352     T + 275      )
+       21 COS (   9037     T + 244      )
+       21 COS (  36001     T +  96      )
+       18 COS (  38280     T + 276      )
+       18 COS (  23703     T +  14      )
+       16 COS (  14580     T + 154      )
+       16 COS (  22176     T + 105      )
+       16 COS (  33720     T + 181      )
+       16 COS (  10034     T + 123      )
+       16 COS (  35982     T + 211      )
+       16 COS (  36020     T + 170      )
+       14 COS (  13482     T +  23      )
+       13 COS (   6844     T + 280      )
+       13 COS (  16107     T +  16      )
+       12 COS (  29178     T + 252      )
+       12 COS (   9106     T + 278      )
+       10 COS (  58520     T +   9      )
+        9 COS (  68965     T + 168      )
+        9 COS (  38263     T + 129      )
+        9 COS (  38300     T +  81      )
+        9 COS (  25211     T + 305      )
+        9 COS (   1936     T +  31      )
+        9 COS (   1932     T + 259      )
+        8 COS (  29174     T +  93      )
+        8 COS (  40562     T + 130      )
```

Table 11. Mars: Apparent geocentric equatorial rectangular coordinates (Continued)

Y

AU °

+ 1.391497 COS (19141.6961T + 265.4263)
+ 125T ″
+ 0.917354 COS (36000.7696T + 190.4541)
+ 91T ″
+ 195813 COS (1.8372T + 66.0424)
+ 212T ″
+ 64845 COS (38281.555 T + 284.812)
+ 69T ″
+ 22995 COS (1.720 T + 12.941)
- 56T ″
+ 19478 COS (19140.925 T + 35.876)
- 17T ″
+ 7664 COS (71999.82 T + 187.97)
- 19T ″
+ 4533 COS (57421.42 T + 304.22)
+ 9T ″
+ 2741 COS (1.07 T + 196.50)
+ 1529 COS (19138.02 T + 133.33)
+ 908 COS (38280.8 T + 55.3)
+ 376 COS (76561.3 T + 323.6)
+ 363 COS (19140.2 T + 346.3)
+ 178 COS (19122.8 T + 19.5)
+ 178 COS (19160.6 T + 331.4)
+ 123 COS (3036.4 T + 307.0)
+ 104 COS (6071 T + 188)
+ 96 COS (107999 T + 186)
+ 76 COS (13069 T + 198)
+ 72 COS (17208 T + 210)
+ 63 COS (57421 T + 75)
+ 51 COS (0 T + 147)
+ 49 COS (35247 T + 44)
+ 48 COS (16861 T + 331)
+ 48 COS (38278 T + 153)
+ 47 COS (34067 T + 136)
+ 45 COS (32212 T + 165)
+ 45 COS (21076 T + 140)
+ 44 COS (2283 T + 301)
+ 43 COS (21422 T + 14)
+ 37 COS (52860 T + 25)
+ 34 COS (95701 T + 343)
+ 33 COS (4563 T + 261)
+ 32 COS (35997 T + 165)
+ 29 COS (37935 T + 65)
+ 28 COS (481268 T + 128)
+ 25 COS (21 T + 132)
+ 25 COS (17 T + 180)
+ 23 COS (3036 T + 123)
+ 21 COS (20240 T + 45)
+ 21 COS (18043 T + 306)
+ 21 COS (19139 T + 3)
+ 21 COS (51352 T + 185)
+ 20 COS (9037 T + 334)
+ 19 COS (36001 T + 6)
+ 17 COS (38280 T + 6)
+ 17 COS (23703 T + 284)
+ 15 COS (14580 T + 64)
+ 15 COS (22176 T + 15)
+ 15 COS (33720 T + 91)
+ 14 COS (10034 T + 213)
+ 14 COS (36020 T + 80)
+ 14 COS (35982 T + 121)
+ 13 COS (13482 T + 293)
+ 12 COS (6844 T + 190)
+ 12 COS (16107 T + 286)

AU ° °

+ 0.000011 COS (29178 T + 162)
+ 11 COS (9106 T + 188)
+ 10 COS (1932 T + 349)
+ 9 COS (58520 T + 279)
+ 9 COS (68965 T + 78)
+ 8 COS (38263 T + 39)
+ 8 COS (38300 T + 351)
+ 8 COS (25211 T + 215)
+ 8 COS (29174 T + 183)

Z

AU ° °

+ 0.603288 COS (19141.6961T + 265.4263)
- 321T ″
+ 397721 COS (36000.7696T + 190.4541)
- 208T ″
+ 84895 COS (1.837 T + 66.042)
+ 39T ″
+ 44925 COS (19140.925 T + 215.871)
- 12T ″
+ 28114 COS (38281.555 T + 284.812)
+ 13T ″
+ 9970 COS (1.72 T + 12.94)
- 30T ″
+ 6322 COS (1.07 T + 16.50)
+ 3323 COS (71999.82 T + 187.99)
- 10T ″
+ 2094 COS (38280.79 T + 235.28)
+ 1965 COS (57421.42 T + 304.22)
+ 663 COS (19138.0 T + 133.3)
+ 163 COS (76561.3 T + 323.6)
+ 157 COS (19140.2 T + 346.3)
+ 146 COS (57420.6 T + 254.7)
+ 77 COS (19123 T + 19)
+ 77 COS (19161 T + 331)
+ 56 COS (21076 T + 140)
+ 53 COS (3036 T + 307)
+ 49 COS (19139 T + 183)
+ 45 COS (6071 T + 188)
+ 42 COS (107999 T + 186)
+ 37 COS (37935 T + 65)
+ 33 COS (13069 T + 198)
+ 22 COS (0 T + 147)
+ 21 COS (35247 T + 44)
+ 21 COS (16861 T + 331)
+ 21 COS (38278 T + 153)
+ 19 COS (32212 T + 165)
+ 19 COS (21422 T + 14)
+ 19 COS (2283 T + 301)
+ 16 COS (52860 T + 25)
+ 15 COS (95701 T + 343)
+ 14 COS (4563 T + 261)
+ 14 COS (35997 T + 165)
+ 12 COS (481268 T + 128)
+ 12 COS (76561 T + 274)
+ 11 COS (21 T + 132)
+ 11 COS (17 T + 180)
+ 10 COS (3036 T + 123)
+ 9 COS (20240 T + 45)
+ 9 COS (18043 T + 306)
+ 9 COS (51352 T + 175)
+ 8 COS (9037 T + 334)
+ 8 COS (36001 T + 6)
+ 8 COS (1936 T + 301)
+ 7 COS (38280 T + 6)

Table 12. Distributions of the differences between the values by the series and the rigorous ones

Coordinates	Unit	series − rigorous												
		less	−10	−8	−6	−4	−2	0	+2	+4	+6	+8	+10	more
Sun														
longitude	1″				141	453	1298	1247	398	116				
distance	10^{-5} AU					46	1796	1788	23					
right ascension	0^{s}.1				75	276	1540	1395	362	5				
declination	1″				91	477	1163	1357	464	90	11			
X 1950.0	10^{-5} AU					18	1748	1887						
Y 1950.0	10^{-5} AU					80	1757	1654	162					
Z 1950.0	10^{-5} AU						1788	1795	70					
Moon														
longitude	1″	11	42	92	295	617	880	917	553	191	47	6	2	
latitude	1″		7	32	141	427	910	1165	710	228	29	3	1	
parallax	0″.1						1817	1836						
right ascension	0^{s}.1	27	55	145	351	544	806	742	538	279	118	29	19	
declination	1″	71	67	158	336	477	617	600	500	365	236	126	100	
Mercury														
longitude	1″	6	17	50	144	547	1102	1067	456	178	65	21		
latitude	1″				7	178	1631	1523	301	13				
radius vector	10^{-5} AU						1760	1893						
right ascension	0^{s}.1				42	491	1391	1306	380	43				
declination	1″		6	34	69	423	1444	1135	416	90	32	4		
Venus														
longitude	1″				66	593	1578	1207	209					
latitude	1″						1516	2137						
radius vector	10^{-5} AU						1693	1960						
right ascension	0^{s}.1	46	63	92	95	390	1502	1086	287	24	15	15	38	
declination	1″				65	355	1204	1134	452	206	83	55	99	
Mars														
longitude	1″			36	75	495	997	1180	619	228	23			
latitude	1″				14	286	1746	1485	122					
radius vector	10^{-5} AU					417	1583	1190	387	76				
right ascension	0^{s}.1		43	103	276	502	801	1371	447	74	12	24		
declination	1″	75	61	92	148	448	1414	837	361	98	99	20		

4. Precision

In order to evaluate the precision of the series presented above, the differences between the values calculated by them and the rigorous values tabulated in the *Japanese Ephemeris* are examined. The comparison is made for every 0^h ET from 1972 January 1 to 1981 December 31 (3653 points in total), and the distributions of the differences are shown in Table 12. Since the series are constructed so as to fit best at J 2000.0, the precision reprsesnted by the distributions is considered to be retained throughout the 60 years centering at 2000.

References

Eckert, W. J., Jones, R., Clark, H. K. 1954: *Improved Lunar Ephemeris 1952-1959*, U. S. Gov. Printing Office, Washington, D. C.

Newcomb, S. 1895a: *Astr. Pap. Amer. Eph.* Vol. VI, Pt. I.

Newcomb, S. 1895b: *Astr. Pap. Amer. Eph.* Vol. VI, Pt. II.

Newcomb, S. 1895c: *Astr. Pap. Amer. Eph.* Vol. VI, Pt. III.

Newcomb, S. 1898: *Astr. Pap. Amer. Eph.* Vol. VI, Pt. IV.

Ross, F. E. 1917: *Astr. Pap. Amer. Eph.* Vol. IX, Pt. II.

REPORT OF HYDROGRAPHIC RESERCHES No. 15, March, 1980

日食図の自動図化

井上圭典*

AN AUTOMATIC DRAWING OF SOLAR ECLIPSE MAP

Keisuke Inoue

Received 1979 September 10

Abstract

A computer program for automatic drawing of an eclipse map by an XY-plotter has been developed. The present paper describes the process of the analysis for the program, showing some difficulties which have arisen in the course of the analysis, and the solutions which were adopted.

Examples of eclipse maps produced by this program are seen in the supplements to the Japanese Ephemeris for 1980 and 1981.

By combining this program with those for computing the coordinates of the Sun and the Moon, which are already available at the Hydrographic Department of Japan, the eclipse map can be drawn automatically for any eclipse in the past or in the future.

The time necessary to complete one eclipse map is at most 80 minutes, including both computing and plotting times.

1. 序　論

日食図作成のためには，非常に多量の計算処理が要求され，この計算結果を世界地図に記入して滑かな曲線を描く作業を経ねばならない．手回し計算器を使っていた時代には，日食の規模によって多少の相違はあるが，熟練した計算者でも一つの日食に対し半年ぐらいの日時を費していたものであり，計算が長大であるだけに誤算の防止に注ぐ労力もかなりの負担であった．

電子計算機の導入により，日食図の計算部分は比較的早く，1969年ころまでには電算化されたが，図化の部分は第3節に述べるような諸問題点があって作業が遅れていた．このたび，これらの問題点もようやく解決し，自動図化プログラムが完成した．これによって作業時間が極端に短縮され，労力が節減され，誤算の防止・成果の均質化等にも大きな効果があった．さらにこれまで時間や労力上の制約から不可能に近かった日食図に関連する研究が容易になったという利点も挙げられる．

日食図の自動図化に関し，米国海軍天文台（ＵＳＮＯ）では数年前に着手したというが完成したという報告はまだない．また，各国の天体暦発行機関でも自動図化が完成したという話はない．

以下，このプログラムの解析的な部分について報告する．

* 編暦課 (Astronomical Division)

2. 日食図とその意義

黄道と白道との交点付近で月・太陽が出合うと太陽・月・地球が空間でほぼ一直線に並び，太陽からの光を月がさえぎってできる円錐状の影が地表に落ちた場合，この影の中では日食現象が見られる．この影の円錐（本影錐と半影錐との二つが必ず存在する）は，地球に対し相対的に西から東に向かって移動し，時の経過とともに連続的にその影を地表上に落とし続けてゆく．この間に地球も自転しているので，この両者の動きの合成結果が時時刻々の影の位置を決めることになる．

地表に落ちた影の縁の線上から有限個の点を計算によって求め，これらを世界地図に記入し滑らかな曲線で結ぶことでその縁は描かれる．日食が継続する時間内の，ある瞬時に対し一つの曲線が対応するから，この時間内で無数の曲線が生ずることになる．この曲線群の中から，日食の見える範囲・日食状況・経過等が読み取れるように選び出して地図上に描いたものが日食図である．図はその目的によって精粗多種多様な描き方が考えられるが，ここでは標準的な日食図として，第4節のような線からなっているものを考える．

この日食図から，ある地点で日食現象が見られるかどうかが分かり，見えたとしたら，食の始めや終わりの時刻，最大食分，方向角等を読み取ることができる．つまり，ある食の状況を観測するための観測点の選定に役立つものでもある．

さらに日食図の重要な役割として，例えば古代の日食を図に再現することによって，月・太陽の運動理論の検証，採用天文定数の当否，地球自転の変動等の検討資料を提供することが挙げられる．実験もできず，繰返しもない日食は，さまざまな情報を込めているのであるから，その現象を伝える日食図は大きな意義を持つものである．各国の天体暦はそれぞれ特色をもって編集されているが，以上述べた日食図だけは必ず掲載されている．

3. 自動図化の方法と問題点

自動図化の方法・手順は幾通りも考えることができ，それに応じて生じる問題点も違ったものとなる．

一つの方法は次のとおりである．日食図は多い場合で6種類の曲線によって構成される（第6節参照）．これらの日食図各線上の有限個の点の経緯度を算出して，これらを電子計算機の記憶装置に記録しておく．所要のある一つの線の経緯度群をその中から拾い出す．この線が閉曲線とならない曲線分であれば，二つの端点があるから，すでに抽出した経緯度群の両端点として最初と最後に付加する．この線が他の線と交わったり接したりする場合には，これらの諸点の経緯度をその占めるべき位置に割り込ませる．こうしてこの線の経緯度群の並べ換えが終わってから出力し，次の線の並べ換えに移る．こうした作業を日食図各線それぞれに対して順次繰返して線ごとの経緯度群を得てゆく方法である．要するに計算結果の選択的な並べ換えを電子計算機で実行させることで，筆算時代の方法・手順をそのまま電子計算機に実行させようという発想である．

他の方法として，次のようなものも考えられる．日食図の各線は，(1) その曲線の一方の端点から始まり，時間の経過に従ってその形を決めつつ長さをのばし，もう一方の端点で終わる場合，(2) 瞬時に曲線が生ずる場合とがある．

(1)の場合は時間経過に従って生ずる通りに，(2)の場合はあるパラメータの増加するに従って生ずる通りに，それぞれ算出する．更に算出時ごとに，この線が他の線と交わるか接するかすることが分かっていればその点も繰込むかどうかを判定し，繰込まれるべき時に繰入れて，この線上の有限個の点をその生ずる順に求めてゆき，これを完成する方法である．この場合，線上の各点は並べ換える必要はないので電子計算機の記憶装置に記録せず即時出力してしまうことができる．要するに日食図の各線を「一筆書き」で完成してしまおうという発想である．

今回完成した自動図化プログラムは後者の方法を採ったが，そこで生ずる問題点とその解決策とを述べる．

日食図は大きく分類すると6種類の線，5種類の端点とからなり，これらは別個に，独立に計算することができ，描くことができる．しかし，それによって日食図が正しく完成する訳ではない．以下に述べるような不完全，不正確な日食図となる．

(1)端点と線とがつながっていない．(2)当然1本の曲線とならなければならないのが，中間で分断され空隙のある2本の線となる．(3)ある線が，他の線上の点から出発しなければならないのに，そうはならない．(4)二つの曲線が1点で接しなければならないのに，2点で交わる，全然交わらない，接しても接点がずれているといった現象を起こす．(5)二つの曲線が正しい位置で交差しない．(6)閉曲線であるべきなのに閉じない．

これらの問題点を解決するために以下のことを行った．

(1) 日食図各線のあらゆる形を，その満たすべき条件によって分類する．

(2) 総合的判断を要する場面ごとに，複合した条件を単純な条件にまで分解する．

(3) 単純な条件判断を組み合わせてトリー（木構造）を構成させ，複合条件の総合的判断を誤りなく下せるようにする．

(4) 方程式の根をより正確に求める方法を開発する．

これらを第4節以下に具体的に述べる．

4. 日食図各線の分類

標準的な日食図を例にして，一覧表の形で各端点，各曲線の分類をした．各線の形状，日食図の中に占める位置等については Figure 1, 2, 3 を参照されたい．分類1，分類2のコードで①，②，……は端点，10, 11, ……は線を意味する．このコードは第6節以下でも使用する（日食図の形から見た大分類に関しては Figure 5 参照．さらに，これより下位の小分類も多種考えられ，それぞれに図としての興味はあるが，自動図化のための解析的な段階では不必要な分類であるから省略する）．

分 類 1 日食図の各端点の名称，満たさるべき条件

端点のコード	端 点 の 名 称	端点の条件
①	中心線の日出端点（日没になる場合もある）	A, SP (SM)
②	〃 日没端点（日出になる場合もある）	A, SM (SP)
③	金環食北限界線の日出端点（日没になる場合もある)*	BZ2, CM2, SP (SM)
④	〃 〃 日没端点（日出になる場合もある)*	BZ2, CM2, SM (SP)
⑤	金環食南限界線の日出端点（日没になる場合もある)*	BZ2, CP2, SP (SM)
⑥	〃 〃 日没端点（日出になる場合もある)*	BZ2, CP2, SM (SP)
⑦	分食北限界線の日出端点（日没になる場合もある）	BZ1, CM1, SP (SM)
⑧	〃 〃 日没端点（日出になる場合もある）	BZ1, CM1, SM (SP)
⑨	〃 南限界線の日出端点（日没になる場合もある）	BZ1, CP1, SP (SM)
⑩	〃 〃 日没端点（日出になる場合もある）	BZ1, CP1, SM (SP)
⑪	日出初き線の端点	BM1, DZ1, SP
⑫	日没復円線の端点	BP1, DZ1, SM
⑬	日出復円線の端点	BP1, DZ1, SP
⑭	日没初き線の端点	BM1, DZ1, SM
⑮	日出食甚線の時間的端点（⑦又は⑨と一致する場合がある）	FZ, H1, SP

端点のコード	端 点 の 名 称	端点の条件
⑯	日没食甚線の時間的端点（⑧又は⑩と一致する場合がある）	FZ, H1, SM

＊ 皆既食の場合は南北が入れかわる.

分 類 2 日食図の各線の描かれる方向，名称，満たさるべき条件

線のコード	両端点と描く方向	線の名称	各線の条件
10	①→②	中心線	A
11	③→④	金環食北限界線*	CM2, BZ2
12	⑤→⑥	金環食南限界線*	CP2, BZ2
21	⑦→D→H→K→⑧	分食北限界線	CM1, BZ1
22	⑨→E→G→J→⑩	分食南限界線	CP1, BZ1
31	⑪→A→⑦	日出初き線	DP1, BM1, SP
31	⑦→C→⑬	日出復円線	DP1, BP1, SP
32	⑪→B→⑨	日出初き線	DM1, BM1, SP
32	⑨→F→⑬	日出復円線	DM1, BP1, SP
41	⑭→L→⑧	日没初き線	DM1, BM1, SM
41	⑧→N→⑫	日没復円線	DM1, BP1, SM
42	⑭→I→⑩	日没初き線	DP1, BM1, SM
42	⑩→M→⑫	日没復円線	DP1, BP1, SM
51	⑮→⑦	日出食甚線	FP, SP, H1
52	⑮→⑨	日出食甚線	FM, SP, H1
61	⑧→⑯	日没食甚線	FP, SM, H1
62	⑩→⑯	日没食甚線	FM, SM, H1
71	A→B	同時初き線	BP1
72	C→D→E→F	同時初き復円線	BP1, BM1
73	G→H→G	〃	〃 〃
74	I→J→K→L	〃	〃 〃
75	M→N	同時復円線	BM1

＊ 皆既食の場合は南北が入れかわる.

分類1，2の端点，線の名称は Figure 1 に対して与えられたものである. Figure 2, 3 の場合には，この分類と合わないこともある.

Figure 1, 2, 3 においてA，B，……，M，N点は2線の交点または接点である. したがって両者の条件を同時に満足していなければならない. 分類1，2の条件の欄の略記号の意味は，それぞれ以下のような条件式を満足することを表わしている. i=1 のときは半影錐，i=2 のときは本影錐を意味する. 式の意味は第6節を参照されたい. なお分類1，2を通じて，第5節の(3)式は必ず満たされるべき条件であるから省いてある.

A： $\xi=x,\ \eta_1=y_1\quad \zeta_1=\sqrt{1-x^2-y_1^2}\geqq 0$

BPi： $(x-\xi)^2+(y-\eta)^2-(l_i-\zeta\tan f_i)^2=0$ かつ $\dot{\Delta}>0$

BMi： $(x-\xi)^2+(y-\eta)^2-(l_i-\zeta\tan f_i)^2=0$ かつ $\dot{\Delta}<0$

BZi： $(x-\xi)^2+(y-\eta)^2-(l_i-\zeta\tan f_i)^2=0$ かつ $\dot{\Delta}=0$

CPi : $(x-\xi)(\dot{x}-\dot{\xi})+(y-\eta)(\dot{y}-\dot{\eta})-(l_i-\zeta\tan f_i)(\dot{l}_i-\dot{\zeta}\tan f_i)=0$ かつ $\sec Q>0$

CMi : $(x-\xi)(\dot{x}-\dot{\xi})+(y-\eta)(\dot{y}-\dot{\eta})-(l_i-\zeta\tan f_i)(\dot{l}_i-\dot{\zeta}\tan f_i)=0$ かつ $\sec Q<0$

DPi : $(l_i-\zeta\tan f_i)^2-(m-p)^2>0$ かつ $P-M>0$

DMi : $(l_i-\zeta\tan f_i)^2-(m-p)^2>0$ かつ $P-M<0$

DZi : $(l_i-\zeta\tan f_i)^2-(m-p)^2>0$ かつ $P-M=0$

FP : $(x-\xi)(\dot{x}-\dot{\xi})+(y-\eta)(\dot{y}-\dot{\eta})=0$ かつ $\alpha>0$

FM : $(x-\xi)(\dot{x}-\dot{\xi})+(y-\eta)(\dot{y}-\dot{\eta})=0$ かつ $\alpha<0$

FZ : $(x-\xi)(\dot{x}-\dot{\xi})+(y-\eta)(\dot{y}-\dot{\eta})=0$ かつ $\alpha=0$

Hi : $(x-\xi)^2+(y-\eta)^2\leqq L_i^2$

SP : $\xi^2+\eta_1^2-1=0$ かつ $\dot{\zeta}>0$

SM : $\xi^2+\eta_1^2-1=0$ かつ $\dot{\zeta}<0$

5. ベッセル座標系とベッセル要素

日食計算は地球楕円体と影の円錐との交線と，この交線が作る包絡線とを求めることにある．そして実際には空間曲面相互の切り口を平面上の二次曲線相互の交点の積み重なりとして解いてゆくのである．これを実行しやすいようにベッセル座標系が導入される訳で，この座標系の特徴は月影方向（その赤経赤緯は a, d）すなわち月・太陽の各中心を通る直線が影の円錐の軸であり，この軸に平行で地心を通る直線をZ軸とする点にある．こうすると空間で時々刻々に方向を変える月影方向の方向余弦は既知量となり，地球楕円体と影の円錐との相対的な位置は（x, y）で定まってしまう．さらに影の円錐を xy 平面（これをベッセル基準面と呼ぶ）に平行な平面で截った切り口は（x, y）を中心とした円となり，この半径 L は円錐の頂角の半分を f とすれば $L=l-\zeta\tan f$ となる．l は xy 平面上の影の半径，ζ は xy 平面から今考えた平面までの距離である．

x, y, l, $\tan f$ を知れば上記二次曲線の交点（ξ, η, ζ）は ζ をパラメータとして

$$(x-\xi)^2+(y-\eta)^2=(l-\zeta\tan f)^2 \tag{1}$$

$$\xi^2+\eta^2=\rho^2-\zeta^2 \tag{2}$$

を解いて得られる．しかし(2)式の右辺の ρ は求めようとする地点の緯度の関数であるから，ベッセルは(2)式を座標変換によって

$$\xi^2+\eta_1^2=1-\zeta_1^2 \tag{3}$$

の式とした．これは地球楕円体上の点（ξ, η, ζ）を半径1の球面上の点（ξ, η_1, ζ_1）に移すことを意味する．(1), (3)式を連立させて解いた ξ, η_1, ζ_1 を経緯度で表すためには，月影方向の暦表時角すなわち暦表子午線上の地点での時角 μ が知られていなければならない．この μ と x, y, l, $\tan f$, $\sin d$, $\cos d$ をベッセル要素と称している．このベッセル要素と(1), (3)式の解 ξ, η_1, ζ_1（この解のうち虚根，無縁根は除いて）とから経度 λ, 緯度 φ が次式によって得られる．

$$\left.\begin{aligned}
&\cos\varphi_1\sin\theta=\xi\\
&\cos\varphi_1\cos\theta=-\eta_1\sin d_1+\zeta_1\cos d_1\\
&\sin\varphi_1\quad=\eta_1\cos d_1+\zeta_1\sin d_1\\
&\lambda=\mu+\theta\\
&\varphi=\tan^{-1}(\tan\varphi_1/\sqrt{1-e^2})
\end{aligned}\right\} \tag{4}$$

ただし e は地球楕円体の離心率で，$\sin d_1$，$\cos d_1$，ρ_1 は

$$\left.\begin{aligned}\sin d_1&=\sin d/\rho_1\\ \cos d_1&=\sqrt{1-e^2}\cos d/\rho_1\\ \rho_1^2&=1-e^2\cos^2 d\end{aligned}\right\}\tag{5}$$

から得られる．

なお ξ，η，ζ と ξ，η_1，ζ_1 の関係は

$$\left.\begin{aligned}\eta_1&=\eta/\rho_1\\ \zeta_1&=\sqrt{1-\xi^2-\eta_1^2}\\ \zeta&=(\sqrt{1-e^2}\,\zeta_1-e^2\sin d\cos d\eta_1)/\rho_1\end{aligned}\right\}\tag{6}$$

である．

第6節では各線の計算式を ξ，η，ζ までにとどめ，それ以後の計算は(4)〜(6)式による単なる座標変換でほとんど同一であるから省略してある．

また，日食時には月影方向と太陽方向とはせいぜい $\tan^{-1}(\pi_\odot/\pi_\mathbb{C})\fallingdotseq 0.^\circ 147$ 程度しか違わないので，ある地点での太陽高度を月影方向の高度で代用している．月影方向の高度 alt は

$$alt=\sin^{-1}(\sin\varphi\sin d+\cos\varphi\cos d\cos\theta)$$

であるが，$\sin alt$ と ζ_1 との間には

$$\zeta_1=\sqrt{1-e^2}\sin alt/(\rho_1\sqrt{1-e^2\sin^2\varphi})\tag{7}$$

の関係があることから，日出日没条件 $\sin alt=0$ は $\zeta_1=0$ で代用できる．$\zeta_1=0$ は一つの平面を表すが，地球上の点であるかぎり $\xi^2+\eta_1^2-1=0$ となる．

6. 各線の計算式

(a) 中心線（線コード10，端点コード①，②，コードの意味は第4節参照）

ある時刻の中心線上の一点（ξ，η，ζ）は，その時刻の月影円錐の軸と地球楕円体との交点のうちの一つである．すなわち $(x-\xi)^2+(y-\eta)^2=0$ から

$$\left.\begin{aligned}\xi&=x\\ \eta&=y\end{aligned}\right\}\tag{8}$$

かつ $\zeta_1>0$ を満足させる ξ，η である．この中心線の両端点の時刻は未知であるから (8) 式と $\zeta_1=0$ を満たす時刻を求め，この時刻に対する ξ，η_1 を計算して端点を得る．

(b) 皆既（金環）食限界線（線コード11，12，端点コード③，④，⑤，⑥）

ある時刻の本影錐とベッセル基準面に平行で距離 ζ にある平面との交線は円

$$(x-\xi)^2+(y-\eta)^2-(l_2-\zeta\tan f_2)^2=0\tag{9}$$

となる．この(9)式と(3)式とを連立させて得た解（ξ，η，ζ）は本影錐と地球楕円体上との交線上の1点である．この交線は時間経過とともに地表上を移動するが，この曲線群によって1本又は2本の包絡線が地表に生ずる．これが限界線である（限界線は Figure 5 に見られるように通常は南北に2本現れるが，その一方を欠く型となることも多い．以下の記述ではその都度断ることを省略する．）．

この線上に ξ，η，ζ が存在する条件は

$$(x-\xi)(\dot{x}-\dot{\xi})+(y-\eta)(\dot{y}-\dot{\eta})-(l_2-\zeta\tan f_2)(\dot{l}_2-\dot{\zeta}\tan f_2)=0\tag{10}$$

である．$\dot{\xi}$，$\dot{\eta}$，$\dot{\zeta}$ は未知数 ξ，η，ζ の時間微分であるが，ξ，η，ζ が地表上にある限り

$$\left.\begin{aligned}\dot{\xi}&=\dot{\mu}(-\eta\sin d+\zeta\cos d)\\ \dot{\eta}&=\dot{\mu}\xi\sin d-\dot{d}\zeta\\ \dot{\zeta}&=-\dot{\mu}\xi\cos d+\dot{d}\zeta\end{aligned}\right\}\tag{11}$$

であるから未知数の数は増えない.

補助角 Q (Q のベッセル基準面上，および天球上における幾何学的意味は第 4a，4b 図のとおりであって，実は月影方向から月の中心へ向かう北極方向角である.) を

$$\left.\begin{aligned}x-\xi&=(l_2-\zeta\tan f_2)\sin Q\\ y-\eta&=(l_2-\zeta\tan f_2)\cos Q\end{aligned}\right\}\tag{12}$$

によって導入すると，これは(9)式を満足させ，(12)式を(10)式に入れて整理すると，

$$\tan Q=(B-\zeta\sec^2 f_2\,\dot{d}-A\sec Q)/(C-\zeta\cos d\sec^2 f_2\dot{\mu})\tag{13}$$

となって，$\tan Q$ を求めることに帰する．ただし A，B，C は

$$\left.\begin{aligned}A&=-\dot{l}_2-x\cos d\tan f_2\dot{\mu}+y\tan f_2\dot{d}\\ B&=-\dot{y}+x\sin d\dot{\mu}+l_2\tan f_2\dot{d}\\ C&=\dot{x}+(y\sin d+l_2\tan f_2\cos d)\dot{\mu}\end{aligned}\right\}\tag{14}$$

である．(13)式の右辺に未知量 Q，ζ が入っているので逐次近似法によって解く．限界線上の点である限り $\sec Q$ は $+1$ 又は -1 に近い値をとり，ζ は 0～1 の範囲の値をとるから，出発値として $\zeta=0$，$\sec Q=\pm1$ を採用する．

(13)式の収束値が限界線上の $\tan Q$ を与え，これから(12)式により，$\sec Q>0$，$\sec Q<0$ に対応して 2 点の ξ，η が求まる．これらの点を連ねた曲線が南北限界線となる．これらはそれぞれ両端をもっているが，その端点の時刻は未知であるから，限界線上にあり，かつ $\zeta_1=0$ を満足させる時刻を求める．この時刻に対する ξ，η から端点の経緯度が得られる．

(c) 分食限界線 (線コード21，22，端点コード⑦，⑧，⑨，⑩)

(9)，(10)，(12)，(13)，(14)式で，l_2，$\tan f_2$，$\sec f_2$ を l_1，$\tan f_1$，$\sec f_1$ にして求めた解が分食南北限界線上の点である．端点についても同様である．

(d) 日出没食甚線 (線コード51，52，61，62，端点コード⑮，⑯，⑦，⑧，⑨，⑩，Figure 6)

この線上の点では，日出没時に食分が最大となる．すなわち $\zeta_1=0$，$\dot{D}=0$ を同時に満たす地点である．ここに $D=(L_1-\Delta)/(L_1+L_2)$，$L_1=l_1-\zeta\tan f_1$，$L_2=l_2-\zeta\tan f_2$，$\Delta^2=(x-\xi)^2+(y-\eta)^2$ である．

補助角 Q を $x-\xi=\Delta\sin Q$，$y-\eta=\Delta\cos Q$ のように導入すると，$\dot{D}=0$ は

$$\tan Q=\frac{\sec Q\{\dot{L}_1L_2-\dot{L}_2L_1+(\dot{L}_1+\dot{L}_2)\Delta\}-(L_1+L_2)(\dot{y}-\dot{\eta})}{(L_1+L_2)(\dot{x}-\dot{\xi})}\tag{15}$$

となる．これを変形したのが筆算時代の計算式であるが，それを適用して逐次近似法で解を求めてゆくと，解があるのに収束せず発散することがある．電子計算機で実行させる場合，逐次近似の繰返し回数の上限を決めれば一つの解決法となるが，ここでは(15)式の微小項を省略して

$$(x-\xi)(\dot{x}-\dot{\xi})+(y-\eta)(\dot{y}-\dot{\eta})=0\tag{16}$$

であることを $\dot{D}=0$ の条件式とした．これはベッセル基準面上でベクトル $(x-\xi,\ y-\eta)$ とベクトル $(\dot{x}-\dot{\xi},\ \dot{y}-\dot{\eta})$ とのスカラー積が 0，すなわち直交するとを意味する．

(16)を満足する ξ，η を求める方法として，$M=\tan^{-1}(x/y)$ によって M を求め，α をパラメータとして

$$\left.\begin{aligned}\xi&=\sin(M\pm\alpha)\\ \eta_1&=\cos(M\pm\alpha)\end{aligned}\right\}\quad(\alpha>0)\tag{17}$$

によって ξ,η_1 を，この ξ,η_1 を用い(6)，(11)式から $\dot{\xi}$，$\dot{\eta}$ を求めて $K=(x-\xi)(\dot{x}-\dot{\xi})+(y-\eta)(\dot{y}-\dot{\eta})$ を計算する．一般に $K\neq0$ であるが，$K=0$ になるせいぜい2個の α_1，$-\alpha_2(\alpha_1,\ \alpha_2>0)$ が見つかれば，この α_1，$-\alpha_2$ に対する2組の $(\xi,\ \eta)$ が日出没食甚線上の点である．勿論 $(x-\xi)^2+(y-\eta)^2\leqq L_1^2$ を満足させない $\xi,\ \eta$ は捨てる．

ある時刻に対し，この線上の2点が存在するならば，端点⑮又は⑯は必ずその付近で見つかる．どの時刻に対しても1点しか存在しなければ端点⑮，⑯いずれも存在しない．詳細は第8節参照（従来，端点⑮，⑯は計算していなかったが，第3節で述べた方法を採用する限り必要な点である．これを仮に日出没食甚線の時間的端点と名づける）．

(e) 同時初き復円線（線コード71，72，73，74，75，端点記号A，B，C，F，I，L，M，N，Figure 7）

ある時刻の地球楕円体と半影錐との交線のうち次式を満足させる ξ，η_1，ζ_1 が同時初き復円線上の点である．

$$\left.\begin{aligned}&(x-\xi)^2+(y-\eta)^2=(l_1-\zeta\tan f_1)^2\\ &\zeta_1=\sqrt{1-\xi^2-\eta_1^2}\end{aligned}\right\}\tag{18}$$

これを解くために補助角 Q をパラメータとして

$$\left.\begin{aligned}\eta&=x-(l_1-\zeta\tan f_1)\sin Q\\ \eta&=y-(l_1-\zeta\tan f_1)\cos Q\end{aligned}\right\}\tag{19}$$

の式から逐次近似法によって(19)式を満たす ξ，η，ζ を求める．出発値として $\zeta=0$ を採用し，解が得られない場合には $\zeta=1$ を出発値として再度解を求め，それでも解がない場合はじめて，その Q に対する解はないと判定する．この時刻に(f)線すなわち日出没初き復円線上の2点が存在すれば，それを両端点とする曲線となる．さらにこの線は一般に(c)線すなわち分食限界線と2点で接している．詳しくは第8節参照．

(f) 日出没初き復円線（線コード31，32，41，42，端点コード⑪，⑫，⑬，⑭，Figure 8）

ある時刻の地球楕円体と半影円錐との交線は楕円体上に閉じた曲線となるが，このうち $\zeta_1<0$ となる点は太陽を地平線下に見る地点であるから捨てる．$\zeta_1>0$ となる点が(e)の同時初き復円線上の点であり，$\zeta_1=0$ になる2点が日出没初き復円線上の2点である．

$M=\tan^{-1}(x/y)$，$m=\sqrt{x^2+y^2}$ によって M，m を定め，

$$\left.\begin{aligned}\sin\frac{P-M}{2}&=\pm\sqrt{\frac{(l_1-\zeta\tan f_1)^2-(m-p)^2}{4mp}}\\ p&=\sqrt{1-e^2\cos^2 d}\Big/\sqrt{(1-e^2)\sin^2P+\cos^2P}\\ \xi&=p\sin P\\ \eta&=p\cos P\end{aligned}\right\}\tag{20}$$

から ξ，η を逐次近似法によって求める．出発値は $\zeta=0$，$p=1$ とする．一般に $\sin\{P-M)/2\}>0$ と $\sin\{(P-M/2\}<0$ との二つの解があるが，時間の経過とともに解の数は次のように変動する．

解の数	0	1	2	[1	0	1]	2	1	0
端点コード		⑪		[⑬		⑭]		⑫	

括弧の中の解が存在しない場合もあり，Figure 5 のⅡ～Ⅴ型がこの場合の日食図の型である．端点⑪，⑫の

時刻では(21)式，端点⑬，⑭の時刻では(22)式を満足する．

$$m-p-l_1+\zeta \tan f_1=0 \tag{21}$$

$$m-p+l_1-\zeta \tan f_1=0 \tag{22}$$

7. 日食図の分類

日食図は(21)，(22)式の解の有無，(a)の中心線の有無によって次のように分類される（Figure 5 参照）．

型	分　　類	日　食　図　の　特　徴
I	(22)式の解がある	第6節の(a)～(f)線全部がある．(d)は2本に，(f)は2つの閉曲線にそれぞれ分離される．(e)線の閉曲線も存在する．
	(22)式の解がなく，(21)式の解はある	(c)線のどちらか1本がある．(d)は1本の曲線に，(f)は1つの閉曲線になる．(e)の閉曲線は存在しない．
	(a)線がある	
II	(b)線　2本がある	
III	(b)線　1本だけある	
	(a)線がない	
IV	(b)線　1本だけある	
V	(b)線　ない	

8. 各線の分類

第6節の(a)，(b)，(c)の各線は，存在するか否かの二者択一であるから自動図化という点から単純な判断ですむ．(d)，(e)，(f)の各線は流れ図1，2，3のような判断のトリーで分類してプログラム化した．

9. 区間縮小法

日食計算では $f(x)=0$ の根，および $f'(x)=0$ の根を求めるという場合がしばしばある．実根の数は0個，1個，2個のうちのいずれかという比較的単純な方程式であるが，根の付近で $f'(x)$ が零に近い場合を解かねばならないことが必ずある．

一般に根を求める方法として

(i) $f(x)$ を多項式 $P(x)$ で近似させ，$P(x)=0$ の根をもって代用する．

(ii) 2分法によって零点を見つける．

(iii) ニュートン法に代表される逐次近似値法による．

などが考えられるが，日食計算の場合は以下のような理由で電子計算機によって根を求める場合いずれも不適当と考えられるので独自の方法を用いることにした．

(i)の場合　$P(x)$ の零点と $f(x)$ の零点との相違が無視し得なくなる場合が生じ，極端な場合 $P(x)$ に零点はあるが，実際には $f(x)$ の零点がない，この逆に $P(x)$ の零点はないが，実際には $f(x)$ に零点があるというようなことが起きる．

(ii)の場合　方法としては確実であるが，零点を見つける過程で，区切りの目が粗いとその間に2根が入ってし

まい，根なしという判断をする可能性が生ずる．それを回避するためには区切り目を密にする他ないが，無駄な計算を多数回実行しなければならなくなる．この無駄を省くために2分法適用の区間を狭めてから実行すればよいようだが，その見当をつけるための判断は容易でない．

(iii)の場合　$f'(x)$ を分母にもつ分数式から近似値を求めるが，$f'(x)\fallingdotseq 0$ 付近の根の場合，近似値の数列が発散する可能性があり，収束したとしても精度の悪い根が得られる．

本プログラムでは，日食計算に登場する $f(x)$ が比較的簡単な関数で解析的な表示で与えられており，$f'(x)$ も容易に求まることを考慮し，日食の継続する時間内では，$f(x)$ をすべて下に凸な関数に変形し，はじめに

(a) $f(x)=0$, $f'(x)<0$　(b) $f'(x)=0$ 又は $f(x)=0$, $f'(x)=0$　(c) $f(x)=0$, $f'(x)>0$

となる点を含む高々3個の区間を下記の方法で見つけ出し，この区間を更に10分割して再び下記の方法で(a), (b), (c)を満たす区間を見つけ出す等等，この手続きを繰返して各区間幅を徐々に狭めてゆく方法を採った．この繰返しの過程で(a), (b), (c)を満たす区間は分離され，3組の非常に狭い区間が見つけ出される．

上記(a), (b), (c)を満足する区間の選び出し方を下に示す．x の関数 $f(x)$ があって，日食の時間中 $f''>0$ であり，かつ $f=0$, $f'=0$ になる x の値を見つけるために，$x=A$, $B(A<B)$ での f, f' をそれぞれ f_A, f_B, f'_A, f'_B とすると，任意の閉区間 $[A, B]$ における $f=0$, $f'=0$ の根の有無を，次のように分類して判定する．

分類3　区間 $[A, B]$ における $f=0$, $f'=0$ の根の有無

分類番号	f_A の値	f_B の値	f'_A の値	f'_B の値	(a)等を満足させる点，又は区間		
					(a)	(b)	(c)
1	0	+	0	+	−	A	−
2	0	+	+	+	−	−	A
3	0	−	−	0	A	B	−
4	0	−	−	−	A	−	−
5	0	−	−	+	A	(A, B)	−
6	+	0	−	0	−	B	−
7	+	0	−	−	B	−	−
8	+	0	−	+	(A, B)	(A, B)	B
9	+	+	0	+	−	A	−
10	+	+	−	0	−	B	−
11※	+	+	−	+	(A, B)?	(A, B)	(A, B)?
12	+	−	−	0	(A, B)	B	−
13	+	−	−	+	(A, B)	(A, B)	−
14	+	−	−	−	(A, B)	−	−
15	−	0	+	+	−	−	B
16	−	+	0	+	−	A	(A, B)
17	−	+	+	+	−	−	(A, B)
18	−	+	−	+	−	(A, B)	(A, B)
19	−	−	−	0	−	B	−
20	−	−	−	+	−	(A, B)	−
21	0	+	−	+	A	(A, B)	(A, B)
22	−	−	0	+	−	A	−
23	−	0	−	+	−	(A, B)	B
24	−	0	0	+	−	A	B
25	0	0	−	+	A	(A, B)	B

※　この場合には開区間 (A, B) 中に $f'=0$ を満たす根は必ずあるが $f=0$ を満たす根は2又は0である．区間を縮小してゆくうちにどちらかであることが分かってくる．

分類3に現れた以外の組合せの場合はすべて，区間 $[A, B]$ 中では(a), (b), (c)のいずれも満足させない．

10. 結　語

このプログラムを用いて描いた日食図は，1980年，1981年の天体位置表付録にそれぞれ「1981～1985年の日食」「1986～1990年の日食」と題した日食予報資料の中の付図として掲載されている．ここでは一例として2012年5月20日の金環食図を第9図に掲げた．中心線が日本を通る一番近い将来の日食である．

プログラムの仕様的なことには一切触れなかったのでここで簡単に述べる．プログラムはフォートラン文で書き，主プログラムは2331ステートメント，サブルーチンは29個で延べ1242ステートメント，総計3573ステートメント，完成時の電子計算機はＮＥＡＣ2200/500であったが，現在はＡＣＯＳ700であるので，そのためのプログラム変換を行った．月・太陽のデータは電子計算機から得られた出力を入力として使用しているが，将来は月・太陽の各プログラムと自動図化プログラムとを連結してゆく予定である．

所要時間は，日食の規模によってかなり変動するが，日食図各線の経緯度群を完成し磁気テープに記録するまで10分，この経緯度群をＸＹプロッター用に変換し，さらに地球の経緯線，世界地図線の xy 座標への変換をも合わせて30分，ＸＹプロッターで日食図各線，経緯線，世界地図を描くのに40分，総所要時間は最大で80分である．作業開始は1975年夏，完成は1977年秋であった．

このプログラムのＸＹプロッター用のための変換と経緯線，世界地図記入の部分のプログラムに関しては小野寺健英氏に，例題の計算とＸＹプロッターによる日食図作成に関しては平岩恒廣，上田守両氏に全面的に負うている．深く感謝の意を表する．またこの小論を草するに当って終始支援下さりいろいろ教示下さった山崎昭編暦課長，佐藤典彦海洋研究室長，斉藤甫海洋研究室研究官，久保良雄主任天文調査官に感謝の意を表する．

参　考　文　献

鈴木敬信，1949：日食計算論，恒星社厚生閣，東京，5～115ページ

Chauvenet, W, 1908: A Manual of Spherical and Practical Astronomy, vol. I, J. B. Lippincott Co., Philadelphia, pp 436—542

Smart, W. M, 1960: Text-Book on Spherical Astronomy, 4th ed., Cambridge University Press, London, pp 386—401

H. M. Nautical Almanac Office, 1961: Explanatory Supplement to the Astronomical Ephemeris, H. M. Stationery Office, London, pp 214—257

流れ図 1　(d) 線の分類のトリー (Figure 6参照)

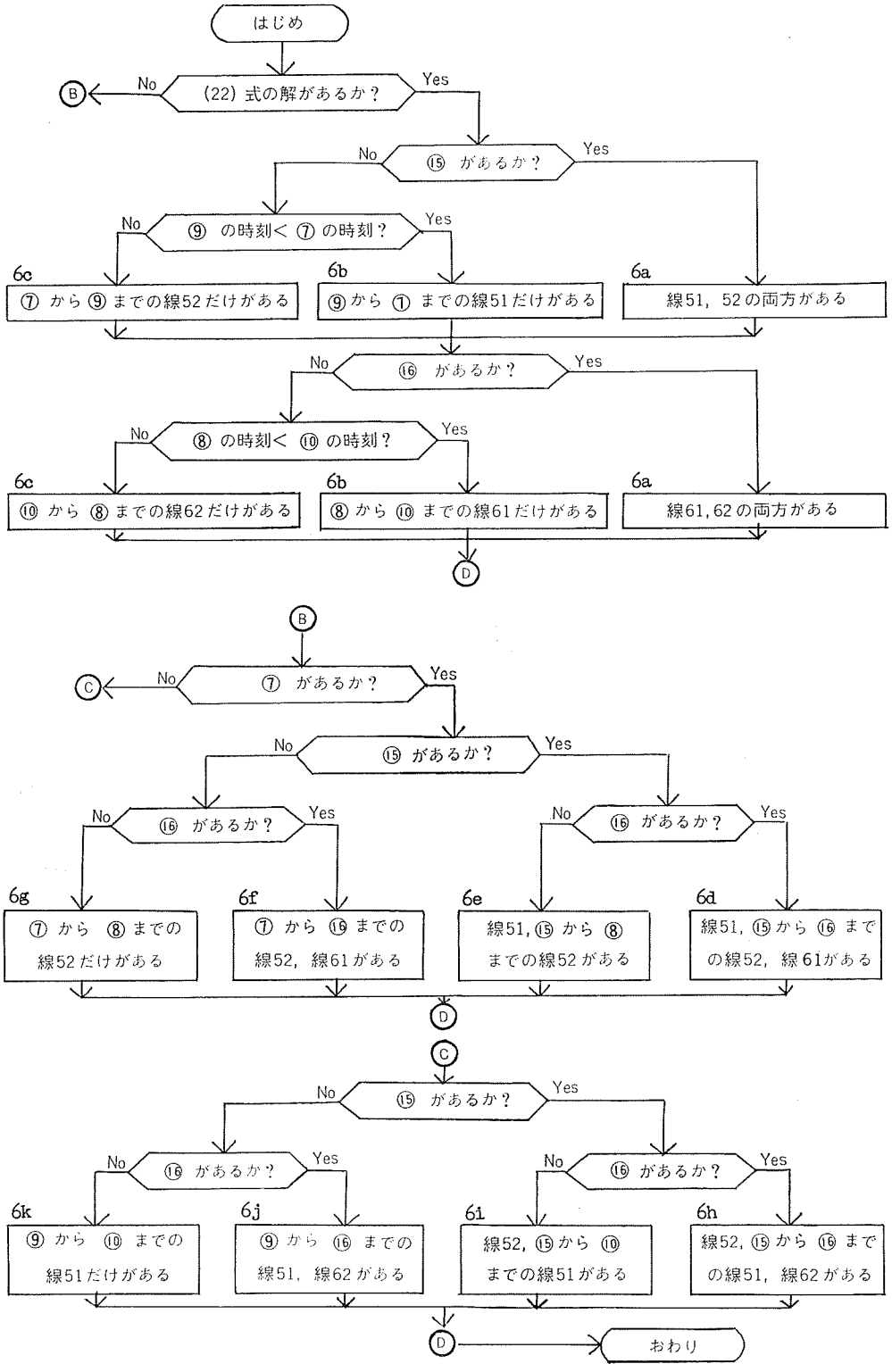

流れ図 2　(e) 線の分類のトリー (Figure 7 参照)

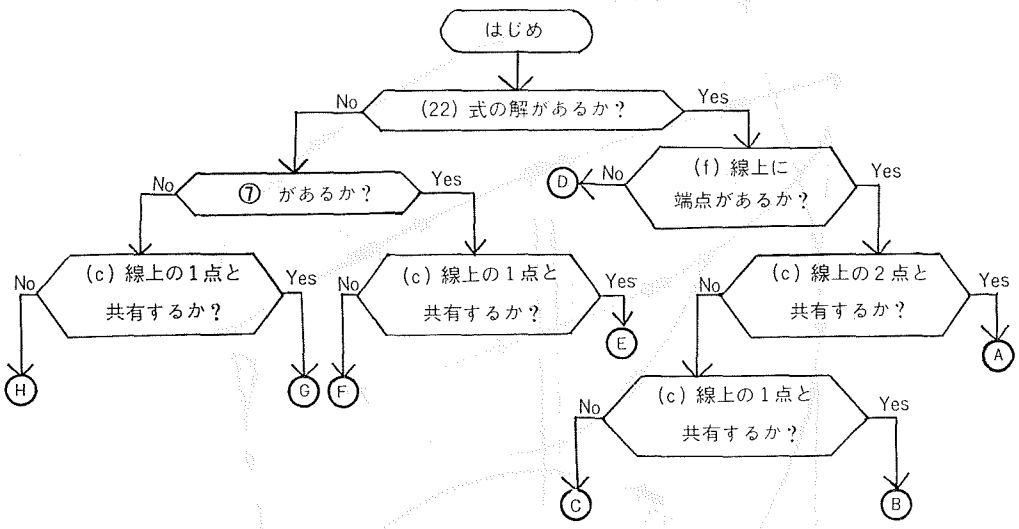

A	(f) 線上に両端点をもち、両 (c) 線に接する	7a
B	(f) 線上に両端点をもち、(c) 線の一方に接する	7b 7c
C	(f) 線上に両端点をもち、(c) 線のどちらにも接しない	7d
D	(c) 線上の2点と共有し、両 (c) 線に接する閉曲線となる	7e
E	(f) 線上に両端点をもち、北の (c) 線に接する	7f
F	(f) 線上に両端点をもち、(c) 線には接しない	7g
G	(f) 線上に両端点をもち、南の (c) 線に接する	7h
H	(f) 線上に両端点をもち、(c) 線には接しない	7i

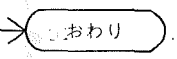

流れ図 3　(f) 線の分類のトリー (Figure 8 参照)

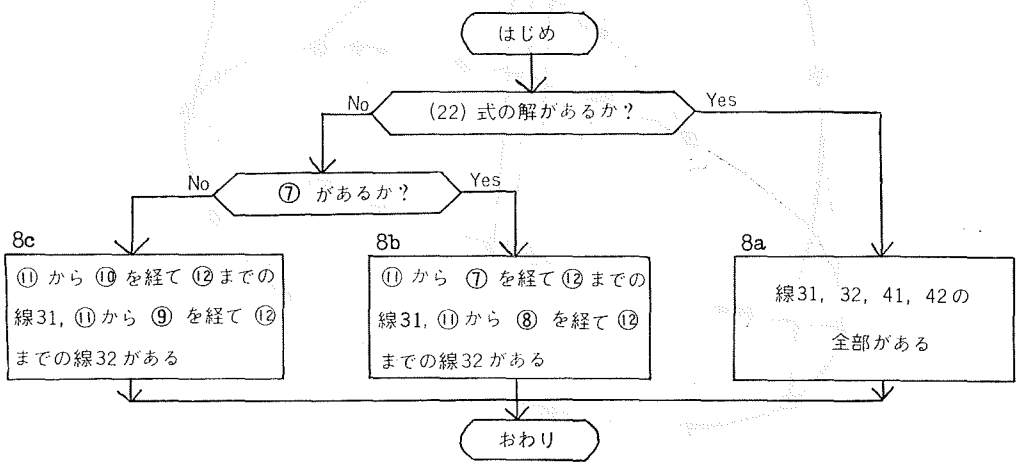

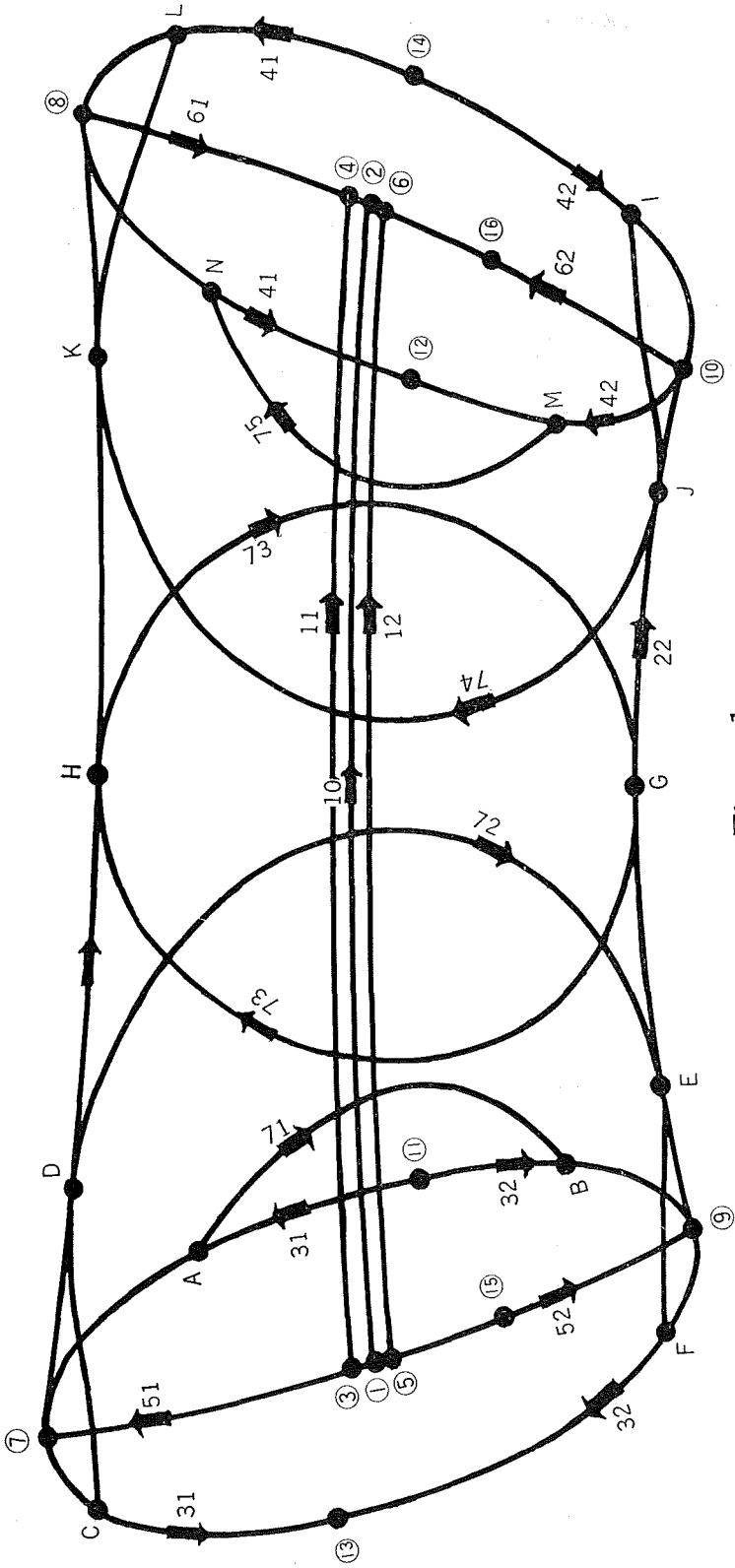
L
⑧
⑭
41
61
42
I
④
②
⑥
⑯
62
N
41
K
⑫
M
42
⑩
J
73
11
12
74
22
H
10
G
72
73
E
71
D
⑪
32
B
⑨
A
31
⑮
52
F
51
③
①
⑤
32
⑦
31
C
⑬

Figure 1

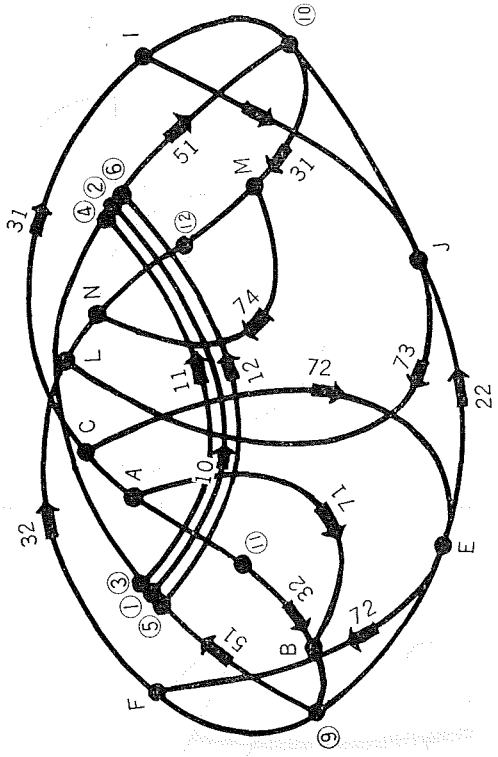

Figure 3

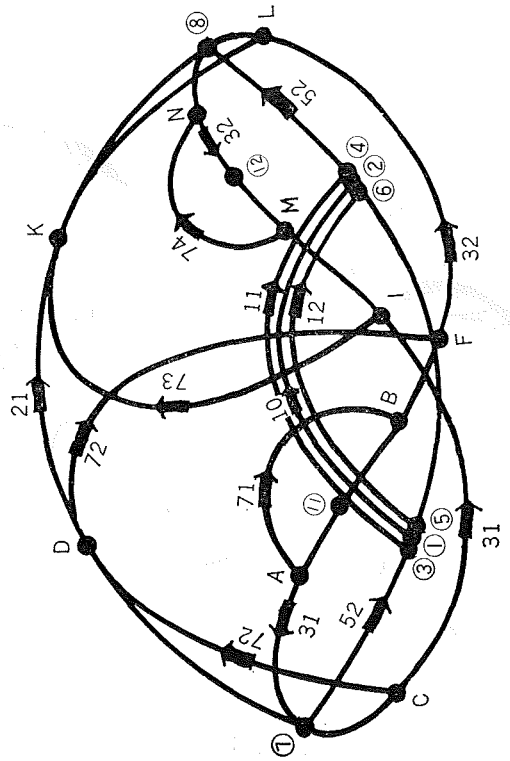

Figure 2

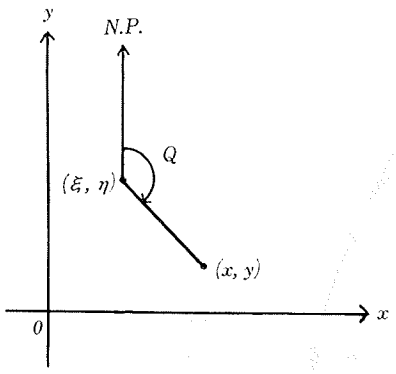

Figure 4a

Q, on the Besselian fundamental plane

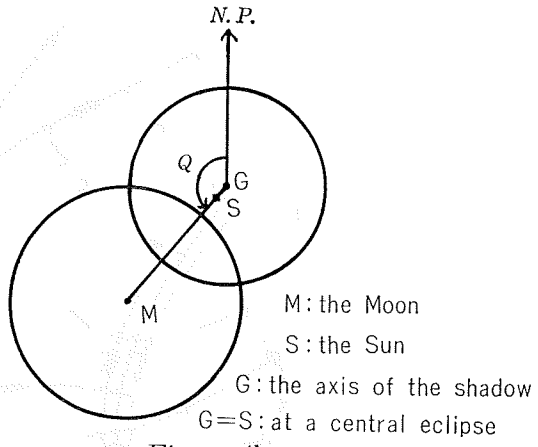

Figure 4b

Q, on the celestial sphere

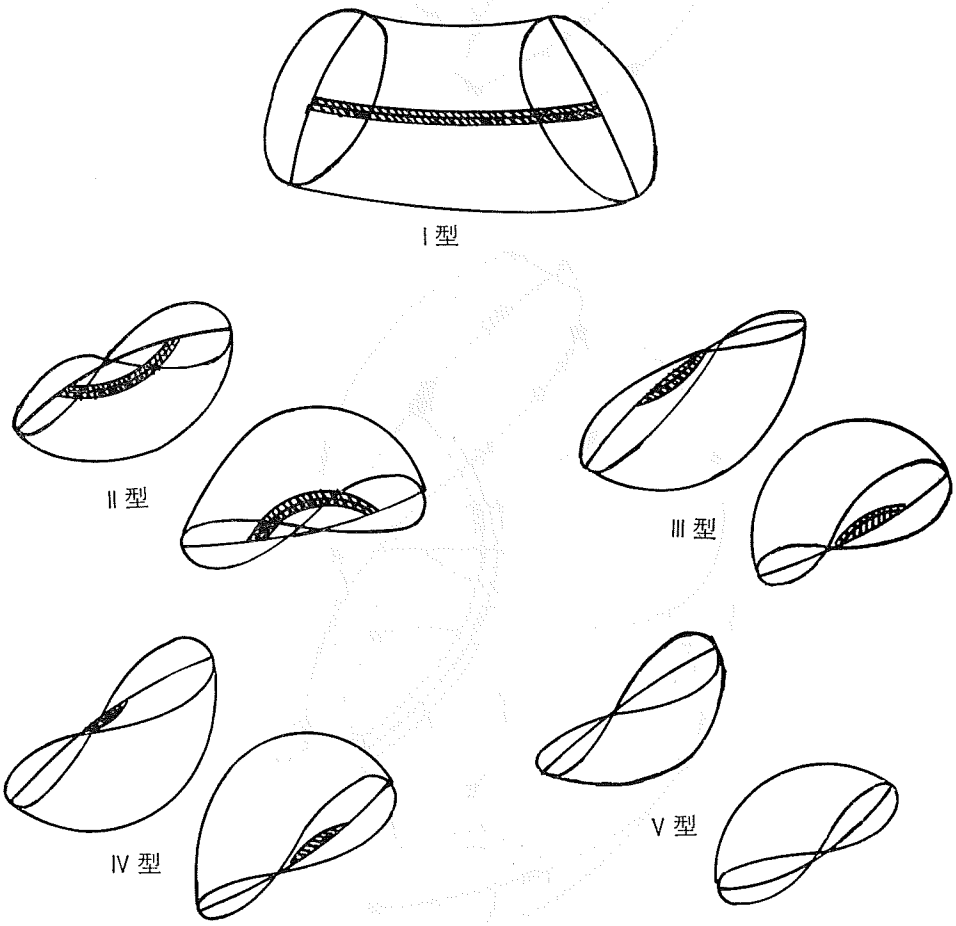

Figure 5

(d) の分類

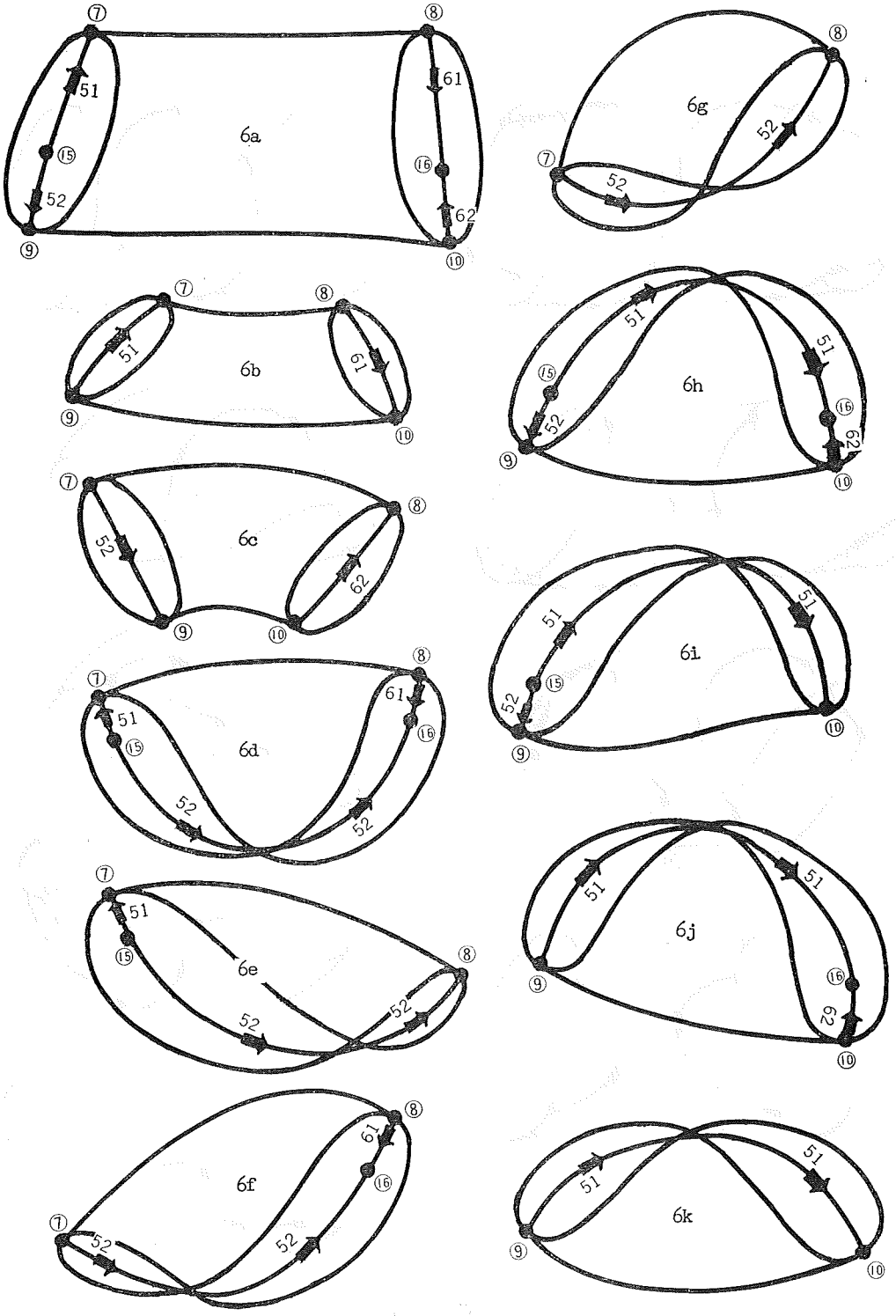

Figure 6

(e) の分類

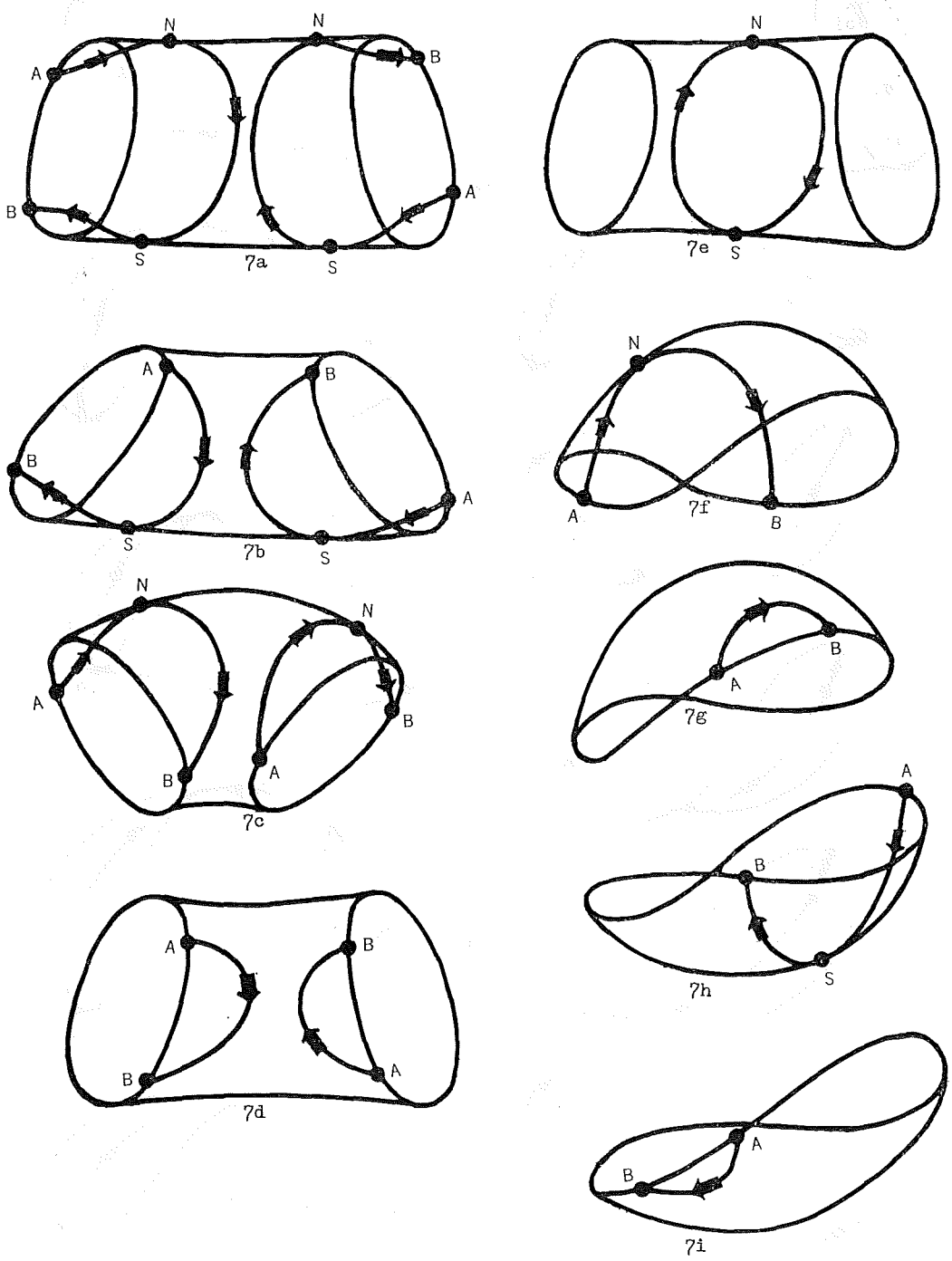

Figure 7

(f) の分類

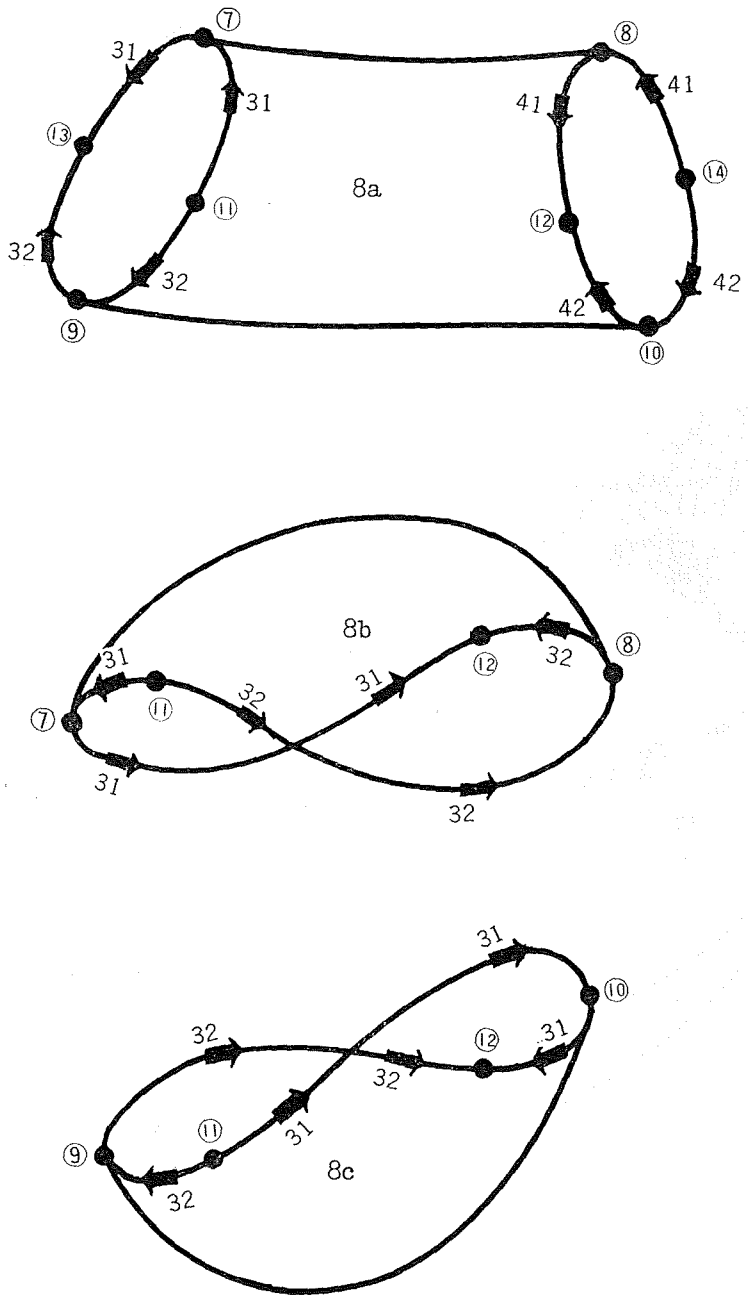

Figure 8

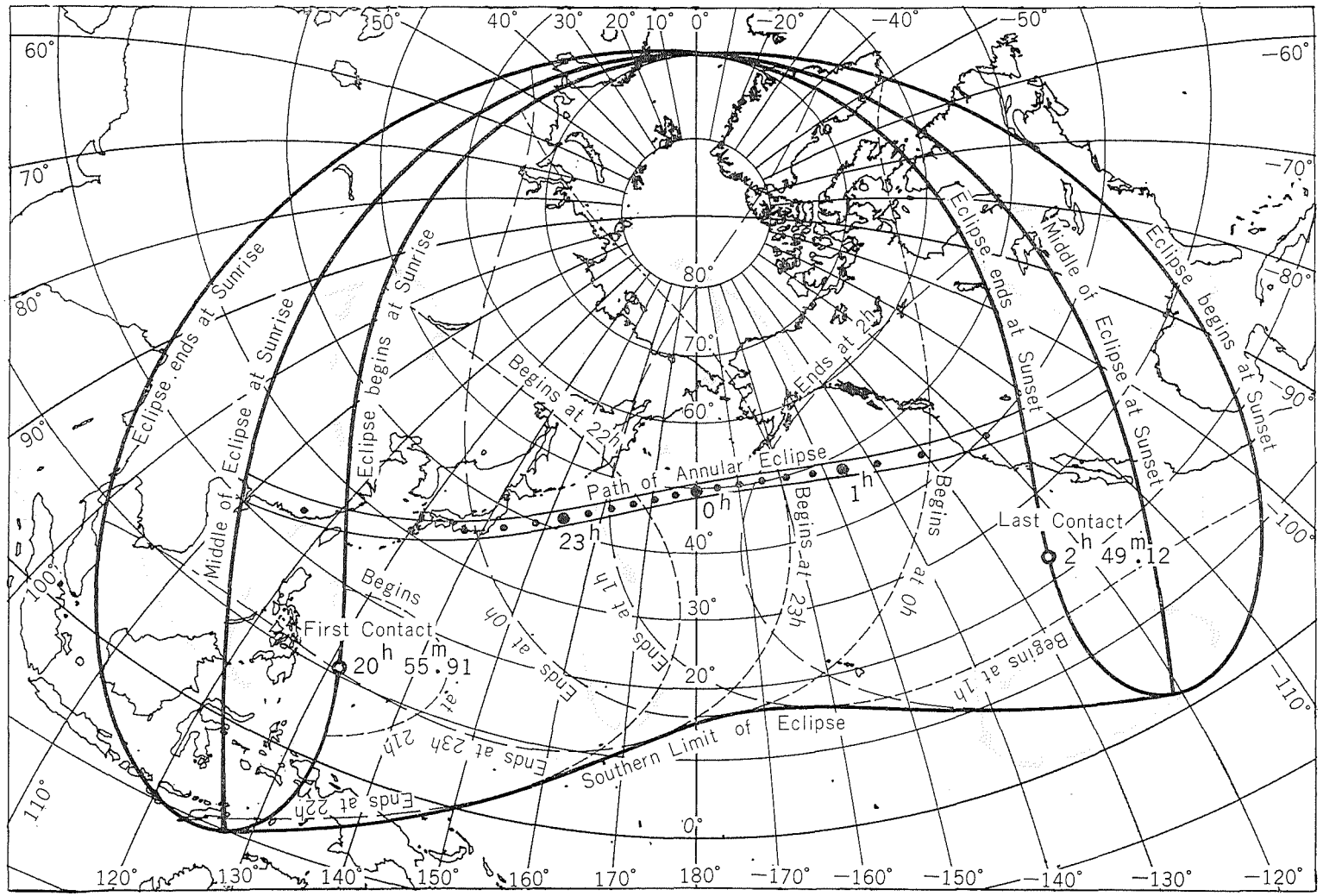

Figure 9 2012 May 20, 21 Annular Eclipse U.T. $\triangle T = 80^s$

REPORT OF HYDROGRAPHIC RESEARCHES No. 15, March, 1980

二重同期による高安定位相同期受信システム

小野房吉*

HIGH-STABILITY PHASE-LOCKED RECEIVING SYSTEM OF THE DOUBLE PHASE-LOCKED CIRCUIT

Fusakichi Ono*

Received 1979 September 10

Abstract

In the cases of the conventional types of receivers designed for the highly accurate measurement of phase by receiving standard radio waves or waves for a radio navigation aid system, it has been customary to depend on the phase-lock receiving method using only one VCO (Voltage Controlled Oscillator); however, the receivers depending on this method are known to have some common shortcomings that are inescapable theoretically. In other words, in the conventional type of receiver, the received wave tends to become unstable, especially after the reception has been interrupted by some cause.

In the phase-locked receiving method introduced here, two phase-locked oscillators (one for a high-sensitivity VCO used in the conventional receiver and the other for a high-stability VCO of low control sensitivity) are used so that, even when the receiving conditions are poor, the performance of the receiver can be kept stable, because the Doppler frequency of the received wave can be corrected for automatically by the second VCO depending on the velocity of motion of the receiver, without adverse effect on the high-speed tracking ability of the receiver.

The principle of this phase-locked receiving method has been applied to the conventional Loran-C automatic tracking receiver as a means for improving its capability. Its accuracy and stability have been improved to almost five times those of the conventional receiver.

1. まえがき

標準電波や無線航行援助システムの電波を受信して，高精度の時刻・位相・周波数等の測定を行う受信機では，電波伝ぱ途中において，信号電波は雑音によって細かな位相変調を受けるから，直接測定では高精度は期待できない．そこで通常このような受信機では局部発振器の位相を受信電波の平均位相に同期させて，この局部発振器の位相又は周波数を測定する間接測定法が用いられる．この報告は，このような位相同期受信システムに関するものである．従来の位相同期受信システムが，同期発振器として高感度な電圧制御発振器1個を用いたのに対して，この報告の方式では，高感度電圧制御発振器と高安定低感度電圧制御発振器の2個を用いて，動く船舶上で

* 編暦課 (Astronomical Division)

使用した場合にも高精度，高安定な位相同期受信を可能にしたものである．以下従来方式の問題点を指摘し，本方式の原理と適用例について述べる．

2. 従来の位相同期受信システムの問題点

Figure 1 は従来の位相同期受信システムのブロック図である．位相同期受信システムとは，受信機内部に受信電波の周波数と同じか，又は整数比の関係の周波数が電圧で制御できる局部発振器（以下ＶＣＯと云う）を内蔵していて，この発振器の位相と受信電波の平均位相を位相比較器（以下ＰＤと云う）で比較して位相誤差電圧を

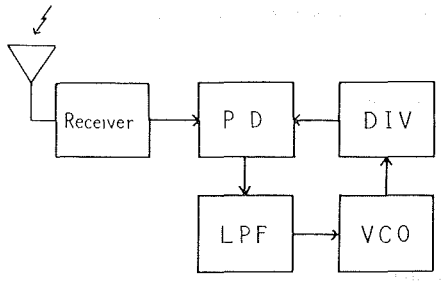

PD ; Phase Detector
DIV ; Divider
VCO ; Voltage Control Oscillator
LPF ; Low Pass Filter

Figure 1 Simplified diagram of the phase-locked receiving system

得，この誤差電圧が零又は一定の電圧になるようにＶＣＯの発振位相を制御して受信電波に同期させ，この発振器の位相を測定することによって，間接的に受信電波の位相を測定する受信方式である．この方式では，同期誤差を少なくし追尾性能をよくするために，制御感度の高いＶＣＯが用いられる．そのため，このＶＣＯは電圧変化に弱く，制御電圧にわずかな雑音が含まれても，同期がはずれて動作が不安定となる欠点がある．図によって少し詳しく説明する．

Figure 2 をＶＣＯの電圧―周波数特性，Figure 3 をＰＤの電圧―位相特性とする．f_0 は同期周波数で受信電波の周波数に等しいとする。ここでＶＣＯが f_0 の発振を行う制御電圧 V は V_0 である．また，点線の特性では V' である．この V_0 または V' が Figure 3 の特性のＰＤから得られるとすると，実線の特性のＶＣＯでは同期点が S の位置であり，位相角は零である．また，点線の特性のＶＣＯでは S'，位相角は $\Delta\varphi$ である．

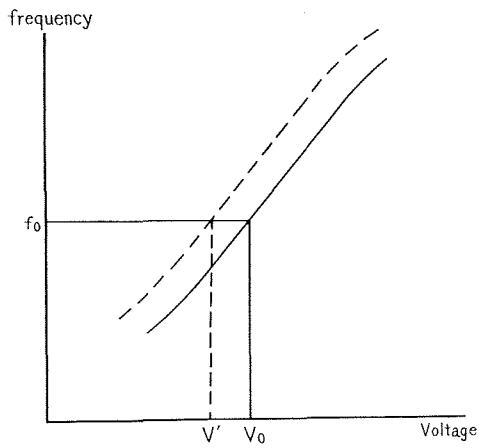

Figure 2 Characteristic curve of voltage-frequency of the VCO

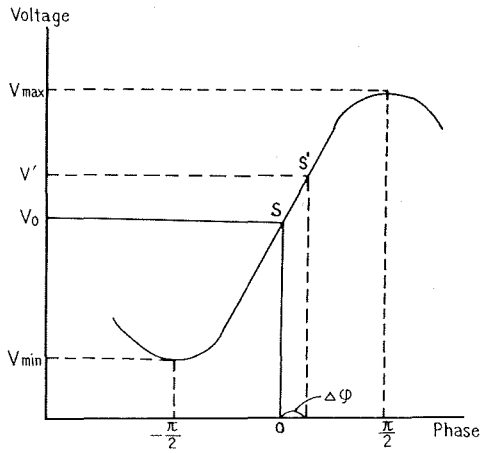

Figure 3 Characteristic curve of voltage-phase of the VCO

いま，実線の特性のＶＣＯが点線の特性まで経時変化したとすると，それはＰＤの動作点を Figure 3 の S から S' に移動させるので，$\Delta\varphi$ の位相誤差を生じる．しかし，この誤差は Figure 2, 3 の特性曲線の急峻なものを用いることによって，いくらでも小さくすることができる．これが前述の制御感度の高いＶＣＯを用いる理由である．

では制御感度の高いＶＣＯを用いるとどうなるか，実例によって説明する．Figure 4 はあるロランＣ自動追尾受信機に用いられたＶＣＯの特性例である．これを見ると電圧に対する周波数変化は $3\times10^{-2}f/V$ である．

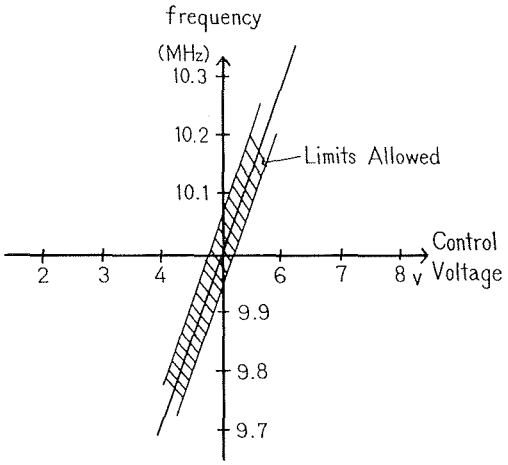

Figure 4 Characteristic curve of an example of the VCO

一方これに用いられていたＰＤの感度は，$\pm\pi/2$ の位相変化に対して $\pm5V$ であった．したがって，ＶＣＯに，1×10^{-4} の経時変化を許したとしても $(1\times10^{-4})/(3\times10^{-2})\times\pi/5=0.002$(rad) つまり比較周波数の約1/3000サイクルの位相誤差しか生じない．しかし，一方これを同期制御動作の安定度の観点から見ると，わずか0.01Ｖの雑音電圧によって，ＶＣＯの周波数は 3×10^{-4} だけ変化することになる．これは１秒間に比較パルスの位相を300マイクロ秒だけ前後させる．0.1秒間でも30マイクロ秒である．しかるに数秒間以上にわたる電波の不調はしばしば起こることであり，通常の使用環境では，ある程度の雑音はさけられないので，このロランＣ受信機は動作が不安定であった．この報告の高安定位相同期受信システムは，このような背景のもとに考案したものであり，受信電波の一時的中断による同期動作の乱調に耐えるための同期安定度の改善と，受信点の移動に伴う受信電波のドップラー周波数に対応する補正電圧が自動的に保存される制御システムとなっている．

3. 二重同期制御システムの原理

Figure 5 で，ＶＣＯ１までのブロックが従来の位相同期受信システム，それ以後のブロックが本考案における付加部分である．動作は，ＶＣＯ１の周波数が適当に分周されて，受信電波の位相とＰＤ１で比較され，この検出電圧がＶＣＯ１に帰還されてＶＣＯ１の位相が受信電波の位相に一定の関係で同期する．一方ＶＣＯ１の位相はＶＣＯ２の位相とＰＤ２で比較され，この比較電圧をＶＣＯ１に供給している．つまりＶＣＯ１は同時に，電波及びＶＣＯ２から同期制御電圧を受けている．そこでＶＣＯ１の同期を電波優先とするために，ＰＤ１からの出力電圧の範囲をＰＤ２からの出力電圧の範囲より，はるかに高く設計しておく．このように設計することによって，受信電波が正常なときは，ＰＤ１に有効な制御電圧が得られ，ＰＤ２からの入力にもかかわらず，ＶＣＯ１は受信電波の位相に優先同期する．次に受信電波が不調のときは，雑音電圧だけとなり，雑音電圧の積

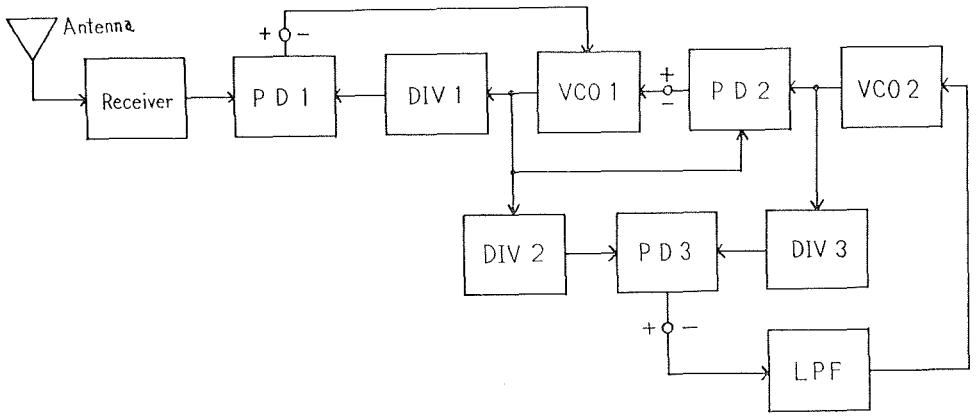

Figure 5 Simplified diagram of double phase-locked receiving system

分は零となって有効な制御電圧がＰＤ１に発生しないから，相対的にＰＤ２からの制御電圧が卓越し，ＶＣＯ１の位相はＶＣＯ２の位相に同期させられる．つまり，受信電波が正常のときはＶＣＯ１は，受信電波の位相に同期し，受信電波が不調のときはＶＣＯ２の位相に同期する．さて，ＶＣＯ１としては先にも述べたとおり，同期精度と制御性能の観点から高安定の発振器は用いることができず，受信電波に対する安定度の低下は止むを得なかったのであるが，Figure 5 の二重同期制御システムでは，ＶＣＯ２に高安定の発振器を用いることによって，ＶＣＯ１に高感度ＶＣＯを用いることから生じる制御動作の不安定を回避することができる．

次に，ＰＤ３による位相比較は，受信電波が正常のときＶＣＯ１と，ＶＣＯ２の間に発生する位相差に対応する誤差電圧をＶＣＯ２に帰還して，受信電波のドップラー周波数偏移を自動補正する回路である．

ＶＣＯ２は高安定発振器で，受信電波の周波数と $\pm 1\times10^{-10}$ 程度に一致させることができる．今ＶＣＯ１とＶＣＯ２の比較がＤＩＶ２，３の分周器で1/100程度に逓降されて行われるとすると，ＰＤ３の出力電圧の最大範囲はＶＣＯ１，ＶＣＯ２の周波数の100サイクルに相当することになる．そこでこの電圧変化に対してＶＣＯ２の周波数変化を，受信点の移動速度の最高値よりやや高い速度対応のドップラー周波数以上に設計しておけば，ＰＤ３には受信点の移動に伴うドップラー周波数に対応した位相差の電圧が発生し，ＶＣＯ２は受信点の移動に伴うドップラー周波数だけオフセットされる．この状態で受信電波がなくなると，ＶＣＯ１は，ＰＤ２の出力電圧によってＶＣＯ２に半サイクル以内で同期させられる．しかるにＶＣＯ２のドップラーによるオフセットは，ＰＤ３の出力電圧で行われており，これはＶＣＯ２の数十サイクルの範囲でなされているから，ＰＤ３にはオフセット電圧が保存されてしまう．これがＶＣＯ２の受信点の移動によるドップラー周波数自動オフセットの原理である．以上がこの考案の最も基本的な部分であり，更に具体的に説明する．

受信電波の周波数を100kHz，ＶＣＯ１，ＶＣＯ２の周波数を10MHz，ＰＤ３での位相比較は100kHzとする．したがってＰＤ２での位相比較は10MHzの半サイクルで最大の位相比較電圧が得られる．通常の位相比較器は，比較周波数の半サイクルの位相変化で，最大範囲の電圧が検出されるが，ＰＤ３はセット・リセットフリップフロップで構成した位相検出器で，この出力電圧を低域フイルタに通して得られる直流電圧の範囲は，比較周波数の１サイクルを最大範囲とし，位相差に直線的に比例する電圧である．このＰＤ３の位相比較電圧の範囲（100kHzの１サイクルに対応）を±５Ｖとし，ＶＣＯ２の周波数変化を±５Ｖの電圧変化に対して $\pm5\times10^{-8}$ とする．いま受信点が電波発射局に対して視線方向に12ノットの速度で近づくとすると，それによるドップラー周波数偏移は 2.1×10^{-8} である．この量がＶＣＯ２に補正されるためには2.1Ｖの電圧がＰＤ３に発生すればよい．ＰＤ３に

2.1Vの電圧が発生するためには，比較周波数の位相差は100kHzの2.1V/10Vサイクル，すなわち2.1マイクロ秒である．これは10MHzでは21サイクルに相当する．さて，受信電波が中断しても，ＰＤ３に10MHzの単位で数えた21サイクル分の位相差が保存されればＶＣＯ２は，電波中断直前の周波数を保持することになる．しかるにＶＣＯ１は，電波中断によって，10MHz の半サイクル以内でＶＣＯ２に同期させられてしまうから，ＰＤ３には確かに10MHzで数えた21サイクル分の位相差は保存される．

4. 適 用 例

水路部測量船「昭洋」に装備されたＬＲ－３型ロランＣ自動追尾受信機は，発振器制御式の位相同期受信システムが採用されているが，前述の理由で，位相同期の安定度は数秒の同期で±１～２マイクロ秒のふらつきを示し，しばしば受信波の１サイクルステップの飛びを生じていた．この不安定を改良するため，前記考案の位相同期システムの適用を試みた．改良は，既存装置にほとんど手をつけることなく，付加装置で行うこととした．装置の設計を Figure 6 に示す．

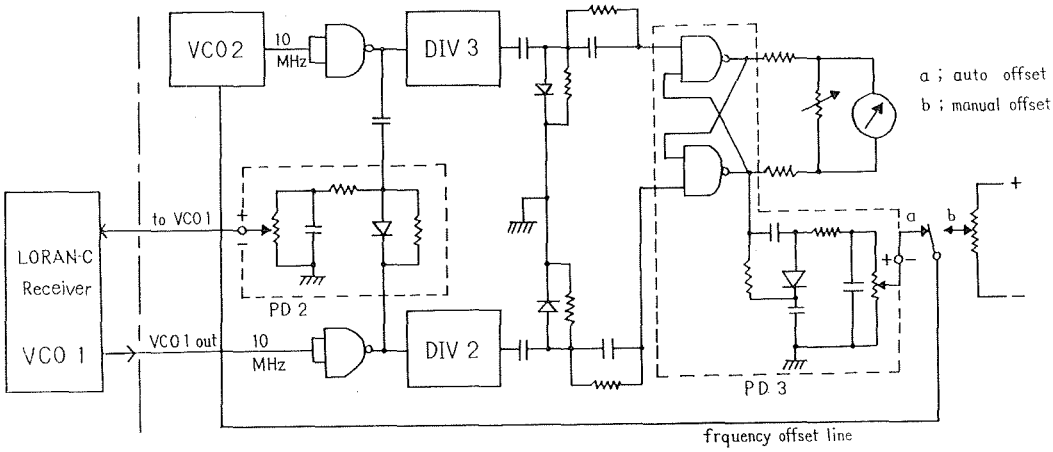

Figure 6 Stabilized circuit of the phase-locked Loran-C receiver

この図で，鎖線の左側が従来のロランＣ受信機で，これに内蔵されたＶＣＯ１を右側の付加装置で安定化するものである．実際のロランＣ自動追尾受信機は同時に３局の電波を受信するのでＶＣＯ１は３個もっている．し

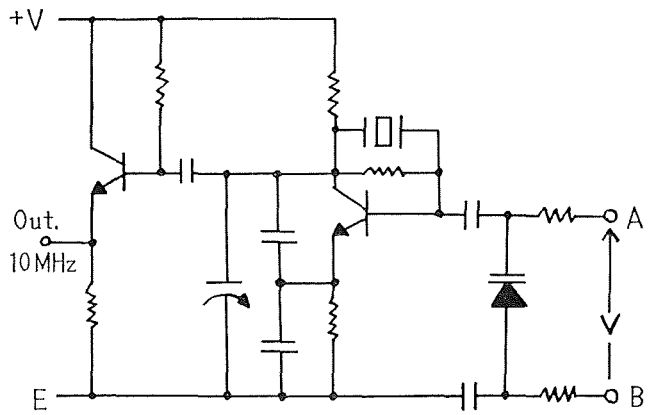

Figure 7 A case of the VCO circuit

たがって Figure 6 の回路は同じものが3セットで1組となる．位相検出器ＰＤ２，ＰＤ３も今回新たに考案したもので，この出力特性はＰＤ２が $V=\kappa\cos\Delta\varphi$，ＰＤ３は $V=\kappa\Delta\varphi$ で $-\pi<\Delta\varphi<\pi$ の範囲では直線的な正負の電圧が得られる．Figure 7 はロランＣ受信機に内蔵されたＶＣＯの回路図である．この発振周波数は，バラクタダイオードの電極間電圧Ｖを変化させることによって変えることができる．Ｖを変化させるには端子Ａの電圧を変えてもよいし，端子Ｂの電圧を変えてもよい．しかし，このＶＣＯは受信電波とＶＣＯ２の二つの比較電圧によって制御するので，端子Ａには受信電波との比較電圧，端子ＢにはＶＣＯ２との比較電圧を加えるようにする．

Figure 8 にこのＶＣＯの合成制御電圧の位相特性を示した．

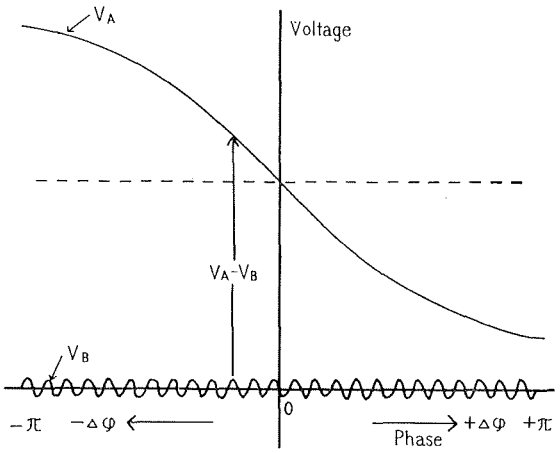

Figure 8 Control voltage of VCO 1

この図から V_A が正常の場合は図のようなカーブを示すので安定点は $\Delta\varphi=0$ の１ケ所であるが，V_A が不調の場合は，このカーブは点線のように横軸に平行になるので，安定点は V_B の零点を切る位置で V_A の半サイクル以内に50ケ所存在することになる．つまり V_A が点線のとき，ＶＣＯ１は直ちにＶＣＯ２の一サイクル以内で同期してしまうので，そのときに加っていたＶＣＯ２のオフセット電圧は保存されてしまう．さて，V_A が正常のとき，受信電波の位相への追尾動作は，V_B の電圧の乗り越えが0.1マイクロ秒ごとなので直線的ではない．しかし V_B の電圧の乗り越えが一定量（受信電波の周波数にＶＣＯ２の周波数が一定の関係で一致したとき）に達すると，ＶＣＯ２が受信電波の周波数にオフセットされてしまうので，V_B の電圧の乗り越えはなくなり直線的な位相追尾が期待できる．

さて，以上の原理で製作された装置は昭和53年11月から12月にかけて測量船「昭洋」で実施された第５次海流観測の際，従来のロランＣ自動追尾受信機に付加設置して洋上試験を実施した．その結果，測定値のふらつきは従来の±１～２マイクロ秒から±0.1～0.2マイクロ秒と約1/10に縮小し，搬送波の一サイクルステップの飛びもほとんどなくなり（数時間に１度程度），まずまずの成果が得られた．Figure 9 に電磁海流計（ＧＥＫ）による海流測定の際，本装置によって得た船位を記入した航跡図の一部を示す．電磁海流計による海流測定のとき航跡は，短時間に針路を直角，180度さらに直角と変針するので，この種の航法装置の分解能，位相追尾性能を確認するには最も好適と考える．これを見ると経度方向にややふらつきが見られるが，緯度方向にはほとんどないことがわかる．

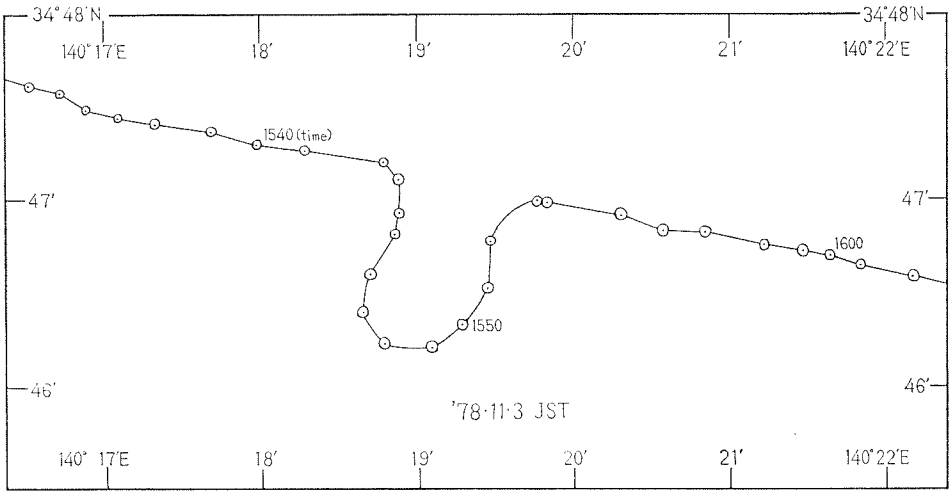

Figure 9 Cruising trail of the sea current observation by GEK

5. あ と が き

ＬＦ電波を用いたロランＣ航法が1955年に米国海軍によって実用化されてからすでに24年，水路部が同航法の利用を始めてからも10年が経過している．にもかかわらず，この受信システムはなお発展段階にあるといってよい．当然，水路部が導入した位相追尾型の受信機も発展途上のもので，精度及び安定度に問題を残していた．本研究はこの改善のために実施したもので，その限りにおいて十分目的を達したものと思う．一方メーカーもこの問題の解決に手をこまねいていたわけではなく，たゆまざる努力の結果，最近では相当安定な受信機を市場に送り出している．しかし，筆者の研究の最終目標は「受信電波の数分間から数十分間にわたる何らかの原因による中断があった場合にも安定動作が可能なこと」でやや厳しく，単なる在来技術の積重ねでは容易に実現不可能と思われたので新技術で対処した．以上，ここでは新技術の一実施例につき詳述したが，この技術はこの他デッカ，オメガ，衛星航法受信機等にも有効であることを付記しておく．最後に本研究の実施にあたって御援助をいただいた徳弘海洋資料センター所長，編暦課森補佐官，試験観測を快く引受けてくれた測量船「昭洋」の観測科の皆さん，そして装置の製作から観測にいたるまで終始協力を惜しまなかった松本邦雄君に深く感謝する．

（この技術は海上保安庁長官から特許出願されている）

参 考 文 献

古野電気ＫＫ：ＬＲ－３型ロランＣ自動航跡記録装置取扱い説明書（1972）

東京計器ＫＫ：ＭＬ―100型マリンロランＡ/Ｃ受信機取扱い説明書（1969）

AUSTRON, Inc. : Model 2000c Loran-C Receiver 取扱い説明書（1967）

小野房吉：ロランＣ電波による時刻及び周波数の比較，水路要報第92号（1973）11―21

電波航法研究会編：電波標識（上，下）鶴巻書店（1975）

光電製作所ＫＫ：ＬＲＭ―710ロランＣ受信観測装置取扱い説明書（1979）